Exclusive ρ^0 production at HERMES

D I S S E R T A T I O N

zur Erlangung des Doktorgrades

des Fachbereichs Physik

der Universität Hamburg

vorgelegt von

Armine Armand Rostomyan

aus Yerevan, Armenien

Hamburg

2008

Gutachter der Dissertation:	Prof. Dr. J. Meyer
	Dr. M. Diehl
Gutachter der Disputation:	Prof. Dr. J. Meyer
	Dr. H. Jung
Datum der Disputation:	1 July, 2008
Vorsitzender des Prüfungsausschusses:	Dr. M. Martins
Vorsitzender des Promotionsausschusses:	Prof. Dr. J. Bartels
Leiter des Departments Physik:	Prof. Dr. R. Klanner
Dekan der Fakultät für Mathematik, Informatik und Naturwissenschaften:	Prof. Dr. A. Frühwald

Abstract

In this thesis the exclusive electroproduction of ρ^0 mesons is analyzed using the data accumulated with the HERMES spectrometer in the years 2002-2005 by scattering the lepton beam of the HERA accelerator off the internal target of HERMES filled with transversely polarized hydrogen gas atoms. The ρ^0 production mechanism and, in a model-dependent way, the structure of the nucleon are studied by measuring the spin-density matrix elements (SDMEs), which parameterize the ρ^0 production and decay angular distribution. The decomposition of the angular distribution in terms of SDMEs was previously done for both polarized and unpolarized lepton beam and unpolarized target. Recently, the angular distribution was decomposed in terms of SDMEs also for a transversely polarized target. A first measurement of the 30 'transverse' SDMEs is reported in this thesis, yielding information on the degree of s-channel helicity conservation and natural-parity exchange in the case of a transversely polarized target. The measured SDMEs are implemented into the rhoMC Monte Carlo generator, which is currently the only one capable of fully simulating the exclusive ρ^0 production and decay for both unpolarized and polarized beam and target. The interest in SDMEs for a polarized target arose after it was shown that at leading twist the corresponding SDMEs can be related to the azimuthal transverse target-spin asymmetry in the cross section of exclusive ρ^0 production which is sensitive to the unknown nucleon helicity-flip GPDs. Since the GPD formalism is only valid for longitudinally polarized vector mesons produced by longitudinal photons, for the first time the transverse target-spin asymmetry of longitudinally polarized ρ^0 mesons is extracted and compared to the available theoretical predictions, specifically considering possible problems with next-to-leading order corrections.

Zusammenfassung

In dieser Arbeit wird die exklusive Elektroproduktion von ρ^0-Mesonen untersucht. Dafür werden Daten aus den Jahren 2002-2005 verwendet, die mit dem HERMES Spektrometer aufgezeichnet wurden, während der Leptonen-Strahl des HERA-Beschleunigers an dem internen HERMES Target streute, das mit transversal polarisiertem atomaren Wasserstoff gefüllt war. Durch die Messung der Spin-Dichte Matrixelemente (SDMEs) werden der Produktionsmechanismus der ρ^0-Mesonen und die modelabhängige Struktur des Nukleons studiert. Diese SDMEs parametrisieren den Produktionsmechanismus der ρ^0-Mesonen und ihre winkelabhängige Zerfallsverteilungsfunktion. Die Zerlegung der Winkelverteilung mit Hilfe von SDMEs war bisher für sowohl polarisierte wie unpolarisierte Leptonenstrahlen sowie unpolarisierte Targets durchgeführt worden. Seit kurzem kann die Winkelverteilung als Funktion der SDMEs auch für ein transversal polarisiertes Target beschrieben werden. In dieser Arbeit wird die erste Messung der 30 "transversalen" SDMEs vorgestellt, welche Informationen liefern über das Maß der Erhaltung der Helizität im s-Kanal und den Austausch der natürlichen Parität im Falle eines transversal polarisierten Targets. Die gemessenen SDMEs wurden in den Monte Carlo Generator rhoMC eingebaut, dem einzigen Generator, der momentan exklusive ρ^0-Produktion sowie deren Zerfall bei sowohl unpolarisiertem als auch polarisiertem Strahl und Target vollständig beschreiben kann. Das Interesse an den SDMEs kam auf nachdem gezeigt worden war, daß man in führendem Twist die entsprechenden SDMEs zu der transversalen Target-Spin Asymmetrie in exklusiver ρ^0-Produktion in Beziehung setzen kann, welche von den unbekannten Generalisierten Partonenverteilungen (GPD) abhängt welche einen Helizitätsflip des Nukleons während der Wechselwirkung beschreiben. Der GPD-Formalismus ist nur für longitudinal polarisierte Vektormesonen gültig, die von longitudinalen Photonen erzeugt werden. Zum ersten Mal wird damit die transversale Target-Spin Asymmetrie von longitudinal polarisierten ρ^0-Mesonen aus experimentellen Daten extrahiert und mit den verfügbaren theoretischen Vorhersagen verglichen, letzteres insbesondere im Hinblick auf mögliche Probleme, die mit Korrekturen jenseits führender Ordnung zusammenhängen.

Contents

“ in memory of Armand Rostomyan ”

—

" for more receipts visit http://particleadventure.org/index.html "

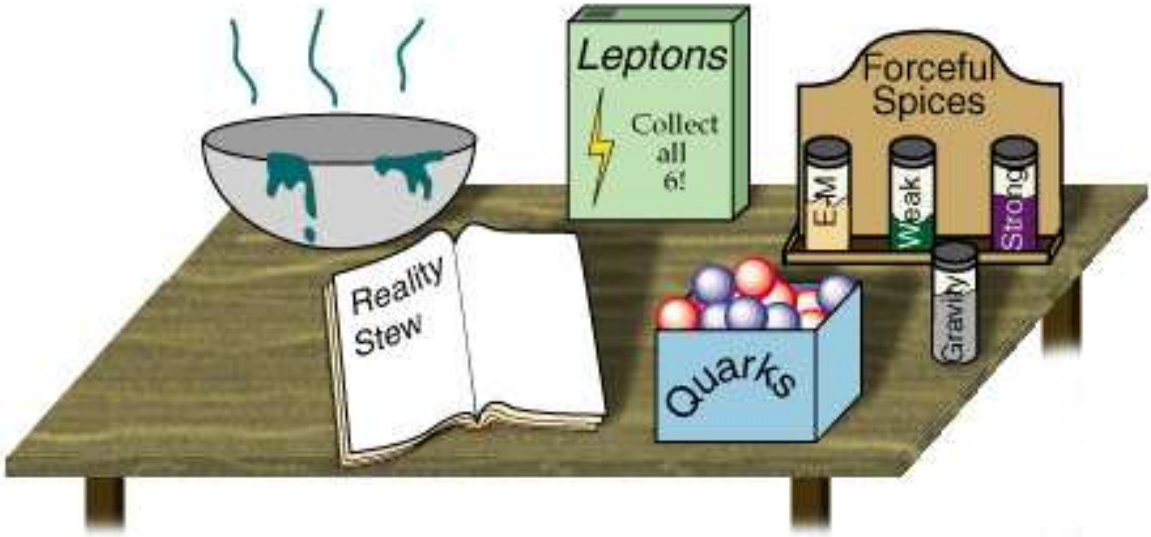

—

Chapter 1

Introduction

"Something unknown is doing we don't know what."
— Sir Arthur Eddington

"The air, with its variety of contents, its universal presence, is the source of all that exists. Everything is air at different degrees of density, and under the influence of heat, which expands, and of cold, which contracts its volume, it gives rise to the several phases of existence. In this way was formed a broad disk of earth, floating on the circumambient air. Similar condensations produced the sun and stars; and the flaming state of these bodies is due to the velocity of their motions." Anaximenes of Miletus

Anaximenes of Miletus
(ca.585 BC - ca.525 BC)

The idea that matter is composed of discrete units and can not be further divided into any tiny quantities, has been around for thousands of years. Democritus explained matter consisting of various basic elements that always existed and named them atoms (Greek, meaning "indivisible"). He assigned them several properties, particularly size, shape, and, perhaps, weight. They can be rearranged into many different forms and the interactions between the atoms led to other properties of matter such as color, taste, hot and cold. For Kanada (6th century BCE), a Hindu philosopher, the atoms themselves were inactive, without physical properties and are ultimately driven by the will of God.

Democritus
(ca.460 BC - ca.370 BC)

Hindu philosophy
(6th century BCE)

The earliest concepts of the atomic nature of matter were based purely on philosophy and up until the beginning of the 19th century no scientific basis was found. In 1803, John Dalton used the concept of atoms to explain a number of chemistry puzzles he was pondering with his contemporaries at that time, *e.g.* why elements always react in simple proportions, why certain gases dissolve better in water than others. He proposed that each element consists of atoms of a unique type, and they can combine to form more complex structures.

John Dalton
(1766 - 1844)

Another hint for the existence of atoms occurred in 1827 when botanist Robert Brown used a microscope to look at dust grains floating in water and discovered that they moved around erratically. This phenomenon, which became known as *Brownian motion*, originates with the atoms which move of themselves and cannon against slightly larger bodies (e.g. dust grains), accelerating them in random directions.

Robert Brown
(1773 - 1858)

In the 1860s Mendeleyev, attempting to classify the elements according to their chemical properties, noticed patterns that led him to postulate his Periodic Table: all known elements, if arranged according to their atomic mass, exhibit an apparent periodicity of properties. But the variety of basic elements and the periodicity of the structure suggest a substructure of those elements.

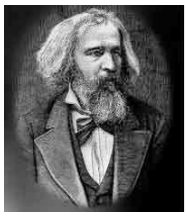

Dimitri Mendeleyev
(1834 - 1907)

The substructure of the atom was discovered in 1897, by Thomson. He investigated the deflection of cathode rays in the electromagnetic field of the atom and concluded that the cathode rays were made of particles, electrons, which came from within the atoms of the electrodes themselves. The measurement of the charge-to-mass ratio of those particles, related to the measurements of the deflection angle and the energy carried by the particles, suggested either the electrons to be very light or the charge to be very high. Thus the concept of atoms as being indivisible units was destroyed, electrons were assumed to be distributed evenly throughout the atom, swarming in a sea of positive charge.

Sir Joseph John Thomson
(1856 - 1940)

In 1909, Rutherford, bombarding a foil of gold with α-particles, discovered that a small percentage of ions were deflected by much larger angles than was predicted by Thomson's model. Rutherford suggested that the positive charge of an atom and most of its mass were concentrated in a nucleus at the center of the atom with the electrons orbiting around, like planets around the sun. Positively charged α-particles passing close to this dense nucleus would then be deflected at much sharper angles.

Ernest Rutherford
(1871 - 1937)

With the advent of quantum mechanics, in 1913, Bohr suggested the electrons to be confined in clearly defined orbits. The electrons could jump between those orbits emitting or absorbing a photon of a certain energy, *i.e.* with a specific frequency, but could not freely spiral inward or outward in intermediate states. In 1924, de Broglie proposed the particles to exhibit not only particle-like, but in addition also wave-like properties. The wave-particle duality was invented to resolve problems such as the diffraction of electrons and the photoelectric effect. As a consequence of the mathematical model of the atom, developed in 1926 by Schrödinger, that describes the electrons as three-dimensional wave forms, it was found

Niels Bohr
(1885 - 1962)

mathematically impossible to obtain precise values for both the position and the momentum of a particle. In our days this phenomenon is known as *Heisenberg's uncertainty principle*. In this concept, for each measurement of a position only a range of probable values for momentum is obtained, and vice versa. In 1928, Dirac combined quantum theory and Einstein's special relativity in the description of the electromagnetic interactions. He showed that if the behavior of one particle (*i.e.* electron) is a solution of the resulting equations, then the equations must also have another solution with the same mass as that particle, but with all charges opposite in sign. In the case of the electron, the new particle would have a positive electric charge, and if one solution exists in the real world, so must the other. The two particles were called *antiparticles*.

Louis de Broglie
(1892 - 1987)

Erwin Schrodinger
(1887 - 1961)

While experimenting with the products of radioactive decay, in 1913, radiochemist Soddy discovered that there appeared to be more than one element at each position on the atomic table. With the development of the mass spectrometer, chemist Aston discovered those elements, called isotopes, to have different masses, but varied by an integer amount. The positively charged nuclei were shown to be consisting of positively charged protons and electrically neutral neutrons (discovered by Chadwick in 1932), surrounded by a much larger negatively charged electron cloud. An atom is electrically neutral if it has the same number of protons and electrons. The number of protons in the atom defines the chemical element, while the number of neutrons determines the isotope of the element.

Werner Heisenberg
(1901 - 1976)

Although nucleons account for nearly all the visible mass in the universe, they have a complicated structure that is still not completely understood. The first indication that nucleons have an internal structure came in 1933 when Otto Stern measured the proton's magnetic moment:

$$\mu_p = 2.79\frac{e_p}{2M_p} = 2.79\mu_N, \tag{1.1}$$

Frederick Soddy
(1877 - 1956)

e_p and M_p being charge and mass of the proton. The deviation of the magnetic moment from unity, expressed in terms of the nuclear magneton μ_N, indicates that the proton is not a pointlike particle but has an internal structure. Afterwords the magnetic moment of the neutron was found to be not equal to zero as well, indicating an internal structure as it carries no net charge but still interacts with a magnetic field. The negative value $-1.91\mu_N$ of the neutron's magnetic moment implies that the neutron has a tendency to align antiparallel to a magnetic field rather than parallel to the field.

Francis William Aston
(1877 - 1945)

Although the proton has a positive charge, and the neutron is neutral, in all other respects they were found to be almost identical: their masses are almost identical; the strength of the strong interaction between any pair of nucleons is the same, independent of whether they are interacting as protons or as neutrons. In addition, the masses of the pions π^+, π^- and π^0, which were believed to mediate the strong interaction between the nucleons, were found to be almost the same, too. A quantum number related to the strong interaction, *isospin*, was introduced by Heisenberg to explain these symmetry properties. The neutron and the proton were assigned to the doublet of a symmetry group SU(2). The discovery of additional particles, both mesons and baryons, made it clear that the concept of isospin symmetry could be broadened to an even larger symmetry group. Once the kaons and their property of strangeness became better understood, it started to become clear that these, too, seemed to be a part of an enlarged, more general symmetry that contained isospin as a subset. The larger symmetry was named *Eight-fold Way* by Gell-Mann. It organizes subatomic baryons and mesons into octets, and was promptly recognized to correspond to the adjoint representation of SU(3). The principles of the Eight-fold Way were also applied to the spin-3/2 baryons, forming a decuplet. The variety of baryons and mesons, similar to the elements in the Periodic Table, was seen as an indication for their substructure.

Sir James Chadwick
(1891 - 1974)

Murray Gell-Mann
(1929)

Otto Stern
(1888 - 1969)

Sir Neville Francis Mott
(1905 - 1996)

Wolfgang Pauli
(1900 - 1958)

Historically, the structure of the nucleon was studied in lepton-nucleon scattering processes where, to a good approximation, a lepton scatters off a nucleon via exchange of a virtual photon which is considered to probe the structure of the nucleon. The four-momentum transfer $q = p' - p$ to the nucleon with p and p' being the nucleon four-momenta before and after the interaction, determines the resolution of the probe. The wavelength of the virtual photon is inversely proportional to its squared four-momentum $Q^2 = -q^2$. So with increasing q different scales of the nucleon can be probed, from the integral properties such as the charge radius, to properties of its internal constituents.

The simplest process to probe the structure of the nucleon, measurable already at low beam energies, is elastic lepton-nucleon scattering: $lN \to l'N'$. Would the nucleon be pointlike, the lN cross section would be equal to the Mott cross section [1] describing the scattering of a relativistic spin[1]-1/2 particle in a pointlike potential. The experimental results [1] show that the elastic lN cross section is smaller than the Mott

[1]Spin is the intrinsic angular momentum of a particle.

cross section. This was explained by the nucleon being not-pointlike, *i.e.* having distributed electric-charge density ρ_e and magnetic-moment density ρ_μ. The electric-charge and normal magnetic-moment distributions are described by the Dirac form factor $F_1(q)$, and the anomalous magnetic moment κ by the Pauli form factor $F_2(q)$,

$$F_1(q) = \frac{1}{e}\int_V \rho_e(r)e^{i\mathbf{qr}}dV \ , \qquad F_2(q) = \int_V \rho_\mu(r)e^{i\mathbf{qr}}dV \ . \tag{1.2}$$

An overview of nucleon form factor measurements can be found in [2].

In the 1960s and 1970s, the attempts to understand the inner structure of the nucleon were continued on both the experimental and theoretical sides. In 1964, Gell-Mann [3] and, independently, Zweig [4] postulated the quark model introducing *quarks*, the particles that the hadrons are composed of. Another model was proposed in 1978 by Feynman [5], who described the nucleon being composed of pointlike constituents, named partons. Experimentally, the inner structure of the nucleon was further studied by probing the nucleon with lepton beams of higher energy, which became available at SLAC in the early 1970s. Here, the inclusive scattering process $e + N \to e' + X$, in which only the scattered electron e' was detected, showed only a weak dependence of the cross section on the four-momentum transfer q to the nucleon [6]. This result indicated that the lepton is scattered off a pointlike constituent inside the nucleon and provided the first convincing evidence of an inner structure of nucleons, which up until then was only a purely mathematical hypothesis. Partons and quarks were recognized to be the same and the Quark-Parton Model (QPM) was developed [7–9].

In the QPM, the nucleon is considered as an object moving with infinite momentum and built of quarks having *momentum distributions* $q(x)$ where x is the longitudinal momentum fraction of quark with respect to the nucleon momentum. The momentum distribution $q(x)$ multiplied by the differential momentum fraction dx gives the probability to find a quark of a certain flavor q carrying a fractional momentum in the range $[x, x + dx]$. At large squared four-momentum transfer Q^2, the lepton-nucleon scattering process is viewed as *deep inelastic scattering* (DIS) off a nucleon or, equivalently, as elastic scattering off one of the constituents inside.

While in the elastic scattering process the kinematics of the event can be fully described by the scattering angle θ, for the inelastic event there exists an additional degree of freedom due to the mass difference between

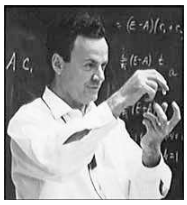

Paul Dirac
(1902 - 1984)

George Zweig
(1937)

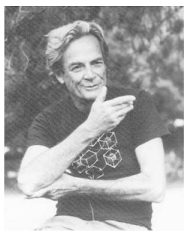

Richard Feynman
(1918 - 1988)

James Bjorken
(1934)

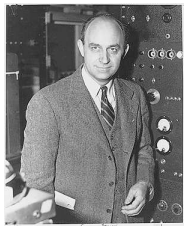

Enrico Fermi
(1901 - 1954)

the final hadronic state and the target nucleon. As such an additional independent quantity *e.g.* the energy transfer ν or the squared four-momentum Q^2 transfer can be chosen. The cross section of the DIS process describes the inner structure of the nucleon similar to the cross section of elastic scattering, but this time introducing non-elastic form factors, which are called *structure functions* $F_1(x)$ and $F_2(x) = 2xF_1(x)$ [8]:

$$F_1(x = Q^2/2M\nu) = \frac{1}{2}\sum_{q,\bar{q}} e_q^2\, q(x)\ . \tag{1.3}$$

Satyendra Nath Bose (1894 - 1974)

Within the QPM, for a fixed value of x and at large enough values of Q^2, Bjorken predicted a Q^2-independence of the cross section, called *scaling behavior*, of the virtual photon scattering off the pointlike constituents inside the nucleon. The scaling behavior of structure functions was experimentally established in 1970 at SLAC. However, more precise measurements in later years at FNAL have shown small deviations. These *scaling violations* can not be explained within the QPM.

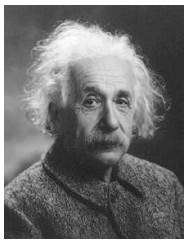

Albert Einstein (1879 - 1955)

Due to conservation of angular momentum, a spin-1/2 quark can absorb a virtual photon if only their relative spin orientations are opposite. The quark momentum distribution can be separated into two parts, for quarks with parallel (+) and antiparallel (−) spin orientations with respect to the nucleon spin: $q(x) = q^+(x) + q^-(x)$. Here, $q^{+(-)}(x)dx$ is the probability to find a quark of flavor q in the nucleon within the fractional momentum range $[x, x+dx]$ with its spin oriented parallel (antiparallel) to that of the nucleon. If the lepton beam and the nucleon target are both polarized, the quark *helicity distribution* $\Delta q(x) = q^+(x) - q^-(x)$ can be probed. In this case the spin-dependent structure function $g_1(x)$ is related to the quark helicity distribution:

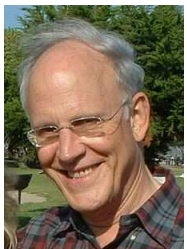

David Jonathan Gross (1941)

$$g_1(x) = \frac{1}{2}\sum_{q,\bar{q}} e_q^2\, \Delta q(x)\ . \tag{1.4}$$

Hugh David Politzer (1949)

In 1987 at CERN, the EMC collaboration measured that only a small fraction of the nucleon spin $(10 - 20\%)$ is made up by the spin of the quarks [10, 11]. This was in unexpected strong contrast to the naive QPM in which the nucleon spin is completely carried by valence quarks. Hence, this discovery was called '*spin crisis*'.

Frank Wilczek (1951)

Today our knowledge of the 'micro world' is contained in the Standard model, where the fundamental constituents of matter are six quarks (see Table A.1) and six leptons (see Table A.2), together with their antipar-

ticles. Quarks are the only elementary particles that interact through all fundamental forces: electromagnetic, weak and strong[2]. A lepton is a particle that does not experience strong interaction. Quarks and leptons have half-integer spins and obey Fermi-Dirac statistics, hence called *fermions* (named after Enrico Fermi). According to the *Pauli exclusion principle* only one fermion can occupy a quantum state at a given time. Thus fermions exhibit space-occupying behavior, otherwise the universe would collapse into a single point! This results into solidness of matter, and fermions are referred to as the constituents of matter. In addition, four *gauge bosons* are elementary particles not known to be composed of other particles. These are photon, $W^{\pm}$ and Z^0 bosons, and *gluons* (see Table A.3). Bosons (named after Satyendra Nath Bose) have integer spin and obey the Bose-Einstein statistics, *i.e.* they can occupy the same quantum state. Therefore bosons are usually related to radiation and are force carrier particles, corresponding to one of the three fundamental interactions (see Table A.3).

The massless photon is the gauge boson mediating the electromagnetic interaction between electrically charged particles which is well-described by the theory of quantum electrodynamics (QED).

The massive bosons $W^{\pm}$ and Z^0 mediate the weak interactions between particles of different flavors. While $W^{\pm}$ mediate the weak interactions between left-handed particles, the electrically neutral Z boson interacts with both left-handed particles and antiparticles.

The eight massless gluons carry the strong nuclear interactions between color-charged quarks. The quantum number *color* (red, green, blue), originally introduced to satisfy the Fermi statistics for the spin-1/2 quarks, provides a tool to disentangle the gluons by various combinations of color and anticolor charges. Quarks and gluons are the only particles that have an effective color charge, the particles that are composed from them are color-neutral. In contrast to QED, where the electrically neutral photons can not couple to each other, gluons interact among themselves due to the effective color charge. Nowadays, the strong interactions of quarks and gluons are described by a field theory of quantum chromodynamics (QCD) which was developed in the late 1970s and successfully describes the experimental results, e.g. the scaling violation.

Bjorken scaling was observed to be only approximately valid in a small kinematic region, $1 < Q^2 < 10$ GeV^2 or $0.18 < x < 0.25$. The scaling violation was explained [8] by the interactions of quarks with each other via the electrically neutral gluons, thus the scaling of the free QPM was broken by the interactions. As a consequence, quarks are considered to be surrounded by a cloud of gluons and virtual quark-antiquark pairs, called *sea quarks*. Since Q^2 defines the resolution the nucleon is probed at, a parton which is not seen at low Q^2 can be resolved at larger values of Q^2 as a quark plus a gluon from the virtual cloud. Hence there will be a depletion of high momentum partons and an increase in the low momentum parton distribution, as Q^2 increases. In addition, due to resolved gluons, there is an enhancement of partons at small x, as Q^2 increases. While at low Q^2 a photon does not interact with the

[2]The gravity is not included in the Standard model.

electrically neutral gluon, the gluon can be resolved in a quark-antiquark pair at sufficiently large Q^2 and the photon can interact with one of them. This feature explains the Q^2 dependence of the structure functions. In contrast to QPM, in QCD the structure functions $F_1(x, Q^2)$ and $g_1(x, Q^2)$ are related to Q^2-dependent quark momentum distributions $q(x, Q^2)$, and respective helicity distributions $\Delta q(x, Q^2)$, called altogether *parton distribution functions* (PDFs):

$$F_1(x, Q^2) = \frac{1}{2} \sum_{q,\bar{q}} e_q^2 \; q(x, Q^2) \; , \qquad\qquad g_1(x) = \frac{1}{2} \sum_{q,\bar{q}} e_q^2 \; \Delta q(x, Q^2) \; . \tag{1.5}$$

The Q^2-evolution of PDFs is described by the Dokshitzer-Gribov-Lipatov-Altareli-Parisi (DGLAP) equations generalizing the quark number densities to include the gluon contribution [12, 13].

Since quarks and gluons interact, *i.e.* quarks can radiate and absorb gluons, gluons can fluctuate into quark-antiquark pairs, etc., these processes cause a scale dependence of the strong interaction coupling constant α_s,

$$\alpha_s(Q^2) = \frac{12\pi}{(33 - 2n_f) ln(Q^2/\Lambda_{QCD})} \; , \tag{1.6}$$

where Λ_{QCD} is the QCD scale that depends on the number of quark flavors n_f and the renormalization scheme. The value of Λ_{QCD} is of the order of $200 - 300$ MeV. With increasing Q^2, the coupling decreases and vanishes at $Q^2 \to \infty$ (equation (1.6)). This feature is called *asymptotic freedom*[3]. Asymptotic freedom implies that within fast moving nucleons the quarks move mostly as *free* non-interacting particles. For $\alpha_s \ll 1$ the method of perturbative expansion is applicable in QCD (pQCD). No search for free quarks or fractional electric charges has returned convincing evidence. The absence of free quarks has therefore been incorporated into the notion of *confinement*, a property that, as it is presently believed, the theory describing quarks must possess. Confinement means that the more quarks are separated from one another, the greater is the attraction due to the strong force, thus it is impossible to separate the quarks into free particles. For small values of $Q^2 \sim 1$ GeV^2, $\alpha_s \geq 1$ is not small anymore, so that a perturbative expansion becomes impossible. Instead, phenomenological models have to be used.

In QCD not only quarks, but also gluons contribute to the properties of the nucleon, such as momentum and spin. Besides their intrinsic spin contributions, quarks and gluons may also carry orbital angular momentum. All the contributions should add up to the nucleon spin of 1/2,

$$S_z = \frac{1}{2} = \frac{1}{2}\Delta\Sigma(\mu^2) + L_z^q(\mu^2) + J^g(\mu^2) \; , \tag{1.7}$$

where $\frac{1}{2}\Delta\Sigma$ is the net integrated contribution of the quark spins, and L_z^q is the z component of the quark orbital angular momentum, while J^g represents the total angular momentum carried by gluons. The individual terms in the sum are μ-scale dependent where μ is the physical scale at which quarks are resolved. Possible non-vanishing contributions from gluon

[3] Asymptotic freedom was discovered in 1973 by David Gross, Frank Wilczek and David Politzer.

total and quark orbital angular momenta could explain the 'spin crisis'. While the quark orbital angular momenta are still unmeasured, one possible access to them is through measurements of Generalized Parton Distributions (GPDs).

The term 'generalized' is referred to the fact that GPDs embody nucleon form factors and parton distribution functions as integrals and limiting cases, respectively. GPDs reflect the 3-dimensional structure[4] of the nucleon independently of the reaction which probes the nucleon, *i.e.* they are universal as PDFs. They are involved in the description of exclusive processes such as real photon production (known also as *Deeply Virtual Compton Scattering* (DVCS)) and scalar or vector meson production. Leading order pQCD predicts [14] that real photon production is sensitive to the quark GPDs: H^q, E^q, $\widetilde{H}^q$ and $\widetilde{E}^q$. Hard exclusive vector meson production is sensitive to both quark and gluon GPDs $H^{q,g}$ and $E^{q,g}$, while pseudo-scalar meson production is only sensitive to $\widetilde{H}^q$ and $\widetilde{E}^q$.

The second moment of the sum of the GPDs H and E can be related to the total angular momenta carried by quarks and gluons in the nucleon [15] (see Section 2.4.5). While the GPDs H^q are already somewhat experimentally constrained, the GPDs H^g and $E^{q,g}$ are completely unknown. The interplay between the GPDs $H^{q,g}$ and $E^{q,g}$ was shown [16] to lead to a cross section asymmetry of exclusive ρ^0 production with respect to the transverse target polarization (*transverse target-spin asymmetry*).

The formalism of GPDs has been introduced quite recently. More than 40 years ago, vector meson electroproduction was related to virtual photoproduction and many of its basic features have been successfully reproduced in terms of the *Vector Meson Dominance* (VMD) model. VMD relates the photoproduction cross section of vector mesons to those of purely elastic hadronic processes, which are parameterized in Regge theory by a sum of two terms: one due to the Pomeron (gluon) exchange and the other due to Reggeon (quark) exchange. The difference between VMD and GPD formalisms is conceptual: in contrast to GPDs, the VMD model does not yield information on the spin structure of the nucleon since the internal structure of the target is not resolved. Both GPD and VMD formalisms are applicable in the intermediate energy range typical for HERMES. The interpretations suggested by the GPD and VMD models will be discussed in the context of this thesis.

One of the interesting features of ρ^0 production, the helicity transfer from the virtual photon to the produced vector meson can be studied through the ρ^0 production and decay angular distribution which is parameterized by spin-density matrix elements (SDMEs). This description was previously done for an (un)polarized lepton beam and an unpolarized target. The interest in SDMEs for a polarized target [17] arose after it was shown that ρ^0 production on a transversely polarized target is sensitive to the unknown nucleon helicity-flip GPD E [16, 18–20].

In this thesis measurements on the transverse target-spin asymmetry of exclusive ρ^0 mesons, as well as first results on the extraction of SDMEs for a transversely polarized hydrogen target

[4]The three dimensions are the transverse localization of partons in the longitudinal momentum structure.

at HERMES using the 27.6 GeV HERA positron beam are reported. A brief discussion of both VMD and GPD models is presented in Chapter 2. The HERMES spectrometer is briefly discussed in Chapter 3. The selection of exclusive ρ^0 production is described in Chapter 4. Chapter 5 contains the discussion and improvement of two Monte Carlo generators, PYTHIA and rhoMC, used to simulate exclusive ρ^0 production and background processes. The interest in measurements of transverse target-spin asymmetry and SDMEs in exclusive ρ^0 production is motivated in Chapter 6. Their extraction is described in Chapter 7. The results are compared to theoretical predictions in Chapter 8 and conclusions are given in Chapter 9.

Chapter 2

Phenomenology of exclusive ρ^0 production

"Imagination is more important than knowledge..."
— Albert Einstein

Exclusive ρ^0 production in lepton-nucleon scattering can be described by various theoretical models. Many of its basic features are reproduced by the *Vector Meson Dominance* (VMD) model. The virtual photon fluctuates into an intermediate hadronic state which scatters off the target nucleon by a strong interaction similar to hadron-hadron scattering. The strong interaction itself can be described by the exchange of trajectories in the phenomenological *Regge theory*. In the context of pQCD, the formalism of *Generalized Parton Distributions* (GPDs) has been introduced. This formalism is of special interest since it also allows to interpret the results in terms of the spin structure of the nucleon. In the following a brief discussion of both formalisms is presented.

The ρ^0 mesons are unstable particles that decay predominantly into two pions. Since the ρ^0 meson is a spin-1 particle and the pions are spin-0 particles, the ρ^0 spin is completely carried by the orbital angular momentum of the pions. Thus the angular distribution of the decay pions with respect to the initial momentum of the ρ^0 meson will have a strong correlation with the polarization of the ρ^0 meson. The latter is correlated with the polarization of the initial virtual photon through the angular distribution of the ρ^0 production. These correlations are reflected in the helicity amplitudes, from which the spin-density matrix elements are constructed. In the following the decomposition of the angular distribution in terms of SDMEs is discussed.

2.1 Kinematics

Throughout this thesis, the exclusive ρ^0 production is considered,

$$e(l) + P(p) \rightarrow e'(l') + P'(p') + \rho^0(v) \,, \tag{2.1}$$

where $l = (E, \mathbf{l})$ and $P = (E_p, \mathbf{p})$ are the four-momenta of the initial lepton e and proton P, and $l' = (E', \mathbf{l}')$, $P' = (E'_p, \mathbf{p}')$ and $v = (E_V, \mathbf{v})$ are those of scattered lepton e', recoiling proton

P' and produced ρ^0 meson. To a very good approximation, the lepton-nucleon interaction is mediated by the exchange of one neutral virtual boson, γ or Z^0. If the lepton-nucleon system center-of-mass energy $\sqrt{s}$, where

$$s = (l + p)^2 \overset{lab}{\approx} M^2 + 2ME \,, \tag{2.2}$$

is much smaller than the Z^0 mass ($m_{Z^0} \approx 91.2$ GeV/c^2), the weak interaction can be neglected. HERMES is a fixed-target experiment, so that the target nucleon is at rest ($P = (M, 0)$) and the center-of-mass energy is defined by the lepton beam energy $E = 27.6$ GeV: $\sqrt{s} = 7.3$ GeV. It is much smaller compared to the Z^0 mass, thus the electromagnetic interaction is the only relevant one. This process is depicted in Figure 2.1.

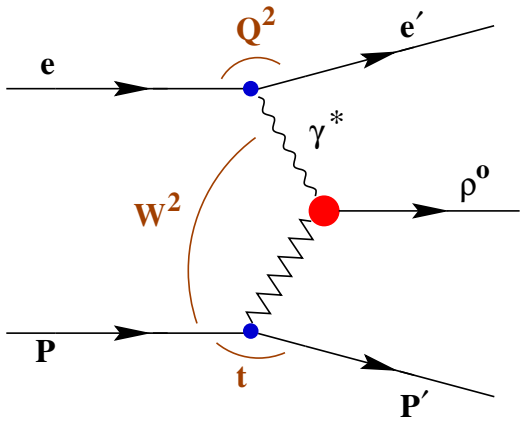

Figure 2.1: Schematic view of exclusive ρ^0 leptoproduction with t-channel exchange.

The measure of the spatial resolution q, can be used to calculate the squared invariant mass of the virtual photon:

$$Q^2 = -q^2 = -(l - l')^2 \overset{lab}{=} 4EE' \sin^2 \frac{\theta}{2} \,. \tag{2.3}$$

The Bjorken scaling variable x_B is defined as

$$x_B = \frac{Q^2}{2\mathbf{p} \cdot \mathbf{q}} \overset{lab}{=} \frac{Q^2}{2M\nu} \tag{2.4}$$

with the energy transfer ν to the target

$$\nu = \frac{\mathbf{p} \cdot \mathbf{q}}{M} \overset{lab}{=} E - E' \,. \tag{2.5}$$

The squared center-of-mass energy W^2 of the photon-nucleon system is given by:

$$W^2 = (q + p)^2 \overset{lab}{=} M^2 + 2M\nu - Q^2 = M^2 + Q^2 \frac{1 - x_B}{x_B} \,. \tag{2.6}$$

In the case of elastic scattering, the target nucleon remains intact, $W^2 = M^2$, which implies

$x_B = 1$. In the case of inelastic scattering, when the target breaks up, the mass of the final hadronic state is larger than the target mass, $W > M$, resulting to $x_B < 1$. The variable y is the fractional energy transfer from the lepton to the nucleon ($0 < y < 1$):

$$y = \frac{\mathbf{p}\cdot\mathbf{q}}{\mathbf{p}\cdot\mathbf{l}} \overset{lab}{=} \frac{\nu}{E} \,. \tag{2.7}$$

The squared four-momentum transfer t to the target or from the virtual photon to the produced meson is defined as

$$t = (p - p')^2 = (q - v)^2 \overset{lab}{=} 2M(M - E_{p'}) \,, \tag{2.8}$$

where $E_{p'}$ is the energy of the recoiling proton.

2.2 Particle's polarization, helicity and spin

As there are several confusing definitions of what is referred to as *polarization*, it seems useful to fix the naming conventions used in this thesis. Spin-1 particles are considered as the most relevant for this work.

The polarization of a particle, represented by the *helicity* λ, is defined as the projection of the spin $\vec{s}$ onto its momentum direction $\hat{p}$. If the spin is parallel (antiparallel) to the momentum, the particle is called longitudinally polarized with helicity $\lambda = 1$ ($\lambda = -1$), while if the spin and the momentum are perpendicular to each other, the particle is called transversely polarized with helicity $\lambda = 0$.

However, the photon polarization definition, originating from optics, differ from the one given above. In the classical electrodynamics, photon polarization is derived from the description of the plane electromagnetic wave. There, the Maxwell equations have a solution in terms of sinusoidal plane waves with the electric ($\vec{E}$) and magnetic ($\vec{B}$) field directions orthogonal to each other and to the direction of propagation ($\vec{k}$). Such a wave is called *transverse*. Individual photons are fully polarized. Depending on the orientation and on the magnitude of $\vec{E}$ and $\vec{B}$ field vectors along the path, they can have a elliptical, linear, or circular polarization (the latter two being extreme cases of the elliptical one).

The photon, being a spin-1 particle, can have either one of the helicity states: $\lambda = +1, 0, -1$. As opposed to the usual definition for particles (see above), the polarization state of the photon is called *transverse* if $\lambda = \pm 1$, otherwise it is *longitudinal*. While the real photons can only be transverse, the virtual photons can be also longitudinal ($\lambda = 0$).

It is often convenient to have the ρ^0 meson polarization definition similar to that of the photon. The ρ^0 meson, being a spin-1 object, is called *transverse*, if its spin is parallel (antiparallel) to the momentum, corresponding to the helicity states $\lambda = \pm 1$. The ρ^0 meson is called *longitudinal*, if its spin and momentum are perpendicular to each other, corresponding to the helicity state $\lambda = 0$.

2.3 Vector meson dominance model

In the Weizsäcker-Williams approach, the lepton-nucleon interaction is factorized into two subsequent processes. The first one is described by the probability of emission of a virtual photon γ^* by the lepton, and the second one is its subsequent absorption by the nucleon (see left panel of Figure 2.2). The lepton-photon vertex is calculable in QED and can be represented by a flux of virtual photons. The virtual-photon absorption cross section can be separated into transverse and longitudinal virtual-photon contributions. The resulting lepton-nucleon cross section can hence be written as a sum of fluxes of transverse Γ_T and longitudinal Γ_L virtual photons, each multiplied with its corresponding absorption cross section [21]:

$$\frac{d\sigma^{eN}}{d\Omega_e\, dE'} = \Gamma_T(E, E', \theta_e)\, \sigma_T^{\gamma^* N}(Q^2, W) + \Gamma_L(E, E', \theta_e)\, \sigma_L^{\gamma^* N}(Q^2, W)\ . \tag{2.9}$$

For exclusive vector meson production the same approach is used in VMD. The lepton-nucleon interaction is reduced to the interaction between virtual photon and nucleon depicted in the right panel of Figure 2.2.

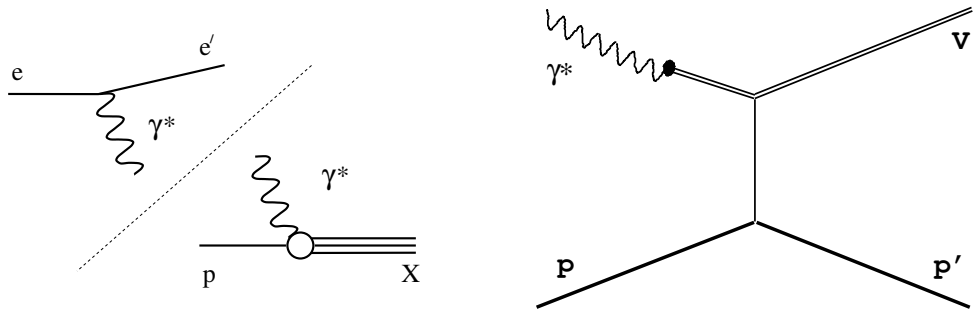

Figure 2.2: Left: Schematic view for the Weizsäcker-Williams factorization where the interaction is separated into two subsequent processes of emission and absorption of the virtual photon. Right: Vector meson production in the VMD model.

In QCD the photon is a massless, neutral gauge boson which couples to charged particles and mediates the electromagnetic interaction. In quantum field theory the electromagnetic field couples to all particles carrying electromagnetic current, enabling a photon to fluctuate into more complex virtual particle states such as fermion-antifermion pairs. Such a pair interacts strongly with the nucleon and is thought to be responsible for the major part of the γp total cross section [22]. The fluctuations can be split into a low and high-virtuality parts. In this chapter[1] only the low-virtuality fluctuations are considered, mainly fluctuations into hadronic states. This phenomenon indicates a hadronic structure of the photon. Thus the photon can be represented by a superposition of a direct-coupling bare photon $|\gamma_B\rangle$ and various virtual hadronic states $|\gamma_h\rangle$ [23]:

$$|\gamma\rangle = c_{bare}\ |\gamma_B\rangle + c_h\ |\gamma_h\rangle\ , \tag{2.10}$$

[1]More details about the structure of the photon can be found in Section 5.1.1.

where coefficients c_{bare} and c_h represent the relative fractions. While c_h is well defined (see equation (2.12)), c_{bare} secures the correct normalization (see Section 5.1.1). The bare photon accounts for the cross section contribution of the purely electromagnetic interaction between the photon and nucleon. This contribution is several orders of magnitude smaller than the cross section of the hadronic interaction [22] and is neglected in further discussions. Since the hadronic states $|\gamma_h\rangle$ have to conserve the quantum numbers of the photon ($J^{PC} = 1^{--}, Q = B = S = 0$), the hadrons are restricted to be spin-1 vector mesons: ρ^0, ω or ϕ. VMD is based on the assumption that these three mesons are the only hadronic constituents of the photon. The formation time t_f of a virtual vector meson with a mass M_V is given by [23]:

$$t_f \approx \frac{2\nu}{Q^2 + M_V^2} \, . \tag{2.11}$$

If t_f is large enough that the virtual meson is formed, the interaction occurs between virtual meson and nucleon. Thus in the context of VMD model the photon-nucleon interaction itself is related to hadron-hadron interactions [24] (see right panel of Figure 2.2). Correspondingly, the hadronic term in equation (2.10) is represented by vector meson states [25]

$$c_h \, |\gamma_h\rangle = \sum_V \frac{e}{f_V} \, |V\rangle \, . \tag{2.12}$$

The factor e/f_V, with $e = \sqrt{4\pi\alpha_{em}}$, describes the strength of the coupling between the virtual photon and various vector meson states. The coupling constant f_V is related to mass M_V and leptonic decay width Γ^V_{ee} of the vector meson [23]:

$$\frac{4\pi}{f_V^2} = \frac{3\Gamma^V_{ee}}{\alpha^3_{em} M_V} \, . \tag{2.13}$$

In the context of the VMD model the interaction between the vector meson states and the nucleon is referred to as *diffractive elastic scattering* [22] based on wave-particle duality in high-energy scattering. The term *diffractive* for exclusive ρ^0 production is derived from classical diffraction in optics. There, diffraction which combines the features of a particle and the wave-like nature of interactions, is a process where a light wave is incident upon an obstacle and a resulting interference pattern with minima and maxima is formed behind the object. Similar patterns are observed in hadron-hadron interactions at low values of squared four-momentum transfer t. There, when the incident particles are left intact after the collision (called *elastic* scattering), the differential cross section is dominated by an exponential peak at very small t, followed by a dip. Such a behavior of the photoproduction cross section is expressed by:

$$\frac{d\sigma}{d|t|} = \left.\frac{d\sigma}{d|t|}\right|_{|t|=0} e^{-b|t|} \, . \tag{2.14}$$

The exponential slope b describes the strong interaction between two extended hadronic objects which can be written as the quadratic sum of the Gaussian widths of both interacting objects:

$$b \propto R_1^2 + R_2^2 \,. \tag{2.15}$$

Since the probability for the transition of the photon into a certain vector meson is given by e^2/f_V^2, the photon-nucleon cross section for vector meson production can be related to the cross section of diffractive vector-meson-nucleon scattering by

$$\left.\frac{d\sigma^{\gamma N \to VN}}{d|t|}\right|_{t=0} = \frac{e^2}{f_V^2} \left.\frac{d\sigma^{VN \to VN}}{d|t|}\right|_{t=0} . \tag{2.16}$$

According to the optical model which relates any elastic cross section to the corresponding total cross section [22],

$$\left.\frac{d\sigma^{VN \to VN}}{d|t|}\right|_{t=0} \approx \frac{1}{16\pi} \left(\sigma_{tot}^{VN}\right)^2 , \tag{2.17}$$

and using the assumption of an exponential behavior of the elastic photoproduction cross section (see equation (2.14)), the latter becomes:

$$\sigma^{\gamma N}(s) \approx \sum_V \frac{1}{b} \left.\frac{d\sigma^{\gamma N \to VN}}{d|t|}\right|_{t=0} \approx \sum_V \frac{1}{b} \frac{e^2}{f_V^2} \frac{1}{16\pi} \left(\sigma_{tot}^{VN}(s)\right)^2 . \tag{2.18}$$

The fractional contributions of various vector mesons to the total photoproduction cross section $\sigma_{tot}^{\gamma N}$ are: $\rho : \omega : \phi = 65\% : 8\% : 5\%$, adding up to 78%.

Equation (2.16) is valid for real photons only. It can be extended to virtual photons by assuming that the Q^2 dependence of the photon-nucleon cross section is fully determined by the propagation of a single vector meson state with a propagator $(1 + Q^2/M_V^2)$. Real photons ($Q^2 = 0$) are strictly transverse while virtual photons ($Q^2 > 0$) may also have a longitudinal component. The longitudinal $\sigma_L^{\gamma^* N}$ and transverse $\sigma_T^{\gamma^* N}$ cross sections (see equation (2.9))

$$\sigma_T^{\gamma^* N}(W, Q^2) = \sum_V \frac{e^2}{f_V^2} \left(1 + \frac{Q^2}{M_V^2}\right)^{-2} \sigma_T^{VN \to VN}(W) \tag{2.19}$$

$$\sigma_L^{\gamma^* N}(W, Q^2) = \sum_V \frac{e^2}{f_V^2} \left(1 + \frac{Q^2}{M_V^2}\right)^{-2} \xi_V^2 \frac{Q^2}{M_V^2} \quad \sigma_T^{VN \to VN}(W) \tag{2.20}$$

are different [26] by the factor $\xi_V^2 \frac{Q^2}{M_V^2}$ that represents the ratio between both:

$$R = \frac{\sigma_L}{\sigma_T} = \xi_V^2 \frac{Q^2}{M_V^2} \,. \tag{2.21}$$

The VMD model predicts ξ_V^2 to be of the order of unity. However, the experimental results [27, 28] on vector meson production indicate lower values. Combining the equations above,

the virtual-photon-nucleon cross section predicted by the VMD model is given by:

$$\sigma^{\gamma^* N}(W, Q^2) = \left(1 + \frac{Q^2}{M_V^2}\right)^{-2} \left(1 + \xi_V^2 \epsilon \frac{Q^2}{M_V^2}\right) \sigma^{\gamma N \to V N}(W, Q^2 = 0) \,, \tag{2.22}$$

where ϵ is the photon polarization parameter, representing the ratio between longitudinal and transverse photon fluxes: $\epsilon = \Gamma_L / \Gamma_T$.

2.3.1 Regge theory

The open point left from the previous section is the hadron-hadron interaction in equation (2.16). In the VMD model, the strong interaction between the virtual meson and the nucleon is described by Regge theory.

In Regge theory the angular momentum l is treated as a complex variable. Therefore the elastic scattering amplitude at a fixed energy as a function of l is analytically continued into the complex angular momentum plane [29]. The Regge poles, which are singularities in the scattering amplitudes found in the complex plane, correspond to either bound states or resonances depending on the angular momentum value.

In the Regge approach, using the non-relativistic quantum mechanics the angular momentum l is described via a *Regge trajectory* $\alpha(E)$ that is a complex function of the total energy: $l = \text{Re } \alpha(E)$. The behavior of such a trajectory is depicted in the left panel of Figure 2.3. Each time the trajectory passes an integer value n in Re $\alpha(E)$, *i.e.* $l = n$, the value $E = E_n$ corresponds to the energy of real bound or a resonant state. The amplitude $f(E, l)$

$$f(E, l = n) = -\frac{R(E)}{\epsilon} \frac{1}{(E - E_n) + i\Gamma/2} \tag{2.23}$$

where $R(E)$ is the residual and

$$\epsilon \equiv \frac{d}{dE} \text{Re } \alpha(E) \bigg|_{E=E_n} \,, \qquad \Gamma = 2/\epsilon \, \text{Im } \alpha(E) \,, \tag{2.24}$$

has a pole. It represents a Breit-Wigner formula for a scattering amplitude near a resonance with angular momentum l and total energy E. In this way a Regge trajectory connects bound states and resonances with momentum l, being the interpolating curve between them. The number of bound states and resonances depend on the energy of the interaction. All quantum numbers, apart from angular momenta, are the same for all poles of the trajectory. The neighboring poles are spaced by $\Delta l = 2$, fixing the parity of the trajectory.

If plotted in the (l, E)-plane, the hadronic states possessing the same quantum numbers such as isospin, baryon number and strangeness, lie on a straight line, when the angular momentum of each state is plotted against the square of its mass $E^2 = M^2$. Thus Regge trajectories appear to be straight lines. An example of such plots are the Chew-Frautschi diagrams (see right panel

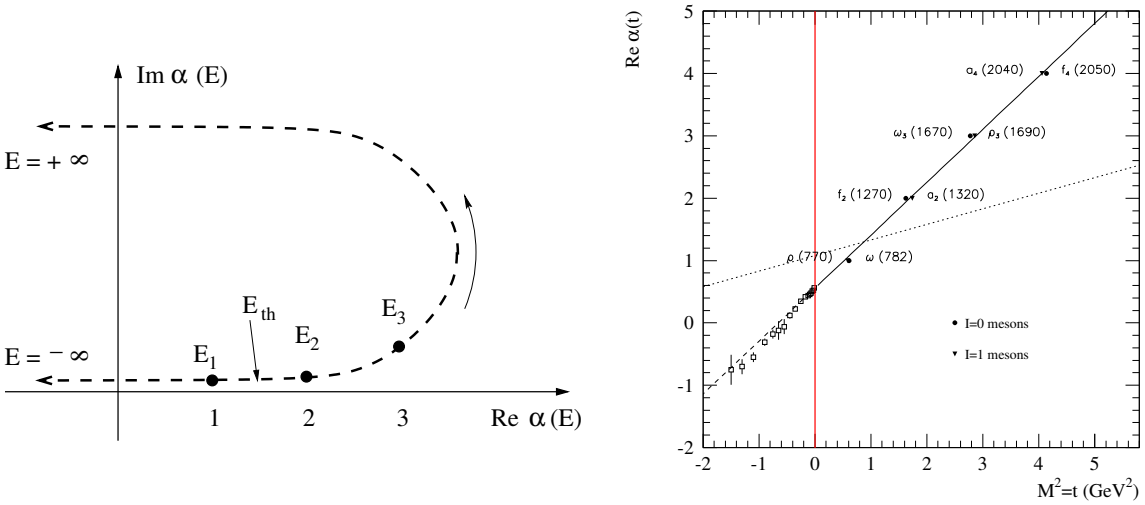

Figure 2.3: Left: Behavior of a Regge trajectory in angular momentum space in non-relativistic quantum mechanics. At energies $E < E_{th}$ there exists a bound state $(E_1, l = 1)$ corresponding to the point $\mathrm{Im}\,\alpha(E) = 0$, $\mathrm{Re}\,\alpha(E) = 1$ on the Regge trajectory. With increasing energy, the trajectory attains a positive imaginary part. Right: Chew-Frautschi plot for few Regge trajectories. The dotted line represents the trajectory corresponding to Pomeron exchange. The solid line indicates almost identical trajectories for isospin-1 and isospin-0 particles which are fits to experimental data points with a function given by equation (2.25). The dashed line is the extension of the fit to $t < 0$ with the points from $\pi^- p \to \pi^0 p$ scattering data on it.

of Figure 2.3). The model makes use of the principle of crossing symmetry (see Appendix B): the exchanged poles in the t-channel of the original reaction become resonances in the s-channel of a crossed reaction. In the t-channel the total energy of the system is given by $\sqrt{t}$, where $t > 0$ (see equation (B.2)). Adding to this Chew-Frautschi diagrams the experimental results on diffractive scattering processes, which have negative momentum transfer t, the data points seem to align along the extensions to $t < 0$ of the Regge trajectories. The quantum numbers of the trajectories match possible resonances that could be exchanged in the crossed processes. With slope α' and intercept $\alpha(0)$ the Regge trajectories are parameterized as

$$\alpha(t) = \alpha(0) + \alpha' t \;, \tag{2.25}$$

relating the squared four-momentum transfer t to the angular momentum of the exchanged object. An additional trajectory represents the exchange of vacuum quantum numbers: isospin, baryon number, and strangeness are equal to zero. This Pomeron trajectory has no hadronic states lying on it. Its intercept is slightly greater than unity. In Regge theory, the hadron interactions are assumed to be mediated by an exchange of resonances in the t-channel whose interpolation is given by a Regge trajectory or Reggeon $\alpha(t)$.

An example is depicted in the right panel of Figure 2.3 for the reaction $\pi^- p \to \pi^0 n$. The parity transfer $\Delta P = (-1)^J P$ with J and P being the angular momentum and parity of the object exchanged in the t-channel, is positive. Conservation of the relevant quantum numbers requires the reaction to proceed via ρ, a_2 or ρ_3 exchange with $J^P = 1^-, 2^+$ and 3^-, all lying

on the Regge trajectory passing through the measured data points. This Regge trajectory is almost identical to the ω/f trajectory, which is also shown in the same figure.

The straight trajectories are a phenomenological observation and they cannot be calculated from first principles. This means that Regge theory can not explain the nature of the strong interaction. Nevertheless, Regge theory delivers the correct energy dependence of the strong interaction cross section in powers of $\alpha(t)$

$$\frac{d\sigma^{VN\to VN}(s)}{d|t|} \propto e^{-b_0|t|}\left(\frac{s}{s_0}\right)^{2\alpha(t)-2} = e^{-b|t|}\left(\frac{s}{s_0}\right)^{2\alpha(0)-2} = \left.\frac{d\sigma^{VN\to VN}}{dt}\right|_{t=0} e^{-b|t|} , \tag{2.26}$$

where s_0 is a scale factor of the order of 1 GeV^2 and b is an energy dependent slope:

$$b = b_0 + 2\alpha' \ln\left(\frac{s}{s_0}\right) . \tag{2.27}$$

The slope of the forward diffractive peak increases with energy, causing a 'shrinkage' of the diffractive forward peak, *i.e.* the peak becomes more narrow. There are no predictions for the values of b_0, s_0 and α' from Regge theory. These parameters have to be obtained experimentally. Together with optical model (see equation (2.17)), the Regge theory describes also the energy dependence of the total cross section:

$$\sigma_{tot}^{VN} \propto s^{\alpha(0)-1} . \tag{2.28}$$

This means that at high center-of-mass energies s, the behavior of the total cross section is dominated by the highest-lying Regge trajectories, *i.e.* the ρ/a_2 and ω/f trajectories. The result of a measurement of their intercepts, $\alpha_{\rho,\omega}(0) \approx 0.5$, requires that the total cross section behaves according to $s^{-1/2}$. This is in conflict with the observed behavior of the hadron-proton scattering total cross section at high energy which remains approximately constant with energy and exhibits a slow rise above $s \approx 10$ GeV. In order to explain this observation in terms of Regge pole exchange, a trajectory with $\alpha(0) \approx 1$ is needed. All known particles have $\alpha(0) < 1$. In addition, the exchanged particle needs to have the quantum numbers of the vacuum. This led to the invention of the Pomeron trajectory. The slope of the Pomeron trajectory is determined in pp and $p\bar{p}$ scattering: $\alpha'_P = 0.25$ GeV^{-2} [30].

Assuming that the vector-meson-nucleon cross section exhibits the typical behavior of the hadron-hadron cross section, the intercepts of the Regge and Pomeron trajectories can be described by the sum of two terms,

$$\sigma_{tot}^{VN} = Xs^{\epsilon} + Ys^{-\eta} , \tag{2.29}$$

where X and Y are arbitrary normalizations. The exponents ϵ and η refer to Pomeron and Reggeon exchange respectively and can be determined from fits to experimental data. Corre-

spondingly, the first term stands for one or multiple Pomeron trajectories, while the second term corresponds to the highest-lying Regge trajectory. The exponents are assumed to be independent of the interacting hadrons, while X and Y depend on a certain process. The values for the exponents ϵ and η can be determined from fits to experimental data. Applying fits to pp and $p\bar{p}$ data [31], they were found to be $\epsilon = 0.0808$ and $\eta = 0.4525$. The model of Donnachie and Landshoff [31] provides a good description of the energy behavior of the total $\rho^0 p$ cross section using

$$\sigma_{tot}^{\rho^0 p} = 13.6 s^{0.08} + 31.8 s^{-0.45} \, . \tag{2.30}$$

2.4 Generalized parton distributions

In the infinite momentum frame, where the nucleon moves fast in the z-direction, the transverse charge distribution of the nucleon [32] is given by the Fourier transform of form factors (see equation (1.2)). Thus, the form factors are interpreted as describing the transverse localization $b_\perp$ of partons in a fast moving nucleon, irrespective of their longitudinal momenta and independent on the resolution scale (see left panel of Figure 2.4).

On the other hand, the ordinary parton distributions (PDFs) represent the probability density to find a parton with a given longitudinal momentum fraction x of the nucleon, containing no information on the transverse position of the parton [32] (see right panel of Figure 2.4).

Both form factors and PDFs reflect only one-dimensional 'slices' of the nucleon structure. The two orthogonal dimensions, the transverse localization of partons in the nucleon and the longitudinal momentum fraction carried by quarks, are described simultaneously by the GPDs (see middle panel of Figure 2.4).

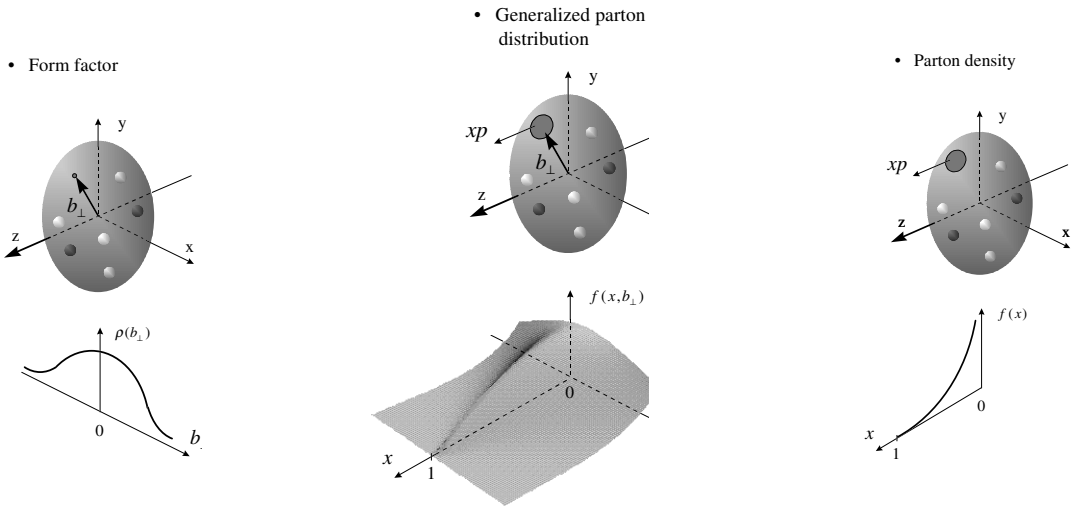

Figure 2.4: Probabilistic interpretation of form factors, GPDs and parton densities in the infinite momentum frame [32].

PDFs (in deep-inelastic scattering processes) and form factors (in elastic-scattering pro-

cesses) appear as the limiting cases and integrals of GPDs, respectively. GPDs are used for the description of many hard exclusive processes, like DVCS, exclusive meson production, etc.. The detected final states can be used as a filter for spin and flavor of the emitted and reabsorbed quarks. GPDs are universal distribution functions which allow to relate various hard processes to each other. However, GPDs are still not very well known which is related to the fact that measurements of exclusive processes are experimentally challenging. High luminosities are required to compensate for small cross sections, and also detectors capable of ensuring the exclusivity of the final state.

2.4.1 Factorization theorem

In inclusive DIS processes, a rapidly moving hadron is treated as a bundle of quasi-real partons moving almost collinear. In the Bjorken limit, *i.e.*, when the photon virtuality Q^2 and the squared hadronic center-of-mass energy $(p+q)^2$ both become large for fixed values of x_B, the cross section of the process is given as a convolution of a hard partonic subprocess that is calculable in perturbative theory, and a parton distribution function that represents the probability density to find a parton with a certain momentum fraction x. Such a factorization approach, which separates the process into short-distance and long-distance subprocesses, is also valid for reactions where the momentum transfer to the target is finite. In the particular case when a light meson is produced (see Figure 2.5), the production amplitude $\mathcal{A}$ consists of two long-distance subprocesses: the structure of the nucleon is parameterized by the GPDs F_i ($F = H, E, \widetilde{H}, \widetilde{E}$) and the structure of the produced meson by the distribution amplitude (DA) Φ_j [14]:

$$\mathcal{A} \propto \sum_{ij} \int dz \int dx \; F_i(x,\xi,t;\mu^2) \cdot K^{ij}(x,\xi,z;\log(Q^2/\mu^2) \cdot \Phi_j(z;\mu^2) \; . \tag{2.31}$$

The functions K^{ij} contain the 'perturbative physics', they describe the short-distance stage of the reaction that corresponds to the interaction of the virtual photon with a parton. The GPDs and the DA depend on the renormalization scale and on the factorization scale μ. In order to reduce NLO corrections, the scale μ is usually chosen to be equal to Q^2. The diagram depicted in Figure 2.5, represents the exclusive meson production at lowest order in α_s.

GPDs depend upon two longitudinal momentum fractions, x and ξ, and in addition on the invariant four-momentum transfer t to the nucleon. They are subject to QCD evolution, *i.e.* depend on Q^2. The light-cone momentum fraction x is defined by $k^+ = xP^+$, where k is the quark loop momentum[2] and P is the average nucleon momentum $P = (p+p')/2$, x runs from -1 to 1. In the region $[0,1]$, the longitudinal momentum fractions are those of quarks, and in

[2]For any four-vector v the light-cone coordinates $v^{\pm} = (v^0 \pm v^3)/\sqrt{2}$ and $v_T = (v^1, v^2)$ are used and light-cone gauge $A^+ = 0$ is assumed.

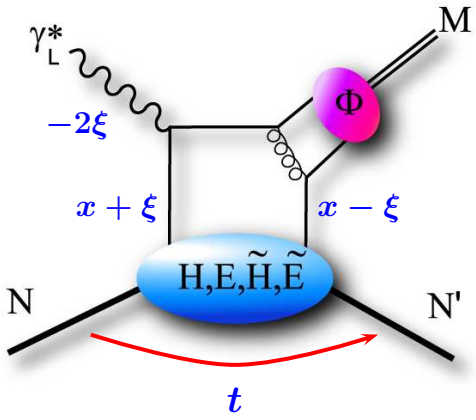

Figure 2.5: The factorization approach for meson production.

the region $[-1, 0]$ of antiquarks. The skewness variable ξ is given as

$$\xi = \frac{(p - p')(q + v)}{(p + p')(q + v)} \,. \tag{2.32}$$

The transformation of a virtual photon into a meson requires a finite longitudinal momentum transfer[3]. The momentum lost by the proton is determined by x_B. If the momentum fractions x and ξ are parameterized in a symmetric way (see Figure 2.5), in the Bjorken limit a relation holds:

$$\xi \approx \frac{x_B}{2 - x_B} \,. \tag{2.33}$$

According to the factorization theorem, the four-momentum transfer t between the initial and final nucleons (equation (2.8)), is assumed to be much smaller than the hard scattering scale Q^2. In general, t has longitudinal and transverse components,

$$t = \Delta^2 = -\frac{4M_p^2\xi^2 + \Delta_\perp^2}{1 - \xi^2} \,, \tag{2.34}$$

where the longitudinal one is given by

$$t_0 = -\frac{4M_p^2\xi^2}{1 - \xi^2} \,. \tag{2.35}$$

The DA describes the coupling of the $q\bar{q}$ or gluon pair to the meson. It depends on the longitudinal momentum fraction z carried by a parton and can be parameterized as:

$$\Phi(z; \mu) = 6z(1 - z)f_\rho \,, \tag{2.36}$$

with the meson decay constant $f_\rho = 0.209$ GeV [33].

[3]'Longitudinal' refers to the direction of the initial proton momentum in a frame where the proton moves fast.

In the factorization approach depicted in Figure 2.5, the momenta of proton and parton are no longer the same before and after the interaction. Therefore a GPD no longer represents a squared amplitude, but instead an interference between amplitudes describing various quantum fluctuations of the nucleon.

For meson production, in contrast to real photon production, the prove of the factorization theorem is presently restricted to longitudinal virtual photons, and in the particular case of ρ^0 production, to longitudinally polarized ρ^0 mesons induced by longitudinal virtual photons [14]. However, the cross section for transversely polarized virtual photons is predicted to be smaller by a factor of $1/Q^2$ compared to that for longitudinally polarized ones [34].

2.4.2 Definition of GPDs

GPDs can be defined through non-forward matrix elements of quark and gluon operators. The generalized quark distributions, defined according to the convention of reference [35],

$$\begin{aligned} F^q &= \frac{1}{2}\int \frac{dz^-}{2\pi} e^{ixP^+z^-} \langle\, p', s' \,|\, \bar{q}(-\frac{1}{2}z)\gamma^+ q(\frac{1}{2}z) \,|\, p, s \,\rangle \Big|_{z^+=0,\, z=0} \qquad (2.37)\\ &= \frac{1}{2P^+}\left[H^q(x,\xi,t,\mu^2)\, \bar{u}(p',s')\gamma^+ u(p,s) \;+\; E^q(x,\xi,t,\mu^2)\, \bar{u}(p',s')\frac{i\sigma^{+a}\Delta_a}{2M_N} u(p,s)\right] \end{aligned}$$

$$\begin{aligned} \widetilde{F}^q &= \frac{1}{2}\int \frac{dz^-}{2\pi} e^{ixP^+z^-} \langle\, p', s' \,|\, \bar{q}(-\frac{1}{2}z)\gamma^+\gamma_5\, q(\frac{1}{2}z) \,|\, p, s \,\rangle \Big|_{z^+=0,\, z=0} \qquad (2.38)\\ &= \frac{1}{2P^+}\left[\widetilde{H}^q(x,\xi,t,\mu^2)\, \bar{u}(p',s')\gamma^+\gamma_5\, u(p,s) \;+\; \widetilde{E}^q(x,\xi,t,\mu^2)\, \bar{u}(p',s')\frac{\gamma_5\Delta^+}{2M_N} u(p,s)\right] \end{aligned}$$

parameterize the Fourier integrals (first lines of equations above) along the light-cone distance z^- of bilocal quark field operators, sandwiched between the initial and final nucleon states. The off-forwardness of the defining hadronic matrix elements, $p' \neq p$, allows for hadron helicity non-flip and helicity flip contributions, enlarging the number of independent functions per quark flavor q. At (leading) twist-two, there are four quark helicity conserving GPDs: $H^q(x,\xi,t)$, $E^q(x,\xi,t)$, $\widetilde{H}^q(x,\xi,t)$ and $\widetilde{E}^q(x,\xi,t)$. The GPDs H^q and $\widetilde{H}^q$ describe hadron helicity non-flip matrix elements ($s = s'$), while E^q and $\widetilde{E}^q$ describe hadron helicity flip matrix elements ($s \neq s'$). For the projections with γ^+ and $\gamma^+\gamma_5$ there are twice as many GPDs than corresponding PDFs.

Similarly, by exchanging the quark operators with gluon operators, the gluon GPDs are defined [36]:

$$\begin{aligned} F^g &= \frac{1}{P^+}\int \frac{dz^-}{2\pi} e^{ixP^+z^-} \langle\, p', s' \,|\, G^{+\mu}(-\frac{1}{2}z) G^+_\mu(\frac{1}{2}z) \,|\, p, s \,\rangle \Big|_{z^+=0,\, z=0} \qquad (2.39)\\ &= \frac{1}{2P^+}\left[H^g(x,\xi,t,\mu^2)\, \bar{u}(p',s')\gamma^+ u(p,s) \;+\; E^g(x,\xi,t,\mu^2)\, \bar{u}(p',s')\frac{i\sigma^{+a}\Delta_a}{2M_N} u(p,s)\right] \end{aligned}$$

$$\widetilde{F}^g = -\frac{i}{P^+}\int \frac{dz^-}{2\pi} e^{ixP^+z^-} \langle\, p', s' \,|\, G^{+\mu}(-\frac{1}{2}z)\widetilde{G}^+_\mu(\frac{1}{2}z) \,|\, p, s \,\rangle \Big|_{z^+=0,\, z=0} \tag{2.40}$$
$$= \frac{1}{2P^+}\left[\widetilde{H}^g(x,\xi,t,\mu^2)\,\bar{u}(p',s')\gamma^+\gamma_5\,u(p,s) \;+\; \widetilde{E}^g(x,\xi,t,\mu^2)\,\bar{u}(p',s')\frac{\gamma_5\Delta^+}{2M_N}u(p,s)\right].$$

There are several observations indicating the kind of additional information on the nucleon structure carried by GPDs compared to the ordinary PDFs:

- Since GPDs depend on the momentum transfer t which has both longitudinal and transverse components, GPDs carry information on the transverse structure of the nucleon in combination with the longitudinal momentum distribution of partons in the nucleon.

- Both momentum and helicity of the target nucleon can be changed during the interaction which may reveal information about the spin structure described by GPDs. The GPDs $E^q(x,\xi,t)$ and $\widetilde{E}^q(x,\xi,t)$ describe reactions with hadron helicity flip while the quark helicity is conserved. This can happen only if quarks carry orbital angular momentum. Thus GPDs $E^q(x,\xi,t)$ and $\widetilde{E}^q(x,\xi,t)$ contain also information about the orbital angular momenta carried by quarks.

- Instead of one-parton emission and absorption, the scattering can proceed via emission of quark-antiquark or gluon pairs, thus probing the $q\bar{q}$ and gluon contents of the nucleon. In this way GPDs contain information on sea quarks, as will become clear in the next section.

2.4.3 Interpretations

The GPDs do not correspond to squared amplitudes (see Figure 2.5) and can hence not be interpreted as probabilities. Instead, they parameterize the interference between amplitudes that describe, *e.g.*, removing a parton from the nucleon with one momentum and inserting it back with another [37, 38]. GPDs are defined in three consecutive intervals of x (see Figure 2.6).

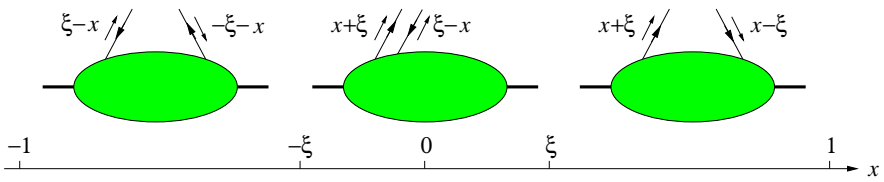

Figure 2.6: The distributions in three x-intervals:$[-1,-\xi]$, $[-\xi,\xi]$ and $[\xi,1]$ [36].

- $x > \xi$: in this case GPDs describe the emission of a quark with longitudinal momentum fraction $x+\xi$ and subsequent reabsorption of the quark with longitudinal momentum fraction $x-\xi$.

- $-\xi < x < \xi$: GPDs represent the emission of a quark-antiquark pair with longitudinal momentum fractions $x + \xi$ and $\xi - x$, respectively.
- $x < -\xi$: this is the case of emission and reabsorption of antiquarks with momentum fractions $\xi - x$ and $-\xi - x$.

Geometrical interpretations

Since GPDs contain information on the longitudinal momentum fraction, Heisenberg's uncertainty principle does not allow a simultaneous determination of the parton's longitudinal position. Instead, determining the distribution of partons in impact parameter space is possible. It has been shown [39] that for the special case $\xi = 0$, GPDs are Fourier transforms of PDFs in the transverse 'impact parameter space':

$$H(x, \xi = 0, t = -\boldsymbol{\Delta}_\perp^2) = \int d^2\mathbf{b}_\perp e^{-i\boldsymbol{\Delta}_\perp \mathbf{b}_\perp} f_1(x, \mathbf{b}_\perp) \; , \tag{2.41}$$

i.e. GPDs can be interpreted as densities of partons with longitudinal momentum fraction x and transverse distance $\mathbf{b}_\perp$ from the proton's center:

$$f_1(x, \mathbf{b}_\perp) = \int \frac{d^2\boldsymbol{\Delta}_\perp}{(2\pi)^2} H(x, \xi = 0, t = -\boldsymbol{\Delta}_\perp^2) e^{i\boldsymbol{\Delta}_\perp \mathbf{b}_\perp} \; . \tag{2.42}$$

Thus GPDs have an geometrical interpretation. Inside the nucleon, a parton i is transversely localized at $\mathbf{b}_{\perp i}$ (see Figure 2.7).

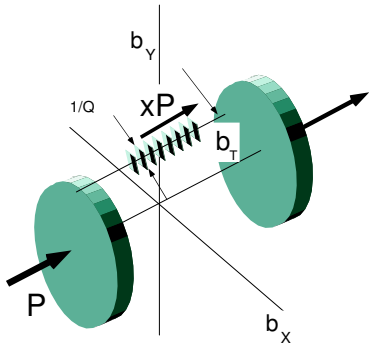

Figure 2.7: Geometrical interpretation of GPDs [39].

The transverse center of momentum $\mathbf{b}_\perp$ is given as

$$\mathbf{b}_\perp = \sum_{i=1}^{N} x_i \mathbf{b}_{\perp i} \; , \tag{2.43}$$

where each parton i contributes to the transverse center of momentum with its impact parameter weighted by its momentum fraction x_i. The generalization of the geometrical interpretation of GPDs in the case of $\xi \neq 0$ is given in [38].

2.4.4 Properties

GPDs are a 'hybrid' objects because they combine the properties of ordinary PDFs and elastic form factors.

Relation to PDFs

The nucleon helicity conserving GPDs $H^{q,g}$ and $\widetilde{H}^{q,g}$ reduce to ordinary PDFs in the forward limit ($\xi \to 0, t \to 0$):

$$H^q(x,0,0) = \begin{cases} q(x) & \text{for } x > 0 \\ -\bar{q}(-x) & \text{for } x < 0 \end{cases} \qquad \widetilde{H}^q(x,0,0) = \begin{cases} \Delta q(x) & \text{for } x > 0 \\ \Delta\bar{q}(-x) & \text{for } x < 0 \end{cases}$$

$$H^g(x,0,0) = xg(x) \quad \text{for } x > 0 \qquad \widetilde{H}^g(x,0,0) = x\Delta g(x) \quad \text{for } x > 0 \tag{2.44}$$

In the forward limit no corresponding relations exist for the nucleon-helicity non-conserving quark and gluon GPDs $E^{q,g}$ and $\widetilde{E}^{q,g}$. These GPDs are defined (see equations (2.37) - (2.40)) using a multiplicative factor Δ ($\Delta^2 = t$), and therefore vanish in the forward limit. For this reason, the GPDs E and $\widetilde{E}$ are accessible only in exclusive reactions.

In analogy to the forward limit, the distributions H and E are referred to as 'unpolarized', and $\widetilde{H}$ and $\widetilde{E}$ as 'polarized'.

Relation to form factors

Form factors constitute boundary conditions for GPDs. Integration over x relates the matrix elements defining the GPDs to the matrix elements of local quark-antiquark or gluon operators, thus the Mellin x-moments of GPDs are related to form factors. The lowest moments of GPDs are related to elastic form factors,

$$\begin{aligned} \int_{-1}^{1} dx H^q(x,\xi,t,\mu^2) &= F_1^q(t)\ , & \int_{-1}^{1} dx E^q(x,\xi,t,\mu^2) &= F_2^q(t)\ , \\ \int_{-1}^{1} dx \widetilde{H}^q(x,\xi,t,\mu^2) &= G_A^q(t)\ , & \int_{-1}^{1} dx \widetilde{E}^q(x,\xi,t,\mu^2) &= G_P^q(t)\ , \end{aligned} \tag{2.45}$$

where the Dirac and the Pauli elastic form factors, F_1^q and F_2^q, as well as the axial and pseudoscalar form factors, G_A^q and G_A^q, are defined for each quark flavor. The full form factors F (equation (1.2)) are obtained by summing over all quark flavors:

$$F(t) = \sum_q e_q F^q(t)\ , \tag{2.46}$$

with e_q being the quark charge for flavor q. The proton (p) and neutron (n) form factors are normalized such that:

$$F_1^p(0) = 1\,, \qquad F_2^p(0) = \kappa^p = 1.793\,, \qquad G_A^p(0) = g_A^p = 1.267\,, \qquad G_P^p(0) = 4g_A^p M_p^2/M_\pi^2\,,$$
$$F_1^n(0) = 0\,, \qquad F_2^n(0) = \kappa^n = -1.913\,, \qquad G_A^n(0) = g_A^n = -1.267\,, \qquad G_P^n(0) = 4g_A^n M_n^2/M_\pi^2\,,$$

where κ is the anomalous magnetic moment of the nucleon (equation (1.1)), g_A the nucleon axial charge, M_p, M_n and M_π are the masses of proton, neutron and pion, respectively.

2.4.5 Angular momentum

After it was found that the nucleon spin is not only made up by the spins of quarks and antiquarks (see Chapter 1), it became clear that the 'missing' angular momentum originates from the quark orbital angular momentum and/or gluon total angular momentum. It has been shown that there exists a gauge-invariant decomposition of the nucleon spin into quark and gluon total angular momentum [15]:

$$\frac{1}{2} = J^q(\mu^2) + J^g(\mu^2)\,. \tag{2.47}$$

The quark total angular momentum $J^q(\mu^2)$ allows a gauge-invariant decomposition into spin $\Delta\Sigma(\mu^2)$ and orbital angular momentum $L_z^q(\mu^2)$ contributions:

$$J^q(\mu^2) = \frac{1}{2}\Delta\Sigma(\mu^2) + L_z^q(\mu^2)\,. \tag{2.48}$$

The gluon angular momentum $J^g(\mu^2)$ does not allow a further gauge-invariant decomposition [15]. Various measurements at CERN [40], SLAC [41] and DESY [42] provided information about the quark polarization, confirming the EMC result, that the quark spin only contributes a small amount to the nucleon spin: $\Delta\Sigma(Q^2 = 5\mathrm{GeV}^2) = 0.330 \pm 0.039$ [42].

It has been shown [15] that the total angular momenta of quarks of a flavor q and gluons, J^q and J^g, are related to the second x-moment of the GPDs $H^{q,g}$ and $E^{q,g}$:

$$\begin{aligned} J^q(\mu^2) &= \frac{1}{2}\lim_{t\to 0}\int_{-1}^{1} dx\, x\,[H^q(x,\xi,t,\mu^2) + E^q(x,\xi,t,\mu^2)]\,, \\ J^g(\mu^2) &= \frac{1}{2}\lim_{t\to 0}\int_{0}^{1} dx\,[H^g(x,\xi,t,\mu^2) + E^g(x,\xi,t,\mu^2)]\,. \end{aligned} \tag{2.49}$$

These relations are referred to as *Ji's sum rules*. An experimental evaluation of them is complicated since separate knowledge of the GPDs $H^{q,g}$ and $E^{q,g}$ as functions of x at fixed values of ξ and in the limit of vanishing t is required for each parton flavor. However, this is the only

presently known way to access experimentally the total angular momentum carried by quarks and gluons in the nucleon.

2.4.6 Modeling GPDs

At present the only known way to learn about GPDs from measurements is to assume a functional form of GPDs with a number of adjustable parameters, and to fit these parameters by comparing the resulting observables with experimental data. Most commonly, GPDs are parameterized using an ansatz based on double distributions [43, 44] complemented with the D-term [45]. Factorizing out the t-dependence (*factorized* ansatz),

$$H^{q,g}(x,\xi,t) = H^{q,g}(x,\xi)\cdot F_1^q(t)\ , \tag{2.50}$$

$$E^{q}(x,\xi,t) = E^{q}(x,\xi)\cdot F_2^q(t)/\kappa^q\ , \tag{2.51}$$

the GPDs can be related to the ordinary PDFs and the nucleon elastic form factors [16].

The t-independent parts of the GPDs $H^{q,g}(x,\xi)$ are related to quark and gluon densities in the nucleon. In contrast to helicity non-flip GPDs, the t-independent parts of the GPDs $E^q(x,\xi)$ can not be related to the spin-flip parton densities. In some models [16, 18], the total angular momenta carried by u- and d-quarks enter directly as free parameters in the parameterization of $E^q(x,\xi)$ and can be used to investigate the sensitivity of hard electroproduction observables to variations in J^u and J^d in a model-dependent way.

The parameterization of the GPD E^g is much more complicated since there is no information about its forward limit. There is an expectation that E^g is small compared to E^u and E^d. This expectation is based on the sum rules for the conservation of momentum,

$$\int\limits_{-1}^{1} dx x \sum_q H^q(x,0,0) + \int\limits_{0}^{1} dx H^g(x,0,0) = 1\ , \tag{2.52}$$

and angular momentum,

$$\frac{1}{2}\int\limits_{-1}^{1} dx x \sum_q (H^q(x,0,0)+E^q(x,0,0)) + \frac{1}{2}\int\limits_{0}^{1} dx (H^g(x,0,0)+E^g(x,0,0)) = \frac{1}{2}\ , \tag{2.53}$$

which can be combined into the sum rule [38]

$$\sum^{q}\int\limits_{-1}^{1} dx\, x E^q(x,0,0) + \int\limits_{0}^{1} dx E^g(x,0,0) = 0\ . \tag{2.54}$$

Lattice QCD calculations [46, 47] obtain a cancellation of the contributions from u- and d-quarks

($\int_{-1}^{1} dx\, xE^u$ vs. $\int_{-1}^{1} dx\, xE^d$). Barring an unexpectedly large contribution from s-quarks, the gluon contribution $\int_{0}^{1} dx E^g$ should be relatively small compared with the u- and d-quark contributions. An example of the t-independent part of the quark and gluon GPD parameterizations are shown in Figure 2.8, where the GPDs E^u and E^d tend to cancel each other, implying $E^g = 0$. This is in contrast to the gluon GPD H^g which is not small compared to the quark GPDs H^u and H^d.

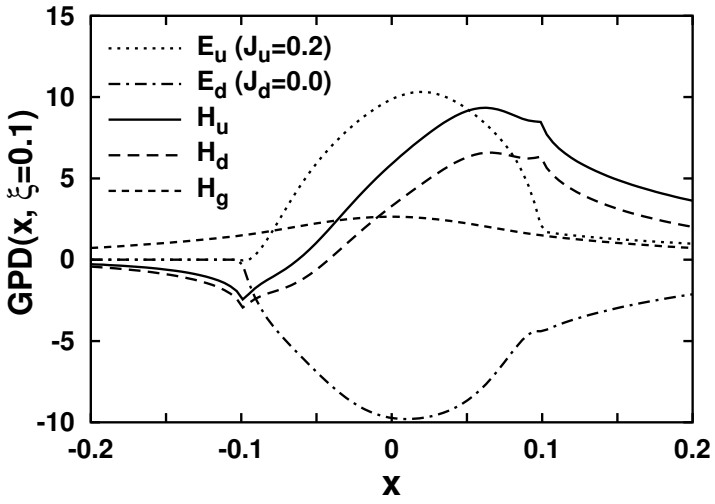

Figure 2.8: t-independent part of quark and gluon GPDs at Q^2=4 GeV^2, ξ=0.1 [18].

The factorized ansatz is the simplest way of modeling GPDs, but recent experimental studies of elastic diffractive processes indicate that the t-dependence of the cross section is correlated with its dependence on the photon-nucleon invariant mass [29]. This is taken into account in the non-factorized *Regge* ansatz, based on a Regge-type parameterization of the t-dependence. In this case the t-dependence is modeled as:

$$H^q(x, \xi = 0, t) = \frac{1}{x^{\alpha' t}} q(x) \,, \qquad H^g(x, \xi = 0, t) = \frac{1}{x^{\alpha' t}} x g(x) \,, \tag{2.55}$$

where α' is interpreted as the slope of a Regge trajectory with $\alpha' = 0.8$ GeV^{-2} for quarks and $\alpha' = 0.25$ GeV^{-2} for gluons [18].

More details about the GPD parameterizations and the theoretical predictions for the transverse target-spin asymmetry based on these parameterizations, are given in Section 8 and Appendix G.

2.5 Vector meson polarization and decay

The virtual photon and the vector meson have the same quantum numbers. The helicity transfer from the virtual photon to the vector meson is one of the interesting features of the production mechanism. The ρ^0 meson, being a spin-1 object, carries a total angular momentum

$J = L+S = 1$ in its rest frame. The ρ^0 meson is an unstable short-living particle that decays into two pions ($\rho^0 \to \pi^+ + \pi^-$) shortly after its formation. Due to angular momentum conservation, the system of decay products should also have $J = 1$. The decay particles are spin-0 objects, so that the angular momentum of the system $L = 1$. This implies that the spin-state of the ρ^0 is reflected in the orbital angular momentum of the decay particles (see Figure 2.9).

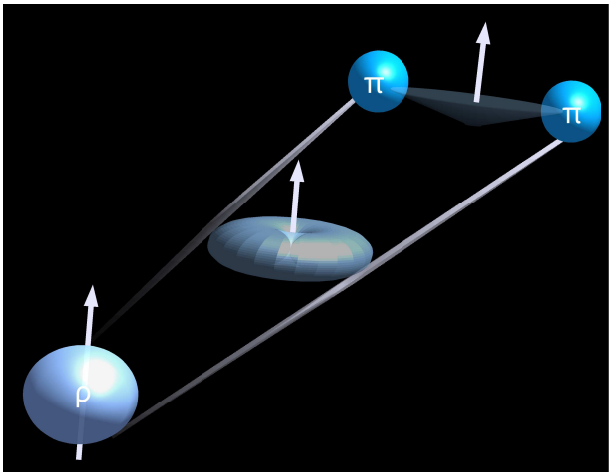

Figure 2.9: Schematic view of decay of exclusive ρ^0 into two pions.

The information on the photon and vector meson polarization states is encoded in the angular distribution of ρ^0 meson production and decay [48]. This 3-dimensional angular distribution is parameterized in terms of helicity amplitudes which construct the spin-density matrix elements (SDMEs). Since the exclusive ρ^0 production may proceed via an exchange of particles through the t-channel (*e.g.* in VMD model), the helicity amplitudes and the SDMEs contain information also on the parity of the exchanged particle.

The angular distribution depends on three angles: the azimuthal production angle Φ and decay angles ϕ and θ (see Figure 2.10). More details about the definition of these angles is given in Section 5.2.6. In the following the decomposition of the angular distribution in terms of SDMEs is discussed in the notation by Schilling-Wolff [48].

2.5.1 The spin-density matrix elements

Similar to the DIS cross section [49], the cross section of diffractive vector meson production can be factorized into a leptonic and a hadronic part:

$$\frac{d\sigma^{eN\to eNV}}{dE'\,d\Omega\,d\Phi\,dt} \propto \frac{1}{4}\sum_{spins}|M|^2 = \frac{1}{4}L_{\mu\nu}T^{\mu\nu}\,, \tag{2.56}$$

where $d\Omega$ is the solid angle of the scattered lepton and M is the matrix element describing the scattering process.

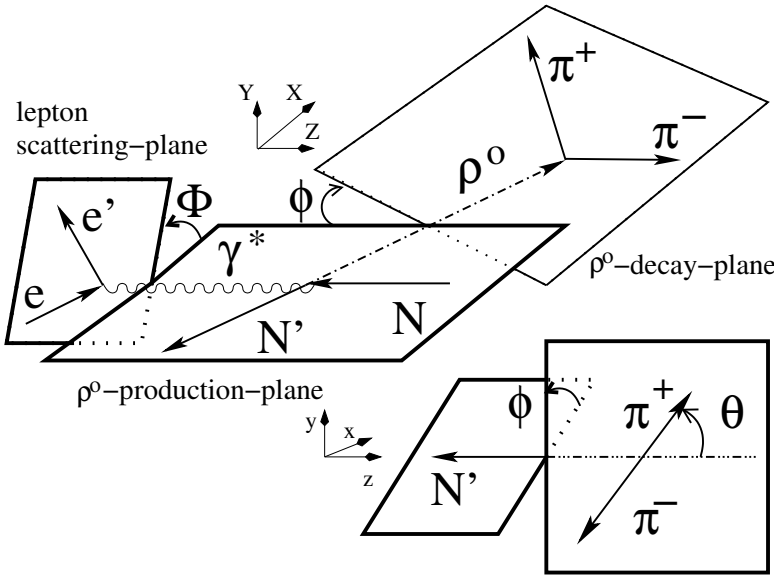

Figure 2.10: Definition of production and decay angles in elastic ρ^0 meson production.

The photon spin density matrix

The emission of the virtual photon is described by the leptonic tensor $L_{\mu\nu}$ representing the photon spin states, and therefore called photon spin density matrix. It can be decomposed in terms of an orthogonal set of hermitian matrices Σ^a,

$$\rho(\gamma) = \frac{1}{2}\sum_{a=0}^{8} \widetilde{\Pi}_a \Sigma^a \ , \tag{2.57}$$

where $\widetilde{\Pi}_a$ is a known normalization vector. Each of the nine hermitian matrices describes a certain photon polarization state. The matrices $\Sigma^{0\ldots3}$ describe unpolarized (0), linearly polarized (1,2) and (in the case of polarized lepton beam) circularly polarized (3) transverse photons, Σ^4 corresponds to longitudinal photons and $\Sigma^{5,6}$ ($\Sigma^{7,8}$) represent the transverse and longitudinal interference terms for an unpolarized (polarized) lepton beam.

The vector meson spin density matrix

In contrast to DIS, the hadronic tensor $T^{\mu\nu}$ representing the production of the vector meson $\gamma^* N \to V N$, is not constructed of structure functions. Instead, the vector meson production is described by a vector meson spin density matrix:

$$\frac{d\sigma^{\gamma^* N \to V N}}{d\Phi\, dt} \propto \frac{1}{4}\sum_{spins} |M|^2 \propto \frac{1}{2}\mathrm{Tr}(\rho(\mathrm{V}));, \tag{2.58}$$

The matrix $\rho(V)$ is related to the photon spin density matrix $\rho(\gamma)$ via the helicity flip amplitudes $T_{\lambda_V,\lambda_{N'},\lambda_\gamma,\lambda_N}$ describing the helicity transfer from the virtual photon (λ_γ) to the vector meson (λ_V):

$$\rho(V) = \frac{1}{2}(T\rho(\gamma)T^+) \Big/ \int \frac{d\Phi}{2\pi}\mathrm{Tr}(\mathrm{T}\rho(\gamma)\mathrm{T}^+) \; . \tag{2.59}$$

The vector meson spin density matrix can also be decomposed in terms of hermitian matrices:

$$\rho_{\lambda_V\lambda'_V}(V) = \sum_{a=0}^{8} \Pi_a \rho^a_{\lambda_V\lambda'_V} \; , \tag{2.60}$$

with the matrix elements

$$\rho^a_{\lambda_V\lambda'_V} = \frac{1}{2N_a} \sum_{\lambda_{N'},\lambda_N,\lambda_\gamma,\lambda'_\gamma} T_{\lambda_V,\lambda_{N'},\lambda_\gamma,\lambda_N}\, \Sigma^a_{\lambda_\gamma,\lambda'_\gamma}\, T^*_{\lambda'_V,\lambda_{N'},\lambda'_\gamma,\lambda_N} \; . \tag{2.61}$$

The N_a and Π_a are known normalization functions. If an unpolarized target is considered [48], the helicities λ_N of the initial and $\lambda_{N'}$ of the scattered target nucleon are summed over. The hermitian 3×3 matrices Σ^a represent the photon density matrix $\rho(\gamma)$ and determine which helicity flip amplitudes contribute to a certain matrix element.

2.5.2 The angular distribution

The ρ^0 vector meson is observed through the products of its two-body decay: $\rho^0 \to \pi^+\pi^-$. The decay is described in the vector meson rest frame by two angles that are the azimuthal angle ϕ between its production and decay planes and the polar angle θ of the positively charged decay particle, with the z-axis of the vector meson rest frame aligned opposite to the direction of the scattered nucleon (see Figure 2.10).

In the ρ^0 rest frame the decay angular distribution $W(\cos\theta,\phi)$ is given by

$$\frac{dN}{d\cos\theta, d\phi} = W(\cos\theta,\phi) = \sum_{\lambda_V\,\lambda'_V} \langle\, \theta,\phi|M|\lambda_V \,\rangle \; \rho_{\lambda_V\,\lambda'_V}(V) \; \langle\, \lambda'_V|M^+|\theta,\phi\,\rangle \; , \tag{2.62}$$

with M being the decay amplitude. The terms $\langle\theta,\phi|M|\lambda_V\rangle$ are expressed in terms of Wigner rotation functions $D^j_{mm'}$ representing the probability of transformation from quantum state $|j,m>$ into $|j,m'>$:

$$\begin{aligned} D^1_{10}(\phi,\theta,-\phi) &= -\frac{1}{\sqrt{2}}e^{-i\phi}\sin\theta \; , \\ D^1_{00}(\phi,\theta,-\phi) &= \cos\theta \, , \\ D^1_{-10}(\phi,\theta,-\phi) &= \frac{1}{\sqrt{2}}e^{i\phi}\sin\theta \; . \end{aligned} \tag{2.63}$$

In terms of SDMEs $\rho^\alpha_{\lambda_V\lambda'_V}$, the 3-dimensional ρ^0 meson production and decay angular dis-

tribution $W(\cos\theta, \phi, \Phi)$ reads [48]:

$$\begin{aligned} W(\cos\theta, \phi, \Phi) &= \frac{3}{4\pi} \sum_{\lambda_V\, \lambda'_V} D^1_{\lambda_V 0}(\phi, \theta, -\phi)^* \rho(V)_{\lambda_V\, \lambda'_V} D^1_{\lambda'_V 0}(\phi, \theta, -\phi) \\ &= \frac{3}{4\pi} \sum_{\alpha=0}^{8} \Pi_a \Big[\sum_{\lambda_V\, \lambda'_V} D^1_{\lambda_V 0}(\phi, \theta, -\phi)^* \rho^a_{\lambda_V \lambda'_V} D^1_{\lambda'_V 0}(\phi, \theta, -\phi) \Big] , \end{aligned} \tag{2.64}$$

where the Φ dependence enters through the vector meson density matrix $\rho(V)$.

The angular distribution can be decomposed into terms W_{XY} describing various polarization states of target (S) and beam (P),

$$W = W_{UU} + P_L W_{LU} + S_L W_{UL} + P_L S_L W_{LL} + S_T W_{UT} + P_L S_T W_{LT} , \tag{2.65}$$

where in W_{XY} X specifies the lepton beam polarization, and Y the target polarization. The lepton beam and the target can be unpolarized (U), longitudinally (L) or transversely (T) polarized. The case of a transversely polarized lepton beam is omitted here, since it does not provide any additional information compared to the case of longitudinal beam polarization.

In the case of a longitudinally polarized beam and an unpolarized target the 3-dimensional angular distribution $W(\cos\theta, \phi, \Phi)$ is a function of 26 independent matrix elements. For fixed beam energy, the polarization parameter ϵ is a constant at given values of E' and Q^2 (see equation (5.19)). Measurements at different values of the ratio ϵ for the same values of E' and Q^2, called *Rosenbluth separation*, are experimentally not feasible. This implies that for fixed beam energy the contributions from transverse and longitudinal photons are not distinguishable. The SDMEs $\rho^0_{\lambda\lambda'}$ and $\rho^4_{\lambda\lambda'}$ are now expressed in terms of the combinations $r^{04}_{\lambda\lambda'}$:

$$r^{04}_{\lambda\lambda'} = \frac{\rho^0_{\lambda\lambda'} + \epsilon R \rho^4_{\lambda\lambda'}}{1 + \epsilon R} . \tag{2.66}$$

The elements $r^{\alpha}_{\lambda\lambda'}$ are also redefined as

$$r^{\alpha}_{\lambda\lambda'} = \begin{cases} \dfrac{\rho^{\alpha}_{\lambda\lambda'}}{1 + \epsilon R} & \alpha = 1,\, 2,\, 3, \\ \dfrac{\rho^{\alpha}_{\lambda\lambda'} \sqrt{R}}{1 + \epsilon R} & \alpha = 5,\, 6,\, 7,\, 8 . \end{cases} \tag{2.67}$$

Here R is the longitudinal-to-transverse cross section ratio (see equation (2.21)). From now on the elements $r^{04}_{\lambda\lambda'}$ and $r^{\alpha}_{\lambda\lambda'}$ are called SDMEs.

The first term $W_{UU}(\cos\theta, \phi, \Phi)$ in equation (2.65) corresponds to the case of unpolarized

beam and target:

$$\begin{aligned} W_{UU}(\cos\theta,\phi,\Phi) &= \frac{3}{4\pi}\left[\frac{1}{2}(1-r^{04}_{00})+\frac{1}{2}(3r^{04}_{00}-1)\cos^2\theta\right. \\ &-\sqrt{2}\ \mathrm{Re}r^{04}_{10}\ \sin 2\theta\cos\phi - r^{04}_{1-1}\ \sin^2\theta\cos 2\phi \\ &-\epsilon\ \cos 2\Phi\left(r^{1}_{11}\ \sin^2\theta + r^{1}_{00}\ \cos^2\theta - \sqrt{2}\ \mathrm{Re}r^{1}_{10}\ \sin 2\theta\cos\phi - r^{1}_{1-1}\ \sin^2\theta\cos 2\phi\right) \\ &-\epsilon\ \sin 2\Phi\left(\sqrt{2}\ \mathrm{Im}r^{2}_{10}\ \sin 2\theta\sin\phi + \mathrm{Im}r^{2}_{1-1}\ \sin^2\theta\sin 2\phi\right) \\ &+\sqrt{2\epsilon(1+\epsilon)}\ \cos\Phi\left(r^{5}_{11}\ \sin^2\theta + r^{5}_{00}\ \cos^2\theta - \sqrt{2}\ \mathrm{Re}r^{5}_{10}\ \sin 2\theta\cos\phi - r^{5}_{1-1}\ \sin^2\theta\cos 2\phi\right) \\ &\left.+\sqrt{2\epsilon(1+\epsilon)}\ \sin\Phi\left(\sqrt{2}\ \mathrm{Im}r^{6}_{10}\ \sin 2\theta\sin\phi + \mathrm{Im}r^{6}_{1-1}\ \sin^2\theta\sin 2\phi\right)\right]. \end{aligned} \tag{2.68}$$

It is parameterized via 15 'unpolarized' SDMEs, with photon polarization states indicated as $0, 1, 2, 4, 5, 6$ (see Section 2.5.1). These 15 unpolarized SDMEs were already measured in various experiments [50, 51].

For a longitudinally polarized beam, the term $W_{LU}(\cos\theta,\phi,\Phi)$ in equation (2.65) provides 8 additional ('polarized') SDMEs with photon polarization states $3, 7, 8$:

$$\begin{aligned} W_{LU}(\cos\theta,\phi,\Phi) &= \frac{3}{4\pi}\left[\sqrt{1-\epsilon^2}\left(\sqrt{2}\ \mathrm{Im}r^{3}_{10}\ \sin 2\theta\sin\phi + \mathrm{Im}r^{3}_{1-1}\ \sin^2\theta\sin 2\phi\right)+\right. \\ &\sqrt{2\epsilon(1-\epsilon)}\ \cos\Phi\left(\sqrt{2}\ \mathrm{Im}r^{7}_{10}\ \sin 2\theta\sin\phi + \mathrm{Im}r^{7}_{1-1}\ \sin^2\theta\sin 2\phi\right)+ \\ &\left.\sqrt{2\epsilon(1-\epsilon)}\ \sin\Phi\left(r^{8}_{11}\ \sin^2\theta + r^{8}_{00}\ \cos^2\theta - \sqrt{2}\ \mathrm{Im}r^{8}_{10}\ \sin 2\theta\sin\phi - \mathrm{Im}r^{8}_{1-1}\ \sin^2\theta\sin 2\phi\right)\right]. \end{aligned} \tag{2.69}$$

These 15+8 SDMEs are measured at HERMES [52].

The normalization of the angular distribution is given by [17]

$$\int\frac{d\Phi}{2\pi}\int d\cos\theta\ d\phi\ W(\theta,\phi,\Phi) = 1\ . \tag{2.70}$$

The measurement of SDMEs on a polarized target, and in particular on a transversely polarized target (term W_{UT} in equation (2.65)) is one of the topics of this thesis and is discussed in Section 6.7.3.

2.5.3 s-channel helicity conservation and natural/unnatural parity exchange

Two main ordering principles are observed in spin-dependent vector meson production, *s-channel helicity conservation* (SCHC) and the dominance of *natural-parity exchange* (NPE).

s-channel helicity conservation

SCHC implies that the vector meson conserves the helicity of the virtual photon γ^*. In this case the transitions $\gamma^* \to \rho^0$ involving a helicity flip vanish,

$$T_{01} = T_{10} = T_{0-1} = T_{-10} = T_{1-1} = T_{-11} = 0 \,, \tag{2.71}$$

compared to those which conserve helicity. Only the three helicity non-flip amplitudes[4] T_{00}, T_{11}, T_{-1-1} for ρ^0 production by a longitudinal or a transverse photon, and consequently the SDMEs related to those amplitudes do not vanish.

In the case of SCHC the angular distribution can be written as a function of $\cos\theta$ and $\Psi = \phi - \Phi$:

$$\begin{aligned} W(\cos\theta, \Psi) &= \frac{3}{4\pi}\left[\frac{1}{2}(1 - r^{04}_{00}) + \frac{1}{2}(3r^{04}_{00} - 1)\cos^2\theta\right] \\ &+ \epsilon r^1_{1-1}\sin^2\theta\cos 2\Psi - 2\sqrt{\epsilon(1+\epsilon)}\,\mathrm{Re}\, r^5_{10}\sin 2\theta\cos\Psi \\ &+ 2P_l\epsilon(1-\epsilon)\,\mathrm{Im}\, r^7_{10}\sin 2\theta\sin\Psi \,. \end{aligned} \tag{2.72}$$

Natural- and unnatural-parity exchange

In Regge theory the diffractive production of vector meson proceeds via an exchange of a particle through the t-channel. The exchanged particle may have natural parity $P = (-1)^J$ or unnatural parity $P = -(-1)^J$, where J and P correspond to the spin and parity of the particle, respectively. Thus NPE is associated with exchanging natural-parity particles, like ρ, ω, f_2, a_2, and unnatural-parity exchange (UPE) with exchanging unnatural-parity mesons, like π, a_1, b_1. The pomeron exchange corresponds to the NPE, since the pomeron has the same quantum numbers as the vacuum (thus the intrinsic parity is equal to 1). Substantial UPE contributions can be expected only at lower values of W, since the reggeon exchanges with unnatural parity are suppressed by a factor $\propto (M/W)^2$, while the exchanges with natural parity only by a factor $\propto M/W$ [53].

Both the helicity amplitudes and the SDMEs can be split into a contribution of natural and unnatural parity exchange. If NPE and SCHC are assumed, only two independent amplitudes are left, T_{00} and T_{11}. With a phase difference δ introduced between these two amplitudes, the angular distribution reads:

$$\begin{aligned} W(\cos\theta, \Psi) &= \frac{1}{1+\epsilon}\frac{3}{8\pi}\Big[\sin 2\theta(1 + \epsilon\cos 2\Psi) + 2\epsilon R\cos^2\theta \\ &- \sqrt{\epsilon(1+\epsilon)R}\cos\delta\sin 2\theta\cos\Psi + P_l\sqrt{\epsilon(1-\epsilon)R}\sin\delta\sin 2\theta\sin\Psi\Big] \,. \end{aligned} \tag{2.73}$$

[4] The nucleon helicity states are omitted.

Chapter 3

The HERMES experiment at HERA

"You see things; and you say, 'Why?' But I dream things that never were; and I say, "Why not?""

— George Bernard Shaw

HERMES was one of the four experiments located at the HERA storage ring (see Figure 3.1) at DESY in Hamburg, Germany. HERA was operated from 1992 until 2007. It has a circumference of 6.3 km and lies about 10 to 25 m under ground. The HERA machine consisted of two storage rings where leptons[1] and protons were accelerated in opposite directions to energies of 27.5 GeV and 920 GeV, respectively. HERMES, located in the East Hall of the ring, was a fixed-target experiment that used only the lepton beam of HERA, sharing it with the two collider experiments H1 and ZEUS located in the North and South halls, respectively. The fourth experiment, HERA-B, located in the West hall, had the proton beam interacting with a fixed target until the year 2003.

HERMES was designed to study the spin structure of the nucleon, in particular the individual quark contributions to the nucleon spin. Due to unique properties of HERA and HERMES, the scope of HERMES was expanded. HERA was the only machine able to accelerate and store both electrons or positrons. The HERMES target had the flexibility to be operated with longitudinally or transversely polarized hydrogen and deuterium gases as well as with unpolarized gases (H, D, ^{3}He, Kr, Ne, Xe). The HERMES spectrometer had a good momentum resolution and excellent particle identification capabilities. Data taking was started in summer 1995 and stopped in 2007. In this chapter a short overview of the experimental setup is given.

3.1 The polarized HERA beam

Hera provided an electron or positron beam consisting of up to 220 bunches with a length of 27 ps, separated by 96 ns. The beam current, initially close to 50 mA, decreased exponentially during the $12-14$ hours of the beam life time. The beam life time was limited due to interactions with residual gas in the storage ring and collisions with the proton beam.

[1]Hearafter leptons stands for either electrons or positrons.

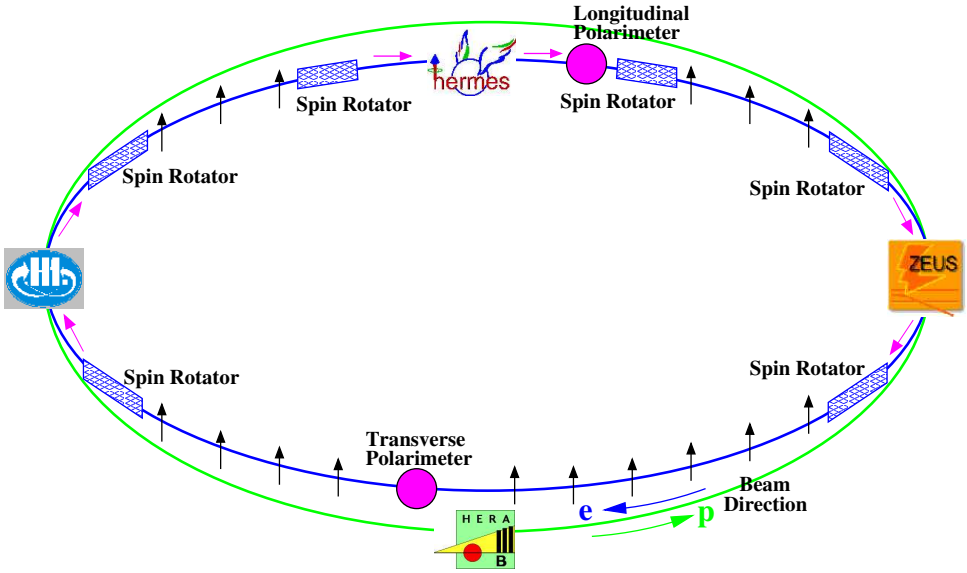

Figure 3.1: Schematic view of the HERA accelerator in the setup of the years 2001-2007 with the four experiments. Spin rotators around H1, HERMES and ZEUS turn the lepton spin orientation from transverse to longitudinal and back.

The beam was transversely self-polarized due to the Sokolov-Ternov effect [54], a tiny asymmetry of the spin-flip amplitude in the synchrotron radiation in favor of an anti-parallel (parallel) spin-orientation for electrons (positrons) relative to the field direction of the bending magnets. As soon as the initially unpolarized beam has been ramped up to its final energy of 27.6 GeV, the polarization began to build up. After a rise time of about 30 minutes typical polarization values of about $50 - 60\%$ were reached in the years 1996-2000. The theoretical possible value of 92% was not reached due to lepton-proton beam interactions, depolarization effects as misalignment of magnets and deviations of the beam from the designed orbit. Upstream of the HERMES target the transverse beam polarization was transformed into a longitudinal one by a set of magnets acting as spin rotators. Another spin rotator returned it back to transverse polarization downstream of HERMES (see Figure 3.1). The polarization was permanently monitored by two polarimeters, one of them measuring the longitudinal polarization [55] downstream of the HERMES spectrometer, and another one measuring the transverse polarization [56] of the beam at the opposite side of the ring. Both polarimeters made use of a cross section asymmetry in Compton backscattering of circularly polarized photons off polarized leptons. The measurement of both polarimeters usually agreed, as shown in Figure 3.2. Until the year 2001 the spin orientation of the beam was rotated only in the HERMES experimental section and the maximum longitudinal polarization of the beam was about 60%. In 2002, two additional pairs of spin rotators were installed in front and behind the H1 and ZEUS experiments, after which the maximum polarization value achieved was 50%.

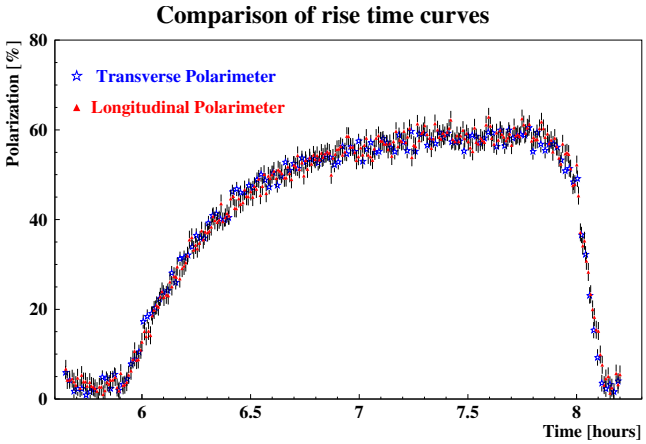

Figure 3.2: The beam polarization build-up due to the Sokolov-Ternov effect vs. the beam life time, as monitored by two polarimeters measuring the longitudinal and transverse polarization of the beam.

3.2 The polarized HERMES target

HERMES used a gaseous target internal to the lepton storage ring. The advantage of such a target was that high polarization values could be achieved without dilutions due to unpolarized materials typical to liquid and solid-state targets. Although the achieved densities of the gas target were much lower compared to the latter, they were still two orders of magnitude higher than those obtained with a gas jet target.

The HERMES target [57] consisted of four main components (see Figure 3.3): an atomic beam source (ABS) producing polarized hydrogen or deuterium atoms[2], a windowless storage cell installed in the vacuum of the beam pipe and two diagnostic devices which measure the polarization (Breit-Rabi Polarimeter (BRP)) and the atomic fraction of the gas (Target gas analyzer (TGA)).

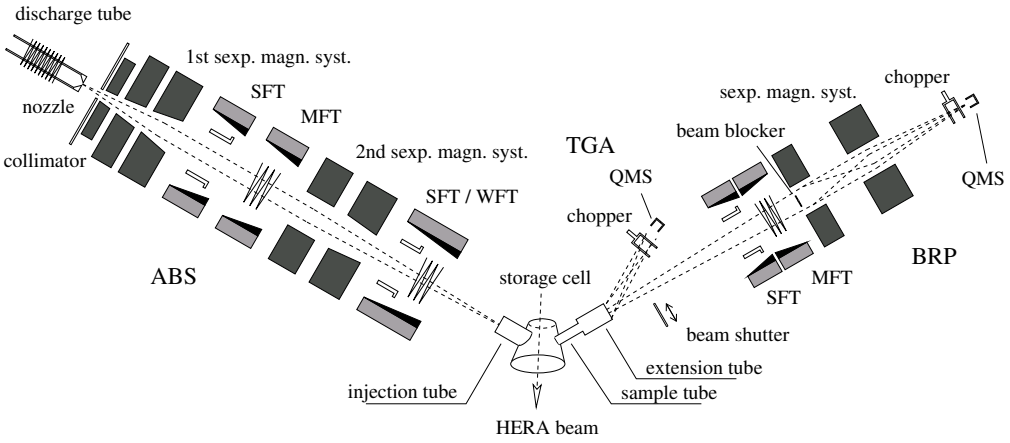

Figure 3.3: Representation of the HERMES target setup.

[2]Unpolarized gases can also be injected into the target cell through a separate capillary near the ABS outlet.

3.2.1 The atomic beam source

The polarized gas was produced by an ABS [58] (see the left-hand side of Figure 3.3) making use of the Stern-Gerlach effect. First, the molecules of hydrogen were dissociated into atomic hydrogen by a radio frequency (RF) discharge in the glass tube with a dissociation degree of up to 80%. Then the hydrogen atoms flew through a cooled nozzle with a temperature of 100 K (which surface was covered with a layer of ice to prevent the recombination), a set of collimators and entered a sextupole magnet system. If no external magnetic field is present, there are only two hyperfine states for the hydrogen atoms corresponding to the energy difference between the states with total spin $F = 0$ and $F = 1$. In the external magnetic field of the sextupole magnet with a gradient perpendicular to the direction of motion of the hydrogen atoms, the latter ones split into four hyperfine energy levels (see Figure 3.4) and experience different forces according to their magnetic moments. The four states are the combinations of the nucleon (I) and of the shell electron (s) up and down spin states: $m_I = \pm 1/2$ and $m_s = \pm 1/2$. Those atoms having the electron spin orientation $+1/2$ were focused toward the axis of the magnet, those with a negative magnetic moment were deflected. A set of RF fields permits to attain a nuclear polarization by interchanging the occupation numbers of hyperfine states. While the weak field transition (WFT) exchanged the occupation numbers of hyperfine states $|1\rangle$ and $|3\rangle$, the strong field transition (SFT) acted on states $|2\rangle$ and $|4\rangle$. The SFT and WFT were operated independently providing atoms in the hyperfine state combinations of either $|1\rangle + |4\rangle$ or $|2\rangle + |3\rangle$. Thus the electron polarization vanished and the nucleon spin projection was either $+1/2$ or $-1/2$. During the data taking with transversely polarized target the spin state was flipped every 90 s and fluxes of up to 6.5×10^{16} atoms/s were injected into the storage cell.

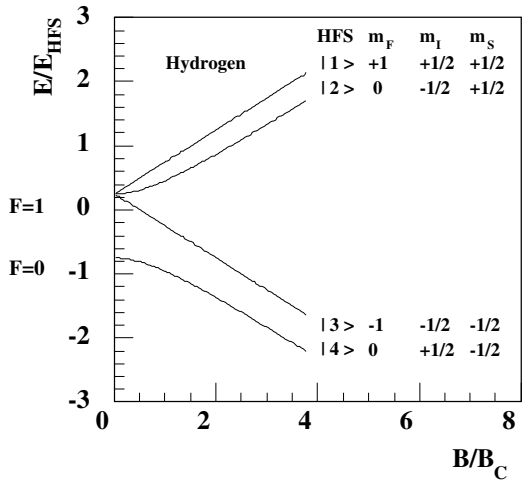

Figure 3.4: Hyperfine energy levels of hydrogen atoms as a function of the strength of an external magnetic field. Field values are given in units of the critical magnetic field B_C defined as external field strength which caused the energy differences between the states $|1\rangle$ and $|3\rangle$ to be equal to the hyperfine splitting E_{HFS}. The energy values are shown in units of E_{HFS}.

3.2.2 The storage cell

The polarized atoms from the ABS were injected through an injection tube to the center of the storage cell [59]. The cell was constructed from 99.5% pure aluminium and was made as thin as possible (75μm) to minimize multiple scattering and bremsstrahlung of the particles passing through its walls. The cell had an elliptical cross section of 21×8.9 mm^2 and usable length to 400 mm limited by the spectrometer acceptance. The interior of the cell was coated with Drifilm and the walls were cooled to a temperature of 100 K to minimize the gas recombination and depolarization caused by wall collisions. Opposite to the injection tube through which the polarized gas was fed in, there was another sample tube installed that led to the TGA and BRP with 5% of the target gas for diagnostic measurements.

3.2.3 The target gas analyzer

The TGA [60] measured the atomic and molecular contents of the gas sample extracted from the storage cell. The differentiation between molecules and atoms was necessary as their nuclear polarizations were different. The main component of the TGA (the right-hand side of Figure 3.3) was a 90° off-axis quadrupole mass spectrometer (QMS) with a cross beam ionizer and a channel electron multiplier (CEM) for single ion detection. In order to avoid interferences with the BRP measurements, the TGA was tilted by 7° with respect to the sampling tube. In front of the QMS a chopper periodically blocked the sample beam in order to distinguish between particles from the sample beam and those from residual gas. Particles entering the detector were ionized by 70 eV electrons, mass filtered with the QMS and detected by the CEM. The measured atomic and molecular signals in the TGA were proportional to the corresponding particle fluxes of atoms Φ_a and of molecules Φ_m. The degree of dissociation of the sample beam is given by:

$$\alpha^{TGA} = \frac{\Phi_a}{\Phi_a + \Phi_m}. \tag{3.1}$$

Using this measurement together with various calibration measurements, two quantities can be calculated [57]: the initial atomic fraction α_0 in the injected gas and the fraction of atoms α_r surviving the recombination in the cell.

3.2.4 The Breit-Rabi polarimeter

The gas sampled in the storage cell was analyzed also for its atomic polarization using a BRP [61] which applied the same principles as the ABS but in reverse order. The strong and medium RF field transitions and a sextupole magnet separated opposite electron spin states. A beam blocker was installed in front of the magnet to prevent the atoms entering the sextupole magnet system on the symmetry axis where the field gradient was zero. Atoms with a selected state entered the QMS and were counted with the CEM. The polarization P_a^{BRP} was calculated by

measuring the relative occupation of the four hyperfine states. The BRP measured the gas polarization in the center of the storage cell. The polarization P_a averaged along the cell was obtained by applying the sampling correction C_P:

$$P_a = C_P \cdot P_a^{BRP}, \tag{3.2}$$

which was estimated with the help of Monte Carlo simulations of the stochastic motion of the particles in the storage cell. The uncertainty of this factor is part of the total systematic uncertainty of the target polarization.

3.2.5 The target polarization

Using the results of the TGA and BRP measurements, the effective target polarization P_T can be calculated:

$$P_T = P_a \alpha_0 [\alpha_r + (1 - \alpha_r)\beta], \tag{3.3}$$

where β is the relative polarization of molecules with respect to the polarization of atoms. As the BRP could measure only the polarization of the atoms, a direct measurement of β was not possible. Dedicated studies have restricted the value of β to be in the range of $\beta = [0.45 : 0.83]$ [62]. The uncertainty on β is another part of the systematic uncertainty of the target polarization measurement.

The HERMES target group provided an average target polarization value for each data taking period, as shown in Table 3.1.

data taking period	average target polarization
2002 (Apr 2002 - Mar 2003)	0.783 ± 0.041
2003 (Sep 2003 - Dec 2003)	0.795 ± 0.033
2004 (Jan 2004 - Aug 2004)	0.737 ± 0.055
2005 (Aug 2004 - Dec 2005)	0.706 ± 0.065
2002-2005	0.724 ± 0.059

Table 3.1: Average target polarization values for different data taking periods using a hydrogen target. The statistical uncertainties are neglected compared to the listed systematic uncertainties.

3.2.6 The target magnet

A uniform magnetic holding field of $B = 297$ mT along the beam axis, surrounding the storage cell, was generated by a superconducting magnet providing the spin quantization axis and

effectively decoupling the electron and nucleon magnetic moments. It also suppressed the spin relaxation due to the splitting of the hyperfine energy levels.

The magnetic force $\mathbf{F}$ caused by the external magnetic field $\mathbf{B}$, on a beam particle of charge q moving with a velocity $\mathbf{v}$ is given by the Lorentz formula:

$$\mathbf{F} = q\mathbf{v} \times \mathbf{B}. \tag{3.4}$$

In case of a longitudinally polarized target, the holding field was parallel to the beam and thus had no effect on the incoming lepton. Since the angular acceptance of the HERMES spectrometer was about ± 140 mrad vertically and ± 180 horizontally, all accepted particles were also nearly parallel to $\mathbf{B}$. Thus the holding field of the target magnet had a marginal effect on the trajectories of scattered particles. In case of a transversely polarized target, the transverse holding field deflected both the beam and the scattered particles, since they were moving perpendicular to $\mathbf{B}$, so that the vertex position and the scattering angles must be corrected for the deflection (see Section 7.7.2).

3.3 The HERMES spectrometer

After the interaction of the beam lepton with the target nucleon, the scattered particles were detected in the HERMES forward magnetic spectrometer [63] built of two identical halves above and beneath the beam pipes (see Figure 3.5). The spectrometer consisted of a magnet and sets of tracking and particle identification (PID) detectors.

The axes of the HERMES right-handed coordinate system are defined in a way that the z direction is along the beam axis, x points towards the center of the HERA ring and y points upwards. The center of the target storage cell is the origin of the HERMES coordinate system.

This section briefly describes the individual components of the detector.

3.3.1 The spectrometer magnet

A dipole magnet with a vertical deflecting power of $\int B\ dl = 1.3$ Tm bent the tracks of the charged particles in the horizontal plane. The influence of this field on the HERA beam was shielded by an 11 cm thick septum steel plate enclosing the beam pipe. The aperture given by the magnet defines the upper limits of the spectrometer acceptance of ± 170 mrad in the horizontal and of ± 140 mrad in the vertical direction. The steel plate limited the lower vertical acceptance to ± 40 mrad. In combination with tracking detectors, the spectrometer magnet permitted a precise measurement of the charged particles' momentum.

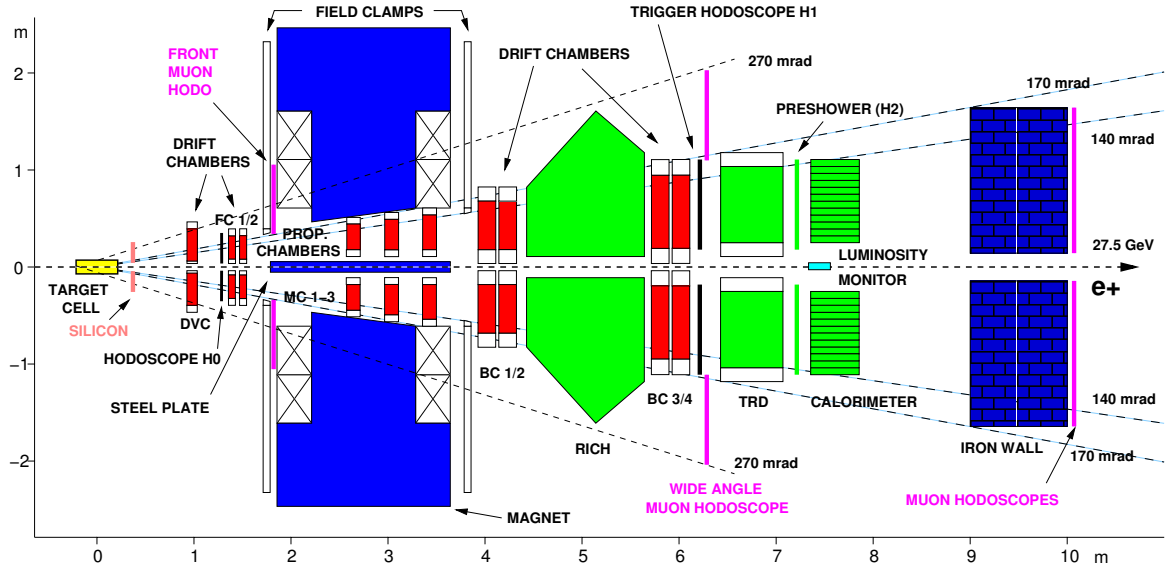

Figure 3.5: Side view of the HERMES spectrometer in the setup of the years 2001-2005. The beam enters from the left side and traverses the target cell centered at position (0,0). The tracking detectors are shown in red and the particle identification detectors in green.

3.3.2 Tracking detectors

The tracking system consisted of tracking chambers in front of, inside and behind the magnet. Except the silicon detector, installed right after the target, all the other tracking detectors were wire chambers, each consisting of several planes oriented in three directions: vertical and tilted by $\pm 30°$ with respect to the vertical axis. Each wire chamber module consisted of six layers where half of the planes were offset by half a cell width, to resolve right-left ambiguities.

The silicon detector (Lambda Wheels) [64] was installed in 2002 in order to increase the acceptance for long-living particles which decay outside of the target region, like Λ, Λ_c, K_s. This detector is mentioned here for completeness as it is not used for the analysis discussed in this thesis.

The drift vertex chambers (DVC) were installed 1.1 m downstream of the target and used the gas mixture $Ar/CO_2/CF_4$. The planes had a wire spacing of 6 mm and the resolution was 200 μm per plane. DVCs were supposed to improve the momentum resolution. However, in practice it was improved only slightly and the DVCs are not used for the front track reconstruction.

The front chambers (FC) [65] were the main detectors used for the front track reconstruction. They were installed in front of the spectrometer magnet, at about 1.6 m from the target center. The two modules of the FC drift chambers had drift cells of 7 mm width and 8 mm depth. They were filled with the same gas as the DVCs. The resolution per plane was 225 μm and the efficiencies per single plane varied between $97\% - 99\%$ depending on the position in the cell.

The magnet chambers (MC) [66] were three set of proportional wire chambers installed in the gap of the spectrometer magnet and used to determine the momentum of low energy particles that did not reach the back part of the detector. The MCs are also not used in the analysis described in this thesis.

The back chambers (BC) [67] were two pairs of drift chamber modules located in front of and behind the RICH detector and used for track reconstruction behind the spectrometer magnet. Each BC plane had a drift size of 15×16 mm and was filled with the same gas mixture as FCs and DVCs. The resolutions were 210 μm for a BC1/2 plane and 250 μm for a BC3/4 plane. The efficiency for positrons was above 99% while for hadrons was slightly smaller (97%) due to lower ionization density.

The reconstruction

Based on the hits in the FCs and BCs, the front and back tracks are reconstructed by a fast tree-search pattern recognition algorithm used by the HERMES reconstruction program (HRC). These partial tracks are straight lines which are combined to full tracks if they intersect in the magnet center within a defined tolerance. At the first step a larger tolerance is taken. Then, fixing the matching point of the higher quality back partial track at the magnet, the front track parameters are recalculated. In an iterative procedure the momentum resolution is improved. This method is called *force bridging* when the front track is forced to match the back track in the center of the magnet. In the next step the momentum of the track is determined comparing the front track position and the slopes in front and behind the magnet with numbers in the look-up tables [68]. There the particle momentum is given as a function of track parameters. For the data taking period from 2002 to 2005 years a momentum resolution of $\Delta P/P < 2.6\%$ and an angular resolution of $\Delta\theta < 1.4$ mrad is achieved[3].

As the transverse target magnet changed the vertex position and the scattering angles of the produced particle (see Section 3.2.6), these reconstructed quantities have to be corrected. The reconstructed partial tracks in front of the spectrometer magnet do not yield the correct vertex positions and scattering angles when they are extrapolated into the target cell by a straight line. The scattering angle at the vertex must be determined from the track positions in the FCs and DVCs, and a correction must be applied to account for the deflections of the trajectory between the vertex point and the FCs and DVCs. This requires knowledge about the magnetic field which was modeled for the 2002 data taking period and measured for the other years starting from 2003. Two different target magnet correction (TMC) methods [69] are available to calculate the interaction point and the scattering angles, before the track was deflected by the transverse field.

[3]The resolutions were better for data taken before 1998 when a gas Čerenkov detector was installed instead of the RICH detector which introduces more material along the particle path.

3.3.3 The particle identification detectors

There were four different PID detectors: a dual-radiator ring-imaging Čerenkov (RICH) detector, a transition radiation detector (TRD), a preshower detector and a lead-glass electromagnetic calorimeter. The responses of these detectors give a very clear separation between leptons and individual hadron types.

The RICH detector [70]. Charged particles which traverse a material with a velocity v higher than the speed c_m of the light in that material, emit electromagnetic (Čerenkov) radiation in a cone around their trajectory with a characteristic opening angle θ_c:

$$\cos\theta_c = \frac{1}{\beta n}, \tag{3.5}$$

which depends on the refractive index $n = c/c_m$ of the material and the velocity v of the particle (as $\beta = v/c$ where c is the speed of light in vacuum). The particle's threshold velocity to radiate Čerenkov light is given by the refractive index of the material : $v >= c_m \equiv c/n$. According to equation (3.5), the particles with the same momentum but different masses emit Čerenkov light with different opening angles. This phenomenon enables the discrimination between various hadrons and leptons.

The RICH detector consisted of two radiators with different refractive indices. The first one with refractive index of 1.0304, was a 5.5 cm thick wall of aerogel tiles (10.5×10.5 cm^2) stacked in 5 layers with 5 horizontal rows and 17 vertical columns, installed right after the entrance window of the detector. The second radiator with refractive index of 1.0014, was a heavy gas (C_4F_{10}) filling the volume of the detector. The particles traversing the detector emitted Čerenkov photons in two radiators if their velocities were above the respective thresholds. The photons, reflected from a spherical mirror, were detected by a photon detector which was an array of photo multiplier tubes (PMTs). The threshold behavior in both radiators as well as the opening angle information are used for discrimination between pions, kaons and protons in the momentum range of $1 < p < 15$ GeV (see Figure 3.6).

The RICH information is used for lepton/hadron separation as well which is quite important in the low momentum ($p < 4$ GeV) region where the other PID detectors were not optimized. A lepton with a momentum[4] of $p > 0.5$ GeV emitted photons in both radiators at angles close to the maximum: $\theta_A \simeq 250$ mrad in the aerogel and $\theta_G \simeq 50$ mrad in the gas. The pions, having the threshold of about $p > 0.6$ GeV in the aerogel, emitted less photons in smaller average opening angle while the threshold for pions to radiate Čerenkov light in the gas was $p > 2.8$ GeV. Thus the RICH is used for lepton identification by analyzing the number of hit PMTs and the characteristic Čerenkov angles in both radiators.

The transition radiation detector, located between the two hodoscopes H1 and H2,

[4]The momentum of 0.5 GeV is the threshold below which the charged particles were bent out of the detector by the spectrometer magnet.

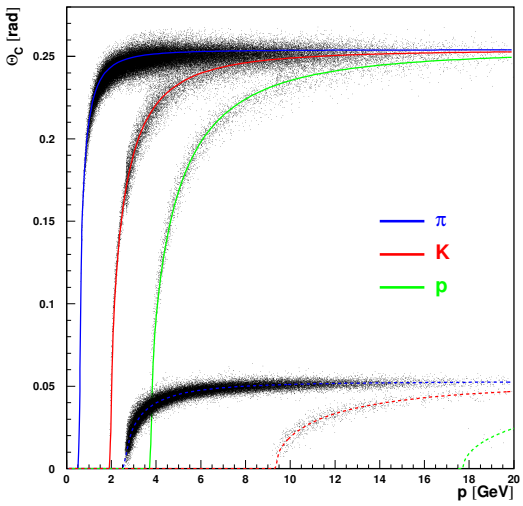

Figure 3.6: The dependence of Čerenkov angles on momentum for aerogel (upper curves) and gas (lower).

was used to distinguish between leptons and hadrons. It employs the emission of transition radiation by a charged particle with a Lorentz boost factor of $\gamma = 1/\sqrt{1-\beta^2} > 500$ when it crosses the boundary between two materials with different dielectric constants. The radiator material of the TRD, a mesh of thin polyethylene/polypropylene fibers, was chosen in a way that only leptons produce transition radiation at HERMES energies. Other particles could deposit energies due to ionization losses. The fiber arrangement provided many boundaries increasing the intensity of radiated photons. At high energies this radiation mainly consisted of X-rays which were emitted in a narrow cone with an opening angle of $\theta \sim 1/\gamma$. The deposited energy of X-ray photons was detected by multi-wire proportional chambers (MWPC) with a mixture of Xe and CH_4 gases having good sensitivity to X-ray photons, one MWPCs connected to each of six 6.35 cm thick modules of TRD in each detector half. The combined information from six modules permits to identify positrons of about 5 GeV with a hadron rejection factor (the number of pions divided by the number of pions misidentified as positrons) > 100 at a lepton identification efficiency of 90%.

The preshower detector. HERMES had three sets of hodoscopes among which only H2, the preshower detector, provides PID information. An 11 mm thick lead plate (corresponding to 2 radiation lengths) in front of the hodoscope initiated electromagnetic showers for leptons. The H2 itself was built of 42 vertical plastic scintillator paddles ($9.3 \times 91 \times 1$ cm^3) and connected to PMTs for readout. Adjacent paddles were overlapping for maximum efficiency. While traversing the lead plate, hadrons deposited only 2 MeV in the scintillators due to ionization losses, while the energy losses of leptons were larger due to showering in the lead and varied between 10 and 100 MeV.

The electromagnetic calorimeter [71] being the last PID detector on the particle's way, was built in a way that the leptons lost almost all of their energy by showering in the 50 cm

depth of the calorimeter blocks (equivalent to 18 radiation lengths). The calorimeter had two identical halves each with 420 lead-glass blocks (9×9 cm^2), coupled to PMTs measuring the amount of Čerenkov light produced by the showers. The ratio of the energy E deposited in the calorimeter blocks and the momentum P of the leptons peaks around $E/P \sim 1$. As for the hadrons, they deposited only a fraction of their kinetic energy through ionization energy losses and nuclear interactions, resulting in an average ratio of $E/P \sim 0.4 - 0.5$. For PID the ratio of E/P of the particle is considered. Besides the lepton/hadron separation, the calorimeter is also used for detection and energy determination of photons.

The particle identification scheme

The final PID decision is done by a highly efficient algorithm developed in [72]. In each PID detector i, for each particle a logarithmic likelihood ratio PID_i of probabilities to find a positron $P(S_e, p)$ or a hadron $P(S_h, p)$ with a momentum p causing a specific signal S,

$$PID_i = lg \frac{P(S_e, p)}{P(S_h, p)}, \tag{3.6}$$

is constructed. These probabilities from each PID detector, called parent distributions, are combined in different ways and assigned to each particle.

$$\begin{aligned} PID3 &= PID_{calo} + PID_{preshower} + PID_{RICH} \\ PID5 &\equiv PID_{TRD} = \sum_{i=1}^{6} PID_{TRD_i}. \end{aligned} \tag{3.7}$$

As seen from Figure 3.7, this algorithm gives a clear separation between leptons and hadrons. The individual hadron identification is done by the RICH detector discussed in the beginning of the section.

3.4 The luminosity measurement

For cross section measurements a precise determination of the luminosity is necessary. The luminosity is the product of the target-gas density and the beam current, integrated over the time of the measurement, corrected for the dead time. The luminosity measurement is based on the observation of the elastic scattering of beam leptons off target gas shell electrons. In case of an electron beam Möller scattering $e^-e^- \to e^-e^-$ takes place while in case of a positron beam two processes contribute to the e^+e^- interaction: Bhabha scattering $e^+e^- \to e^+e^-$ and e^+e^- annihilation into photon pairs $e^+e^- \to \gamma\gamma$. In both cases the precise cross sections are known from QED.

Both the scattered lepton and the hit electron were detected by the luminosity monitor [73]. It consisted of two small calorimeters, located at about 7.2 m downstream the target, mounted

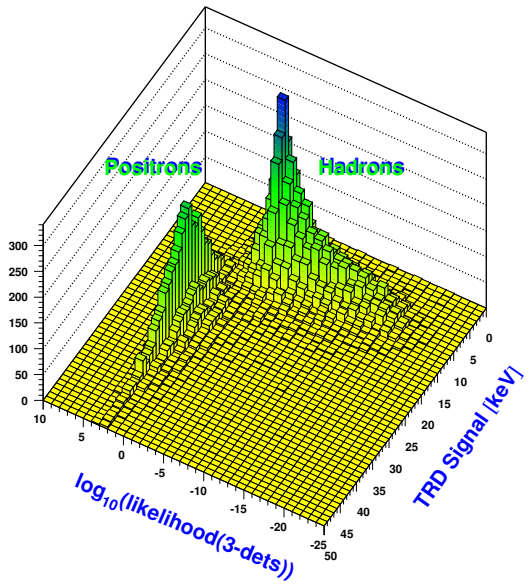

Figure 3.7: The HERMES particle identification: PID3 vs TRD.

as close as possible to both sides of the beam pipe, as the scattered angles of the leptons and photons were small. The calorimeters consisted of 3×4 arrays of radiation resistant Čerenkov crystals ($22 \times 22 \times 200$ mm^3), connected to PMTs. The resulting horizontal acceptance was $4.6 - 8.9$ mrad. The particles from desired reactions were detected in coincidence in the two calorimeters with the requirement of high (at least 4.5 GeV) energy deposition in both of them as most of the background events had a high energy deposition in only one detector.

The absolute luminosity is given by the ratio of the event rates R and the integrated cross section of the processes folded with the detector acceptance $\Delta\Omega$ and efficiency ϵ :

$$L = \frac{R}{\int \frac{d\sigma}{\Delta\Omega}\, \epsilon\, \Delta\Omega}. \tag{3.8}$$

The resulting luminosity is determined with an accuracy of $\Delta L/L \approx 6\%$.

For cross section asymmetry measurements it is sufficient to use only the rate R, the relative luminosity, since the denominator in equation (3.8) cancels when asymmetries are constructed. In this case the uncertainty is much smaller, $\Delta R/R \approx 0.9-1.5\%$, since the main contribution to the systematic uncertainty of the absolute luminosity measurement is coming from the denominator of equation (3.8), mainly from the estimation of the luminosity monitor's geometrical acceptance.

3.5 The trigger system

The trigger system was designed to select potentially interesting events and reject background events, thus decreasing the dead time of the data acquisition system (DAQ). In addition to the

described detectors, there were two hodoscopes, H0 and H1, used in the trigger system. The H1 had the same construction as H2 except the lead sheet in front. The H0 was installed right before the FCs, built from a single sheet of 3.2 mm thick plastic scintillator and read out with PMTs. It was meant to suppress triggers caused by showers originating from the proton beam pipe. The difference in time at which a signal in the front and rear hodoscopes was registered permitted to discriminate between forward and backward going particles.

The first level trigger (Trigger 21) for a scattered lepton was formed by the coincidence of signals from all these hodoscopes, H0, H1, H2, and the calorimeter where an energy deposition in two adjacent columns of lead-glass blocks was required to be larger than the threshold energy E_{thr}. The E_{thr} value was set to 1.4 GeV (3.5 GeV) for data taken with polarized (unpolarized) target. This trigger was required to appear in coincidence with the bunch signal from the accelerator. In addition various triggers were used for photoproduction events, calibration and detector monitoring.

Not all the generated triggers could be accepted by the HERMES DAQ system. During the time needed for readout, newly generated triggers could not be accepted, leading to a dead time of the DAQ system. As the latter influenced the number of selected events, it has to be taken into account in the normalization of the measured data. The dead time is defined as a ratio of the number of rejected trigger requests to the total number of generated triggers. The trigger decision was made within about 400 ns for each event and the maximum trigger rate handled by the DAQ system was about 500 Hz.

3.6 The data structure

For an accepted trigger the values of all detector channels digitized by analog-to-digital converters (ADCs) and time-to-digital converters (TDCs) were collected and stored on hard disks and on tapes for backup. An amount of raw data of about 450 MB was grouped together as a *run*. These runs were further divided into time pieces of $\sim$10 s, called *bursts*. For every burst the detector, beam and target characteristic quantities like beam currents, target and beam polarizations, dead time of the spectrometer, etc. were read out. These quantities were stored separately in the SLOW data tables.

The raw data containing the ADC and TDC values have to be transformed into physical values. This transformation is performed by the HERMES Decoder (HDC) system. Using general geometry and alignment information, the HDC calculates the hit positions in every detector part separately and assigns to each hit a coordinate in the HERMES coordinate system. Afterwords, in the first step of the data production chain, the HRC chain reconstructs the tracks assigning momentum and charge to each particle. The above mentioned SLOW data is synchronized with the HRC tables and all is written as ADAMO [74] tables in μDSTs. These tables contain the full physical information necessary to perform the data analysis.

Chapter 4

Data selection

"The first step to getting the things you want out of life is this: Decide what you want."
— Ben Stein

4.1 Data quality

In parallel to the data taking the trigger and event rates as well as the condition of detectors (SLOW control) are used to monitor the quality of the taken data. However, since the requirements on the detector performance and data taking conditions, like the target and beam polarizations, may differ for various analyses, a detailed offline study of the data quality is necessary. The final data production is done after all detector calibrations and additional corrections have been performed. During the final data productions the detector responses as well as the SLOW information are distilled into a 32-bit number pattern created per burst and detector half reflecting the conditions under which the burst has been taken. Those numbers are stored in a special burstlist and are compared to a bit pattern defined in accordance to the purposes of the specific analysis, thus ensuring a high quality of the analyzed data. The detailed information about the definition of the bits can be found on the HERMES Data Quality page [75].

For the following analysis, data with a transversely polarized hydrogen target and an unpolarized beam is required. The data were accumulated during the running period 2002-2005. The 2002 and 2003 data is a small fraction of the whole data, the main statistics is from 2004 and 2005 data taking periods. The positron (2002-2004) or electron (2005) beam was scattered off a transversely polarized hydrogen target with an average polarization of 0.72 (see Section 3.2.5). The latest data productions are used: 02c0, 03c0, 04c1 and 05c1.

4.2 ρ^0 event selection

To each track in the burst that passed the above mentioned data quality criteria, characteristic quantities, *e.g.* event number, particle type, its momentum and scattering angles are assigned.

Since the transverse holding field of the target magnet changes the vertex position and the scattering angles of the charged particles (see Section 3.3.2), these reconstructed quantities are corrected for the deflections of the trajectories. Two different target magnet correction methods [69] are available for 2004 and 2005 data taking periods, while only one is available for 2002 and 2003 data productions.

As the HERMES spectrometer is sensitive to a wide variety of processes, a further set of criteria must be applied to select the events of particular interest. For the analysis described in this thesis, the events of exclusive ρ^0 meson production will be selected (see Section 2.1): $e(l) + P(p) \rightarrow e'(l') + P'(p') + \rho^0(v)$.

A ρ^0 meson (see Table 4.1) is an unstable short-living resonances that decays in $\tau = 4.4\ 10^{-24}$ s after its formation. For a particle with a velocity close to the speed of the light this time is not sufficient to reach the spectrometer. The distance it will fly before decaying is approximately the size of a nucleon. Thus only the ρ^0 decay particles may occur in the HERMES spectrometer. Since a ρ^0 meson decays into two pions with a branching ratio of 100%, $\rho^0 \rightarrow \pi^+ + \pi^-$, the experimental signature of ρ^0 are two oppositely charged pions reconstructed in the HERMES acceptance.

	mass (MeV)	full width (MeV)	decay mode
ρ^0 (770)	770 ± 0.8	150.7 ± 1.1	$\pi^+\pi^-(100\%)$

Table 4.1: ρ^0 meson properties from particle data book [49].

4.2.1 Lepton/hadron separation

For the analyzed data the HERMES spectrometer had no means of recoil particle detection[1]. Since most of the recoil protons didn't enter the HERMES acceptance, the desired events are expected to consist of three particles in the final state. These are the scattered lepton and two oppositely charged pions. As the recoiling proton is left intact, the information of those tracks is sufficient to reconstruct the kinematics of the exclusive event.

The sum of the parent distributions from all PID detectors, denoted as PID3 + PID5 (see Section 3.3.3), is used for lepton/hadron separation. Figure 4.1 represents the PID3 + PID5 distribution of all tracks in the HERMES acceptance. As indicated by the shaded areas, the leptons and hadrons are identified in the regions:

$$\begin{aligned} PID3 + PID5 &> 1 \text{ for leptons,} \\ PID3 + PID5 &< 1 \text{ for hadrons.} \end{aligned} \tag{4.1}$$

[1] A recoil detector has been installed in 2006.

The statistics in the region close to $PID3 + PID5 \sim 1$ is relatively small, resulting in minimal contamination ($< 1\%$) of misidentified particles in either hadron or lepton sample.

Pion discrimination can be done using the RICH information in the momentum range of $1 < P_\pi < 15$ GeV (see Section 3.3.3). Since ρ^0 mesons mainly decay asymmetrically, one of the pions is carrying more energy than the other, there are still quite some decay pions out of this range. In order to gain statistics, the ρ^0 meson reconstruction is performed under the assumption of 'all hadrons are pions'. The advantages of this approach will be discussed in Section 4.5. In the following, pions are referred to as hadrons.

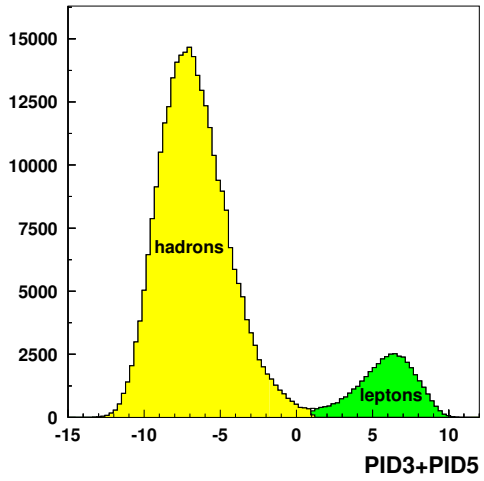

Figure 4.1: The PID3 + PID5 distribution of hadrons (< 1) and leptons (> 1) in the HERMES acceptance.

4.2.2 Geometrical restrictions

In order to make sure that the detected lepton originates from the lepton beam scattered inside the target cell and not from electromagnetic showers due to scattering at the collimator preceding the target, a cut on the vertex position is imposed. As ρ^0 mesons decay practically at the production point, both pions should originate from within the target cell as well. Thus the requirement upon the vertex position is applied also on the pion tracks.

The geometrical acceptance of the HERMES spectrometer implies additional restrictions on the track parameters. In order to reject these tracks which might be affected by edge effects of the detector, a set of geometrical requirements, referred to as *fiducial volume cuts*, is imposed on the vertical and horizontal positions of the tracks. These cuts discard tracks which *e.g.* point to edge or corner blocks of the calorimeter, thus affecting the completeness of the measurement of the energy deposited by the particle in the calorimeter. The tracks are also checked for the positions in several detector components where the tracks can run very close to the detector mountings or shielding materials and cause electromagnetic showers. The list of all geometrical

restrictions is presented in Table 4.2.

vertex position	$-18 < z_{vertex} < 18$ cm
position in the calorimeter	$\|x_{calo}\| < 175$ cm $30 < y_{calo} < 108$ cm
front field clamp position	$\|x_{ffc} < 31\|$ cm
septum plate position	$\|y_{sp} > 7\|$ cm
rear field clamp position	$\|y_{rfc} < 54\|$ cm
rear clamp position	$\|x_{rc}\| <= 100$ cm $\|r_{rc}\| <= 54$ cm

Table 4.2: The geometrical cuts applied on the lepton and both pion tracks.

4.2.3 Candidates of ρ^0 production

On the identified lepton track, which fulfills the geometry criteria, further requirements are imposed. A squared four-momentum transfer Q^2 of more than 1 GeV^2 is required to resolve the nucleon structure and to allow a proper comparison with GPD model predictions. In order to suppress the contribution from the nucleon resonance region, a cut on the invariant mass of the final hadronic state of $W^2 > 4$ GeV^2 is imposed.

The ρ^0 mesons are identified by studying the invariant mass distribution $M_{2\pi}$ of the two decay particles,

$$M_{2\pi} = \sqrt{(p_{\pi^+} + p_{\pi^-})^2} \tag{4.2}$$

where p_{π^+} and p_{π^-} are the four-momenta of the decay pions. The ρ^0 events show up as a clear bump around the expected mass value (see Figure 4.2). However, due to the restricted spectrometer acceptance, the observation of exactly two pions in the final state does not exclude the possibility that other particles were produced in the same event in addition to the detected particles. Although the ρ^0 events can be selected by imposing a mass window cut of $0.6 < M_{2\pi} < 1$ GeV, this sample is still diluted with background events of hadron pairs produced in various processes. Since the non-exclusive events may be misidentified as exclusive ρ^0 events, further restrictions are required for background suppression.

4.2.4 Selection of exclusive events

In the elastic scattering, where the target proton stays intact, the quantity defined as

$$\Delta E = E - E' - E_\rho + (E_p - E_{p'}) \tag{4.3}$$

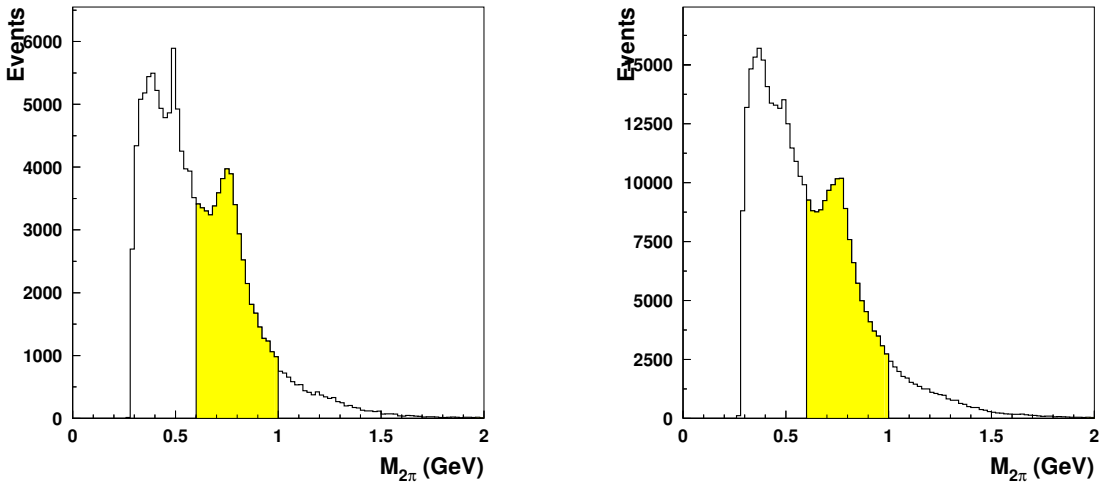

Figure 4.2: The reconstructed invariant mass distribution $M_{2\pi}$ of two pions (left) and two unidentified hadrons (right). The narrow peak in the lower mass region corresponds to K^0_S production. The shaded area indicates the mass window for the ρ^0 selection used in the analysis.

should be equal to zero due to energy conservation. Here E_p and $E_{p'}$ are the energies of the initial and recoiling proton. This quantity is referred to as *missing energy* and can be used as a measure of exclusivity. According to equation (2.8), in the laboratory frame the missing energy ΔE accounts for the kinetic energy $E_{kin} \equiv (E_p - E_{p'}) \stackrel{lab}{=} -t/2M$ transferred to the proton, which is assumed to be small since the proton remains intact. Therefore, the energy of the reconstructed ρ^0 meson is expected to be close to the energy of the virtual photon.

The missing energy ΔE is an invariant quantity, defined also via the missing mass squared $M_X^2 = (q + p - v)^2 = p'^2$:

$$\Delta E = \frac{(M_X^2 - M^2)}{2M} \, . \tag{4.4}$$

For exclusive ρ^0 production the missing mass is equal to the target rest mass, $M_X = M$, the missing energy vanishes: $\Delta E = 0$. For non-exclusive ρ^0 production, $M_X \neq M$, resulting in $\Delta E > 0$. In this case the target proton dissociates. The non-exclusive background events can be suppressed requiring $\Delta E \approx 0$. However, a larger range of ΔE values has to be used for selection of exclusive ρ^0 event. Due to the limited experimental resolution, the reconstructed values of ΔE are smeared to a Gaussian distribution with a width of about 500 MeV in both positive and negative directions (see Figure 4.12).

Expanding equation (2.8) the expression for the squared four-momentum transfer t will become

$$t = (E_\gamma - E_\rho)^2 - (|\mathbf{q}| - |\mathbf{v}|)^2 - \mathbf{2}|\mathbf{q}||\mathbf{v}| \sin^2(\theta_{\gamma^* \mathbf{v}}) \, , \tag{4.5}$$

where $\theta_{\gamma^* \mathrm{V}}$ is the angle between the virtual photon and the produced ρ^0 meson in the photon-nucleon center-of-mass system. At the minimum of four-momentum transfer, the momentum

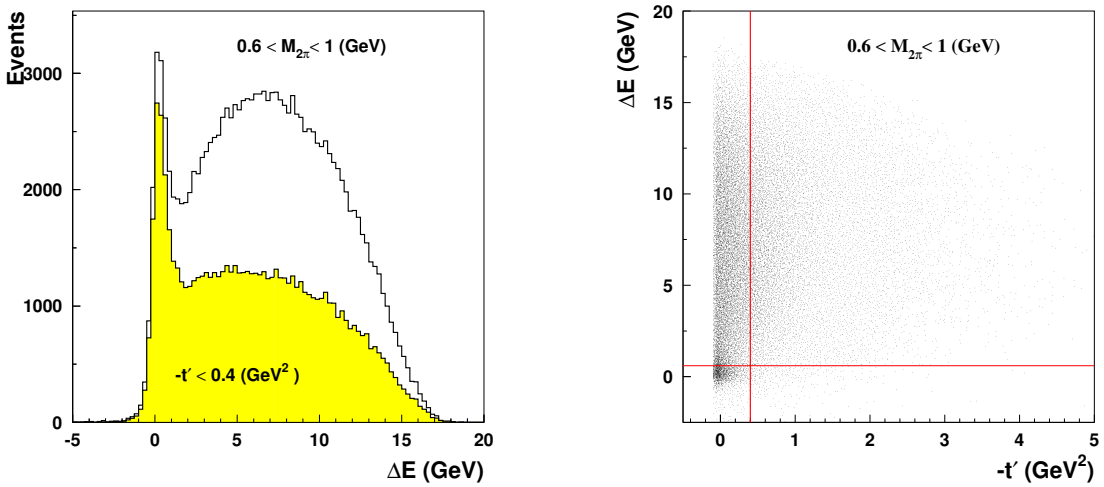

Figure 4.3: The ΔE distribution (left) is presented in the ρ^0 invariant mass window for all values of $-t'$ (the white area) and for $-t' < 0.4$ GeV^2 (yellow shaded area). The correlation between ΔE and $-t'$ (right) of the events within the ρ^0 invariant mass window is presented as well. The lines indicate the cuts on ΔE and $-t'$ values which are used in the analysis and will be discussed later.

of the produced meson is parallel to the direction of the virtual photon:

$$t_0 = (E_\gamma - E_\rho)^2 - (|\mathbf{q}| - |\mathbf{v}|)^2 \,. \tag{4.6}$$

Since t_0 is not a Lorenz invariant quantity, the energy and the momentum of the virtual photon and the produced meson are defined in the center-of-mass system as:

$$\begin{aligned} E_\gamma &= \frac{W^2 - Q^2 - M^2}{2W} \,, & |\mathbf{q}| &= \sqrt{E_\gamma^2 + Q^2} \,, \\ E_\rho &= \frac{W^2 + M_\rho^2 - M_X^2}{2W} \,, & |\mathbf{v}| &= \sqrt{E_\rho^2 - M_\rho^2} \,. \end{aligned} \tag{4.7}$$

In the analysis, the quantity

$$t' = t - t_0 \tag{4.8}$$

is often used. Since the t_0 subtraction removes the longitudinal component of the transferred four-momentum, t' is the measure of the transverse four-momentum transfer. All three variables t, t_0 and t' have negative values by definition, and $|t_0|$ is the minimum kinematically allowed value of $|t|$.

As the target nucleon stays intact, with only little energy transferred to the target, t has small values. Typically, $|t_0|$ is much smaller than $|t|$, resulting in $t' \approx t$. Hence, exclusive ρ^0 production has its main contribution at small values of ΔE and t'.

The ΔE distribution for ρ^0 candidates is presented in the left panel of Figure 4.3. Exclusive ρ^0 production shows up as a narrow peak around $\Delta E \approx 0$ while most of the non-exclusive events have larger values of ΔE. The correlation between ΔE and $-t'$ is presented in the right

panel of Figure 4.3 where the exclusive ρ^0 meson production is located in the lower left corner of the histogram. Restrictions imposed on the ΔE and $-t'$ values will reduce the background contamination in the selected exclusive sample (see Figure 4.3). However, as it is seen from the ΔE distribution, there would be still a background contamination in the low ΔE region.

In the following sections an estimate of the background contamination as well as requirements on ΔE and $-t'$ will be discussed.

4.2.5 Beam energy correction

The comparison of ΔE distributions from various years has revealed a shift in the position of the exclusive peak. As illustrated in the left panel of Figure 4.4, the peak positions from the dE distributions in 2004 and 2005 data taking periods are shifted with respect to that of the year 2000. Detailed studies have found the shift to be present not only in exclusive ρ^0 production, but also in other reactions. A possible explanation was found to be the uncertainty in the measurement of the initial beam energy [76]. The actual value of the beam energy for the 2002-2005 data taking periods was found to be slightly smaller than the measured value. The true values of the initial beam energy P_{true} were estimated [76] for each data taking period (see Table 4.3).

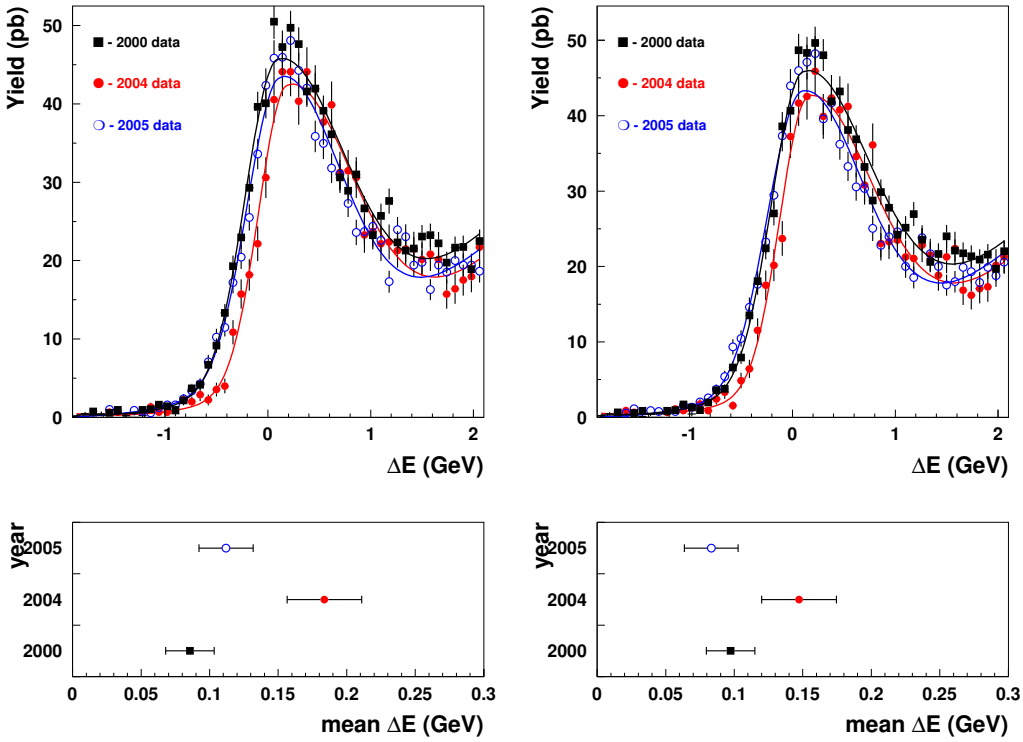

Figure 4.4: The ΔE distributions and mean values of the ΔE peak for 2000, 2004 and 2005 data production periods before (left) and after (right) implementation of the beam energy correction.

year	P_{meas}	P_{true}
2000	27.597	27.611
2002	27.541	27.511
2003	27.619	27.587
2004	27.618	27.583
2005	27.613	27.578

Table 4.3: Measured and true values of the initial beam energies for 2000-2005 data production period.

The missing energy ΔE is directly affected by the uncertainty in the beam energy measurement (see equation (4.3)). The analysis in the following chapters is performed using the true values of the initial beam energy P_{true}. In the resulting ΔE distributions the exclusive ρ^0 peak positions agree within statistical uncertainties for all years (see right panel of Figure 4.4).

4.3 Background treatment

For the selection of a certain physics process, the knowledge of other processes contributing to the observed events is crucial. The selection of three-track events in the corresponding ρ^0 invariant mass window and requirements for low ΔE and $-t'$ values do not fully exclude the background contamination in the exclusive sample. The latter is still diluted by *semi-inclusive*, *non-resonant*, *single-* and *double-diffractive* background events as well as by events from *exclusive* ω and ϕ production.

4.3.1 Semi-inclusive background contamination

Semi-inclusive events are the main source of the background contamination. The spectrometer resolution in ΔE and the restricted acceptance are not capable of fully rejecting events that are not exclusive but have the same topology as the exclusive ones. Together with the scattered lepton and two pions in the ρ^0 invariant mass window, additional undetected particle may have been produced in the low ΔE region or, alternatively, an event from the higher ΔE region may have been smeared into the low ΔE region.

The PYTHIA generator [77] contains a large variety of processes[2] and the cross sections of those processes are tuned to describe the HERMES data in the whole Q^2 range. A fully tracked PYTHIA Monte Carlo simulation[3] is used to estimate the semi-inclusive background contamination in the exclusive sample. The same kinematic and geometrical requirements

[2]PYTHIA does not generate elastic *ep* process which is irrelevant when estimating the semi-inclusive background.

[3]More details about Monte Carlo generators used for HERMES analyses are presented in Chapter 5.

are imposed on both simulated and real data samples. Since in the real data, the exclusive ρ^0 mesons are selected using two unidentified hadrons, also in the simulated data exclusive ρ^0 mesons are selected using all combinations of pions, kaons and (anti)protons. The events produced in non-exclusive processes are treated as background events.

The comparison of the ΔE distributions from data and Monte Carlo simulation gives an estimate of the background size. For a proper comparison of Monte Carlo and data, the kinematic distributions have to be normalized. Depending on the purpose, various normalization methods can be used. If the Monte Carlo describes the cross section with reasonable accuracy, the absolute luminosity can be used for normalization (*absolute normalization*, see Appendix C). Otherwise, an *arbitrary normalization* can be used. In this case, the distributions from data and Monte Carlo are normalized in a certain or in the whole region. For a background estimation the absolute normalization method is preferable, as then the behavior of the background distribution is not affected by the choice of the normalization region. In addition, the radiative tail (see Figure 4.5), which reaches up to $\sim$10 GeV, would lead to an overestimation of the semi-inclusive background at $2 < \Delta E < 10$ GeV region if it is not properly accounted during the arbitrary normalization.

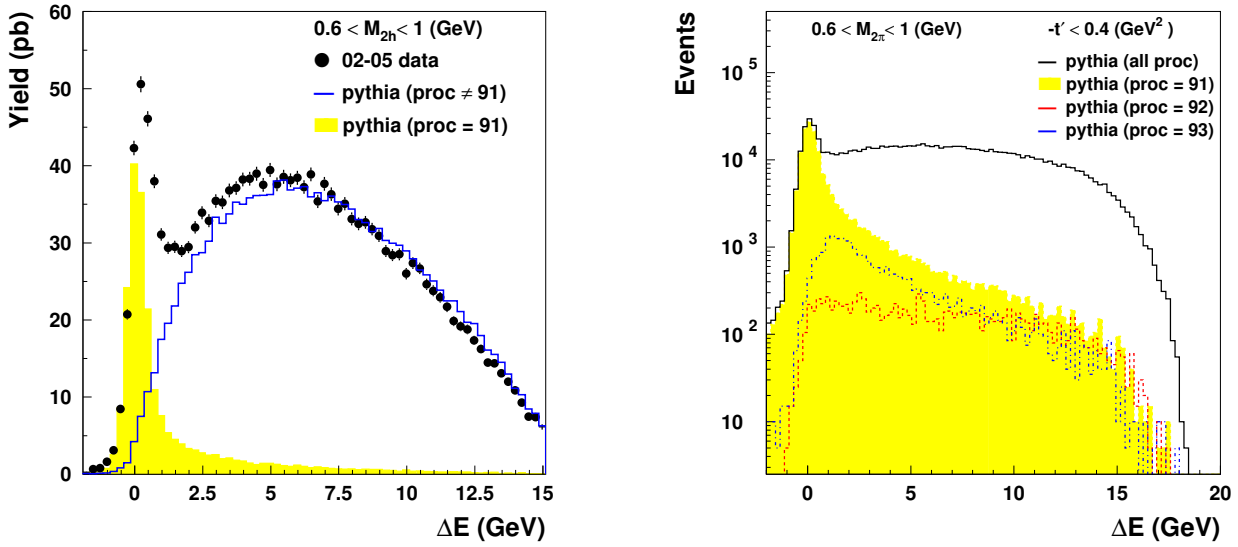

Figure 4.5: Left: PYTHIA Monte Carlo simulation of ΔE distribution of semi-inclusive background (blue histogram) and exclusive ρ^0 production (yellow shaded area), compared to 2002-2005 data (black points). Right: PYTHIA Monte Carlo simulation of ΔE distribution for various diffractive processes compared to the whole distribution (black histogram). The yellow shaded area stands for elastic diffractive process, while the other histograms show the contributions from single-diffractive processes. The process 92 (93) stands for the ρ^0 (proton) dissociation process. The double-diffractive process is negligible.

Left panel of Figure 4.5 shows the absolutely normalized ΔE distributions of data (black points) and of the semi-inclusive background from the PYTHIA Monte Carlo (blue histogram).

The yellow area stands for exclusive ρ^0 production from the PYTHIA simulation. The amount of Monte Carlo background events in a certain ΔE region gives an estimate of semi-inclusive background contamination.

4.3.2 Single and double diffractive background

At an energy transfer $\Delta E > 0$, the produced ρ^0 can still be the only produced particle, but the target proton may give a rise to a resonance or dissociate into a multi-particle state whose total quantum numbers match exactly to those of the initial proton. This is an example of a single-diffractive event. Similarly, the momentum transferred to the ρ^0 can be large enough that it breaks up directly after the formation while the target proton stays intact. In the case that both ρ^0 meson and target proton produce a bunch of particles and a resonance, respectively, the reaction is double-diffractive. As the final hadronic state remains undetected, these events are indistinguishable from elastic diffractive events (see Section 2.3). The requirement $\Delta E \approx 0$ is imposed to suppress contaminations from single- and double-diffractive events. However, due to the resolution and smearing in ΔE they still may contribute to the elastic diffractive ρ^0 sample (see Figure 4.6).

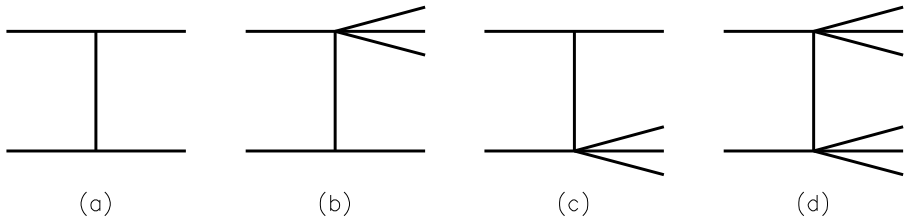

Figure 4.6: Various types of diffraction: elastic (a), single-diffraction (b, c) and double-diffraction (d).

In the simulation, all ρ^0 events produced in processes other than elastic are treated as background. The double-diffractive model in PYTHIA might be incomplete, showing no contribution at all. However, this contribution should be less than those from single-diffractive processes, since more energy transferred is needed to dissociate both the target nucleon and the produced ρ^0 meson. This is particularly true in the low ΔE region. In view of the considerations made above, no additional correction is performed for double diffractive background estimation.

4.3.3 Contribution from exclusive ω and ϕ meson productions

The $\omega(782)$ and $\phi(1020)$ light mesons may contribute to the ρ^0 event sample since they have decay modes containing two oppositely charged pions. The cross section of exclusive ω mesons

with the decay channels

$$\omega \rightarrow \begin{cases} \pi^+ + \pi^- + \pi^0 & 89.1\% \\ \pi^+ + \pi^- & 1.70\%, \end{cases} \tag{4.9}$$

is estimated to be about $15 - 20\%$ of the exclusive ρ^0 cross section in the acceptance [78]. It was shown [78] that the $\omega \rightarrow 3\pi$ events for which the π^0 was not detected, are concentrated at an invariant mass of 0.45 GeV with a Gaussian width of about 0.075 GeV, which means that most of those events are rejected by imposing an invariant mass cut of $0.6 < M_\rho < 1$ GeV. The contribution from the $\omega \rightarrow 2\pi$ decay mode is indistinguishable from the $\rho^0 \rightarrow 2\pi$ decay thereby implying a $\omega - \rho^0$ interference. However, this contribution is not significant ($< 0.4\%$).

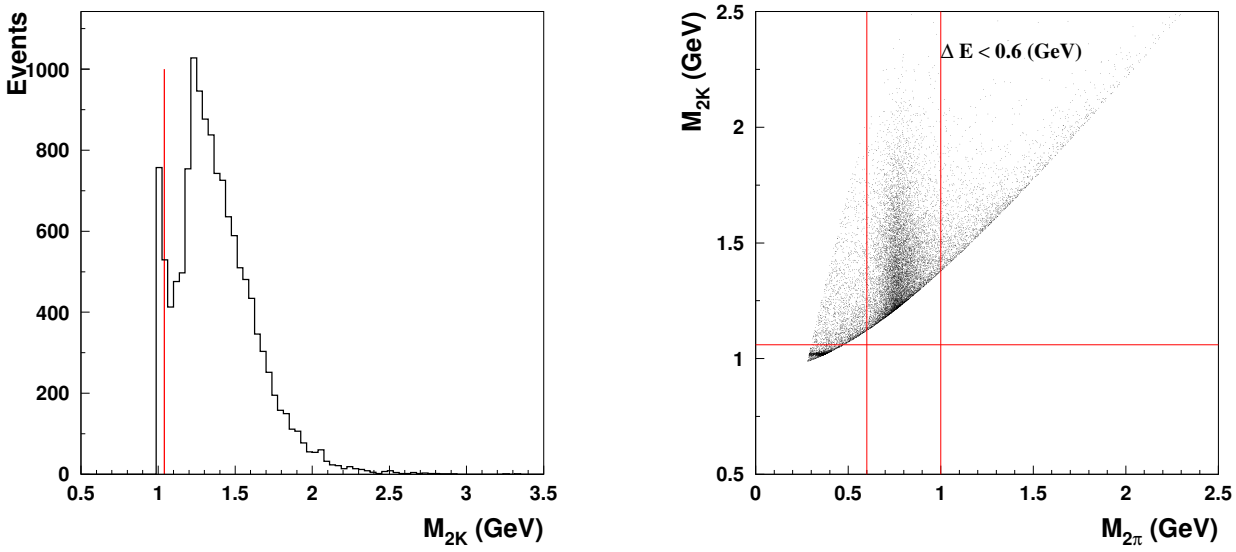

Figure 4.7: The 2-kaon invariant mass distribution (left) where the ϕ mesons show up at the expected mass value and the correlation between ρ^0 and ϕ invariant masses (right). The solid lines on both plots indicate the cuts used in the analysis.

Compared to exclusive ω production, the production of exclusive ϕ mesons is even more suppressed. Since the ρ^0 mesons are identified with the prior assumption of all hadrons to be pions, the $2K$ decay mode of the ϕ meson:

$$\phi \rightarrow \begin{cases} K^+ + K^- & 49.1\% \\ \pi^+ + \pi^- + \pi^0 & 15.5\% \end{cases} \tag{4.10}$$

may also contribute to the ρ^0 sample. The same data set as used for ρ^0 sample is analyzed with an assumption of all hadrons to be kaons. In Figure 4.7, the reconstructed invariant mass

of the ϕ meson,

$$M_{2K} = \sqrt{(p_{K^+} + p_{K^-})^2} \tag{4.11}$$

with p_K being the four-momenta of kaons, is illustrated in the left panel and the correlation between the ρ^0 and ϕ invariant masses in the right panel. The ϕ contamination can be minimized by requiring M_{2K}, the recalculated invariant mass of detected hadrons, to be above 1.06 GeV. The other decay modes of ϕ mesons can be safely neglected due to small branching ratios.

4.3.4 Non-resonant background

The detected ρ^0 signal also receives a contribution from non-resonant exclusive two-pion production (see Figure 4.8). These pion pairs are also characterized by a missing energy $\Delta E \approx 0$, but their invariant mass may not necessarily correspond to the mass of the ρ^0. However, the non-resonant $\pi^+\pi^-$ pairs are indistinguishable from the ρ^0 decay products as both final states are produced coherently and hence interfere.

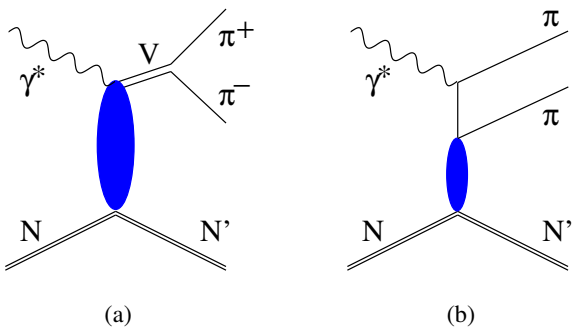

Figure 4.8: Resonant vector meson production (a) and non-resonant $\pi^+\pi^-$ pair production (b).

In PYTHIA, the process 91 includes also a contribution from non-resonant exclusive $\pi^+\pi^-$ production. The separation between resonant and non-resonant events is accomplished by an additional requirement on the pion's parent. The non-resonant contribution predicted by PYTHIA is of the order of $4-5\%$ (see Figure 4.11) which might be overestimated.

Experimentally, the contribution from non-resonant background events can be estimated from data through a fit to the invariant-mass distribution. The latter has to be corrected for the acceptance, since the invariant mass of two-pions receives non-linear distortions from the acceptance [78]. In addition, the semi-inclusive background should be subtracted first, since it contributes to the two-pion invariant mass distribution as well.

The invariant mass distribution can be described with a relativistic p-wave Breit-Wigner function describing a spin-1 object decaying into two spin-0 objects,

$$\frac{dN}{dM_{2\pi}} = BW(M_{2\pi}) = \frac{2}{\pi}\frac{M_{2\pi}M_\rho\Gamma(M_{2\pi})}{(M_\rho^2 - M_{2\pi}^2)^2 + M_\rho^2\Gamma^2(M_{2\pi})}\ , \tag{4.12}$$

where M_ρ is the mass and $\Gamma(M_{2\pi})$ the energy-dependent width of the ρ^0 resonance:

$$\Gamma(M_{2\pi}) = \Gamma_\rho \Big(\frac{q}{q_0}\Big)^3 \frac{2}{1+\Big(\frac{q}{q_0}\Big)^2} \qquad \frac{q}{q_0} = \frac{\sqrt{M_{2\pi}^2 - 4M_\pi^2}}{\sqrt{M_\rho^2 - 4M_\pi^2}} \tag{4.13}$$

But the relativistic Breit-Wigner shape alone can not describe the invariant mass distribution in the data. The skewing of the ρ^0 peak to lower mass values is taken into account by using models of Ross-Stodolsky and Söding.

Ross-Stodolsky model

In the phenomenological model by Ross-Stodolsky, to describe the skewing of the ρ^0 invariant mass, a skewing parameter n_{skew} is invented:

$$\frac{dN}{dM_{2\pi}} = BW(M_{2\pi}) \Big(\frac{M_\rho}{M_{2\pi}}\Big)^{n_{skew}} . \tag{4.14}$$

An additional constant parameter is added to the parameterization given by equation (4.14) to estimate the flat non-resonant background.

The result of the fit to the invariant mass distribution with the function given by equation (4.14) is shown in the left panel of Figure 4.9. The non-resonant background contamination is found to be 1.1%.

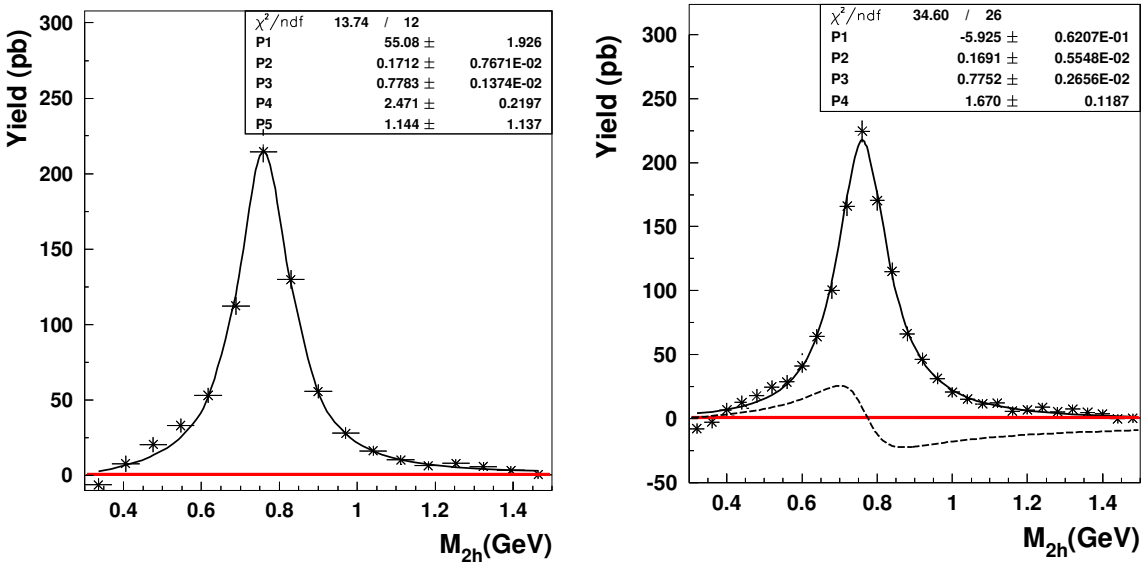

Figure 4.9: The two-pion invariant mass distribution fitted with the Breit-Wigner distribution using mass skewing models of Ross and Stodolsky (left) and Söding (right). The full curves are the final fit. The red bands indicate the flat non-resonant background contamination. The dashed line represents the interference term in the parameterization (4.15).

Söding model

Another phenomenological approach to explain the exclusive ρ^0 mass shift is done by Söding. Here the skewing of the invariant mass is explained by the interference between two-pion resonant (A_{reso}) and non-resonant (A_{nr}) processes:

$$\frac{dN}{dM_{2\pi}} = \left| A_{reso} \frac{\sqrt{M_{2\pi} M_\rho \Gamma(M_{2\pi})}}{M_{2\pi}^2 - M_\rho^2 + i M_\rho \Gamma(M_{2\pi})} + A_{nr} \right|^2 \tag{4.15}$$

The invariant-mass distribution fitted with the function given by equation (4.15) is shown in the right panel of Figure 4.9. The non-resonant background contamination is found to be 1.6%.

Both models describe the invariant mass distribution well, the reduced $\chi^2/n.d.f.$ values being somewhat higher for Söding model. Since both models predict a small contamination of non-resonant background compared to semi-inclusive background, in the following analysis no correction for the non-resonant background is performed.

4.4 Exclusive Cuts

In order to suppress the background and provide a cleanest possible exclusive sample, certain requirements have to be imposed on ΔE and t' values. Applying tight cuts on these variables ensures a cleaner sample but reduces the statistics while loose cuts provide higher statistics together with higher background contamination, thus introducing a larger systematic uncertainty due to background correction. The cuts $\Delta E < 0.6$ GeV and $t' < 0.4$ GeV^2 used in a previous exclusive ρ^0 analysis [78] might not be optimal due to different spectrometer acceptance caused by the transverse target magnet and also due to different background correction methods used in the analyses.

The optimal cuts on ΔE and t' values are those that result in the minimum total relative error, obtained in quadrature from the relative statistical and systematic uncertainties. The deviation of the ratio of Monte Carlo and data ΔE distributions from unity is treated as a systematic uncertainty on the number of exclusive ρ^0 mesons. The total relative error as well as the relative statistical and systematic uncertainties for various ΔE values at fixed value of $t' = 0.4$ GeV^2 are shown in the left panel of Figure 4.10. The total relative error in dependence on ΔE and t' cuts is shown in the right panel of Figure 4.10. The relative total uncertainty shows that the best ΔE cut is between 0.6 and 1 GeV. The t' dependence of the total relative error is weak since the t' cut reduces the background mainly in the high ΔE region.

Although the number of exclusive ρ^0 events increases with a larger ΔE requirement, also the background contamination increases from 11% to 17% for $\Delta E < 0.6$ Gev to 1 Gev. The angular distribution of the semi-inclusive background is unknown, which intoduces an uncontrolled systematic uncertainty. In addition, the single- and double-diffractive background contaminations are not completely controlled and the systematic uncertainty might be underestimated for the

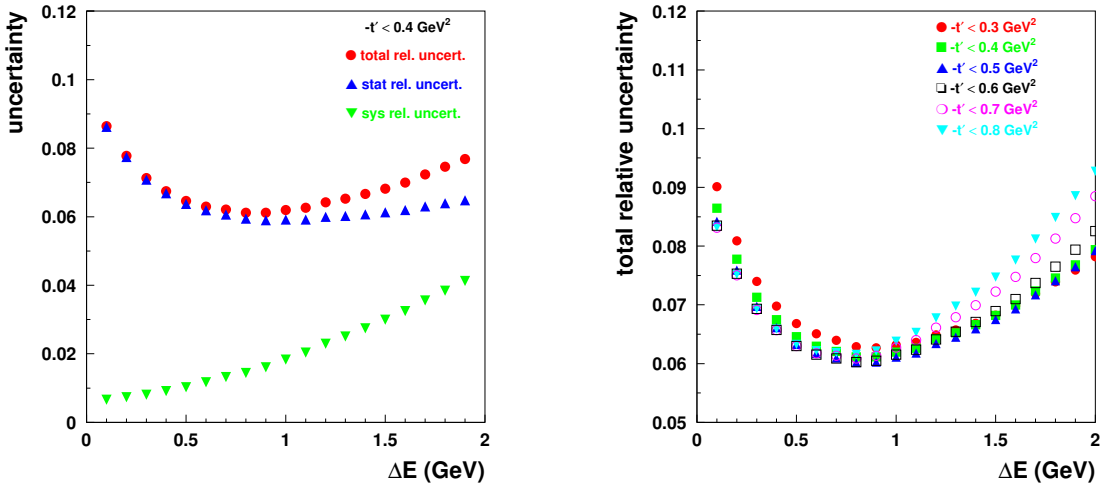

Figure 4.10: The total relative uncertainty on the number of the exclusive ρ^0 events for various choices of the ΔE cut at $t' < 0.4$ GeV^2 (left) and at variable t' values (right).

larger values of ΔE. Hence the choice is made towards $\Delta E < 0.6$ GeV and $t' < 0.4$ GeV^2 in order to avoid larger background contaminations. The resulting data set is calles *exclusive sample*.

4.5 ρ^0 meson reconstruction through two pions or two hadrons

As ρ^0 production is suppressed by $1/Q^2$ compared to inclusive DIS production, maximizing the statistics of the exclusive sample is very important. The RICH detector provides pion identification in the momentum range $1 < p_\pi < 15$ GeV. If one of the pions is out of this range, the ρ^0 can not be identified. In earlier analyses, the ρ^0 candidates were reconstructed through unidentified hadron pairs. In this case the gain in statistics with respect to the case of identified pions is about 22%. Although most of the hadrons are pions in the HERMES kinematics, it is worth to check that indeed the cuts on ΔE and t' discussed above select ρ^0 events only.

For such a check, a PYTHIA simulation is treated as real data. Three track events are selected with one positron and two oppositely charged hadrons (all combinations of pions, kaons, (anti)protons) which fulfill all the kinematic and geometrical requirements applied on real data. All the events from elastic processes are selected which is considered to be equivalent to the subtraction of semi-inclusive background in the data. About 99% of the remaining particles are found to be pions. Thus reconstructing the ρ^0 through two unidentified hadrons and imposing the exclusive cuts eventually selects only the two-pion events. Besides the exclusive ρ^0 events, the sample contains a contribution from ω and $\rho^\pm$ mesons and also a contribution from non-resonant background where the transition into pions starts from u and d quarks (see Figure 4.11). The contribution from exclusive ω and $\rho^\pm$ mesons is less than 1% in total. The contribution from non-resonant background is discussed in Section 4.3.4.

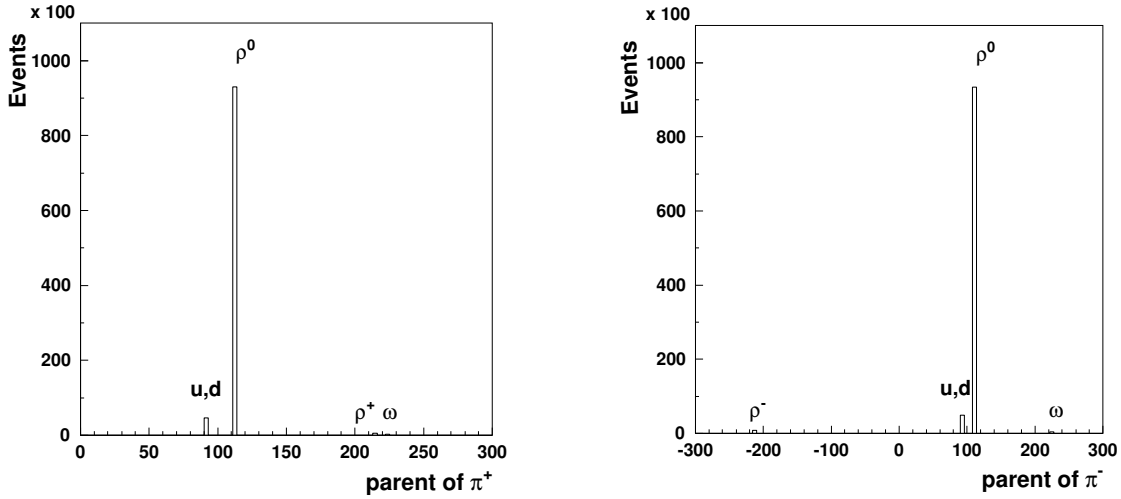

Figure 4.11: PYTHIA Monte Carlo result: The parents of decay pions in elastic processes after applying the cuts $\Delta E < 0.6$ GeV and $t' < 0.4$ GeV^2. The candidates of exclusive ρ^0 mesons are reconstructed through two unidentified hadrons.

4.6 Kinematic coverage and available statistics

Summarizing the chapter, the restrictions on the relevant kinematic variables as well as the kinematic coverage of some more variables are presented in the Table 4.4. On the identified lepton track the requirements $Q^2 > 1$ GeV^2 and $W^2 > 4$ GeV^2 are imposed. However, in the HERMES acceptance most of the exclusive ρ^0 events are anyway located at $W^2 > 10$ GeV^2. Due to the kinematics of the reaction, the fractional energy transfer y is restricted to 0.85. The range of the Bjorken scaling variable x is determined by the HERMES acceptance and the cuts on Q^2 and W^2. Exclusive ρ^0 candidates are selected requiring exactly two (unidentified) hadrons. The cuts ensuring the exclusivity of the events are listed at the end of the table. The available statistics from the whole data taking period with transversely polarized target are presented in Table 7.1. The selected ρ^0 candidate sample contains of about 11% of semi-inclusive background events which includes contributions from semi-inclusive ρ^0 mesons as well as from fragmentation events with two hadrons being in the HERMES acceptance (left panel of Figure 4.12). The ΔE distribution for exclusive events, after the background correction, is shown in the right panel of Figure 4.12. A clear Gaussian distribution is an indication of a proper treatment of the background contamination. The small discrepancy between the Gaussian fit and the data of about $2 - 2.5$ GeV may occur from an imperfect description of the double diffractive process in PYTHIA. However, the low ΔE region where the data is selected as exclusive should be not affected by double diffractive background.

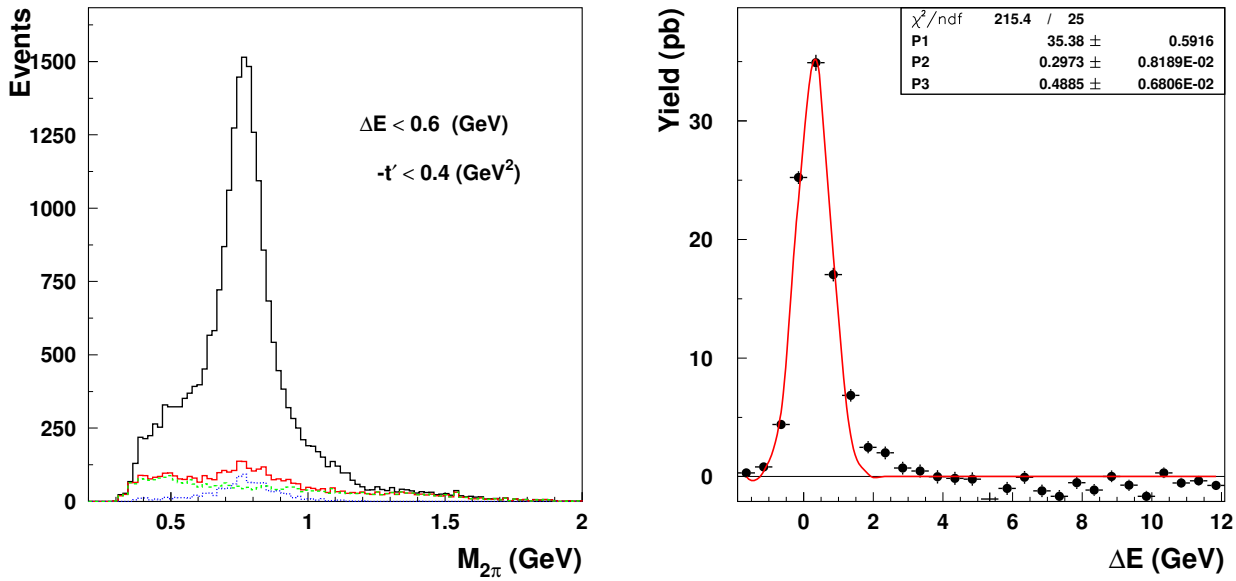

Figure 4.12: Left: the invariant mass distribution of two pions obtained from PYTHIA Monte Carlo before background correction. The red solid histogram in the bottom represents the total semi-inclusive background which receives contributions from semi-inclusive ρ^0 mesons (blue dotted histogram) and from DIS processes (green dashed histogram). Right: the ΔE distribution of exclusive ρ^0 production after the background subtraction. The red line illustrates a fit with a Gaussian function.

negative squared four-momentum of γ^*	$Q^2 = -(l - l')^2 \overset{lab}{\approx} 4EE' \sin^2 \frac{\theta}{2}$	$1 < Q^2 < 7$ GeV^2
energy of the virtual γ^*	$\nu = \mathbf{p} \cdot \mathbf{q}/M \overset{lab}{=} E - E'$	
squared mass of the final state	$W^2 = (q + p)^2 \overset{lab}{=} M^2 + 2M\nu - Q^2$	$W^2 > 10$ GeV^2
Bjorken scaling variable	$x_B \equiv Q^2/(2p \cdot q) \overset{lab}{=} Q^2/2M\nu$	$0.023 < x_B < 0.4$
fractional energy transfer	$y \equiv (p \cdot q)/(p \cdot l) \overset{lab}{=} \nu/E$	$y < 0.85$
reconstructed invariant mass of $\pi^+\pi^-$	$M_{2\pi} = \sqrt{(p_{\pi^+} + p_{\pi^-})^2}$	$0.6 < M_{2\pi} < 1$ GeV
reconstructed invariant mass of K^+K^-	$M_{2K} = \sqrt{(p_{K^+} + p_{K^-})^2}$	$M_{2k} > 1.06$ GeV
squared four-momentum transfer from γ^* to ρ^0	$t = (q - v)^2 = (p - p')^2$	
minimum squared four-momentum transfer from γ^* to ρ^0	$t_0 = (E_\gamma - E_V)^2 - (\lvert\mathbf{q}\rvert - \lvert\mathbf{v}\rvert)^2$	
squared transverse four-momentum transfer from γ^* to ρ^0	$t' = t - t_0$	$-t' < 0.4$ GeV^2
missing mass	$M_x = \sqrt{(p + q - v)^2}$	
missing energy	$\Delta E = (M_x^2 - M^2)/2M \overset{lab}{=} \nu - E_V + \frac{t}{2M}$	$\Delta E < 0.6$ GeV

Table 4.4: Definitions and descriptions of most relevant kinematic variables in exclusive ρ^0 production.

Chapter 5

Monte Carlo generators

"You have to know how to accept rejection and reject acceptance."
— Ray Bradbury

Experimental results for a special reaction rely on the ability to evaluate the influence of various background processes, of the limited acceptance, the reliability of extraction methods etc., which all can not be quantified in an analytical way. Instead, parameterizations and models are implemented into Monte Carlo generators which simulate 'reality' on a statistical basis. In this case the results rely on the input parameterizations and models. It is hence important to show the reliability of the Monte Carlo simulations.

In this chapter two generators are described, PYTHIA 6.2 [77] and rhoMC [79]. It has already been mentioned (see Section 4.3.1) that PYTHIA 6.2 generates a large variety of DIS processes with unpolarized beam and target. All those processes have been tuned to describe the HERMES data [80, 81]. In contrast to PYTHIA, rhoMC is only capable of generating exclusive vector mesons, but for both unpolarized and polarized beam and target. The generated particles and their decay channels can be selected individually. For this reason rhoMC needs significantly less time to generate the same amount of exclusive events compared to PYTHIA. The main feature of rhoMC is the ability to generate the full angular distribution of vector mesons and their decay products while in PYTHIA those possibilities are restricted.

While for vector meson production studies both Monte Carlo generators can be used, many other analyses at HERMES had to use the PYTHIA Monte Carlo simulation to estimate, *e.g.*, the contribution of exclusive vector meson decay products in the semi-inclusive sample. Initially, because of bugs in rhoMC code which didn't allow to reproduce the cross section of vector meson production, it was not possible to cross check the predictions from PYTHIA: the rhoMC cross section was off by an order of magnitude, having kinematic dependences [82]. In the course of actual PhD work, some parts of rhoMC had to be rewritten completely. While fixing the bugs in rhoMC, a bug was also found in PYTHIA, and modifications were required in PYTHIA parameterizations.

In this chapter the predictions from both generators for exclusive ρ^0 production are compared with data.

5.1 The PYTHIA 6.2 generator

PYTHIA generates events according to the cross section, using the '*accept/reject*' method. A scheme of the PYTHIA Monte Carlo simulation procedure is shown in Figure 5.1. In the first step PYTHIA generates the kinematics of the scattered lepton (Q^2 and y). If radiative corrections have to be taken into account, the generated *observed* kinematics is passed to an external program RADGEN [83] which makes a decision whether a photon is radiated or not and recalculates the *true* kinematics of the scattered lepton. Next, the interaction process is chosen and if this is not a VMD process (see Section 5.2), quark, diquark and strings[1] are generated. Because of QCD confinement, particles carrying a color charge cannot exist in free form. Therefore they fragment into hadrons. The transformation of outgoing colored partons into color singlet hadrons, called *hadronization*, is performed by the JETSET code [84] that is based on the LUND string model [85].

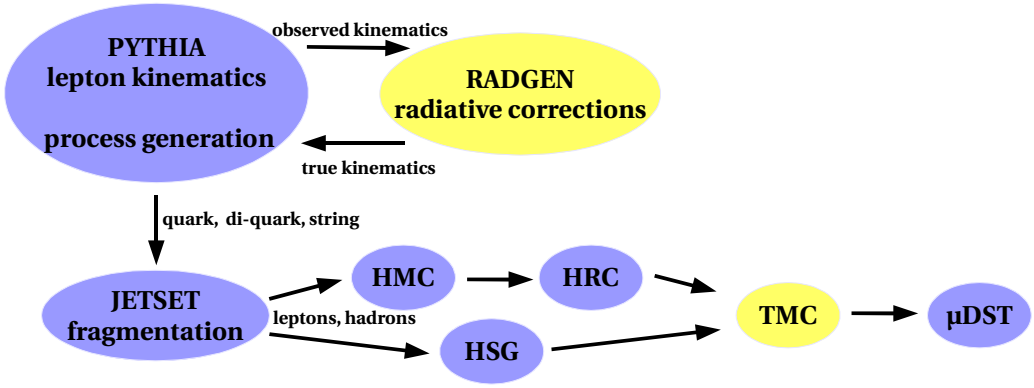

Figure 5.1: PYTHIA Monte Carlo production chain. The radiative corrections and the transverse magnet corrections (TMC) are optional.

The information from the generator is fed to a GEANT [86] implementation of the HERMES detector, called HMC. There the characteristics of generated particles are transformed into 'detector information', *i.e.* the track information of a particle traversing the detector material is simulated. This detector information is passed to the HRC program that treats the Monte Carlo simulation as real data (see Section 3.3.2) and reconstructs the particle tracks (see Section 3.3.2). As a full GEANT simulation is very time consuming, an alternative approach can be used instead, the HERMES smearing generator (HSG), which parameterizes all smearing and resolution effects instead of a full GEANT simulation. If the influence of the transverse holding field of the magnet has to be taken into account, the same TMC correction as for real data is applied on the reconstructed particles (see Section 3.3.2). All the information from each stage is stored in ADAMO tables of μDSTs.

The three main parts of the PYTHIA generator are described in this section: the generation

[1] In the LUND model the gluons are treated as field lines, which are attracted to each other due to the gluon self-interaction and so form a narrow tube of strong color field, called *string*.

of the lepton-nucleon scattering process, the radiative corrections and the hadronization of the individual quarks and anti-quarks (strings).

5.1.1 Generation of lepton kinematics

In PYTHIA the ep cross section is represented in the one-photon exchange approximation through the $\gamma^* p$ cross section, *i.e.* the lepton-proton scattering is replaced by scattering of a photon off a proton. In quantum mechanics the photon may fluctuate into a fermion-antifermion pair. Thus the wave function of the real photon is given by a superposition of a bare photon (direct coupling) and fluctuations of the photon into either a vector meson, a $q\bar{q}$ pair or a lepton pair l^+l^-:

$$|\,\gamma\rangle = c_{bare}|\,\gamma_{bare}\rangle + \sum_{V=\rho^0,\omega,\phi} c_V|\,V\rangle + \sum_{q=u,d,s,c,b} c_q|\,q\bar{q}\rangle + \sum_{l=e,\mu,\tau} c_l|\,l^+l^-\rangle\ . \tag{5.1}$$

The coefficients c_q and c_l depend on the scale μ. The fluctuations into l^+l^- are negligible for γp, since this contribution is suppressed by α_{em}^2. The probability for a photon to fluctuate into a vector meson is proportional to c_V^2 with $c_V^2 = 4\pi\alpha_{em}/f_V^2$, where f_V^2 is the coupling constant between photon and vector meson. The coefficient c_{bare} is obtained using unitarity: $c_{bare}^2 = 1 - \sum c_V^2 - \sum c_q^2 - \sum c_l^2$.

In view of considerations made above, there are three main classes of real photon-nucleon scattering processes, shown in Figure 5.2. These are the direct photon interaction, in which the bare photon interacts with the nucleon ($\gamma g \to q\bar{q}$, $\gamma q \to qg$); the VM interaction (see Section 2.3), in which the photon fluctuates into a vector meson (VM) before the interaction with the nucleon ($\gamma p \to Vp$); and the 'anomalous photon' process, in which the photon is resolved, *i.e.* it splits into a parton pair and one of these partons interacts with a parton in the nucleon ($q_i q_j \to q_i q_j$, $q\bar{q} \to gg$, etc). The total γp cross section is written as the sum of the three contributions:

$$\sigma_{tot}^{\gamma p} = \sigma_{direct}^{\gamma p} + \sigma_{VM}^{\gamma p} + \sigma_{anomalous}^{\gamma p}\ . \tag{5.2}$$

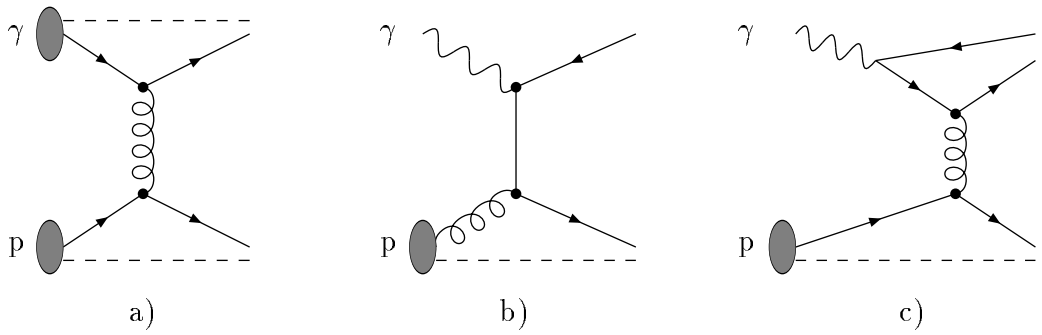

Figure 5.2: Possible processes in hard γp interaction: a) VM, b) direct, c) anomalous.

The three classes of processes can be distinguished by considering the virtuality scale in the photon fluctuation, given by the transverse momentum k_T of the partons emerging from the photon. The discrimination between low- and high-virtuality processes is done introducing a cutoff parameter k_0 of the order of 0.5 GeV (see Figure 5.3). The low-virtuality fluctuations ($k_T < k_0$) can not be described by pQCD and are approximated with the VMD ansatz (see Section 5.2), where the low-mass vector meson states are summed over. Thus a VM process is generated. The high-virtuality fluctuations ($k_T > k_0$) can be described by pQCD. Further discrimination of the processes is accomplished by introducing an additional scale of transverse momentum, namely p_T of partons emerging from the nucleon. In the case of high-virtuality fluctuations there are two possible processes distinguishable along $k_T = p_T$: direct ($k_T > p_T$) and anomalous ($k_T < p_T$). For real photons directly scattering off the nucleon Photon-Gluon Fusion (PGF) $\gamma g \to q\bar{q}$ and QCD Compton (QCDC) scattering $\gamma q \to qg$ are allowed. If the photon is virtual, $Q^2 > 0$, in leading order (LO) DIS there is an additional process[2] allowed in which the photon is absorbed by partons of the proton ($\gamma^* q \to q$). The virtuality Q^2 of the photon introduces another scale dependence into the cross section. An arbitrary line $Q^2 = k_T^2$ is introduced to distinguish between the LO DIS processes vanishing at $Q^2 \to 0$ and the PGF and QCDC processes.

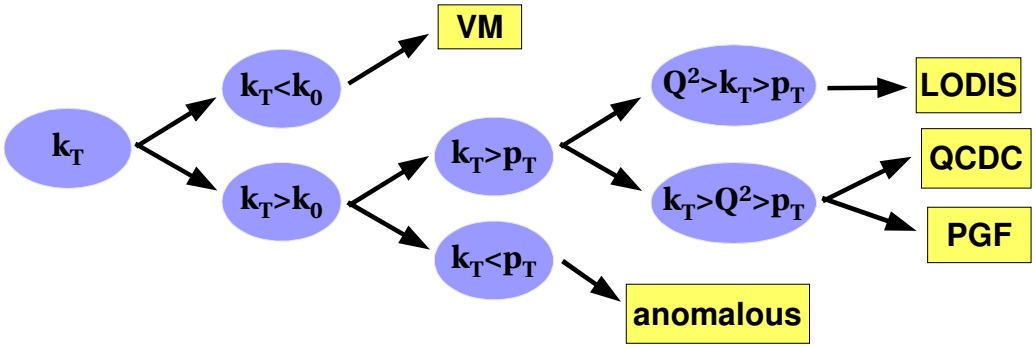

Figure 5.3: Classification of processes generated by PYTHIA Monte Carlo according to scales k_T, p_T and Q^2.

The quasi-real photoproduction cross section has contributions from all above described processes:

$$\sigma_{tot}^{\gamma^* p} = \underbrace{\sigma_{PGF}^{\gamma^* p} + \sigma_{QCDC}^{\gamma^* p} + \sigma_{LODIS}^{\gamma^* p}}_{\sigma_{direct}^{\gamma^* p}} + \sigma_{VM}^{\gamma^* p} + \sigma_{anomalous}^{\gamma^* p} \,. \tag{5.3}$$

The transition between the cross sections for real and virtual photons is accomplished by introducing reduced probabilities given by factors $\left(\frac{m_V^2}{m_V^2+Q^2}\right)^2$ and $\left(\frac{4k_T^2}{4k_T^2+Q^2}\right)^2$ for vector meson states and $q\bar{q}$ pairs, respectively. At HERMES center-of-mass energy $\sqrt{s} \approx 7$ GeV, the contribution of the anomalous process is smaller compared to the direct and VM interactions. The

[2]The similar process $\gamma q \to q$ in the photoproduction regime is forbidden.

semi-inclusive background in the exclusive ρ^0 sample (see Section 4.3.1) is mainly coming from direct processes.

The $\gamma^* p$ cross sections are converted to ep cross sections by weighting with the virtual-photon flux factor Γ_T,

$$\frac{d\sigma^{ep}}{d\log y \;\; d\log Q^2} = \Gamma_T(1+\epsilon R)\frac{d\sigma^{\gamma^* p}}{d\log y \;\; d\log Q^2} \;, \tag{5.4}$$

where $R = \sigma_L/\sigma_T$ (see Section 2.3) is the longitudinal-to-transverse cross section ratio for each process and

$$\begin{aligned} \Gamma_T &= \frac{\alpha_{em}(1-x)}{2\pi Q^2 y}\Big[y^2\Big(1-\frac{2m_e^2}{Q^2}\Big)+\frac{2}{1+\gamma^2}\Big(1-y-\frac{Q^2}{4E^2}\Big)\Big], \\ \epsilon &= \Big[1+\frac{1}{2}\Big(1-\frac{2m_e^2}{Q^2}\Big)\frac{y^2+Q^2/E^2}{1-y-Q^2/4E^2}\Big] \;. \end{aligned} \tag{5.5}$$

5.1.2 Radiative corrections

Any Monte Carlo generator simulates the ep cross section at Born level (see Figure 5.4, a)), *i.e.*, neither the radiation of a real photon by the incoming (b)) or outgoing (c)) lepton nor the loop corrections coming from effects of vacuum polarization (e)) and exchange of an additional virtual photon (d)) are taken into account.

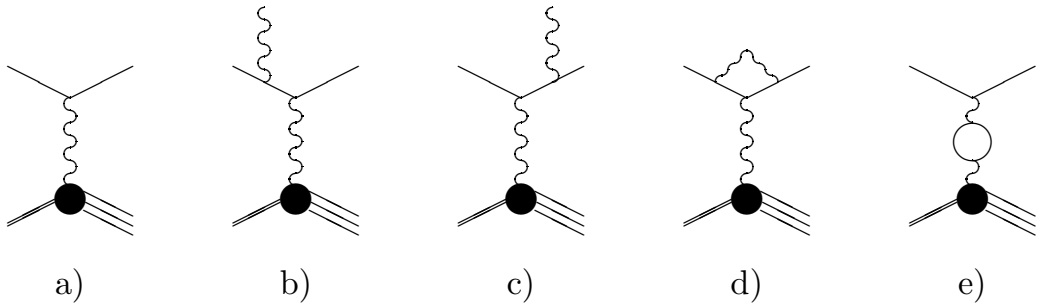

Figure 5.4: Feynman diagrams contributing to the Born (a) and the radiative correction (b-e) cross sections in lepton-nucleus scattering at $O(\alpha_{em}^2)$.

The real photon from initial or final state radiations can be detected while in the case of loop corrections there is no photon emitted. The observed cross section is the quadratic sum of all contributions where the processes with the same final state may interfere. The difference between observed and Born cross sections, called *radiative corrections*, have to be included in the Monte Carlo simulation since the experimental data contains contributions from both the Born process and from QED radiative effects. The measured cross sections and asymmetries possibly contain large contribution from radiative corrections, which have to be estimated and corrected.

At Born level the values of Q^2 and y for each event are given by the scattering angle and the energy of the lepton. Radiation of a photon changes the kinematics of the whole reaction,

because the reconstructed (observed) kinematics of the lepton (Q^2_{obs}, y_{obs}) is somewhat different due to the losses caused by the emitted photon. In this case the energy E_γ and the scattering angles θ_γ and ϕ_γ of the emitted photon are independent quantities. In order to reconstruct the true kinematics, the energy E_γ of the radiated photon has to be included in the calculation of kinematic variables. In general, the radiative corrections are due to three different processes: the elastic (el) scattering of the lepton off the nucleon as a whole, in the case of a target heavier than hydrogen the quasi-elastic (q) interaction of the lepton with one of the nucleons inside the nucleus, and the inelastic (in) scattering of the lepton on a single quark inside the nucleon. The total radiative correction at lowest order is obtained as the sum of these contributions together with the loop corrections σ_ν:

$$\sigma_{rad.corr.} = \sigma_{in} + \sigma_q + \sigma_{el} + \sigma_\nu \ . \tag{5.6}$$

Since PYTHIA does not generate the inclusive cross section, the corrections for elastic and quasi-elastic contributions are not used. The probability of a photon radiation is estimated according to the cross section of a certain event. The observed cross section can be represented as

$$\sigma_{obs} = \sigma_{non-rad}(\Delta) + \sigma_{in}(\Delta) \ . \tag{5.7}$$

A cut-off parameter Δ of the order of 100 MeV splits the observed cross section into a non-radiative and a radiative part [87]. The part $\sigma_{non-rad}$ contains not only the Born cross section but also the contributions from loop corrections σ_ν and from multiple soft photon production with a total energy not exceeding the cut-off parameter Δ. The reason to include those corrections together with the Born cross section is to account for interferences between the processes where there is no a real photon radiated. In the case the event is radiative, the radiative corrections are computed using the code RADGEN [83]. The emitted photon is generated and the values of the kinematic variables are recalculated to get the true kinematics,

$$\begin{aligned} W^2_{true} &= W^2 - 2E_\gamma(\nu + M - \sqrt{\nu^2 + Q^2}\cos\theta_\gamma) \ , \quad \nu_{true} = \nu - E_\gamma \ , \\ Q^2_{true} &= Q^2 + 2E_\gamma(\nu - \sqrt{\nu^2 + Q^2}\cos\theta_\gamma) \ , \qquad\qquad x_{true} = \frac{Q^2_{true}}{2M\nu_{true}} \ . \end{aligned} \tag{5.8}$$

5.1.3 The hadronization

After the lepton-nucleon scattering process is generated and the radiative corrections are performed, some more effort is needed to produce the outgoing, final state particles. The generation of outgoing particles in the case of the VM scattering process will be described in Section 5.2. Below a brief description of hadronization in the case of direct or anomalous scattering processes is given.

The phenomenological fragmentation models bridge the gap between the short time scale,

hard scattering process and the transformation of outgoing partons into hadrons. There are three main categories of fragmentation models: string, cluster and independent fragmentation [88].

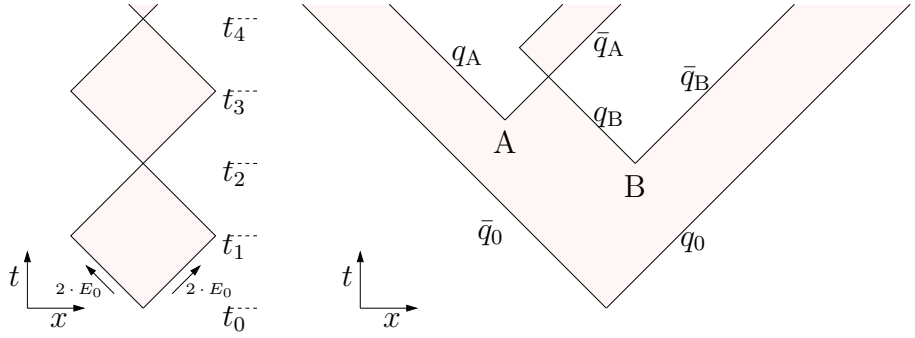

Figure 5.5: The massless relativistic string in the Lund model. The left hand side illustrates a bound state of two particles. At the turning points of the particles (t_1, t_3) the complete energy of the system is contained within the string spanned between the two particles. The process of fragmentation in the Lund model is shown on the right hand side: New $q\bar{q}$ pairs can be produced along the string, causing a breakup into separate bound states which contain different fractions of the total original energy.

The HERMES Monte Carlo generators use the LUND [85] model which is based on the massless relativistic string model. It describes the QCD color force fields between quarks and gluons. If a $q\bar{q}$ pair is produced at a single point in the space-time (left panel of Figure 5.5), carrying the energy obtained in the original process, the quark and anti-quark move apart in opposite directions. The attractive force due to the color field between them is represented by the massless relativistic string spanned between two objects. The constant force k caused by this string gives rise to a linear potential. Thus a stable meson configuration is produced in which the system oscillates between states where all energy is contained in the momentum of the particle (t_0, t_2) or in the turning points (t_1, t_3) where the energy is contained in the string. At sufficiently high energies, new $q\bar{q}$ pairs can be produced along the direction of the force field. This corresponds to creating new end points and thus to the breakup of the string into two parts. As there is no force field between the new particles but an attractive force towards the original ones, the two systems immediately separate and can be treated as isolated. Several string breaks can occur, until the individual system reaches a cut-off energy threshold. In right panel of Figure 5.5 an example with two string breaks at the vertices A and B is shown. In this case the final state would consist of three mesons.

5.2 The rhoMC Monte Carlo generator

In this generator the mechanism of event generation and reconstruction is similar to that of PYTHIA (see Figure 5.6). The simulation of the final state particles is done in the generator itself, so no fragmentation models are required. The radiative corrections are not yet imple-

mented in the generator. This issue will be discussed in Section 5.3.3. The produced events pass through the same chain of reconstruction, HMC, HRC (or HSG) and, if the transverse magnet correction is needed, through TMC. In the end the results are written to μDSTs.

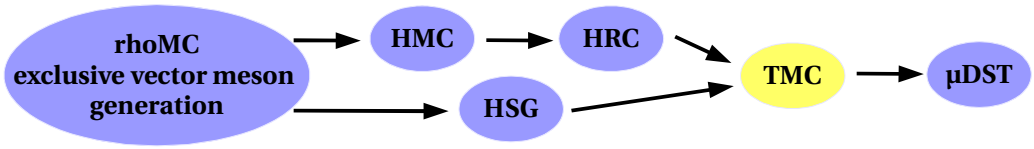

Figure 5.6: RhoMC Monte Carlo production chain. TMC is used only to simulate the deflections by the transverse magnet.

The VMD model is implemented in the rhoMC Monte Carlo generator, although it uses parameterizations different from the ones in PYTHIA. While PYTHIA generates the events according to the cross section, for most of the kinematic variables rhoMC generates flat distributions in a kinematic box and weights each event with the corresponding cross section, called *weight*. So, in contrast to PYTHIA, the *weight* always differs from 1 in rhoMC.

In the case of an unpolarized or longitudinal polarized beam and an unpolarized target, the exclusive electroproduction and decay of ρ^0 mesons[3] is described by 8 independent variables listed in Table 5.1. In the following the more natural choice $\phi = \Psi - \Phi$ is used instead of the generated angle Ψ.

E' (GeV)	Q^2 (GeV^2)	ϕ_e	t (GeV^2)	M_ρ (GeV)	Φ	$\cos\theta$	Ψ
$[0:27.57]$	$[0.1:30]$	$[0:2\pi]$	$[t_{min}:t_{max}]$	$[M_{min}:M_{max}]$	$[0:2\pi]$	$[-1:1]$	$[0:2\pi]$

Table 5.1: 8 independent variables to generate a ρ^0 meson and its decay.

The cross section of exclusive ρ^0 production can be factorized in terms of angle-independent and angular dependent parts:

$$\frac{d\sigma}{dE'\,dQ^2\,dt\,dM_\rho\,d\Phi\,d\phi\,d\cos\theta} \sim \frac{d\sigma}{dE'\,dQ^2\,dt\,dM_\rho} W(x_B, Q^2, t, \Phi, \phi, \cos\theta). \tag{5.9}$$

The angle-independent part is the diffractive ρ^0 electroproduction cross section depending on negative squared four-momentum of the virtual photon Q^2, the momentum E' of the scattered lepton and on the four-momentum transfer $\sqrt{-t}$ to the proton at a fixed value of the ρ^0 mass M_ρ.

The angle-dependent part is the angular distribution $W(x_B, Q^2, t, \cos\theta, \phi, \Phi)$ of the ρ^0 and its decay products, which for fixed values[4] of x_B, Q^2 and t depends on three angles Φ, ϕ and

[3]Hearafter only ρ^0 is referred. However, the principles of the VMD model are true for all vector mesons.
[4]For simplicity hereafter x_B, Q^2 and t are omitted.

θ (see Figure 2.10). For an unpolarized target and longitudinally polarized lepton beam the angular distribution reads:

$$W(\cos\theta, \phi, \Phi) = W_{UU}(\cos\theta, \phi, \Phi) + P_l W_{LU}(\cos\theta, \phi, \Phi) \; . \tag{5.10}$$

In the following the details of each generation step are given. In this section the main focus is on rhoMC, however the differences between two Monte Carlo generators are highlighted.

5.2.1 Cross section $\sigma^{\gamma p}$ of ρ^0 production by a real photon

Both Monte Carlo generators first generate the cross section for the real photon scattering off the nucleon, $\sigma^{\gamma p}$.

For the simulation of photoproduction cross section, the generator rhoMC uses a parameterization suggested by a fit to the world photoproduction data [89]:

$$\sigma^{\gamma p}(W) = A_\gamma \frac{2M_p}{W^2 - M_p^2} + B_\gamma \; , \tag{5.11}$$

with $A_\gamma = 29.4$ μb GeV and $B_\gamma = 9.5$ μb.

In PYTHIA the photon-nucleon cross section $\sigma_{VM}^{\gamma p}$ for vector meson production (see equation (5.2)) is related to the cross section of vector meson scattering off the nucleon:

$$\sigma_{VM}^{\gamma p}(W) = \sum_V \frac{4\pi\alpha_{em}}{f_V^2} \sigma_{tot}^{Vp}(W) \; . \tag{5.12}$$

The elastic diffractive vector meson (in particular ρ^0) production given by equation (2.18) is only one of the processes generated by PYTHIA. PYTHIA generates also the single- and double-diffractive vector meson productions, as well as the extensions to the VMD model which for instance include the off-diagonal, or non-resonant couplings between the different vector meson states or a continuous mass spectrum of vector mesons, called Generalized Vector Meson Dominance (GVMD) model.

The hadronic cross section σ_{tot}^{Vp} is given by the Donnachie and Landshoff parameterization [31] (see equation (2.30)). In contrast to rhoMC (see Section 5.2.5), in this case the t dependence of the cross section is not factorized and is given by the parameterization of σ_{tot}^{Vp}. Single and double diffractive processes are modeled by a pomeron-type parameterization while the elastic cross section contains also the Regge behavior for small energies.

5.2.2 Cross section $\sigma^{\gamma^* p}$ of ρ^0 production by a virtual photon

The photoproduction cross section ($Q^2 = 0$) of exclusive ρ^0 mesons has a contribution from transverse photons only. The ρ^0 production cross section from a virtual photon ($Q^2 > 0$) has contributions from both transverse and longitudinal photons. By imposing a Q^2 dependent

propagator $\left(\frac{M_\rho^2}{Q^2+M_\rho^2}\right)^m$, the cross section of ρ^0 production by a real photon is extended to a cross section of ρ^0 production by a virtual photon. The contributions from transverse and longitudinal photons are expected to have different W and Q^2 dependences:

$$\sigma^{\gamma^* p}(Q^2, W) = \sigma_T^{\gamma^* p}(Q^2, W) + \epsilon\, \sigma_L^{\gamma^* p}(Q^2, W) \; . \tag{5.13}$$

The longitudinal and transverse cross sections, σ_L and σ_T, are distinguishable in the $\sigma^{\gamma^* p}$ cross section introducing a cross section ratio $R = \sigma_L/\sigma_T$ (see Section 2.3). The cross section of ρ^0 production by a virtual photon reads:

$$\sigma^{\gamma^* p}(Q^2, W) = \sigma^{\gamma p}(W) \left(\frac{M_\rho^2}{Q^2 + M_\rho^2}\right)^m (1 + \epsilon R(W, Q^2)) \; . \tag{5.14}$$

The VMD model predicts the exponent m to be equal to 2 (see Section 2.3), while the data from E665 [28] and H1 [51] as well as from HERMES [90] yield a different value. At an average W value of about 5 GeV at HERMES kinematics, m is found to be $m = 2.575$ [78] which is in agreement with the results 2.51 ± 0.07 and 2.24 ± 0.09 from E665 ($W \approx 17$ GeV) and H1 ($W \approx 75$ GeV).

For the cross section ratio R a parameterization of the form

$$R(W, Q^2) = c_0(W) \left[\frac{Q^2}{M_\rho^2}\right]^{c_1} \tag{5.15}$$

is used, which is suggested by the boundary condition $R(Q^2 \to 0) \to 0$ and by several model predictions assuming the longitudinal and transverse cross sections differ by some power of Q^2. Both Monte Carlo generators were using the values of parameters $c_0(W)$ and c_1 obtained from a fit to the world data at center-of-mass energies above and below $W = 7$ GeV (left panel of Figure 5.7) where the full cross section of the ρ^0 production is supposed to have a transition between the Reggeon and Pomeron exchange mechanisms [91]:

$$\begin{aligned} c_0 &= \begin{cases} 0.33 \pm 0.03, & 4 < W < 7\text{GeV} \\ 0.48 \pm 0.03, & W > 7\text{GeV} \end{cases} \\ c_1 &= 0.61 \pm 0.04 \; . \end{aligned} \tag{5.16}$$

The parameters for the low center-of-mass energy range $4 < W < 7$ GeV were obtained from HERMES He^3 data. Data from DESY and Cornell at $2 < W < 4$ GeV were not included in the fit. Recent results from hydrogen and deuterium data of HERMES suggest higher values of R compared to the He^3 results (right panel of Figure 5.7). Also the low center-of-mass energy data from CLAS [92] shows a better agreement with high center-of-mass energy data. While theoretically the cross section ratio R is expected to have a W dependence, at low Q^2 region

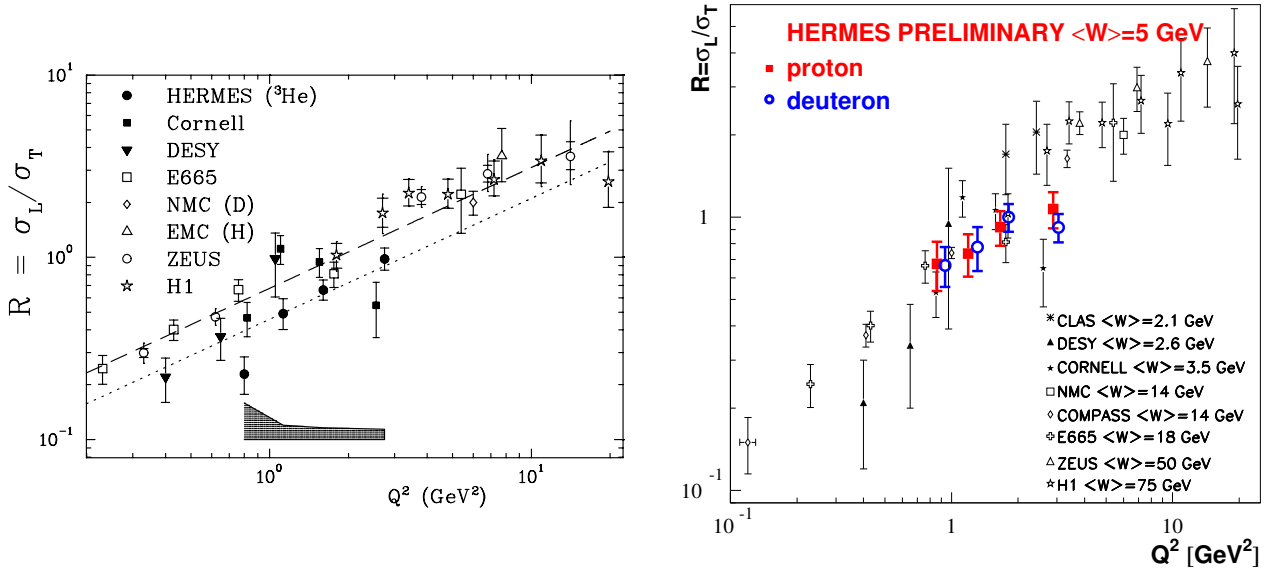

Figure 5.7: The ratio $R = \sigma_L/\sigma_T$ determined from various experiments. Left: The dashed (dotted) line represents a fit to the data above (below) 7 GeV data which are shown as open (filled) points. The DESY and Cornell data are not included in the fit. All error bars are statistical only, the shaded area indicates the systematic uncertainty of He^3 HERMES data. The plot is from reference [91]. Right: recent results from various experiments. As before, only statistical error bars are presented.

the possible W-dependence seems to be not confirmed experimentally. Using the recent results from various experiments, a new fit to the world data is performed covering a wide range of center-of-mass energies resulting in

$$\begin{aligned} c_0 &= 0.48 \pm 0.02 \\ c_1 &= 0.68 \pm 0.02 \,. \end{aligned} \tag{5.17}$$

Currently these values of the parameters c_0 and c_1 are used in both PYTHIA and rhoMC.

5.2.3 Electroproduction cross section σ^{ep} of ρ^0 mesons

The cross section of ρ^0 production by a virtual photon, $\sigma^{\gamma^* p}$, is related to the electroproduction cross section σ^{ep} through the virtual photon flux factor Γ_T (see Section 2.3),

$$\frac{d\sigma}{d\Omega_e\, dE'} = \Gamma_T(E, E', \theta_e)\, \sigma^{\gamma^* p}(Q^2, W) \,, \tag{5.18}$$

where (see also equation (5.5))

$$\Gamma_T = \frac{\alpha_{em}}{4\pi^2} \frac{W^2 - M_p^2}{M_p} \frac{1}{Q^2} \frac{E'}{E} \frac{1}{1-\epsilon} \,, \qquad \epsilon = \frac{1 - y - Q^2/4E^2}{1 - y + y^2/2 + Q^2/4E^2}. \tag{5.19}$$

The variables E' and Ω_e are the ones commonly used in the literature [89]. Since RhoMC does not generate the angle θ_e of the scattered lepton, instead it generates the invariant Q^2, the

cross section is rewritten in terms of E' and Q^2. The two cross sections are related to each other using the corresponding Jacobian:

$$\frac{d\sigma}{dQ^2\,dE'} = \frac{d\sigma}{d\theta_e\,dE'}\;\frac{1}{2EE'} \tag{5.20}$$

5.2.4 Generation of mass distribution

In order to produce an exclusive ρ^0 meson, the center-of-mass energy W calculated through the generated values of Q^2 and E' (see equation (2.6)), should be larger than the sum of the masses of the vector meson (M_ρ) and of the recoiling proton ($M_{p'}$):

$$W^2 > (M_\rho + M_{p'})^2. \tag{5.21}$$

As the ρ^0 meson is a broad resonance, there is a large variety of ρ^0 mass values at fixed values of Q^2 and E', *i.e.* the mass of the produced vector meson is an independent variable that has to be generated.

There are several options to generate the ρ^0 mass distribution in rhoMC, in particular the non-relativistic or relativistic Breit-Wigner distributions (see equation (5.23)). The best description of the real data is achieved by a skewed Breit-Wigner distribution proposed by Ross and Stodolsky [78],

$$\frac{dN}{dM_{2\pi}} \propto \frac{M_{2\pi}M_\rho\Gamma(M_{2\pi})}{(M_\rho^2 - M_{2\pi}^2)^2 + M_\rho^2\Gamma^2(M_{2\pi})}\left(\frac{M_\rho}{M_{2\pi}}\right)^{n_{skew}} \tag{5.22}$$

with a skewing factor $n_{skew} = 2.2$ and an energy dependent width $\Gamma(M_{2\pi})$ of the ρ^0 resonance (see equation (4.13)). In the calculation of the energy dependent width $\Gamma(M_{2\pi})$, the values $M_\rho = 0.770$ GeV, $\Gamma_\rho = 0.1507$ GeV (see Table 4.1) and $M_\pi = 0.134$ GeV have been used.

In PYTHIA two options exist to generate the ρ^0 mass distribution, the non-relativistic and relativistic Breit-Wigner distributions:

$$\frac{dN^{non-rel}}{dM_{2\pi}} \propto \frac{\Gamma_\rho/2}{4(M_\rho - M_{2\pi})^2 + \Gamma_\rho^2}\,, \qquad \frac{dN^{rel}}{dM_{2\pi}} \propto \frac{M_\rho^2\Gamma_\rho}{4(M_\rho^2 - M_{2\pi}^2)^2 + M_\rho^2\Gamma_\rho^2}\,. \tag{5.23}$$

5.2.5 Generation of t dependence

Typical for diffractive processes (see Section 2.3), the t dependence is expected to have a steep, exponential-like fall-off with increasing $|t|$:

$$\frac{d\sigma}{d|t|} \propto e^{-b|t|}. \tag{5.24}$$

The value of the diffractive slope parameter b may be interpreted in the terms of combined size of the strongly interacting hadrons (see equation (2.15)). The values of b measured in

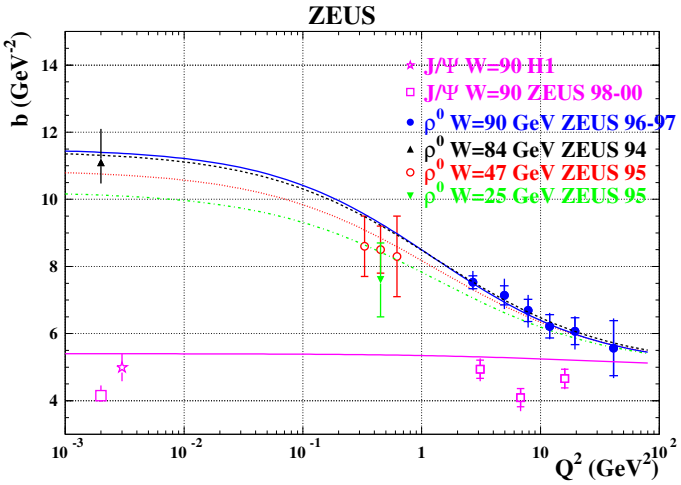

Figure 5.8: The measured values of the diffractive slope parameter b from ρ^0 and J/Ψ production as a function of Q^2. For comparison the parameterization given by equation (5.26) is presented by various lines (solid, dashed, dotted and dashed-dotted), calculated for average W values ($W = 90, 84, 47$ and 25 GeV) of each measurement [93].

collider experiments at HERA (see Figure 5.8) indicate for a Q^2 dependence. The average value of $b = 6.76$ GeV^{-2} at HERMES kinematics was previously used as a default parameter in both generators. Alternatively, a parameterization [93] can be used to express the b slope as a function of Q^2,

$$b(Q^2) = \frac{b_0/M_\rho^2}{1 + R(Q^2)} + b_\infty, \tag{5.25}$$

where $b_0 = 3.9 \pm 0.8$ GeV^{-2}, $b_\infty = 5.0 \pm 0.4$ GeV^{-2}. The first term is interpreted as a measure of the size of the hadronic component of the photon, while b_∞ represents the size of the proton.

This parameterization is based on the fact that the $q\bar{q}$ pairs from the longitudinal virtual photon γ_L^* prefer to have a symmetric momentum configuration and large relative transverse momentum k_T. They are expected to have a smaller spatial configuration than the $q\bar{q}$ pairs from a transversely polarized virtual photon γ_T^*, which have an asymmetric momentum configuration and small k_T. Therefore the effective size of γ_L^* is expected to be smaller than that of γ_T^*, which should be then reflected in the value of the b slope. Indeed, a decrease of the b slope with Q^2 is observed. However, the values of b slopes of the differential cross section in t, extracted as a function of Q^2 for two samples, γ_L^* and γ_T^* samples, do not show significant differences. This implies that the effective sizes of γ_L^* and γ_T^* are similar. Therefore, the slope b and SDME r_{00}^{04} ($r_{00}^{04} = \sigma_L/\sigma_{tot}$) must be correlated by their dependence on Q^2. A linear correlation is observed between them [93].

Furthermore, the parameterization given by equation (5.25) may be modified by adding also a W dependent term,

$$b(Q^2, W) = \frac{b_0/M_\rho^2 + ln(W/W_0)}{1 + R(Q^2)} + b_\infty, \tag{5.26}$$

with $W_0 = 90$ GeV [93]. The HERA collider data (see Figure 5.8) and the parameterization

given by equation (5.26) indicate that at HERMES kinematics the W dependence of the b slope is not strong, so the parameterization given by equation (5.25) is used with $b_\infty = 4.5$ GeV^{-2} and $b_0 = 3.46$ GeV^{-2} [94].

5.2.6 The 3-dimensional angular distribution

The production and decay angles Φ, ϕ and θ can be defined in several reference frames. The frames used in rhoMC and PYTHIA generators are defined following the reference [95].

Definition of Φ, θ and ϕ angles

The coordinate system of the $\gamma^* p$ center-of-mass system ($\gamma^*(q) + P(p) \to P'(p') + \rho^0(v)$) is defined through the orthogonal set of unit vectors (see Figure 2.10),

$$Z = \frac{\mathbf{q}}{|\mathbf{q}|} \qquad Y = \frac{\mathbf{q}\times\mathbf{v}}{|\mathbf{q}\times\mathbf{v}|} \qquad X = Y \times Z \ . \tag{5.27}$$

All vectors refer to the $\gamma^* p$ center-of-mass system which Z-axis points along the direction of the virtual photon. The ρ^0 decay distribution is described in the ρ^0 rest frame with a coordinate system defined as (see Figure 2.10):

$$z = -\frac{\mathbf{p}'}{|\mathbf{p}'|} \qquad y = Y \qquad x = y \times z \ , \tag{5.28}$$

where the z-axis is opposite to the direction of the outgoing proton in center-of-mass system, *i.e.* preserves the positive direction of the produced ρ^0.

The angle Φ is defined through unit vectors $\hat{\mathbf{l}}$, $\hat{\mathbf{l}}'$, $\hat{\mathbf{q}}$ and $\hat{\mathbf{v}}$ referring to the center-of-mass system and pointing along the direction of the incident and scattered leptons, virtual photon and produced ρ^0, respectively,

$$\sin\Phi = \frac{\left[(\hat{\mathbf{q}}\times\hat{\mathbf{v}})\times(\hat{\mathbf{l}}\times\hat{\mathbf{l}}')\right]\cdot\hat{\mathbf{q}}}{|\hat{\mathbf{q}}\times\hat{\mathbf{v}}|\cdot|\hat{\mathbf{l}}\times\hat{\mathbf{l}}'|} \qquad \cos\Phi = \frac{(\hat{\mathbf{q}}\times\hat{\mathbf{v}})\cdot(\hat{\mathbf{l}}\times\hat{\mathbf{l}}')}{|\hat{\mathbf{q}}\times\hat{\mathbf{v}}|\cdot|\hat{\mathbf{l}}\times\hat{\mathbf{l}}'|} \ . \tag{5.29}$$

This angle represents the angle between the ρ^0 production and the lepton scattering planes (see Figure 2.10) which is equal to the azimuthal angle ϕ_ρ of the ρ^0 in the center-of-mass system up to the sign: $\Phi = -\phi_\rho$.

The angles θ and ϕ are defined according to

$$\begin{aligned} &\cos\theta = (\hat{\mathbf{v}}\cdot\hat{\pi}^+) \\ &\sin\phi = -\frac{\left[(\hat{\mathbf{q}}\times\hat{\mathbf{v}})\times\hat{\mathbf{v}}\right]\cdot(\hat{\mathbf{v}}\times\hat{\pi}^+)}{\left|(\hat{\mathbf{q}}\times\hat{\mathbf{v}})\times\hat{\mathbf{v}}\right|\cdot|\hat{\mathbf{v}}\times\hat{\pi}^+|} \qquad \cos\phi = \frac{(\hat{\mathbf{q}}\times\hat{\mathbf{v}})\cdot(\hat{\mathbf{v}}\times\hat{\pi}^+)}{|\hat{\mathbf{q}}\times\hat{\mathbf{v}}|\cdot|\hat{\mathbf{v}}\times\hat{\pi}^+|} \end{aligned} \tag{5.30}$$

with all the unit vectors referring to the ρ^0 rest frame and $\hat{\mathbf{p}}'$ and $\hat{\pi}^+$ point along the direction of scattered proton and decay product π^+. The angles θ and ϕ are the polar and azimuthal angles of the positively charged pion in the ρ^0 rest frame.

Generation of angular distribution

- In the case of an unpolarized target and a longitudinally polarized beam, rhoMC is capable of generating the angular distribution $W(\cos\theta, \phi, \Phi)$ given by equation (5.10). The angular distributions $W_{UU}(\cos\theta, \phi, \Phi)$ (see equation (2.68)) and $W_{LU}(\cos\theta, \phi, \Phi)$ (see equation (2.69)) are parameterized with 15 unpolarized and 8 polarized SDMEs. These SDMEs, previously extracted from HERMES data [52], are fed to the rhoMC generator that generates the three independent angles and calculates the 3-dimensional angular distribution. The value P_l of the beam polarization is an input parameter that can vary between -1 and 1.

  Only rhoMC can simulate the 3-dimensional angular distribution $W(\cos\theta, \phi, \Phi)$ which gives the best description of the real data.

- The other possibility is to generate the angular distribution $W(\cos\theta)$ integrated over the angles Φ and ϕ. The polarized angular distribution $W_{LU}(\cos\theta, \phi, \Phi)$ does not survive the integration over these angles. The unpolarized angular distribution $W_{UU}(\cos\theta, \phi, \Phi)$ reduces to

$$W(\cos\theta) = \frac{3}{4}\Big[1 - r_{00}^{04} + (3r_{00}^{04} - 1)\cos^2\theta\Big] = \frac{3}{4}\Big[\sin^2\theta - r_{00}^{04} + 3r_{00}^{04}\cos^2\theta\Big]\,, \tag{5.31}$$

  where only the terms associated with the SDME r_{00}^{04} are left. Here the value of SDME r_{00}^{04} is not an input parameter. Assuming s-channel helicity conservation, the cross section ratio R is related to r_{00}^{04} as:

$$R = \frac{1}{\epsilon}\frac{r_{00}^{04}}{1 - r_{00}^{04}} \tag{5.32}$$

  The ratio R is calculated using the parameterization given by equation (5.15) and is used to compute the value of r_{00}^{04}.

  Both PYTHIA and rhoMC are capable of generating the angular distribution $W(\cos\theta)$.

- There are cases when it is important to estimate the distortions of the angular distribution caused by the limited acceptance. In such a case the angular distribution can be generated isotropically (flat) and all the distortions observed after the reconstruction give an estimate of acceptance effects.

  Both generators can simulate the isotropic angular distribution.

- A simulation, assuming SCHC, can be performed by rhoMC. In this case the angular distribution is generated according to equation (2.72).

- RhoMC is capable of generating some more particular cases, namely only longitudinally or transversely polarized ρ^0 mesons.

5.2.7 Generation of final states

The generated angles Φ, θ and ϕ are used to reconstruct the 4-momenta of the produced ρ^0 and the decay pions. Note that this is different from the simulation of the direct and anomalous processes in PYTHIA where a fragmentation model is used for generation of the final state products.

Generation of ρ^0 meson

In the frame where the axes are defined according to equation (5.27), the four-momentum of virtual photon and ρ^0 meson are defined as $q(\nu, 0, 0, |\mathbf{q}|)$ and $v(E_\rho, |\mathbf{v}|\sin\theta_\rho, 0, |\mathbf{v}|\cos\theta_\rho)$ (see Figure 5.9 right panel), respectively, where

$$\begin{aligned} E_\rho &= \nu + \frac{t - (M_{p'} - M_p)}{2M_p} \\ |\mathbf{v}| &= \sqrt{E_\rho^2 - M_\rho^2} \\ \theta_\rho &= \frac{t + Q^2 - M_\rho^2 + 2\nu E_\rho}{2|\mathbf{q}||\mathbf{v}|}. \end{aligned} \tag{5.33}$$

The generated angle Φ, defined by equation (5.29), can be treated as the azimuthal angle $\phi_{e'}$ of the scattered lepton in the XYZ system. The same angle can be treated also as the negative azimuthal angle $-\phi_\rho$ of the produced ρ^0 in the $X'Y'Z$ system where the Z-axis is aligned along the virtual photon direction, the Y'-axis points along the normal $n_{ll'}$ to the leptonic frame and the X'-axis points along the positive direction of the incoming or outgoing lepton. In rhoMC the angle Φ together with E_ρ, $|\mathbf{v}|$ and θ_ρ is used to reconstruct the 4-momentum of the produced ρ^0 in the $X'Y'Z$ system. Transitions between this system and any other system (*e.g.* ρ^0 rest frame or laboratory system) are performed by two rotations along the corresponding axes and, if necessary, by a Lorenz boost.

Generation of decay pions

The momentum of the produced ρ^0 is equal to zero in its rest frame. Thus the momentum of the decay pions have to be of the same size but oppositely directed, so that their sum is equal to zero as well. Since both decay products are pions, this means that the energy of the ρ^0 meson is equally shared between the two pions:

$$E_\pi = E_\rho/2 \tag{5.34}$$

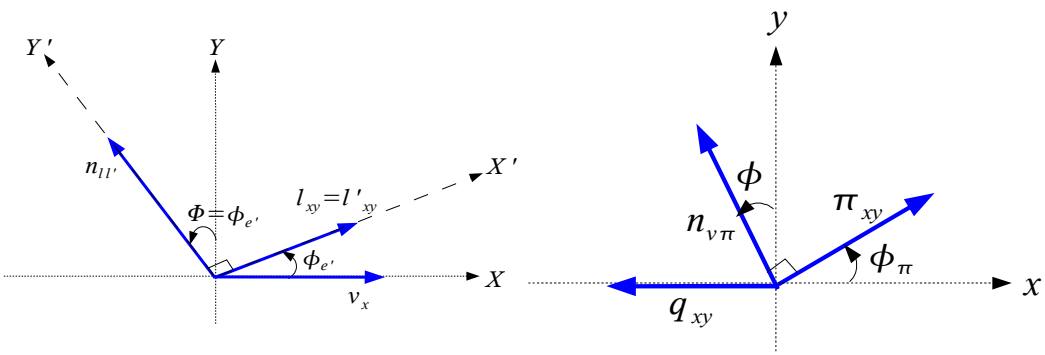

Figure 5.9: Definition of generated Φ (left) and ϕ (right) angles.

The magnitude of the pion momentum $\pi^{\pm}$ can be reconstructed as:

$$|\pi^{\pm}| = \sqrt{E_\pi^2 - M_\pi^2}. \tag{5.35}$$

The θ and ϕ angles defined as in equation (5.30), are the polar and azimuthal angles of the positively charged pion (see Figure 5.9 left panel). Thus the 4-momentum of the π^+ can be calculated. The 4-momentum of the π^- which flies opposite to the π^+ in the ρ^0 rest frame, is then given as:

$$E_{\pi^-} = E_{\pi^+} \ , \qquad \pi_x^- = -\pi_x^+ \ , \qquad \pi_y^- = -\pi_y^+ \ , \qquad \pi_z^- = -\pi_z^+ \ . \tag{5.36}$$

5.2.8 The weight

RhoMC is a mixed-mode generator: the variables t and M_ρ are generated using the 'accept/reject' method, the other independent kinematic quantities are generated flat in corresponding kinematic boxes (Table 5.1). Each event is weighted by its cross section, *weight*. In order to be independent of the generation box, the *weight* is corrected for the size of the generation box:

$$weight = \Delta E' \Delta log(Q^2) \underbrace{\Delta\phi_e \Delta \cos\theta \Delta\Psi}_{8\pi^2} \times \frac{d^3\sigma^{ep}}{dQ^2 dE' d\phi_e} \ \times \ W(\cos\theta, \Phi, \phi) \ . \tag{5.37}$$

Since the normalization of the angular distribution is given by equation (2.70), the *weight* is already corrected for the size of $\Delta\Phi$.

5.3 Kinematic distributions from PYTHIA and rhoMC

In this section the kinematic distributions generated by the Monte Carlo generators PYTHIA and rhoMC are compared. First, the kinematic distributions generated in the full solid angle

4π are shown, and then the distributions reconstructed in the acceptance are compared to the data.

5.3.1 Generated distributions

For a proper comparison of kinematic distributions generated in 4π, both simulations, when possible, are performed under the same conditions. Since PYTHIA generates the 1-dimensional angular distribution $W(\cos\theta)$ (see equation (5.31)), the rhoMC simulation is also performed generating $W(\cos\theta)$. In addition, as rhoMC is not able to account for radiative effects, the PYTHIA simulation is performed at the Born level.

The dependences of the exclusive ρ^0 production cross section on the lepton kinematic variables, as well as on the characteristic variables of produced ρ^0 and decay pions are compared between PYTHIA and rhoMC (see Figure 5.10). The absolutely normalized (see Section 4.3.1) distributions are shown for $Q^2 > 0.1$. The generated values of ΔE at the Born level, as expected, peak around 0 GeV. The t' and M_ρ distributions are presented in the whole generated region while other distributions correspond to the sample restricted by exclusive requirements (see Table 4.4). As the cross section is integrated over the angles ϕ and Φ, the corresponding distributions are flat. From equation (5.31) it is obvious that for photoproduction regime ($Q^2 = 0$ GeV^2), when the SDME $r^{04}_{00} = 0$, only transverse ρ^0 mesons are produced, with the characteristic $\sin^2\theta$ behavior. At the moderate Q^2 values of HERMES, the angular distribution is a superposition of longitudinal and transverse ρ^0 contributions which is reflected in the $\cos\theta$ dependence of the cross section.

All distributions in 4π are mostly similar, however there are some differences, since the models in both generators are not identical. The same holds true also for the generation in the acceptance. The differences are more clearly seen in the ratio plots (see Figure D.2). Due to the limited experimental acceptance, the distributions in 4π do not provide a preference within models. The discrimination between the models can be done by comparing to real data in the acceptance.

5.3.2 Reconstructed Monte Carlo distributions compared to data

In order to compare the reconstructed Monte Carlo distributions with the data, the statistical precision of the Monte Carlo simulation should be at least of the same order of magnitude as that of the data, it would be even better if the statistical uncertainty of the generated sample is negligible. For the generation of exclusive events, where the acceptance is of the order of a few percent, the simulation in 4π is time consuming. If the properties of events in 4π are not as important, as the ones in the acceptance, preferentially reconstructed distributions are compared. Thus the simulation can be performed inside a geometrical box defined by the acceptance. In order to avoid any edge effects introduced by such an artificial box, the borders

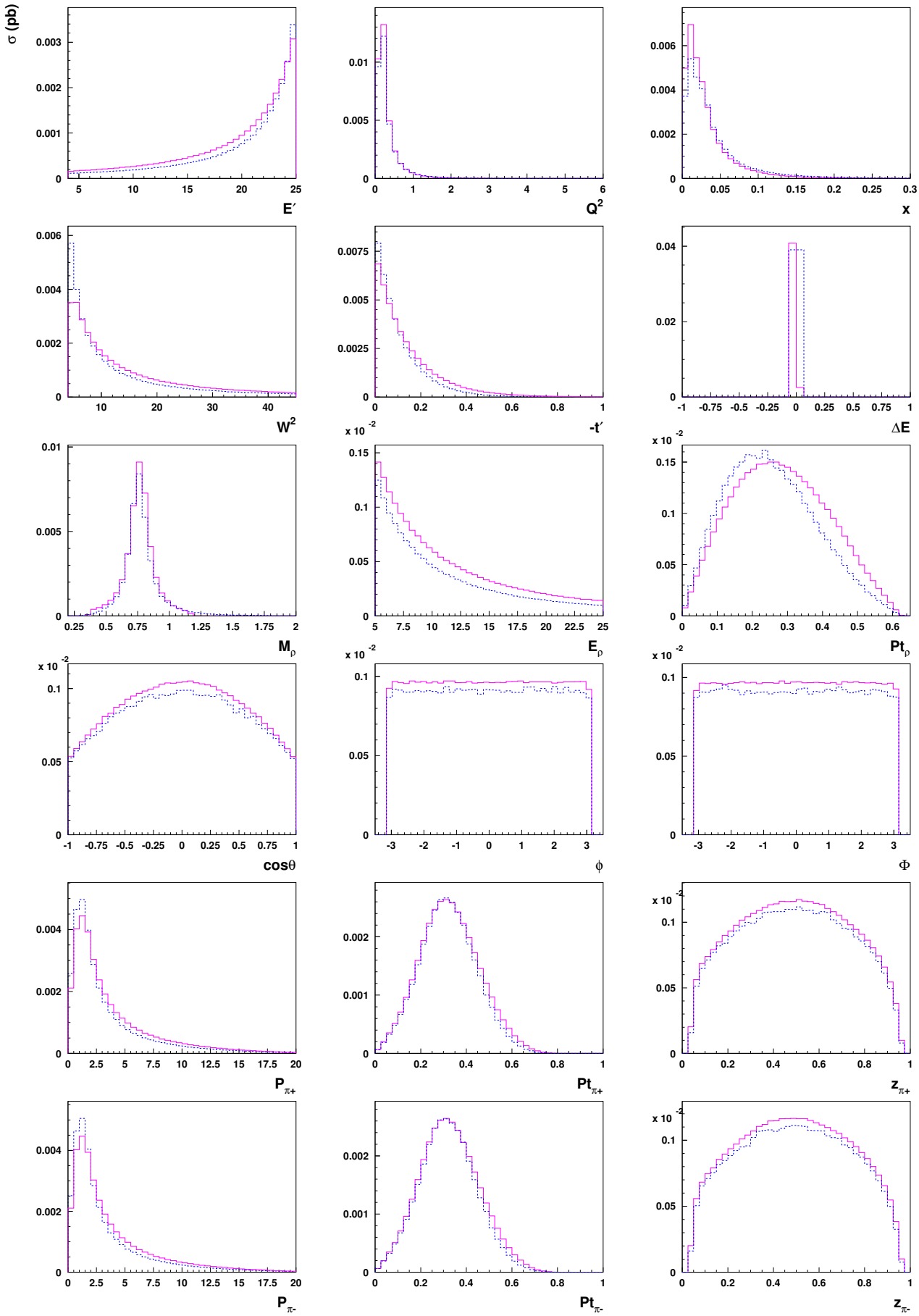

Figure 5.10: The absolutely normalized kinematic distributions from rhoMC (blue dashed histograms) and PYTHIA (magenta solid histograms) Monte Carlo simulations generated in 4π.

of the geometrical box are taken wider than the actual experimental acceptance suggests.

The reconstructed distributions are almost the same when comparing PYTHIA and rhoMC. The absolute yields from PYTHIA (see Figure 5.11) and from rhoMC (see Figure 5.12) are compared to that of real data in various observables.

For this comparison both Monte Carlo simulations are treated in the same way as the data. After selection of a hadron pair and applying the requirements described in Table 4.4, the exclusive ρ^0 sample of the real data still contains contributions from background processes (see Section 4.3). PYTHIA is capable of simulating the background processes, while rhoMC generates the exclusive elastic ρ^0 production only. Thus, the reconstructed distributions generated by PYTHIA are directly compared to the ones of real data. In order to have a better agreement with data, the PYTHIA simulation is performed including radiative corrections. As for the reconstructed distributions generated by rhoMC, the background distributions predicted by PYTHIA are added to those of pure exclusive ρ^0 and then compared to real data.

Absolute yields of PYTHIA compared to data

For lepton kinematic variables the differences between absolute yields of PYTHIA and data are of the order of $20 - 30$ % (see Figure D.3). On the edges with low statistics (*e.g.* $Q^2 > 4$) the discrepancy is larger which can be explained by lack of statistics. The invariant mass, ΔE and t' distributions are well reproduced. The agreement for the kinematics of the decay pions and of the angular distributions is not perfect, mainly because there is no complete description of the angular distribution in PYTHIA. For instance, the angle Φ being generated flat, it is not flat anymore after the acceptance led to 'distortions' in the distributions. The generated cross section versus $\cos\theta$ (see Figure 5.10) also suffers from 'distortions' by the acceptance. Comparing of the $\cos\theta$ distribution from PYTHIA and data it is obvious that the SDME r^{04}_{00} (see equation (5.31)) alone is not able to reproduce the shape of the data distribution. This means that momentum and the fractional energy $z = E_\pi/\nu$ of the pions, which are correlated to $\cos\theta$, are not fully reproduced.

Absolute yields of rhoMC compared to data

Compared to PYTHIA, the agreement between absolute yields of rhoMC and data with respect to the lepton kinematics is worse, of the order of $30 - 40$ % (see Figure D.4). On the other hand, generating the full angular distribution[5] (see equation (2.68)), rhoMC well describes the full kinematics of decay pions. The shape of the generated $\cos\theta$ distribution shows that rhoMC is able to better simulate the more complicated superposition of longitudinal and transverse ρ^0 contributions, than PYTHIA does (see Figure D.1). However, the reconstructed $\cos\theta$ distribution and that of real data are too different from the generated $\cos\theta$ distribution. This acceptance effect can be explained in the following way. The transverse ρ^0 mesons ($\sin^2\theta$)

[5]Here only the unpolarized angular distribution is generated and compared to unpolarized data.

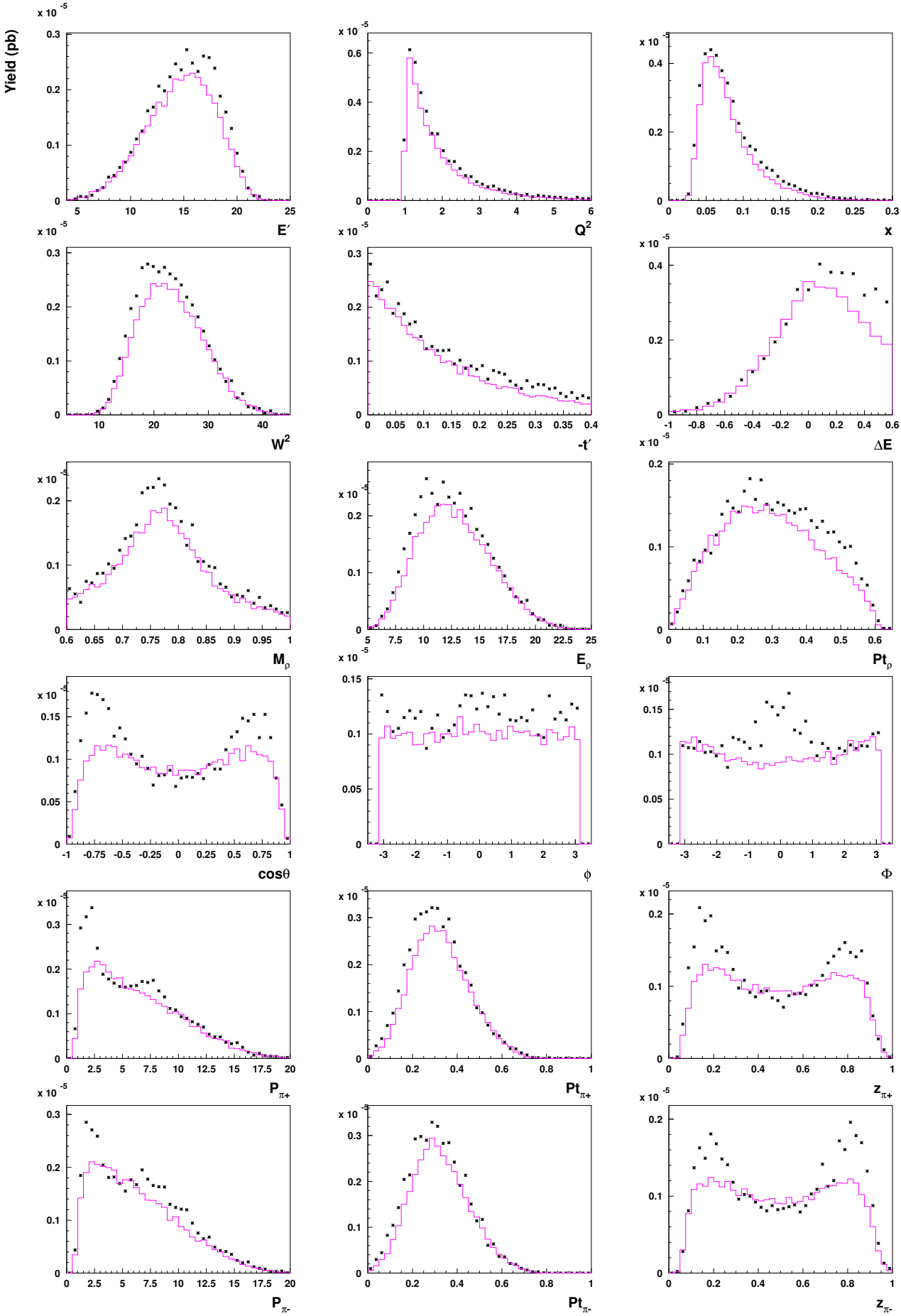

Figure 5.11: The absolutely normalized reconstructed kinematic distributions from PYTHIA Monte Carlo simulation (magenta solid histograms) and data (black points).

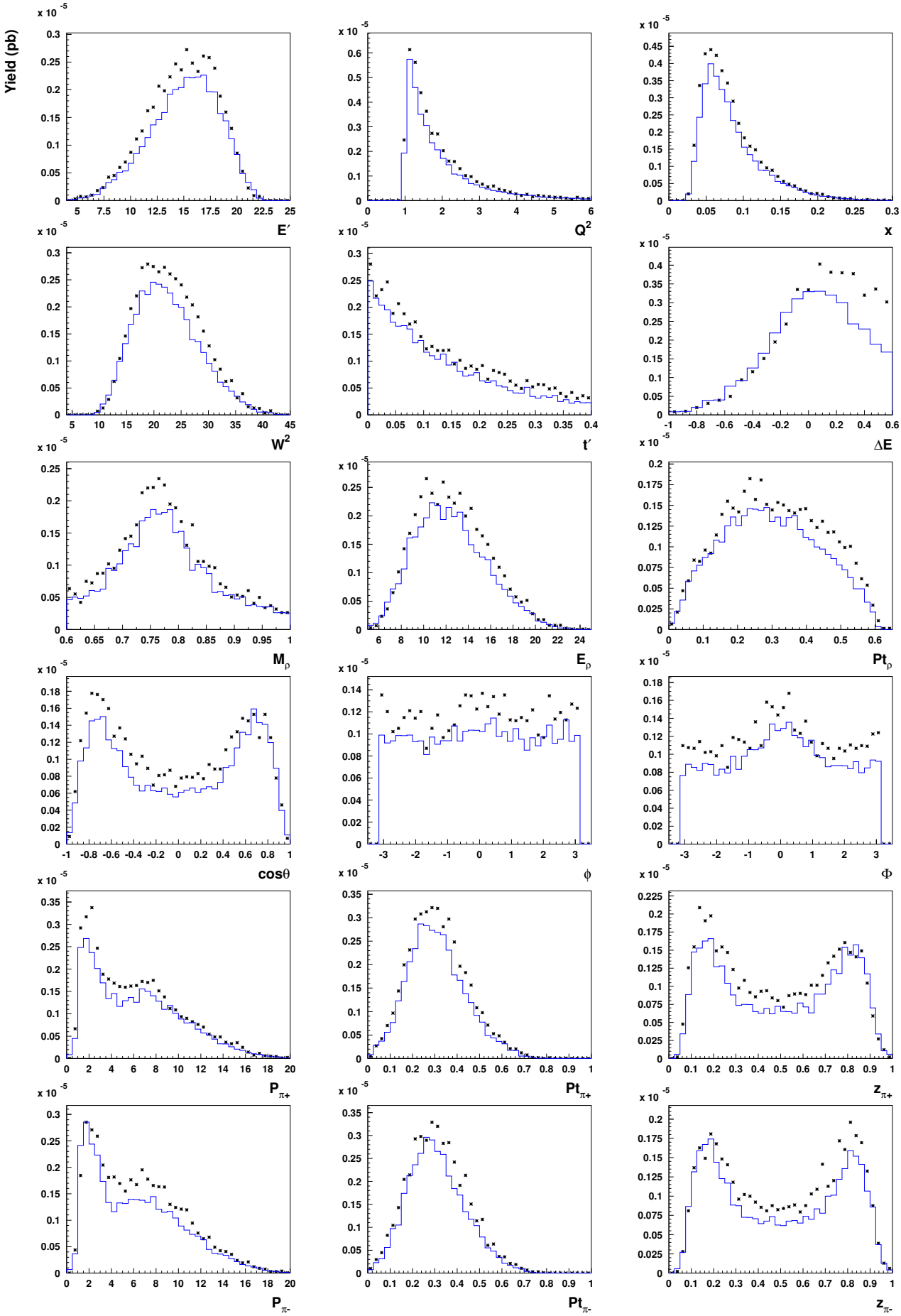

Figure 5.12: The absolutely normalized reconstructed kinematic distributions from rhoMC Monte Carlo simulation (blue solid histograms) and data (black points).

prefer to decay to pions which leave under 90° with respect to the ρ^0 direction in the ρ^0 rest frame. In the laboratory system this translates to equally shared pion momenta, each carrying roughly half of the ρ^0 momentum. If the ρ^0 meson momentum in the laboratory system is small, the transverse component of the momentum of such pions is comparable to the longitudinal component and the decay pion escapes the acceptance. Thus the $\cos\theta$ shape has a dip in the region close to 0 (corresponding to $\theta \approx 90°$). This explains also why the ρ^0 mesons with low momenta generated in 4π (see Figure D.1) do not appear in the reconstructed distribution. The longitudinal ρ^0 mesons ($\cos^2\theta$) prefer to decay in a way that one of the pions preserves the direction of the ρ^0 in its rest frame while the other one flies backward. In the laboratory system, one of the pions takes almost all of the ρ^0 momentum, the other one is very slow. The bending in the spectrometer magnet reduces the chances for slow pions to reach the back chambers, which would allow to reconstruct both pions in the spectrometer. This is reflected by low statistics at the regions ± 1 in the $\cos\theta$ distribution. To complete the discussion about the reconstructed distributions from rhoMC, the pion momentum and z distributions are well reproduced.

5.3.3 Radiative corrections

The radiative corrections discussed in Section 5.1.2 are implemented in the PYTHIA generation chain while rhoMC generates only Born level cross sections. In this section the effect of radiative corrections is discussed.

The lepton kinematics, thus the missing energy ΔE defined as in equation (4.3), are affected by the radiation of a real photon. For both initial and final state radiations the values of ΔE get larger. This implies that for exclusive ρ^0 production the radiative corrections mainly smear the events out of the ΔE peak. This is clearly seen in Figure 5.13 comparing the ΔE distribution with and without radiative corrections. The radiative-corrected cross section is smaller in the $\Delta E < 0.6$ GeV region, which means there is a loss of events. Only those events stay inside the peak for which a low-energy photon was radiated that does not considerably change the lepton kinematics. Instead the Born cross section is smaller in the $\Delta E > 0.6$ GeV region, which implies that the events which are smeared out from $\Delta E < 0.6$ GeV region, appear in the higher ΔE region. The loss of events from the ΔE peak yield to a smaller observed cross section of exclusive ρ^0 production versus other kinematic variables (see Figure 5.13). As expected, the Q^2 and W^2 Born level distributions are higher compared to radiative-corrected distributions showing almost no kinematic dependences within statistics. A possible influence of radiative effects to the angles Φ, ϕ and $\cos\theta$ is of special interest, as this may influence the calculation of the angular distribution. The values of the angle Φ may be changed by the radiation of a real photon, while neither ϕ nor $\cos\theta$ depend on the lepton kinematics. The distributions with and without radiative corrections indicate a marginal effect caused by radiative corrections as they are identical within statistics. The overall differences are of the order of $10 - 20$ % showing

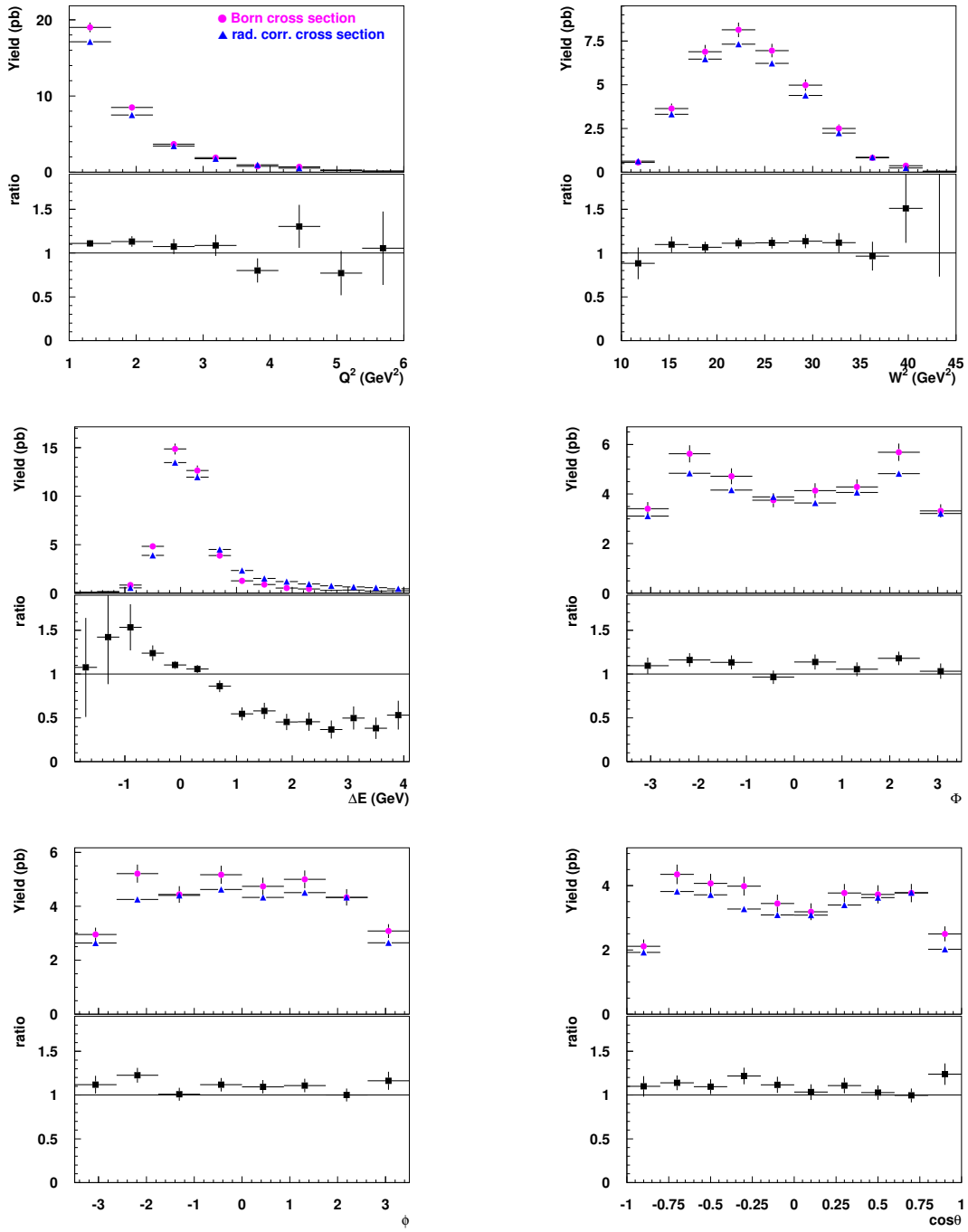

Figure 5.13: Comparison of kinematic distributions from PYTHIA simulations with and without radiative corrections.

almost no kinematic dependences.

5.4 The resolution

The analysis to be discussed in the following chapters, presents the kinematic dependences of asymmetries and SDMEs on Q^2, x_B or $-t'$. In general, the bin width for a certain kinematic

quantity should not be smaller than the spectrometer resolution, *i.e.* the precision in the measurement of that quantity.

The resolution δ can be obtained from Monte Carlo simulations as the absolute (or relative) deviation between the generated and reconstructed values of a certain kinematic quantity. For this purpose the PYTHIA Monte Carlo simulation with radiative corrections is used. The width of a fit with a Gaussian shape to the absolute deviation gives the estimate of the resolution of that quantity.

The left panels of Figure 5.14 represent the absolute resolution δ in Q^2, x_B and $-t'$. A relative resolution of about 2.5% is obtained for Q^2 which is reconstructed through the scattered lepton momentum and the scattering angle. The resolution in x_B, determined from Q^2 and E', is correlated to their resolutions and is about of 6 %. The four-momentum transfer $-t'$ is computed from the lepton kinematics and the reconstructed ρ^0 kinematics. Thus the relative resolution of $-t'$ of about 20 % is worse than the ones for Q^2 and x_B.

Since the resolution varies with Q^2, x_B and $-t'$, it is investigated in equidistant bins for $0.5 < Q^2 < 7$ GeV^2, $x < 0.25$ and $-t' < 0.4$ GeV^2. The right panels of Figure 5.14 show the absolute resolution in each Q^2, x_B and $-t'$ bins. The binning used for the following analysis (see Section 7.2) is suggested by the resolution estimates obtained here.

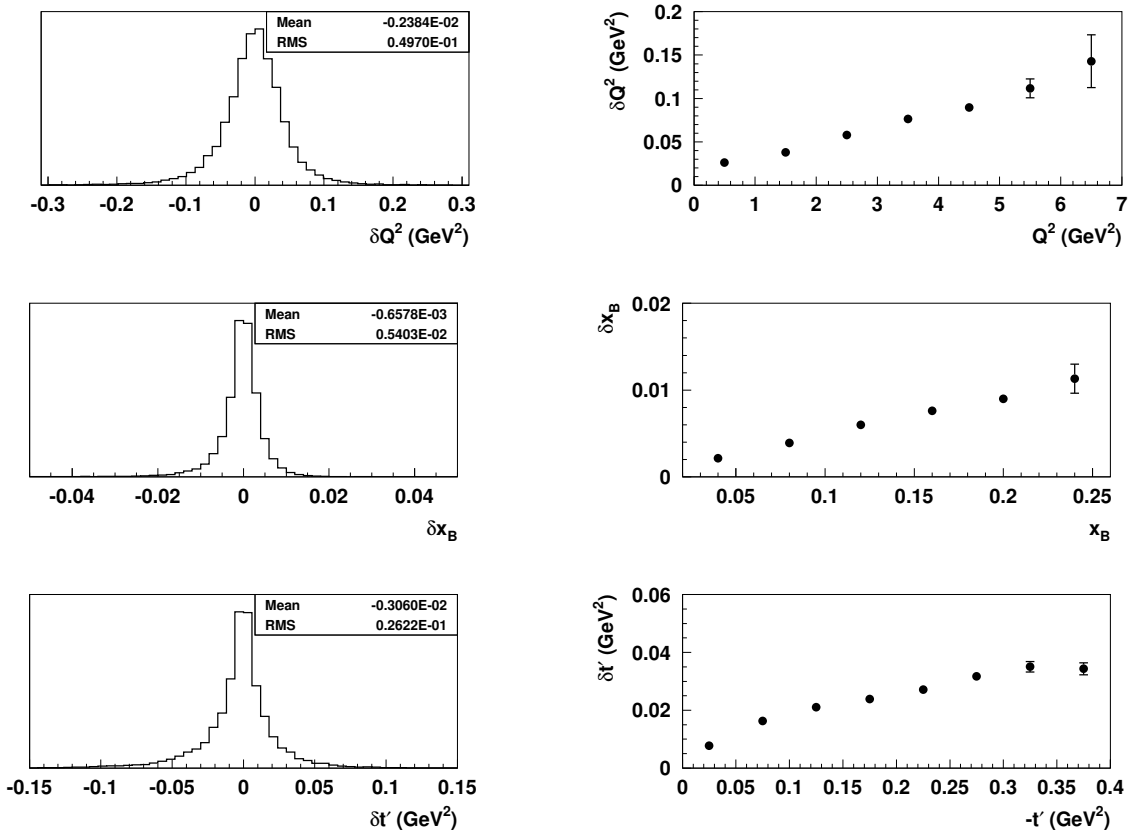

Figure 5.14: The spectrometer resolution in Q^2, x_B and $-t'$. The upper plots represent the average resolution while the lower plots show the resolution in various bins of a certain kinematic quantity.

5.5 Summary

Summarizing the discussion about the two available Monte Carlo generators, the ρ^0 leptoproduction cross section is well reproduced by PYTHIA, which uses the Donnachie-Landshoff parameterization of the photoproduction cross section and is able to account for radiative corrections. A considerable underestimation of the cross section is observed for the Monte Carlo simulation by rhoMC that uses the parameterization of the world data for the photoproduction cross section. Radiative corrections are not implemented in the rhoMC generation chain yet. Compared to PYTHIA, the angular distribution and the decay pion properties are better reproduced by rhoMC which simulates the whole angular distribution of the ρ^0 and decay pions.

So far only an unpolarized target has been considered. The first attempts of enhancement of rhoMC for transversely polarized target is discussed in Section 8.1.3.

Chapter 6

Transverse target-spin asymmetry and transverse SDMEs

"The nice thing about standards is that there are so many of them to choose from."
— Andrew S. Tanenbaum

In the analysis by Diehl-Sapeta [33], the polarized lepton-proton cross section is derived in terms of various virtual-photon-proton cross sections and interference terms. In the specific case of exclusive ρ^0 production, at leading-twist some of these terms are related to the GPDs $E^{q,g}$ and $H^{q,g}$. While extracting the asymmetry of longitudinally polarized ρ^0 mesons, the interference between various ρ^0 helicity states is not considered.

Alternatively, the transverse target-spin asymmetry of longitudinally polarized ρ^0 mesons can be extracted analyzing the full angular distribution which is parameterized in terms of SDMEs. It allows to take into account the interference between various ρ^0 helicity states in the measurement of the asymmetry. In Section 2.5.2, mainly an unpolarized target was considered, and the SDMEs were defined in the Schilling-Wolf formalism [48]. In this chapter, also a transversely polarized target is considered and the SDMEs are defined in the recently developed formalism by Diehl [17].

In this chapter the transverse target-spin asymmetry and the SDMEs in exclusive ρ^0 production on a transversely polarized target are discussed.

6.1 Motivation

It has already been mentioned in Chapter 1 that hard exclusive vector meson production is sensitive to the GPDs $H^{q,g}$ and $E^{q,g}$, which are related to the total angular momentum J^q and J^g of quarks and gluons in the nucleon, respectively (see Section 2.4.5). The GPD H is already constrained by the PDFs $q(x)$ and the Dirac form factor F_1 (see Section 2.4.4). The GPD E is still unknown since there is no corresponding relation to PDFs in the forward limit (see Section 2.4.4) and it is much harder accessible in exclusive processes.

In the case of a transversely polarized target, the interference between the form factors $\mathcal{H}$

and $\mathcal{E}$ gives rise to a transverse target-spin asymmetry in exclusive ρ^0 production [16],

$$A_{UT}^{\gamma^*}(\phi,\phi_s) = \frac{1/M_N \ \sqrt{t_0 - t} \ \sqrt{1-\xi^2} \ \mathrm{Im}\big(\mathcal{E}^*\mathcal{H}\big)}{(1-\xi^2)\,|\mathcal{H}|^2 - \big(\xi^2 + t/(4M_N^2)\big)\,|\mathcal{E}|^2 - 2\xi^2\,\mathrm{Re}\big(\mathcal{E}^*\mathcal{H}\big)} \,. \tag{6.1}$$

Here, the form factor $\mathcal{F} = \mathcal{H}, \mathcal{E}$ is the convolution integral over the distribution amplitude $\phi_\rho(z)$ and the GPDs H or E [33],

$$\begin{aligned}\mathcal{F} \;=\; & \frac{4\pi\alpha_s}{9}\,\frac{f_\rho}{\sqrt{2}}\int_0^1 dz\,\frac{\phi_\rho(z)}{z(1-z)}\int_{-1}^1 dx\left[\frac{1}{\xi - x - i\varepsilon} - \frac{1}{\xi + x - i\varepsilon}\right] \\ & \times\left(e_u F^u(x,\xi,t) - e_d F^d(x,\xi,t) + e_g F^g(x,\xi,t)/x\right),\end{aligned} \tag{6.2}$$

where $e_u = 2/3$, $e_d = -1/3$ and $e_g = 3/8$ for u-, d-quarks and gluons, respectively. The meson decay constant f_ρ is equal to $f_\rho \approx 209$ MeV (see Section 2.4.1) and the light-cone distribution amplitude $\phi_\rho(z)$ is normalized in a way that $\int_0^1 dz\,\phi(z) = 1$. In equation (6.2), the form factors $\mathcal{H}$ and $\mathcal{E}$ are decomposed into quark and gluon contributions. There is no kinematic suppression of gluon GPDs, since gluons and quarks contribute to exclusive ρ^0 meson production at the same order of α_s (see Figure 6.1). From the behavior of the usual quark and gluon densities, ρ^0 production is expected to be dominated by gluons at smaller x_B and by quarks at larger x_B. At the intermediate energies of HERMES, both contributions were shown [96] to be comparable, thus providing information about gluon GPDs as well.

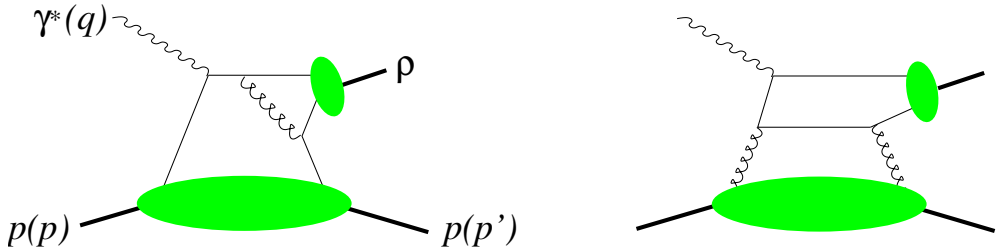

Figure 6.1: Diagrams for hard ρ^0 meson production with quark and gluon GPDs [96].

In addition, the transverse target-spin asymmetry in exclusive ρ^0 production has the advantage to be one of the rare observables[1] where the asymmetry depends linearly on the helicity-flip GPDs $E^{q,g}$ [16, 33] with no kinematic suppression of their contributions with respect to the GPDs $H^{q,g}$.

The concept of GPDs applies to hard exclusive ρ^0 production in the limit of large Q^2 and small t [14], if the longitudinally polarized ρ^0_L meson is induced by a longitudinal virtual photon γ^*_L (see Section 2.4.1). The factorization theorem [14] also suggests the transition from

[1] Other observable that was shown to be sensitive to the GPD E is the asymmetry with respect to transverse target polarization in DVCS.

longitudinal virtual photon to longitudinal ρ^0 ($\gamma_L^* \to \rho_L^0$) to dominate, with the helicity-flip transitions being suppressed at least by $1/Q$ [33]. Theoretical calculations in the context of GPD models are available mainly for the transition $\gamma_L^* \to \rho_L^0$.

The measured values of the ratio $R = \sigma_L/\sigma_T$ of longitudinal and transverse cross sections (see Figure 5.7) is not large at Q^2 values of a few GeV^2, typical for the HERMES kinematics. This implies that the kinematic suppression by $1/Q^2$ of the transverse photon amplitudes, predicted by the factorization theorem, is not yet very effective in these kinematics. Therefore in this kinematic domain the contribution from longitudinally polarized ρ^0 mesons induced by longitudinal virtual photons has to be separated from the experimental results.

6.2 Definition of the transverse target polarization

Experimentally, the target polarization P_T is defined with respect to the lepton beam direction, while theoretically it is more natural to define the target polarization S_T with respect to the direction of the virtual photon. In order to relate the experimentally and theoretically defined cross sections and cross section asymmetries, two coordinate systems are introduced in the target rest frame (left panel of Figure 6.2).

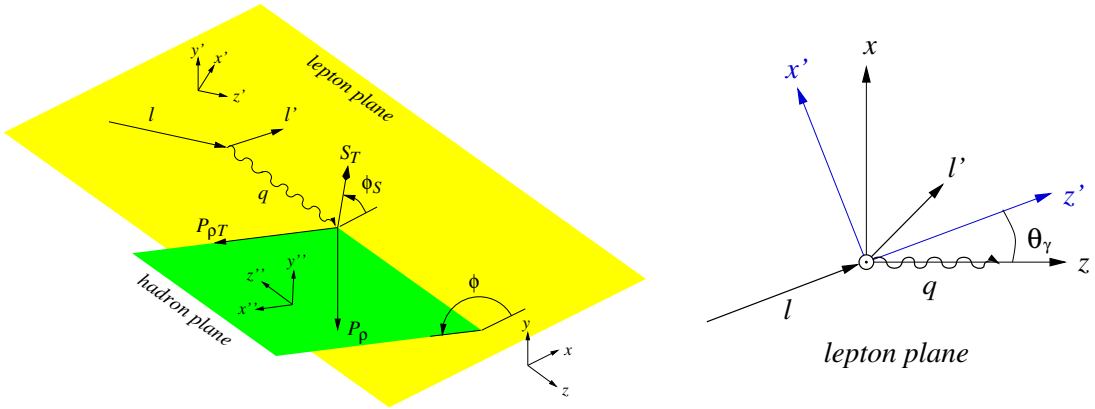

Figure 6.2: Left: kinematics of $ep \to ep\rho^0$ in the target rest frame. Right: the two coordinate systems of the lepton plane. The y and y' axes point out of the paper plane [33].

The first one is $C'(x', y', z')$, which corresponds to the coordinate system of the experimental setup (see Section 3.3), in which z' points along the incoming lepton beam direction l. The second one is $C(x, y, z)$, in which z points along the virtual-photon direction q. Both systems are chosen in a way that the scattered lepton l' lies in the xz or $x'z'$ plane and has a positive x or x' component. The y and y' axes are then fixed, they point out of the paper plane. The relation between the two coordinate systems is a rotation around the y axis by the angle θ_γ which is the angle between the directions of the incoming lepton beam l and the virtual photon

q (right panel of Figure 6.2):

$$\sin\theta_\gamma = \gamma\sqrt{\frac{1-y-\frac{1}{4}y^2\gamma^2}{1+\gamma^2}}\,, \qquad \text{with} \quad \gamma = 2x_B M_p/Q\,. \tag{6.3}$$

The target spin vector $\boldsymbol{S}$ is parameterized in the two coordinate systems as:

$$\boldsymbol{S} \overset{C}{=} \begin{pmatrix} S_T\cos\phi_S \\ S_T\sin\phi_S \\ -S_L \end{pmatrix}\,, \qquad \boldsymbol{S} \overset{C'}{=} \begin{pmatrix} P_T\cos\psi \\ P_T\sin\psi \\ -P_L \end{pmatrix}\,, \tag{6.4}$$

where S_L and S_T, or P_L and P_T, specify the magnitudes of the longitudinal and transverse target polarizations with respect to the virtual photon or lepton beam directions, respectively. The longitudinal target polarizations S_L and P_L vary between -1 and 1, while the transverse target polarizations S_T and P_T vary between 0 and 1. The angles ϕ_s and ψ are the azimuthal angles of the target spin vector around the virtual photon and lepton beam directions, respectively. The relation between the angles ϕ_s and ψ is given as:

$$\sin\psi = \frac{\cos\theta_\gamma\,\sin\phi_S}{\sqrt{1-\sin^2\theta_\gamma\,\sin^2\phi_S}}\,, \qquad \cos\psi = \frac{\cos\phi_S}{\sqrt{1-\sin^2\theta_\gamma\,\sin^2\phi_S}}\,. \tag{6.5}$$

Only the case of longitudinal target polarization was considered in the previous sections. In this case the target polarization vectors P_L and S_L are not very much different in the two coordinate systems, since

$$S_L = \cos\theta_\gamma P_L \tag{6.6}$$

and the angle θ_γ is small, resulting in $S_L \approx P_L$.

In the case when a target is polarized transversely with respect to the lepton beam direction, the target polarization vectors S_T and P_T are related to each other as [33]:

$$S_T = \frac{\cos\theta_\gamma}{\sqrt{1-\sin^2\theta_\gamma\,\sin^2\phi_S}}\,P_T\,, \qquad S_L = \frac{\sin\theta_\gamma\,\cos\phi_S}{\sqrt{1-\sin^2\theta_\gamma\,\sin^2\phi_S}}\,P_T\,. \tag{6.7}$$

The third coordinate system $C''(x'',\,y'',\,z'')$, also shown in Figure 6.2, is used to describe the $\gamma^* p$ center-of-mass system. The z'' axis points along the opposite direction of $\boldsymbol{q}$, the x'' axis is chosen in a way that $\boldsymbol{P}_\rho$ lies in the $x''z''$ plane and has a positive x'' component. In this case the target spin vector is parameterized as

$$\boldsymbol{S} \overset{C''}{=} \begin{pmatrix} S_T\cos(\phi-\phi_S) \\ S_T\sin(\phi-\phi_S) \\ S_L\,. \end{pmatrix} \tag{6.8}$$

6.3 Definition of ρ^0 production and decay angles

The definitions of the ρ^0 production and decay angles are the conventional ones. The definitions of Φ, ϕ and θ established in the analysis of Schilling-Wolf [48, 95] and so far used in the previous sections (see equation (5.10)), are presented in Section 5.2.6.

In a recent analysis by Diehl [17], the azimuthal angle ϕ (see Figure 6.2) of the produced ρ^0 meson is defined according to [97] :

$$\sin\phi = \frac{(\hat{\mathbf{q}}\times\mathbf{l})\times(\hat{\mathbf{q}}\times\mathbf{v})}{|\hat{\mathbf{q}}\times\mathbf{l}|\cdot|\hat{\mathbf{q}}\times\mathbf{v}|}\,, \qquad \cos\phi = \frac{(\mathbf{l}\times\mathbf{v})\cdot\hat{\mathbf{q}}}{|\hat{\mathbf{q}}\times\mathbf{l}|\cdot|\hat{\mathbf{q}}\times\mathbf{v}|}\,. \tag{6.9}$$

The ρ^0 meson decay angles φ and ϑ are defined in the ρ^0 rest frame similar to [48, 95]. The relation between the two conventions is

$$\phi\,[17] = -\Phi\,[48]\,, \qquad \varphi\,[17] = \phi\,[48]\,, \qquad \vartheta\,[17] = \theta\,[48]\,. \tag{6.10}$$

In the following the angles ϕ, φ and ϑ are used.

6.4 Cross section for ρ^0 production on a polarized target

The complete expression for the polarized lepton-proton cross section is given in [33] (Diehl-Sapeta formalism). There the cross section is presented as a superposition of unpolarized and polarized cross sections with various polarization states of target and beam:

$$\sigma = \sigma_{UU} + P_L\sigma_{LU} + S_L\sigma_{UL} + P_LS_L\sigma_{LL} + S_T\sigma_{UT} + P_LS_T\sigma_{LT}\,. \tag{6.11}$$

Here, the same notations hold as in equation (2.65). The individual contributions to the total cross section are written in terms of photoabsorption cross sections or interference terms σ^{ij}_{mn}, where the subscripts $m, n = 0, \pm 1$ stand for the polarization states of the photon and the superscripts $i, j = \pm 1/2$ for those of the proton.

For an unpolarized lepton beam and a transversely polarized nucleon target the cross section reduces to a superposition of unpolarized and transversely polarized cross sections:

$$\begin{aligned}
&\left[\frac{\alpha_{\rm em}}{8\pi^3}\,\frac{y^2}{1-\varepsilon}\,\frac{1-x_B}{x_B}\,\frac{1}{Q^2}\right]^{-1}\frac{d\sigma}{dx_B\,dQ^2\,d\phi\,d\psi} \qquad (6.12)\\
&= \frac{1}{2}\Big(\sigma^{++}_{++}+\sigma^{--}_{++}\Big) + \varepsilon\sigma^{++}_{00} - \varepsilon\cos(2\phi)\ \mathrm{Re}\,\sigma^{++}_{+-} - \sqrt{\varepsilon(1+\varepsilon)}\,\cos\phi\ \mathrm{Re}(\sigma^{++}_{+0}+\sigma^{--}_{+0})\\
&\quad - S_T\left[\sin(\phi-\phi_S)\ \mathrm{Im}(\sigma^{+-}_{++}+\varepsilon\sigma^{+-}_{00}) + \frac{\varepsilon}{2}\sin(\phi+\phi_S)\ \mathrm{Im}\,\sigma^{+-}_{+-} + \frac{\varepsilon}{2}\sin(3\phi-\phi_S)\ \mathrm{Im}\,\sigma^{-+}_{+-}\right.\\
&\qquad\left. + \sqrt{\varepsilon(1+\varepsilon)}\,\sin\phi_S\ \mathrm{Im}\,\sigma^{+-}_{+0} + \sqrt{\varepsilon(1+\varepsilon)}\,\sin(2\phi-\phi_S)\ \mathrm{Im}\,\sigma^{-+}_{+0}\right],
\end{aligned}$$

where the target polarization S_T is defined relative to the virtual-photon direction. In the unpolarized part of the cross section the angle-independent terms are the longitudinal and transverse components of the cross section:

$$\sigma_T = \frac{1}{2}\left(\sigma_{++}^{++} + \sigma_{++}^{--}\right), \qquad \sigma_L = \sigma_{00}^{++}. \tag{6.13}$$

If the target polarization is defined with respect to the lepton beam direction, the polarized cross section receives an additional contribution due to the longitudinal component of the target polarization S_L with respect to the virtual photon direction [33]:

$$\begin{aligned}
&\left[\frac{\cos\theta_\gamma}{1-\sin^2\theta_\gamma\,\sin^2\phi_S}\right]^{-1}\left[\frac{\alpha_{\rm em}}{8\pi^3}\,\frac{y^2}{1-\varepsilon}\,\frac{1-x_B}{x_B}\,\frac{1}{Q^2}\right]^{-1}\frac{d\sigma}{dx_B\,dQ^2\,d\phi\,d\phi_S}\,\Bigg|_{P_L=0}\\
&\quad=\frac{1}{2}\Big(\sigma_{++}^{++}+\sigma_{++}^{--}\Big)+\varepsilon\sigma_{00}^{++}-\varepsilon\cos(2\phi)\;\mathrm{Re}\,\sigma_{+-}^{++}-\sqrt{\varepsilon(1+\varepsilon)}\,\cos\phi\;\mathrm{Re}(\sigma_{+0}^{++}+\sigma_{+0}^{--})\\
&\quad-\frac{P_T}{\sqrt{1-\sin^2\theta_\gamma\,\sin^2\phi_S}}\Bigg[\sin\phi_S\;\cos\theta_\gamma\sqrt{\varepsilon(1+\varepsilon)}\;\mathrm{Im}\,\sigma_{+0}^{+-}\\
&\qquad+\sin(\phi-\phi_S)\Big(\cos\theta_\gamma\;\mathrm{Im}(\sigma_{++}^{+-}+\varepsilon\sigma_{00}^{+-})+\frac{1}{2}\sin\theta_\gamma\sqrt{\varepsilon(1+\varepsilon)}\;\mathrm{Im}(\sigma_{+0}^{++}-\sigma_{+0}^{--})\Big)\\
&\qquad+\sin(\phi+\phi_S)\Big(\cos\theta_\gamma\,\frac{\varepsilon}{2}\;\mathrm{Im}\,\sigma_{+-}^{+-}+\frac{1}{2}\sin\theta_\gamma\sqrt{\varepsilon(1+\varepsilon)}\;\mathrm{Im}(\sigma_{+0}^{++}-\sigma_{+0}^{--})\Big)\\
&\qquad+\sin(2\phi-\phi_S)\Big(\cos\theta_\gamma\sqrt{\varepsilon(1+\varepsilon)}\;\mathrm{Im}\,\sigma_{+0}^{-+}+\frac{1}{2}\sin\theta_\gamma\,\varepsilon\;\mathrm{Im}\,\sigma_{+-}^{++}\Big)\\
&\qquad+\sin(2\phi+\phi_S)\,\frac{1}{2}\sin\theta_\gamma\,\varepsilon\;\mathrm{Im}\,\sigma_{+-}^{++}+\sin(3\phi-\phi_S)\;\cos\theta_\gamma\,\frac{\varepsilon}{2}\;\mathrm{Im}\,\sigma_{+-}^{-+}\Bigg].
\end{aligned}\tag{6.14}$$

Here the additional term arising with $\sin(2\phi+2\phi_s)$ modulation originates from the longitudinal component S_L of the target polarization vector. The coefficients of the $\sin(\phi-\phi_s)$, $\sin(\phi+\phi_s)$ and $\sin(2\phi-2\phi_s)$ terms contain two contributions corresponding to the transverse and longitudinal components, S_T and S_L, disentangled by the $\cos\theta_\gamma$ and $\sin\theta_\gamma$ factors, respectively.

In the particular case of ρ^0 meson production, as a consequence of the factorization theorem, a hierarchy of the various photoabsorption cross sections and interference terms is obtained:

- The only leading-twist observables are the longitudinal cross section σ_{00}^{++} and the interference term σ_{00}^{+-}.
- Transverse-longitudinal interference terms σ_{+0}^{ij} are suppressed by at least one power of $1/Q$ compared with σ_{00}^{++}.
- Cross sections and interference terms σ_{++}^{ij} and σ_{+-}^{ij} with transverse photon polarization are suppressed by at least $1/Q^2$ compared with σ_{00}^{++}.

Thus at leading-twist the longitudinal cross sections σ_{00}^{++} and the interference term σ_{00}^{+-} can be written in terms of the GPDs $H^{q,g}$ and $E^{q,g}$ [33], appearing as nominator and denominator

in equation (6.1). These quantities that correspond to longitudinally polarization photons, do not contain information about the ρ^0 polarization states, since the ρ^0 production cross section (see equations (6.12) or (6.14)) is integrated over the decay angles ϑ and φ. The dependence on ϑ arises if the various ρ^0 polarization states have to be considered, and the φ dependence describes the interference between those polarization states. Thus in this formalism, the ρ^0 production cross section can be separated for longitudinally and transversely polarized ρ^0 meson contributions, introducing an explicit dependence on ϑ (see equation (6.29)), however, the interference between those polarization states is neglected.

6.5 Definition of the asymmetry

6.5.1 Definition of the asymmetry with respect to the virtual-photon direction

In accordance with the Trento convention [97], the transverse spin-asymmetry for an unpolarized beam and a transversely polarized proton target is defined as

$$\mathcal{A}_{UT}^{\gamma^*}(\phi,\phi_s) = \frac{1}{S_T}\frac{d\sigma(\phi,\phi_s) - d\sigma(\phi,\phi_s+\pi)}{d\sigma(\phi,\phi_s) + d\sigma(\phi,\phi_s+\pi)} \,, \tag{6.15}$$

with the target polarization S_T defined with respect to the virtual-photon direction. A definition of an asymmetry as in equation (6.15) results in the cancellation of the unpolarized cross section in the nominator and of the polarized cross section in the denominator:

$$\mathcal{A}_{UT}^{\gamma^*}(\phi,\phi_s) = \frac{\sigma_{UT}}{\sigma_{UU}} \,. \tag{6.16}$$

The 'theoretical' expression for the transverse target-spin asymmetry, according to the hierarchy predicted by factorization (see Section 6.4), can be obtained at leading-twist as

$$A_{UT}^{\gamma^*}(\phi,\phi_s) = \frac{\operatorname{Im}\sigma_{00}^{+-}}{\sigma_{00}^{++}}\ \sin(\phi-\phi_s) \,. \tag{6.17}$$

According to equation (6.17), where the denominator has no ϕ-dependence, the $\sin(\phi-\phi_s)$ azimuthal amplitude of the asymmetry is of theoretical interest (see equation (6.12)).

As it was discussed in Section 5.2, the cross section of exclusive ρ^0 production can be separated into angle-independent and angular dependent parts. In the case of a transversely polarized target the angular distribution integrated over the angles ϑ and φ reads,

$$W(\phi,\phi_s) = W_{UU}(\phi) + S_T W_{UT}(\phi,\phi_s) \,, \tag{6.18}$$

where there is an additional dependence on ϕ_s compared to the case of an unpolarized target.

The separation of the cross section into angle-independent and angular dependent parts results in a cancellation of the former in nominator and denominator of equation (6.16). Thus the asymmetry $\mathcal{A}_{UT}^{\gamma^*}(\phi, \phi_s)$ reduces from the cross section ratio to the ratio of the polarized and unpolarized angular distributions:

$$\mathcal{A}_{UT}^{\gamma^*}(\phi, \phi_s) = \frac{W_{UT}(\phi, \phi_s)}{W_{UU}(\phi)} \,. \tag{6.19}$$

This allows rewriting the angular distribution given by equation (6.18) in terms of this asymmetry:

$$W(\phi, \phi_s) = W_{UU}(\phi)\big(1 + S_T \mathcal{A}_{UT}^{\gamma^*}(\phi, \phi_s)\big) \,. \tag{6.20}$$

In equation (6.17) the denominator has no ϕ-dependence, hence the unpolarized angular distribution can be separated into ϕ-independent and ϕ-dependent terms, $\widehat{W}_{UU}$ and $\widehat{W}_{UU}(\phi)$, respectively. This allows us to modify equation (6.20) as

$$W(\phi, \phi_s) = \widehat{W}_{UU}\big(1 + A_{UU}(\phi) + S_T A_{UT}^{\gamma^*}(\phi, \phi_s)\big) \tag{6.21}$$

in such a way, that the unpolarized

$$A_{UU}(\phi) = \frac{\widehat{W}_{UU}(\phi)}{\widehat{W}_{UU}} \tag{6.22}$$

and the transverse

$$A_{UT}^{\gamma^*}(\phi, \phi_s) = \frac{W_{UT}(\phi, \phi_s)}{\widehat{W}_{UU}} \tag{6.23}$$

azimuthal asymmetries do not have a ϕ-dependence in the denominator anymore. Thus the above introduced asymmetries, $\mathcal{A}_{UT}^{\gamma^*}(\phi, \phi_s)$ and $A_{UT}^{\gamma^*}(\phi, \phi_s)$, are different by definition. In contrast to equation (6.23), the denominator in equation (6.19) is ϕ-dependent.

6.5.2 Definition of the asymmetry with respect to the lepton beam direction

In the experiment, the target polarization P_T is transverse with respect to the lepton beam direction, being parallel ($\uparrow$) or antiparallel ($\downarrow$) to the direction of the transverse magnet field. Then the experimental target-spin asymmetry with respect to the lepton beam direction is defined as the cross section asymmetry for two opposite spin states of the transversely polarized target,

$$\mathcal{A}_{UT}^{l}(\phi, \phi_s) = \frac{1}{P_T} \frac{d\sigma^{\uparrow}(\phi, \phi_s) - d\sigma^{\downarrow}(\phi, \phi_s)}{d\sigma^{\uparrow}(\phi, \phi_s) + d\sigma^{\downarrow}(\phi, \phi_s)} \,. \tag{6.24}$$

Theoretically, only one target polarization state is defined having values between 0 and 1. The angle ϕ_s is always calculated with respect to the positive spin direction of the target nucleon.

The negative polarization state is then equivalent to the rotation $\phi_s \to \phi_s + \pi$, so that:

$$\mathcal{A}^l_{UT}(\phi, \phi_s) = \frac{1}{P_T} \frac{d\sigma(\phi, \phi_s) - d\sigma(\phi, \phi_s + \pi)}{d\sigma(\phi, \phi_s) + d\sigma(\phi, \phi_s + \pi)} \,. \tag{6.25}$$

In the same way as in previous section, also in this case the cross section asymmetry reduces to the ratio of polarized and unpolarized angular distributions and the angular distribution can be redefined as

$$W(\phi, \phi_s) = \widehat{W}_{UU}\big(1 + A_{UU}(\phi) + P_T A^l_{UT}(\phi, \phi_s)\big) \,, \tag{6.26}$$

with

$$A^l_{UT}(\phi, \phi_s) = \frac{W_{UT}(\phi, \phi_s)}{\widehat{W}_{UU}}, \tag{6.27}$$

being the transverse azimuthal asymmetry defined with respect to the lepton beam direction.

The asymmetry $A^l_{UT}(\phi, \phi_s)$ (see equation (6.27)) defined with respect to the lepton beam direction, is the experimentally accessible one, while the asymmetry $A^{\gamma^*}_{UT}(\phi, \phi_s)$ (see equation (6.23)) defined with respect to the virtual-photon direction, is the one appearing in the theoretical calculations. The asymmetries $A^{\gamma^*}_{UT}(\phi, \phi_s)$ and $A^l_{UT}(\phi, \phi_s)$ differ by the additional contribution of the longitudinal component of the target polarization vector S_L with respect to the virtual-photon direction:

$$P_T A^l_{UT}(\phi, \phi_s) = S_T A^{\gamma^*}_{UT}(\phi, \phi_s) + S_L A^{\gamma^*}_{UL}(\phi) \,, \tag{6.28}$$

where $A^{\gamma^*}_{UL}(\phi)$ is the longitudinal asymmetry with respect to the virtual-photon direction [17].

6.6 First results on ρ^0 transverse target-spin asymmetry

The transverse target-spin asymmetry of ρ^0 mesons originating from longitudinal photons is of theoretical interest. Each ρ^0 helicity state results in a characteristic dependence of the $\gamma^* p$ cross-section on the polar angle ϑ [33]:

$$\frac{d\sigma^{ij}_{mn}(\gamma^* p \to \pi^+\pi^- p)}{d(\cos\vartheta)} = \frac{3\cos^2\vartheta}{2}\, \sigma^{ij}_{mn}(\gamma^* p \to \rho_L p) + \frac{3\sin^2\vartheta}{4}\, \sigma^{ij}_{mn}(\gamma^* p \to \rho_T p) \,. \tag{6.29}$$

The interference terms between different ρ^0 helicities are canceled as the cross section is integrated over the azimuthal decay angle φ. The angular distribution, including the dependence on the polar angle ϑ, can be written separately for longitudinal and transverse mesons, ρ^0_L and ρ^0_T:

$$\begin{aligned} W(\cos\vartheta, \phi, \phi_s) \quad \propto \quad & \Big[\frac{3}{2}\cos^2\vartheta\ \widehat{W}^{\rho_L}_{UU}\ \Big(1 + A^{\rho_L}_{UU}(\phi) + P_T A^{l,\rho_L}_{UT}(\phi, \phi_s)\Big) \\ + \quad & \frac{3}{4}\sin^2\vartheta\ \widehat{W}^{\rho_T}_{UU}\ \Big(1 + A^{\rho_T}_{UU}(\phi) + P_T A^{l,\rho_T}_{UT}(\phi, \phi_s)\Big)\Big] \,. \end{aligned} \tag{6.30}$$

The SDME r^{04}_{00} which represents the averaged longitudinal ρ_L contribution to the cross section, and $1-r^{04}_{00}$ the averaged transverse ρ_T contribution, is used to write the ϕ-independent angular distributions for longitudinal or transverse ρ^0 mesons:

$$\widehat{W}^{\rho_L}_{UU} \overset{[48]}{=} r^{04}_{00} \qquad\qquad \widehat{W}^{\rho_T}_{UU} \overset{[48]}{=} 1 - r^{04}_{00} \,. \tag{6.31}$$

Using equation (6.14), the unpolarized and transverse azimuthal asymmetries for longitudinal ρ^0 mesons, $A^{\rho_L}_{UU}(\phi)$ and $A^{l,\rho_L}_{UT}(\phi,\phi_s)$, are obtained as:

$$\begin{aligned}
A^{\rho_L}_{UU}(\phi) &= A^{\rho_L,\cos(\phi)}_{UU}\cos(\phi) + A^{\rho_L,\cos(2\phi)}_{UU}\cos(2\phi), \\
A^{l,\rho_L}_{UT}(\phi,\phi_s) &= A^{\rho_L,\sin(\phi_s)}_{UT}\sin(\phi_s) \;+\; A^{\rho_L,\sin(\phi-\phi_s)}_{UT}\sin(\phi-\phi_s) \;+ \\
&\quad A^{\rho_L,\sin(\phi+\phi_s)}_{UT}\sin(\phi+\phi_s) \;+\; A^{\rho_L,\sin(2\phi-\phi_s)}_{UT}\sin(2\phi-\phi_s) \;+ \\
&\quad A^{\rho_L,\sin(2\phi+\phi_s)}_{UT}\sin(2\phi+\phi_s) \;+\; A^{\rho_L,\sin(3\phi-\phi_s)}_{UT}\sin(3\phi-\phi_s) \,.
\end{aligned} \tag{6.32}$$

The unpolarized and transverse azimuthal asymmetries for transverse ρ^0 mesons, $A^{\rho_T}_{UU}(\phi)$ and $A^{l,\rho_T}_{UT}(\phi,\phi_s)$, are similar to those of equation (6.32), replacing the notation ρ_L by ρ_T. The unpolarized asymmetries for both transverse and longitudinal ρ^0 mesons, $A^{\rho_L}_{UU}(\phi)$ and $A^{\rho_T}_{UU}(\phi)$, are related to the already measured SDMEs:

$$A^{\rho_L,\cos(\phi)}_{UU} \overset{[48]}{=} \frac{\sqrt{2\epsilon(1+\epsilon)}\,r^5_{00}}{r^{04}_{00}} \,, \qquad A^{\rho_L,\cos(2\phi)}_{UU} \overset{[48]}{=} -\frac{\epsilon r^1_{00}}{r^{04}_{00}} \,,$$

$$A^{\rho_T\cos(\phi)}_{UU} \overset{[48]}{=} \frac{2\sqrt{2\epsilon(1+\epsilon)}\,r^5_{11}}{1-r^{04}_{00}} \,, \qquad A^{\rho_T,\cos(2\phi)}_{UU} \overset{[48]}{=} -\frac{2\epsilon r^1_{11}}{1-r^{04}_{00}} \,.$$

The only azimuthal amplitude of transverse target-spin asymmetry of ρ^0 mesons produced from longitudinal photons that is related to the GPDs H and E, is the $\sin(\phi-\phi_s)$ azimuthal amplitude $A^{\rho_L,\sin(\phi-\phi_s)}_{UT}$ (see discussion of equation (6.17)).

The first results of the transverse target-spin asymmetry in exclusive ρ^0 production, separated for ρ^0_L and ρ^0_T contributions, have been extracted [98, 99] using the above mentioned characteristic dependences of the $\gamma^* p$ cross-section on the polar angle ϑ. The results are presented in Figure 6.3. The panels show from left to right the integrated value and the Q^2, x_B and t' dependences of the asymmetry. For the x_B and t' dependences, Q^2 is required to be above 1 GeV^2, while the Q^2 dependence is shown also for $Q^2 < 1$ GeV^2. The upper panels represent the ρ^0 total asymmetries, while the middle and the lower panels represent the separated longitudinal and transverse ρ^0 asymmetries, respectively. The error bars represent the statistical uncertainties only, while the bands indicate the systematic uncertainties due to the target polarization, the background subtraction procedure, the uncertainty resulting from the measurement of the unpolarized SDMEs as well as the influence of the beam polarization on the final result.

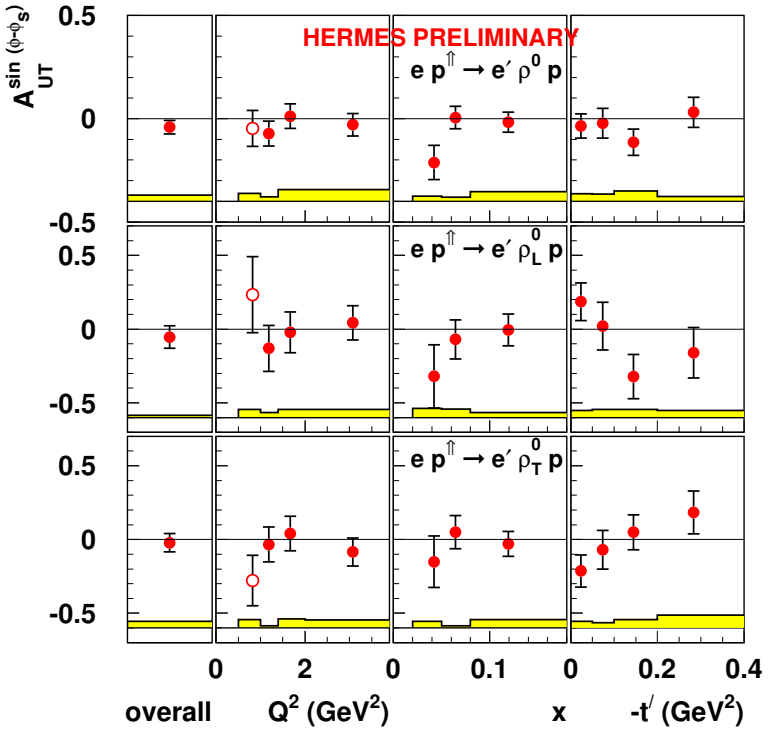

Figure 6.3: The azimuthal amplitude $A_{UT}^{\sin(\phi-\phi_s)}$ of the transverse target-spin asymmetry in exclusive ρ^0, ρ^0_L and ρ^0_T meson productions at average kinematics and as a function of Q^2, x_B, or t'[99].

6.7 The angular distributions

At the time when the first results on ρ^0 transverse target-spin asymmetry were obtained, it was unclear what the influence is of the interference terms between different ρ^0 helicity states on the final result. The separation of the longitudinal and transverse ρ^0 contributions taking into account the interference amplitudes became possible using the full expression of the ρ^0 angular distributions on a transversely polarized target. From the recent analysis by Diehl [17], there is a new concept of representation both the polarized and unpolarized angular distributions via SDMEs.

6.7.1 The SDMEs in the new formalism by Diehl

In the notation of Diehl [17], the matrix

$$\rho^{\nu\nu'}_{\mu\mu',\lambda\lambda'} = (N_T + \epsilon N_L)^{-1} \sum_{\sigma} T^{\nu\sigma}_{\mu\lambda} \left(T^{\nu'\sigma}_{\mu'\lambda'}\right)^* \tag{6.33}$$

is defined using the helicity amplitudes $T^{\nu\sigma}_{\mu\lambda}$ that are introduced to describe the subprocess $\gamma^*(\mu) + p(\lambda) \to \rho(\nu) + p'(\sigma)$ with certain helicity states of initial (μ and λ) and final (ν and σ) state particles. According to this notation, the upper indices of $\rho^{\nu\nu'}_{\mu\mu',\lambda\lambda'}$ represent the polariza-

tion of the vector meson, while the lower indices specify the polarizations of the virtual photon and target proton. The normalization factors

$$N_T = \tfrac{1}{2}\sum_{\lambda,\nu,\sigma}\left|T^{\nu\sigma}_{+\lambda}\right|^2 , \qquad N_L = \tfrac{1}{2}\sum_{\lambda,\nu,\sigma}\left|T^{\nu\sigma}_{0\lambda}\right|^2 \tag{6.34}$$

are proportional to the differential transverse and longitudinal cross sections, $d\sigma_T/dt$ and $d\sigma_L/dt$, respectively .

If the polarization of the target is considered, then in the $\gamma^* p$ center-of-mass system the polarization state of the proton is represented by a proton spin density matrix,

$$\tau_{\lambda\lambda'} = \frac{1}{2}\begin{pmatrix} 1+S_L & S_T\, e^{-i(\phi-\phi_S)} \\ S_T\, e^{i(\phi-\phi_S)} & 1-S_L \end{pmatrix} . \tag{6.35}$$

When the two matrices, $\rho^{\nu\nu'}_{\mu\mu',\lambda\lambda'}$ and $\tau_{\lambda\lambda'}$, are contracted,

$$\sum_{\lambda,\lambda'}\tau_{\lambda\lambda'}\,\rho^{\nu\nu'}_{\mu\mu',\lambda\lambda'} = u^{\nu\nu'}_{\mu\mu'} + S_L\, l^{\nu\nu'}_{\mu\mu'} + S_T\cos(\phi-\phi_S)\, s^{\nu\nu'}_{\mu\mu'} - S_T\sin(\phi-\phi_S)\, i\, n^{\nu\nu'}_{\mu\mu'} . \tag{6.36}$$

the result is expressed in terms of SDMEs for unpolarized (u), longitudinally (l) and transversely (n and s) polarized targets. The SDMEs s ('sideways') and n ('normal') correspond to the transverse target polarization in the hadron plane and perpendicular to it. The matrices u, l and s are hermitian, while n is antihermitian:

$$u^{\nu'\nu}_{\mu'\mu} = \left(u^{\nu\nu'}_{\mu\mu'}\right)^* , \qquad l^{\nu'\nu}_{\mu'\mu} = \left(l^{\nu\nu'}_{\mu\mu'}\right)^* ,$$
$$s^{\nu'\nu}_{\mu'\mu} = \left(s^{\nu\nu'}_{\mu\mu'}\right)^* , \qquad n^{\nu'\nu}_{\mu'\mu} = -\left(n^{\nu\nu'}_{\mu\mu'}\right)^* .$$

The diagonal elements $u^{\nu\nu}_{\mu\mu}$, $l^{\nu\nu}_{\mu\mu}$ and $s^{\nu\nu}_{\mu\mu}$ are purely real, while $n^{\nu\nu}_{\mu\mu}$ is purely imaginary.

6.7.2 The angular distribution in case of an unpolarized proton target

If both lepton beam and proton target are unpolarized, the angular distribution W_{UU} is decomposed into three terms:

$$W_{UU}(\phi,\varphi,\vartheta) = \frac{3}{4\pi}\left[\cos^2\vartheta\; W^{LL}_{UU}(\phi) + \sqrt{2}\cos\vartheta\,\sin\vartheta\; W^{LT}_{UU}(\phi,\varphi) + \sin^2\vartheta\; W^{TT}_{UU}(\phi,\varphi)\right] , \tag{6.37}$$

where W^{LL}_{UU}, W^{TT}_{UU} and W^{LT}_{UU} are the angular distributions for longitudinal and transverse ρ^0 meson production and of the interference between longitudinal and transverse ρ^0 polarization states, respectively. The longitudinal and transverse ρ^0 mesons are characterized by a $\cos^2$-like and $\sin^2$-like distributions, while the interference between them is characterized by a $\sqrt{2}\cos\vartheta\,\sin\vartheta$ behavior.

The individual angular distributions in equation (6.37) are parameterized by the SDMEs $u^{\nu'\nu}_{\mu'\mu}$ described above, further referred to as 'unpolarized SDMEs':

$$
\begin{aligned}
W^{LL}_{UU}(\phi) &= \left(u^{00}_{++} + \epsilon u^{00}_{00}\right) - 2\cos\phi\,\sqrt{\epsilon(1+\epsilon)}\,\mathrm{Re}\,u^{00}_{0+} - \cos(2\phi)\,\epsilon u^{00}_{-+}\,,\\
W^{LT}_{UU}(\phi,\varphi) &= \cos(\phi+\varphi)\,\sqrt{\epsilon(1+\epsilon)}\,\mathrm{Re}\left(u^{0+}_{0+} - u^{-0}_{0+}\right)\\
&\quad - \cos\varphi\;\mathrm{Re}\left(u^{0+}_{++} - u^{-0}_{++} + 2\epsilon u^{0+}_{00}\right) + \cos(2\phi+\varphi)\,\epsilon\,\mathrm{Re}\,u^{0+}_{-+}\\
&\quad - \cos(\phi-\varphi)\,\sqrt{\epsilon(1+\epsilon)}\,\mathrm{Re}\left(u^{0-}_{0+} - u^{+0}_{0+}\right) + \cos(2\phi-\varphi)\,\epsilon\,\mathrm{Re}\,u^{+0}_{-+}\,,\\
W^{TT}_{UU}(\phi,\varphi) &= \tfrac{1}{2}\left(u^{++}_{++} + u^{--}_{++} + 2\epsilon u^{++}_{00}\right) + \tfrac{1}{2}\cos(2\phi+2\varphi)\,\epsilon u^{-+}_{-+}\\
&\quad - \cos\phi\,\sqrt{\epsilon(1+\epsilon)}\,\mathrm{Re}\left(u^{++}_{0+} + u^{--}_{0+}\right) + \cos(\phi+2\varphi)\,\sqrt{\epsilon(1+\epsilon)}\,\mathrm{Re}\,u^{-+}_{0+}\\
&\quad - \cos(2\varphi)\;\mathrm{Re}\left(u^{-+}_{++} + \epsilon u^{-+}_{00}\right) - \cos(2\phi)\,\epsilon\,\mathrm{Re}\,u^{++}_{-+}\\
&\quad + \cos(\phi-2\varphi)\,\sqrt{\epsilon(1+\epsilon)}\,\mathrm{Re}\,u^{+-}_{0+} + \tfrac{1}{2}\cos(2\phi-2\varphi)\,\epsilon u^{+-}_{-+}\,.
\end{aligned}
$$

The longitudinal angular distribution $W^{LL}_{UU}(\phi)$ has no dependence on φ, so that all the terms will survive the integration over it. The transverse angular distribution $W^{TT}_{UU}(\phi,\varphi)$ gets additional terms that depend on the angle φ. The interference angular distribution $W^{LT}_{UU}(\phi,\varphi)$ does not survive the integration over φ, as was discussed in Section 6.6.

There are two terms that are independent of the angles ϕ and φ, namely $u^{00}_{++} + \epsilon u^{00}_{00}$ and $u^{++}_{++} + u^{--}_{++} + 2\epsilon u^{++}_{00}$. These terms represent the production of longitudinal (u^{00}) or transverse (u^{++},u^{--}) ρ^0 mesons and are related as

$$
u^{++}_{++} + u^{--}_{++} + 2\epsilon u^{++}_{0\,0} = 1 - \left(u^{0\,0}_{++} + \epsilon u^{0\,0}_{0\,0}\right)\,. \tag{6.38}
$$

The representation of the angular distribution via SDMEs in the Diehl notation is equivalent to the one given by equation (2.68) in the notation of Schilling-Wolf. The corresponding relations between the SDMEs by Diehl, $u^{\nu'\nu}_{\mu'\mu}$, and Schilling-Wolf, $\rho^{\alpha}_{\lambda\lambda'}$, are given in Appendix E.1.

An important feature of the unpolarized SDMEs $u^{\nu\nu}_{\mu\mu}$ is their $t_0 - t$ behavior, when the scattering angle of the ρ^0 meson Θ in the $\gamma^* p$ center-of-mass system is small. As $\Theta \propto (t_0 - t)^{1/2}$, it follows:

$$
u^{\nu\nu'}_{\mu\mu'} \underset{t\,\to\,t_0}{\sim} (t_0 - t)^{p/2}\,. \tag{6.39}
$$

Here p is the value of the power that controls the $t \to t_0$ behavior of SDMEs, which assumes values above the minimum value p_{min} for each SDME:

$$
p \;\geq\; p_{\min} \;=\; \min_{\sigma,\lambda\,=\,\pm 1/2} \left\{ \left|\nu - \mu - \sigma + \lambda\right| + \left|\nu' - \mu' - \sigma + \lambda\right| \right\}\,, \tag{6.40}
$$

The values of p_{min} for each SDME are given in [17].

6.7.3 The angular distribution in case of a transversely polarized proton target

For an unpolarized lepton beam and a transversely polarized proton target, the angular distribution W_{UT} is decomposed analogously to equation (6.37):

$$W_{UT}(\phi_S,\phi,\varphi,\vartheta) = \frac{3}{4\pi}\Big[\cos^2\vartheta\; W_{UT}^{LL}(\phi_S,\phi) + \sqrt{2}\cos\vartheta\,\sin\vartheta\, W_{UT}^{LT}(\phi_S,\phi,\varphi) + \sin^2\vartheta\; W_{UT}^{TT}(\phi_S,\phi,\varphi)\Big]\,, \tag{6.41}$$

where all individual distributions depend additionally on ϕ_s. Since there exist two independent transverse polarizations relative to the hadron plane, $n_{\mu\mu}^{\nu\nu}$ and $s_{\mu\mu}^{\nu\nu}$, the angular dependence contains a larger number of independent terms. There are 16 terms with $\operatorname{Im} n$ and 14 terms with $\operatorname{Im} s$, further referred to as 'transverse SDMEs'.

$$\begin{aligned}
W_{UT}^{LL}(\phi_S,\phi) &= \sin(\phi-\phi_S)\Big[\operatorname{Im}\big(n_{++}^{00}+\epsilon n_{00}^{00}\big) \\
&\quad - 2\cos\phi\,\sqrt{\epsilon(1+\epsilon)}\,\operatorname{Im} n_{0+}^{00} - \cos(2\phi)\,\epsilon\,\operatorname{Im} n_{-+}^{00}\Big] \\
&\quad + \cos(\phi-\phi_S)\Big[-2\sin\phi\,\sqrt{\epsilon(1+\epsilon)}\,\operatorname{Im} s_{0+}^{00} - \sin(2\phi)\,\epsilon\,\operatorname{Im} s_{-+}^{00}\Big]\,, \\
W_{UT}^{LT}(\phi_S,\phi,\varphi) &= \sin(\phi-\phi_S)\Big[\cos(\phi+\varphi)\,\sqrt{\epsilon(1+\epsilon)}\,\operatorname{Im}\big(n_{0+}^{0+}-n_{0+}^{-0}\big) \\
&\quad - \cos\varphi\,\operatorname{Im}\big(n_{++}^{0+}-n_{++}^{-0}+2\epsilon n_{00}^{0+}\big) + \cos(2\phi+\varphi)\,\epsilon\,\operatorname{Im} n_{-+}^{0+} \\
&\quad - \cos(\phi-\varphi)\,\sqrt{\epsilon(1+\epsilon)}\,\operatorname{Im}\big(n_{0+}^{0-}-n_{0+}^{+0}\big) + \cos(2\phi-\varphi)\,\epsilon\,\operatorname{Im} n_{-+}^{+0}\Big] \\
&\quad + \cos(\phi-\phi_S)\Big[\sin(\phi+\varphi)\,\sqrt{\epsilon(1+\epsilon)}\,\operatorname{Im}\big(s_{0+}^{0+}-s_{0+}^{-0}\big) \\
&\quad - \sin\varphi\,\operatorname{Im}\big(s_{++}^{0+}-s_{++}^{-0}+2\epsilon s_{00}^{0+}\big) + \sin(2\phi+\varphi)\,\epsilon\,\operatorname{Im} s_{-+}^{0+} \\
&\quad - \sin(\phi-\varphi)\,\sqrt{\epsilon(1+\epsilon)}\,\operatorname{Im}\big(s_{0+}^{0-}-s_{0+}^{+0}\big) + \sin(2\phi-\varphi)\,\epsilon\,\operatorname{Im} s_{-+}^{+0}\Big]\,, \\
W_{UT}^{TT}(\phi_S,\phi,\varphi) &= \sin(\phi-\phi_S)\Big[\tfrac{1}{2}\operatorname{Im}\big(n_{++}^{++}+n_{++}^{--}+2\epsilon n_{00}^{++}\big) + \tfrac{1}{2}\cos(2\phi+2\varphi)\,\epsilon\,\operatorname{Im} n_{-+}^{-+} \\
&\quad - \cos\phi\,\sqrt{\epsilon(1+\epsilon)}\,\operatorname{Im}\big(n_{0+}^{++}+n_{0+}^{--}\big) + \cos(\phi+2\varphi)\,\sqrt{\epsilon(1+\epsilon)}\,\operatorname{Im} n_{0+}^{-+} \\
&\quad - \cos(2\varphi)\,\operatorname{Im}\big(n_{++}^{-+}+\epsilon n_{00}^{-+}\big) - \cos(2\phi)\,\epsilon\,\operatorname{Im} n_{-+}^{++} \\
&\quad + \cos(\phi-2\varphi)\,\sqrt{\epsilon(1+\epsilon)}\,\operatorname{Im} n_{0+}^{+-} + \tfrac{1}{2}\cos(2\phi-2\varphi)\,\epsilon\,\operatorname{Im} n_{-+}^{+-}\Big] \\
&\quad + \cos(\phi-\phi_S)\Big[\tfrac{1}{2}\sin(2\phi+2\varphi)\,\epsilon\,\operatorname{Im} s_{-+}^{-+} \\
&\quad - \sin\phi\,\sqrt{\epsilon(1+\epsilon)}\,\operatorname{Im}\big(s_{0+}^{++}+s_{0+}^{--}\big) + \sin(\phi+2\varphi)\,\sqrt{\epsilon(1+\epsilon)}\,\operatorname{Im} s_{0+}^{-+} \\
&\quad - \sin(2\varphi)\,\operatorname{Im}\big(s_{++}^{-+}+\epsilon s_{00}^{-+}\big) - \sin(2\phi)\,\epsilon\,\operatorname{Im} s_{-+}^{++}
\end{aligned}$$

$$+ \sin(\phi - 2\varphi)\,\sqrt{\epsilon(1+\epsilon)}\,\mathrm{Im}\,s^{+-}_{0+} + \tfrac{1}{2}\sin(2\phi - 2\varphi)\,\epsilon\,\mathrm{Im}\,s^{+-}_{-+}\Big] \tag{6.42}$$

Similar to the unpolarized case, the term $W^{LL}_{UT}(\phi_S, \phi)$ has no φ dependence. The corresponding terms from the angular distribution $W^{TT}_{UT}(\phi_S, \phi)$ after integration over the angle φ are identical to the ones given in equation (6.30) (see also equation (6.32)). Although, the representation of the cross section is different in both equations, they can be related to one another by simple trigonometric equations:

$$\begin{aligned}
2\cos(\phi - \phi_s)\sin\phi &= \sin(2\phi - \phi_s) + \sin\phi_s\ , \\
2\sin(\phi - \phi_s)\cos\phi &= \sin(2\phi - \phi_s) - \sin\phi_s\ , \\
2\cos(\phi - \phi_s)\sin(2\phi) &= \sin(3\phi - \phi_s) + \sin(\phi + \phi_s)\ , \\
2\sin(\phi - \phi_s)\cos(2\phi) &= \sin(3\phi - \phi_s) - \sin(\phi + \phi_s)\ .
\end{aligned} \tag{6.43}$$

Also in the case of a transversely polarized target there are two terms $\mathrm{Im}\big(n^{00}_{++} + \epsilon n^{00}_{00}\big)$ and $\mathrm{Im}\big(n^{++}_{++} + n^{--}_{++} + 2\epsilon n^{++}_{00}\big)$, which are independent of the angles ϕ and φ. But unlike the case of unpolarized SDMEs, they are not independent, so that there exists no relation similar to equation (6.38).

The prediction for the $t \to t_0$ behavior of the transverse SDMEs $n^{\nu\nu}_{\mu\mu}$ and $s^{\nu\nu}_{\mu\mu}$ at small scattering angles Θ is similar to that of the unpolarized case:

$$n^{\nu\nu'}_{\mu\mu'}\ , s^{\nu\nu'}_{\mu\mu'} \underset{t \to t_0}{\sim} (t_0 - t)^{q/2}\ , \tag{6.44}$$

where

$$q \;\geq\; q_{\min} \;=\; \min_{\sigma,\lambda\,=\,\pm 1/2} \Big\{ \big|\nu - \mu - \sigma + \lambda\big| + \big|\nu' - \mu' - \sigma - \lambda\big| \Big\}\ . \tag{6.45}$$

The minimum values q_{min} for each SDME are also given in [17].

If the target polarization is defined with respect to the lepton beam direction, the angular distribution receives also a contribution from the longitudinal component of the target polarization (see equation (E.1)). The equations of the angular distribution are much more complicated, representing combinations of SDMEs $l^{\nu\nu}_{\mu\mu}$, $n^{\nu\nu}_{\mu\mu}$ and $s^{\nu\nu}_{\mu\mu}$ (see Appendix E.2).

6.7.4 Main features of exclusive ρ^0 production

Two main ordering principles for SDMEs, SCHC and NPE, were described in the notation of Schilling-Wolf in Section 2.5.2. In this section the SCHC and NPE features are described in the notation of Diehl. First experimental results are presented and discussed in Section 7.4.

s-channel helicity conservation

The information whether the SDMEs correspond to s-channel helicity conserving or non-conserving amplitudes, is encoded in the notation of Diehl. If the SDME is a product of two helicity conserving amplitudes, then the left and right symbols of the lower and upper indices are the same, *e.g.* u^{00}_{00} or n^{0+}_{0+}. If one helicity flip is involved, right or left indices are different, *e.g.* n^{0+}_{-+}, and all indices are different for SDMEs describing the product of two helicity flip amplitudes, *e.g.* n^{0+}_{-0}.

For the unpolarized SDMEs u, both experimental results [52] and theory expectations indicate that SCHC is approximately valid. Theory expectations for the transverse SDMEs n and s are similar to those for the unpolarized SDMEs: the SDMEs involving the product of two helicity conserving amplitudes are larger than those describing the interference between helicity conserving and helicity-flip amplitudes, and the latter are larger than SDMEs involving the product of two helicity-flip amplitudes. But these expectations are not proved experimentally yet. Exceptions are possible, since two large amplitudes can have a small interference term because of their relative phase. The SCHC in the case of a transversely polarized target, involving additional SDMEs, is of special interest.

Natural parity exchange

A second ordering principle for SDMEs is the dominance of NPE which originates from the Regge theory (see Section 2.5.3), referring to the quantum numbers of the exchanged particles. This feature can be more generally be characterized by the symmetry properties of the NPE and UPE amplitudes, denotes as N and U, respectively:

$$\begin{aligned} N^{\nu\sigma}_{\mu\lambda} &= \frac{1}{2}\left[T^{\nu\sigma}_{\mu\lambda} + (-1)^{\nu-\mu}\, T^{-\nu\sigma}_{-\mu\lambda}\right] = \frac{1}{2}\left[T^{\nu\sigma}_{\mu\lambda} + (-1)^{\lambda-\sigma}\, T^{\nu-\sigma}_{\mu-\lambda}\right] , \\ U^{\nu\sigma}_{\mu\lambda} &= \frac{1}{2}\left[T^{\nu\sigma}_{\mu\lambda} - (-1)^{\nu-\mu}\, T^{-\nu\sigma}_{-\mu\lambda}\right] = \frac{1}{2}\left[T^{\nu\sigma}_{\mu\lambda} - (-1)^{\lambda-\sigma}\, T^{\nu-\sigma}_{\mu-\lambda}\right] , \end{aligned} \tag{6.46}$$

under the helicity reversal of the virtual photon and ρ^0 meson:

$$N^{-\nu\sigma}_{-\mu\lambda} = (-1)^{\nu-\mu}\, N^{\nu\sigma}_{\mu\lambda} , \qquad\qquad U^{-\nu\sigma}_{-\mu\lambda} = -(-1)^{\nu-\mu}\, U^{\nu\sigma}_{\mu\lambda} . \tag{6.47}$$

Thus for a proton helicity the relations $N^{\nu+}_{\mu+} = N^{\nu-}_{\mu-}$ and $N^{\nu+}_{\mu-} = -N^{\nu-}_{\mu+}$ hold for NPE, and $U^{\nu+}_{\mu+} = -U^{\nu-}_{\mu-}$ and $U^{\nu+}_{\mu-} = U^{\nu-}_{\mu+}$ for UPE. Therefore, in the description of exclusive ρ^0 production using GPDs, NPE amplitudes are related to the GPDs H and E, while UPE amplitudes are related to the GPDs $\widetilde{H}$ and $\widetilde{E}$ [100]. Since $U^{0\sigma}_{0\lambda} = 0$ (see equation (6.47)), unnatural parity exchange amplitudes are power suppressed at large Q^2 and the leading-twist factorization [14] only applies to the natural parity exchange amplitudes $N^{0\sigma}_{0\lambda}$.

The pomeron exchange in Regge phenomenology is related to the gluon exchange in the GPD formalism (see Figure 6.1) corresponding to NPE processes, and the reggeon exchange is

related to the quark exchange corresponding to both NPE and UPE processes.

In terms of NPE and UPE amplitudes the SDMEs are defined as:

$$
\begin{aligned}
u^{\nu\nu'}_{\mu\mu'} &= (N_T + \epsilon N_L)^{-1} \sum_{\sigma} \left[N^{\nu\sigma}_{\mu+} \left(N^{\nu'\sigma}_{\mu'+}\right)^* + U^{\nu\sigma}_{\mu+} \left(U^{\nu'\sigma}_{\mu'+}\right)^* \right] , \\
l^{\nu\nu'}_{\mu\mu'} &= (N_T + \epsilon N_L)^{-1} \sum_{\sigma} \left[N^{\nu\sigma}_{\mu+} \left(U^{\nu'\sigma}_{\mu'+}\right)^* + U^{\nu\sigma}_{\mu+} \left(N^{\nu'\sigma}_{\mu'+}\right)^* \right] , \\
s^{\nu\nu'}_{\mu\mu'} &= (N_T + \epsilon N_L)^{-1} \sum_{\sigma} \left[N^{\nu\sigma}_{\mu+} \left(U^{\nu'\sigma}_{\mu'-}\right)^* + U^{\nu\sigma}_{\mu+} \left(N^{\nu'\sigma}_{\mu'-}\right)^* \right] , \\
n^{\nu\nu'}_{\mu\mu'} &= (N_T + \epsilon N_L)^{-1} \sum_{\sigma} \left[N^{\nu\sigma}_{\mu+} \left(N^{\nu'\sigma}_{\mu'-}\right)^* + U^{\nu\sigma}_{\mu+} \left(U^{\nu'\sigma}_{\mu'-}\right)^* \right] .
\end{aligned} \tag{6.48}
$$

The SDMEs u and n are superpositions of two products each involving only NPE or UPE amplitudes, while l and s involve the interference between NPE and UPE amplitudes. Since the UPE amplitudes are expected to be smaller than the NPE amplitudes, also the SDMEs l and s are expected to be smaller compared to u and n with identical helicity indices. However, exceptions are possible since the products $N^{\nu\sigma}_{\mu+} \left(N^{\nu'\sigma}_{\mu'+}\right)^*$ or $N^{\nu\sigma}_{\mu-} \left(N^{\nu'\sigma}_{\mu'+}\right)^*$ may have a small real or imaginary part due to the relative phase between the two amplitudes.

6.8 Definition of the asymmetry in the Diehl formalism

In Section 6.5 the transverse target-spin asymmetry was defined as ratio of transversely polarized and unpolarized cross sections (see equation (6.16)). There, the cross section was integrated over the azimuthal decay angle φ. In this section the possibilities are discussed of an asymmetry measurement on a transversely polarized target using the full angular distribution. With the knowledge of the latter there are two possibilities for a transverse target-spin asymmetry extraction. The first relates the transverse target-spin asymmetry to the corresponding SDMEs, and the asymmetry measurement is based on the SDME measurement. The other possibility is the direct extraction of the asymmetries writing the angular distribution in terms of asymmetries (see Section 6.5).

6.8.1 Transverse target-spin asymmetry related to SDMEs

Since factorization is proved for longitudinal photons only, and the leading transitions are the ones where both the virtual photon and the produced ρ^0 are longitudinal, the only observables to which both criteria apply are the SDMEs $\operatorname{Im} n^{0\,0}_{0\,0}$ and $u^{0\,0}_{0\,0}$. The asymmetry, being the ratio of polarized and unpolarized angular distributions (see equation (6.23)), is defined at leading order in $1/Q$ as:

$$
A^{\gamma^*}_{UT}(\phi, \phi_s) = \frac{\operatorname{Im} n^{0\,0}_{0\,0}}{u^{0\,0}_{0\,0}} \sin(\phi - \phi_s) \, . \tag{6.49}
$$

Thus the transverse target-spin asymmetry can be obtained from the measured values of the SDMEs $\mathrm{Im}\, n^{0\,0}_{0\,0}$ and $u^{0\,0}_{0\,0}$. These SDMEs can be measured only in the combinations $u^{00}_{++} + \epsilon u^{00}_{00}$ and $\mathrm{Im}\big(n^{00}_{++} + \epsilon n^{00}_{00}\big)$, similar to the SDMEs $r^{04}_{\lambda\lambda'}$ in the Schilling-Wolf notation. The production of longitudinal ρ^0 mesons from longitudinal and transverse virtual photons is indistinguishable without a Rosenbluth separation (see Section 2.5). However, the terms u^{00}_{++} and n^{00}_{++} are expected to be suppressed compared to the terms u^{00}_{00} and $\mathrm{Im}\, n^{0\,0}_{0\,0}$, since they are a product of two helicity-flip amplitudes.

6.8.2 Extraction of transverse target-spin asymmetry using the angular distributions

Asymmetry defined with respect to the virtual-photon direction

Recalling equation (6.21)

$$W(\phi, \phi_s) = \widehat{W}_{UU}(1 + A_{UU}(\phi) + S_T A^{\gamma^*}_{UT}(\phi, \phi_s))\,,$$

in order to separate the ρ^0_L contribution, the additional dependences of the angular distribution on the angles ϑ and φ have to be taken into account:

$$\begin{aligned} W(\phi, \phi_s, \vartheta, \varphi) = \frac{3}{4\pi}\Bigg[& \cos^2\vartheta && \widehat{W}^{LL}_{UU} \left(1 + A^{LL}_{UU}(\phi) + S_T\, A^{\gamma^*,\,LL}_{UT}(\phi, \phi_s)\right) \\ & + \sqrt{2}\cos\vartheta\, \sin\vartheta && W^{LT}_{UU}(\phi, \varphi)\ (1 + S_T\, A^{\gamma^*,\,LT}_{UT}(\phi, \phi_s, \varphi)) \\ & + \sin^2\vartheta && \widehat{W}^{TT}_{UU} \left(1 + A^{TT}_{UU}(\phi) + S_T\, A^{\gamma^*,\,TT}_{UT}(\phi, \phi_s)\right) \Bigg] \end{aligned} \tag{6.50}$$

The dependence of the angular distribution on the angle φ originates from the interference between longitudinal and transverse contributions. In the case of a longitudinal or transverse ρ^0 meson, the ϕ-independent angular distribution $\widehat{W}_{UU}$ is given as:

$$\begin{aligned} \widehat{W}^{LL}_{UU} &\overset{[17]}{=} u^{00}_{++} + \epsilon u^{00}_{00} &&\overset{[48]}{=} r^{04}_{00} \\ \widehat{W}^{TT}_{UU} &\overset{[17]}{=} u^{++}_{++} + u^{--}_{++} + 2\epsilon u^{++}_{00} &&\overset{[48]}{=} 1 - r^{04}_{00}\,. \end{aligned} \tag{6.51}$$

As for the interference angular distribution $\widehat{W}^{LT}_{UU}$, there is no corresponding ϕ-independent term.

Since the unpolarized and polarized angular distributions for longitudinal ρ^0 mesons do not contain a dependence on the angle φ (see equation (**??**) and equation (6.42)), the number of various azimuthal amplitudes of asymmetries are the same compared to equation (6.32), though the azimuthal amplitudes themselves are different for polarized asymmetry:

$$A^{LL}_{UU}(\phi) = A^{LL,\,\cos\phi}_{UU} \cos\phi + A^{LL,\,\cos(2\phi)}_{UU} \cos(2\phi) \tag{6.52}$$

$$
\begin{aligned}
A_{UT}^{LL\,\gamma^*}(\phi,\phi_s) &= A_{UU}^{LL,\,\sin(\phi-\phi_s)}\sin(\phi-\phi_s) \\
&+ A_{UU}^{LL,\,\sin(\phi-\phi_s)\cos\phi}\sin(\phi-\phi_s)\cos\phi + A_{UU}^{LL,\,\sin(\phi-\phi_s)\cos(2\phi)}\sin(\phi-\phi_s)\cos(2\phi) \\
&+ A_{UU}^{LL,\,\cos(\phi-\phi_s)\sin\phi}\cos(\phi-\phi_s)\sin\phi + A_{UU}^{LL,\,\cos(\phi-\phi_s)\sin(2\phi)}\cos(\phi-\phi_s)\sin(2\phi)\ .
\end{aligned} \tag{6.53}
$$

The trigonometric modifications (see equation (6.43)) show the similarity of the equations. The unpolarized and polarized azimuthal asymmetries for transverse ρ^0 mesons contain more terms compared to equation (6.32), associated with additional φ-dependent terms. The $\sin(\phi-\phi_s)$ amplitude of the asymmetry $A_{UT}^{LL\,\gamma^*}(\phi,\phi_s)$ is of theoretical interest (see Section 6.5.1).

Asymmetry defined with respect to the lepton beam direction

Recalling equation (6.26),

$$
W(\phi,\phi_s) = \widehat{W}_{UU}\big(1 + A_{UU}(\phi) + P_T A_{UT}^{l}(\phi,\phi_s)\big)\ ,
$$

the angular distribution is written in terms of asymmetries. Here the unpolarized angular distribution $\widehat{W}_{UU}$ and the asymmetry $A_{UU}(\phi)$ are the same as in previous section, but the polarized azimuthal asymmetry $A_{UT}^{l}(\phi,\phi_s)$ is different from $A_{UT}^{\gamma^*}(\phi,\phi_s)$. The angular distribution, decomposed into longitudinal, transverse and interference contributions,

$$
\begin{aligned}
W(\phi,\phi_s,\vartheta,\varphi) = \frac{3}{4\pi}\Big[\quad & \cos^2\vartheta \quad & \widehat{W}_{UU}^{LL} \ \Big(1 + A_{UU}^{LL}(\phi) + P_T\, A_{UT}^{l,LL}(\phi,\phi_s)\Big) + \\
& \sqrt{2}\cos\vartheta\,\sin\vartheta \quad & W_{UU}^{LT}(\phi,\varphi)\ \Big(1 + P_T\, A_{UT}^{l,LT}(\phi,\phi_s,\varphi)\Big) + \\
& \sin^2\vartheta \quad & \widehat{W}_{UU}^{TT}\ \Big(1 + A_{UU}^{TT}(\phi) + P_T\, A_{UT}^{l,TT}(\phi,\phi_s)\Big) \quad \Big]\ ,
\end{aligned} \tag{6.54}
$$

receives additional contributions from the longitudinal component of the target polarization. For example, the longitudinal component of the asymmetry contains an additional term $A_{UU}^{LL,\,\sin(\phi_s+2\phi)}$ which is coming from only the longitudinal component S_L of the target polarization:

$$
\begin{aligned}
A_{UT}^{l,LL}(\phi,\phi_s) &= A_{UU}^{LL,\,\sin(\phi-\phi_s)}\sin(\phi-\phi_s) \\
&+ A_{UU}^{LL,\,\sin(\phi-\phi_s)\cos\phi}\sin(\phi-\phi_s)\cos\phi + A_{UU}^{LL,\,\sin(\phi-\phi_s)\cos(2\phi)}\sin(\phi-\phi_s)\cos(2\phi) \\
&+ A_{UU}^{LL,\,\cos(\phi-\phi_s)\sin\phi}\cos(\phi-\phi_s)\sin\phi + A_{UU}^{LL,\,\cos(\phi-\phi_s)\sin(2\phi)}\cos(\phi-\phi_s)\sin(2\phi) \\
&+ A_{UU}^{LL,\,\sin(\phi_s+2\phi)}\sin(\phi_s+2\phi)\ .
\end{aligned} \tag{6.55}
$$

There are five more additional terms for the asymmetries $A_{UT}^{LT,l}(\phi,\phi_s,\varphi)$ and $A_{UT}^{TT,l}(\phi,\phi_s)$ compared with $A_{UT}^{LT,\gamma^*}(\phi,\phi_s,\varphi)$ and A_{UT}^{TT,γ^*} given by equation (6.50). The $\sin(\phi-\phi_s)$ amplitude of the asymmetry $A_{UT}^{l,LL}(\phi,\phi_s)$ is the one experimentally accessible.

Chapter 7

Extraction of transverse target-spin asymmetry and transverse SDMEs

"Never express yourself more clearly than you are able to think."
— Niels Bohr (1885 - 1962)

Experimentally, the cross sections as well as the angular distributions are derived from the number of events or yield $dN^{\uparrow(\downarrow)}$, where the subscript $^{\uparrow(\downarrow)}$ stands for a positive (negative) transverse target polarization state. Neglecting radiative and smearing effects, the yield is related to the cross section by the acceptance ϵ of the spectrometer $dN^{\uparrow(\downarrow)} = \epsilon d\sigma^{\uparrow(\downarrow)}$. The acceptance is a multiplicative factor that does not depend on the transverse polarization state and thus should cancel in the asymmetry definition equation (6.24). However, if the asymmetries are calculated in bins of one kinematic quantity while integrated over the others, the effect of acceptance cancellation may not happen. In this case simpler asymmetry extraction methods like *moments* method or *fit* method [101] are biased. In addition, detailed studies show that for low statistics samples these methods are not applicable. Hence in this thesis the transverse SDMEs as well as the transverse target-spin asymmetry are extracted using the unbinned *maximum likelihood* (ML) method.

7.1 Maximum likelihood method

For a set of independent quantities x following a *probability density function* (p.d.f.) $f(x;\lambda)$, where λ ($\lambda_1, \lambda_2 ... \lambda_n$) is a set of parameters which values are unknown, the estimator for the mean of λ is obtained by the *maximum likelihood method* [49]. The maximum likelihood estimators are approximately unbiased and efficient. The parameter values are found as the point in parameter space where the *likelihood function*, the joint of N univariate probability densities,

$$L(\lambda) = \prod_{i}^{N} f_i(x_i;\lambda) \ , \tag{7.1}$$

is at its maximum, or equivalently, its negative logarithm

$$-\ln L(\lambda) = -\sum_{i}^{N} f_i(x_i;\lambda) \tag{7.2}$$

is at the minimum. Thus the maximum likelihood estimators $\widehat{\lambda}$, *i.e.* the parameters, are found solving the likelihood equations

$$\frac{\partial \ln L}{\partial \lambda_i} = 0, \qquad\qquad i = 1, ...n\ . \tag{7.3}$$

The p.d.f. is usually normalized to unity: $\int dx f(x;\lambda) = 1$. However, this is not always the case. In evaluating the likelihood function, it is important to include all normalization factors that depend on λ. Instead, any multiplicative λ-independent factor in the p.d.f. $f(x;\lambda)$ may be omitted, since the purpose of interest is the maximum of the likelihood function L.

The estimator for the inverse covariance matrix is given by the matrix of second derivatives:

$$(\widehat{V}^{-1})_{ij} = -\frac{\partial^2 \ln L}{\partial\lambda_i \partial\lambda_j}\bigg|_{\widehat{\lambda}}\ . \tag{7.4}$$

7.1.1 Implementation of the maximum likelihood method

In the case of an unpolarized beam and a transversely polarized target, the p.d.f.

$$dN^{\uparrow(\downarrow)} = \epsilon\big(\phi_s, \phi, \varphi, \vartheta\big)\ W^{\uparrow(\downarrow)}\big(\lambda;\ P^{\uparrow(\downarrow)}, \phi_s, \phi, \varphi, \vartheta\big) \tag{7.5}$$

is used to describe the yield of the exclusive ρ^0 sample[102], where $P^{\uparrow(\downarrow)}$ is the target polarization state. Conventionally in theory, the target polarization P_T is positive and varies between 0 and 1 (see Section 6.2), while experimentally the transverse target polarization is positive (negative) when it is oriented parallel along (opposite to) the direction of the transverse magnetic field. The existence of two experimental target polarization states reduces the systematic uncertainties due to a possible geometric asymmetry of the detector with respect to the direction of the target polarization. In the following, the superscript $^{\uparrow(\downarrow)}$ is omitted.

While maximizing the likelihood function

$$L(\lambda) = \prod_{i}^{N_\rho} \frac{\epsilon\big(\phi_{s_i}, \phi_i, \varphi_i, \vartheta_i\big) W\big(\lambda;\ P_i, \phi_{s_i}, \phi_i, \varphi_i, \vartheta_i\big)}{\mathcal{N}(\lambda)}\ . \tag{7.6}$$

the SDMEs or the various azimuthal amplitudes of the asymmetry that parameterize the angular distribution, are considered as free parameters $\lambda_1 ... \lambda_n$. In fitting the parameters λ, the acceptance efficiency in the numerator can be omitted since it does not depend on the fit parameters. However, it has to be taken into account in evaluating the normalization integral

$\mathcal{N}$ [102]:

$$\mathcal{N}(\lambda) = \int dP\, d\phi_s\, d\phi\, d\varphi\, d\vartheta\, \epsilon(\phi_s, \phi, \varphi, \vartheta)\, W(\lambda; P, \phi_s, \phi, \varphi, \vartheta) \tag{7.7}$$

The further implementation of the maximum likelihood method for each particular case is discussed in the following.

7.2 Exclusive ρ^0 sample on a transversely polarized target

Information on the whole available statistics from the 2002-2005 data taking period with a transversely polarized proton target is presented in Table 7.1. In total 9.3 million DIS events are analyzed. In Chapter 4, the selection of exclusive ρ^0 events is discussed in detail. The SDMEs and the transverse target-spin asymmetry are extracted for the full kinematic region of $1 < Q^2 < 7$ GeV, $0.02 < x_B < 0.35$ and $0.00 < -t' < 0.40$ GeV^2. The results are also presented in bins of Q^2, x_B or t', while integrating over the other two kinematic quantities. The bin limits and the mean kinematics are listed in Table 7.2.

year	production	beam	bursts	N_{DIS}	N_ρ
2002	02c0	e^+	177952	708817	549
2003	03c0	e^+	136174	427200	305
2004	04c1	e^+	433497	2764494	2000
2005	05c1	e^-	848155	5452045	4536

Table 7.1: Data sample on a transversely polarized target after requirements ensuring good data quality and exclusivity of the sample.

bin	$< Q^2 >$ (GeV^2)	$< x_B >$	$< -t' >$ (GeV^2)
$1.0 < Q^2 < 7.0$ GeV^2	1.95	0.08	0.13
$0.5 < Q^2 < 1.0$ GeV^2	0.82	0.03	0.12
$1.0 < Q^2 < 1.4$ GeV^2	1.19	0.06	0.13
$1.4 < Q^2 < 2.0$ GeV^2	1.67	0.08	0.13
$2.0 < Q^2 < 7.0$ GeV^2	3.08	0.12	0.14
$0.02 < x_B < 0.07$	1.33	0.05	0.13
$0.07 < x_B < 0.10$	1.83	0.08	0.13
$0.10 < x_B < 0.40$	3.14	0.14	0.14
$0.00 < -t' < 0.05$ GeV^2	1.89	0.08	0.02
$0.05 < -t' < 0.10$ GeV^2	1.97	0.08	0.07
$0.10 < -t' < 0.20$ GeV^2	1.97	0.09	0.15
$0.20 < -t' < 0.40$ GeV^2	2.00	0.09	0.28

Table 7.2: Kinematic bins and mean values for Q^2, t' and x_B bins.

The requirements used for the selection of exclusive ρ^0 events (see Table 4.4) do not fully exclude the background contributions from background processes. The exclusive sample receives contributions from double-diffractive processes, which should be negligible in the low ΔE region (see Section 4.3.2), and from non-resonant $\pi^+\pi^-$ pair production, which is of the order of $1-2\%$ (see Section 4.3.4). The results are not corrected for these contributions.

7.3 Background correction

The contribution of semi-inclusive processes, which is the main origin of the background contamination, is discussed and presented in Section 4.3.1 for the overall kinematics. Since the asymmetries, as well as the SDMEs are calculated in bins of Q^2, x_B or t' and also the semi-inclusive background contribution have a kinematic dependence, the background contamination is estimated in each bin of Q^2, x_B or t' (see Figure 7.1).

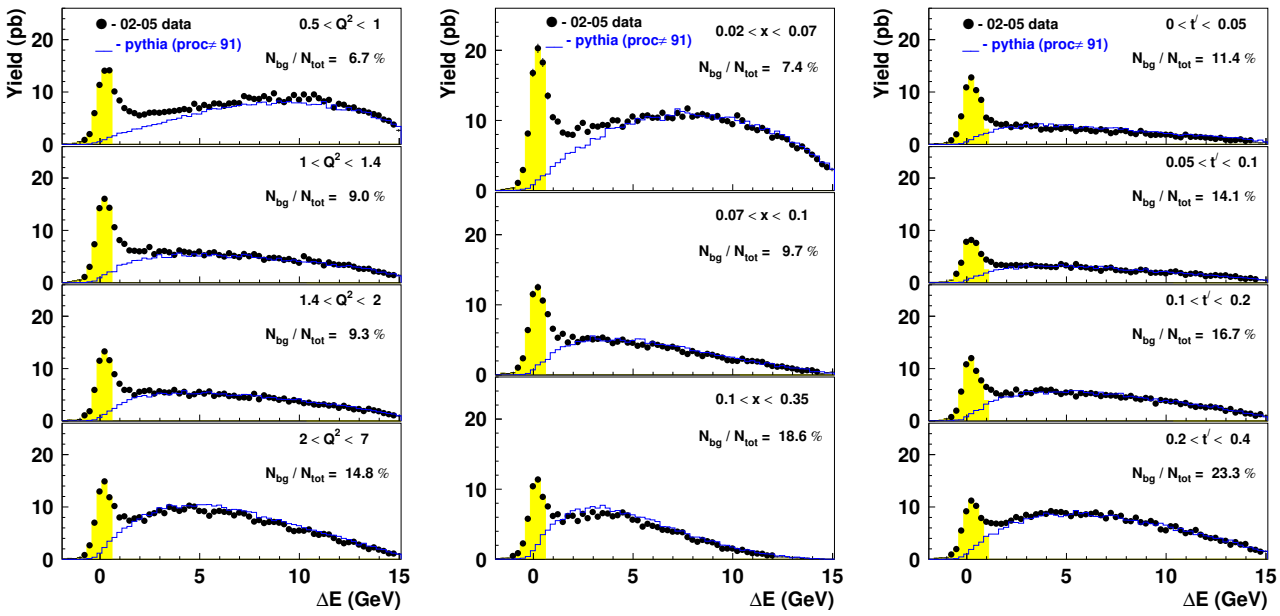

Figure 7.1: The semi-inclusive background contamination in each bin of Q^2, x_B and t'.

For the data with $N_{tot} = N_\rho + N_{bg}$ total events, where N_ρ is the number of exclusive ρ^0 events and N_{bg} the number of semi-inclusive background events, an unbinned maximum likelihood fit is performed to extract asymmetries and SDMEs. The exclusive ρ^0 events and the semi-inclusive background are mixed in the data sample and they enter the maximum likelihood fit with their characteristic ϕ, $\cos\vartheta$ and φ distributions. For an background event, if it does not belong to semi-inclusive vector meson production, the angles ϑ and φ have no physical meaning, since these two angles are properties of the vector meson decay. However, as the background events are indistinguishable from exclusive events in the data sample, the same definition of angles is also used for all two-hadron events misidentified as exclusive ρ^0 events.

There are two possibilities to correct the measured quantities, both requiring a pure background sample. This background sample can not be taken from the real data at high ΔE, since the angular distributions have a ΔE dependence. In Figure 7.2 the angular distributions from the PYTHIA simulation of the background sample are shown for various ΔE regions. The ϕ and φ distributions do not show a strong ΔE dependence, while the $\cos\vartheta$ distributions are different for low ($\Delta E < 0.6$ GeV) and high ($\Delta E > 2.4$ GeV) values of ΔE.

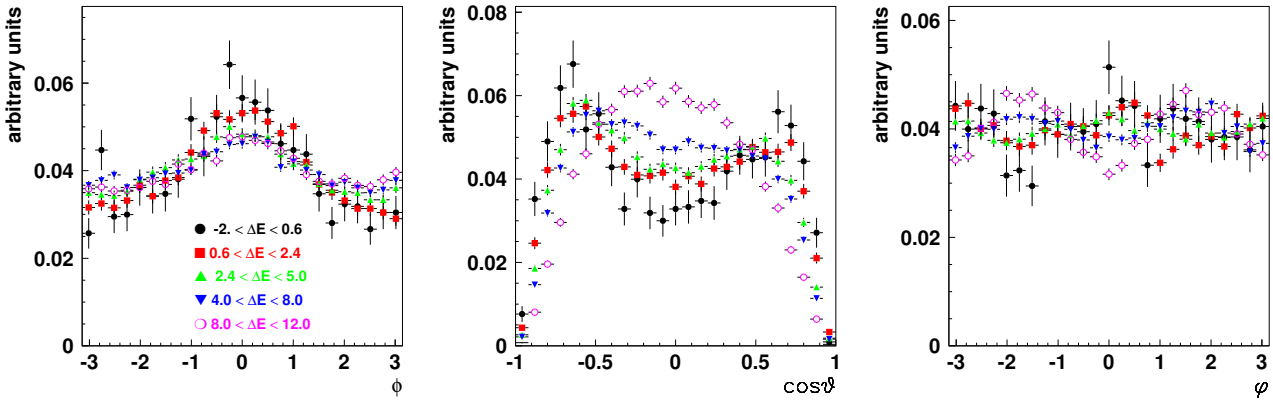

Figure 7.2: The ϕ, $\cos\vartheta$ and φ distributions for semi-inclusive sample simulated by the PYTHIA Monte Carlo in various ΔE regions.

The PYTHIA Monte Carlo sample in the same ΔE region as the real data, $\Delta E < 0.6$ GeV, is used as background sample. Ideally, the angular distributions of the background sample of the Monte Carlo simulation should perfectly match those of the real data. However, as it is seen from a comparison of Monte Carlo simulation and data in various high ΔE regions (see Figure 7.3), where the data receives no contribution from exclusive reactions, the Monte Carlo simulation does not fully describe the data. While the ϕ and φ distributions of the data are well described by PYTHIA, the $\cos\vartheta$ distributions of the Monte Carlo simulation seems to be mirrored compared to the real data. The origin of this behavior is presently not known.

7.3.1 Background correction by assigning a negative weight to background events

Since background and exclusive ρ^0 events are indistinguishable in the exclusive sample, another independent Monte Carlo sample, namely a purely semi-inclusive sample with its own characteristic angular distributions, is used to subtract the semi-inclusive background. Using the advantages of the maximum likelihood fit, this can be done simultaneously with the estimation of the λ parameters in equation (7.6). In the log-likelihood function the events from the real data are weighted with a positive weight, while for the semi-inclusive background events a

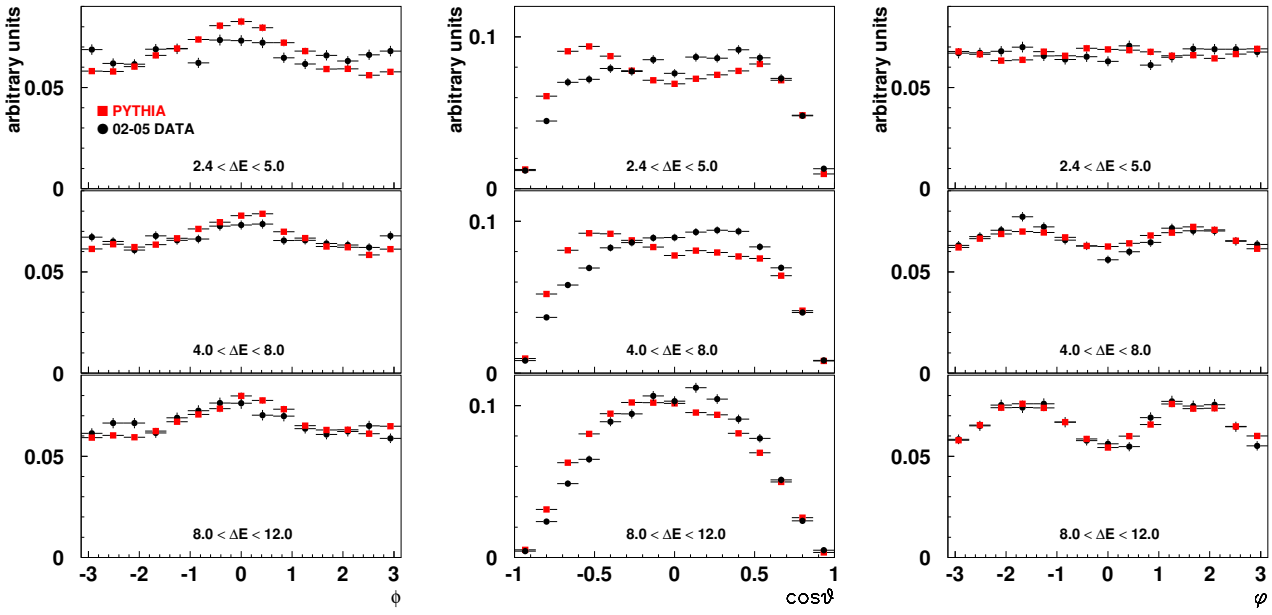

Figure 7.3: The ϕ, $\cos\vartheta$ and φ distributions for semi-inclusive sample simulated by the PYTHIA Monte Carlo compared to real data in various ΔE regions, where the real data sample can also be treated as semi-inclusive.

negative weight is used:

$$\ln L(\lambda) = \sum_{i=1}^{N} \ln\, W(\lambda; P_i, \phi_i, \phi_{s_i}, \vartheta_i, \varphi_i)^{\omega_i} = \sum_{i=1}^{N} \omega_i \ln\, W(\lambda; P_i, \phi_i, \phi_{s_i}, \vartheta_i, \varphi_i)\ . \tag{7.8}$$

Here the weight w is the absolute luminosity of the data ($w = L_{data}$) or Monte Carlo simulation ($w = -L_{MC}$). In this case, according to [103], the covariance matrix has to be corrected:

$$\widehat{V}^{-1} = \mathcal{F}\left(\mathcal{F}'^{-1}\mathcal{F}\right), \tag{7.9}$$

The matrices $\mathcal{F}$ and $\mathcal{F}'$ are calculated similar to equation (7.4)

$$\mathcal{F}_{mn} = \left.\frac{\partial^2 \ln L}{\partial\lambda_m \partial\lambda_n}\right|_{\widehat{\lambda}}, \qquad \mathcal{F}'_{mn} = \left.\frac{\partial^2 \ln L'}{\partial\lambda_m \partial\lambda_n}\right|_{\widehat{\lambda}} \tag{7.10}$$

where L' is given as:

$$\ln L'(\lambda) = \sum_{i=1}^{N} \omega_i^2 \ln\, W(\lambda; P_i, \phi_s, \phi, \vartheta, \varphi). \tag{7.11}$$

7.3.2 Background correction parameterizing the background sample

Similar to the background correction method described above, a semi-inclusive Monte Carlo sample is used to parameterize the background contamination. This implies to estimate the vector of background parameters that parameterize the angular distribution. The angular

distribution is defined for exclusive vector mesons only. But, since the background and exclusive ρ^0 events are mixed in the data sample, the same definition of the angular distribution is used also for semi-inclusive data, being only a tool to correct for the background.

If the vector of the background parameters θ is known, then each event from the data sample has a certain probability to be an exclusive ρ^0 or a background event, given by the ratio N_ρ/N_{tot} or N_{bg}/N_{tot}, respectively. Thus each event can be treated first as an exclusive event, and the angular distribution $W(\lambda; P_i, \phi_i, \phi_{s_i}, \vartheta_i, \varphi_i)$ is computed for a given set of fit parameters λ. Then the same event is treated as a semi-inclusive event, and the angular distribution $W(\theta; P_i, \phi_i, \phi_{s_i}, \vartheta_i, \varphi_i)$ is calculated with the known background parameters θ:

$$\ln L(\lambda) = \sum_{i=1}^{N} \left[\frac{N_\rho}{N_{tot}} \ln W\big(\lambda; P_i, \phi_i, \phi_{s_i}, \vartheta_i, \varphi_i\big) + \frac{N_{bg}}{N_{tot}} \ln W\big(\theta; P_i, \phi_i, \phi_{s_i}, \vartheta_i, \varphi_i\big) \right]. \tag{7.12}$$

In this case, the covariance matrix is given by equation (7.4).

7.4 SDMEs

7.4.1 Unpolarized SDMEs

Unpolarized SDMEs of ρ^0 production at HERMES had been already extracted from the 1996-2005 data taking period using the Schilling-Wolf convention. Since the binning used in the current analysis is different from that of the previous analysis, in the course of this thesis the unpolarized SDMEs are extracted from the 2002-2005 data taking period using both formalisms.

In the case of unpolarized target and beam, the likelihood function is given as:

$$L(\lambda) = \frac{\prod_i^{N_\rho} W_{UU}(\lambda;\, \phi_i,\, \cos\vartheta_i,\, \varphi_i)}{\mathcal{N}_{UU}^{N_\rho}(\lambda)}\,. \tag{7.13}$$

The normalization integral is computed from an isotropically generated PYTHIA Monte Carlo simulation, reconstructed in the HERMES acceptance:

$$\mathcal{N}_{UU}(\lambda) = \sum_{i}^{N_{MC}} W_{UU}(\lambda;\, \phi_i,\, \cos\vartheta_i,\, \varphi_i)\,. \tag{7.14}$$

There the events are distributed according to $\epsilon(\phi, \vartheta, \varphi)\, W_{UU}(\lambda;\, \phi,\, \cos\vartheta,\, \varphi)$. All distortions of the angular distribution are purely due to the acceptance since the angular distribution itself is generated flat.

In Figure 7.4 the SDMEs are shown as calculated at the average kinematics. First the results using the Schilling-Wolf notations are compared to the ones extracted previously from HERMES data (see left panel of Figure 7.4). The extracted values of SDMEs from this analysis are in good agreement with the values of SDMEs extracted previously. The observed small differences

are due to different data samples, extraction methods and background subtraction methods.

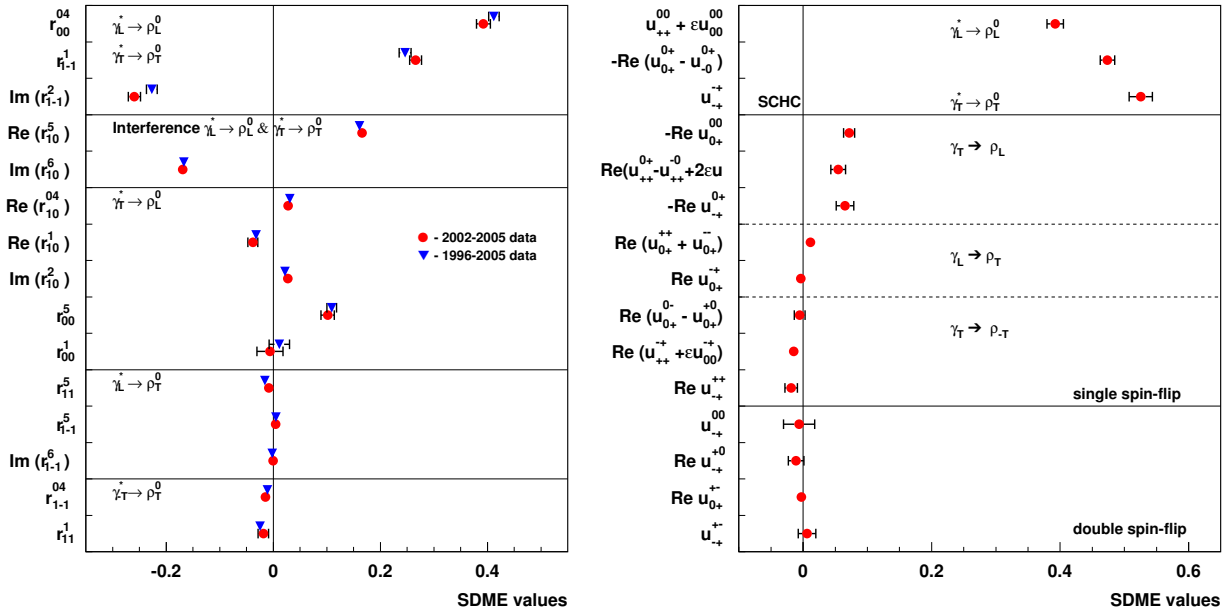

Figure 7.4: The unpolarized SDMEs extracted at average kinematics in the formalisms of Schilling-Wolf (left) and Diehl (right) separated for various helicity transfer from virtual photon to ρ^0 meson. The error bars represent the statistical uncertainties only.

The extracted SDMEs are categorized into five classes according to the hierarchy [52]:

$$|T_{00}| \approx |T_{11}| \gg |T_{01}| > |T_{10}| \geq |T_{1-1}| \tag{7.15}$$

The first two classes contain SDMEs that are dominated by the helicity-conserving amplitudes T_{00} and T_{11} or their interference. These SDMEs describe the dominant transitions $\gamma_L^* \to \rho_L^0$ or $\gamma_T^* \to \rho_T^0$. The other three classes correspond to SDMEs that contain contributions from the s-channel helicity non-conserving amplitude T_{01}, T_{10} or T_{1-1}, corresponding to the transition $\gamma_T^* \to \rho_L^0$, $\gamma_L^* \to \rho_T^0$ or $\gamma_{-T}^* \to \rho_T^0$, respectively. An overview of the SDME extraction using the Schilling-Wolf notation at HERMES can be found in [52].

The results are also shown in the notation of Diehl (see right panel of Figure 7.4) using the hierarchy predicted by the factorization theorem (see Section 6.7.4). Here the SDMEs are sorted into three main classes. The first class contains SDMEs that conserve helicity in transitions from virtual photon to ρ^0 meson. The second class consists of SDMEs that are a product of one helicity-conserving and one helicity-flip amplitude. This class is subdivided into three parts, describing $\gamma_T^* \to \rho_L^0$, $\gamma_L^* \to \rho_T^0$ and $\gamma_{-T}^* \to \rho_T^0$ transitions. The SDMEs of the third class involve the product of two helicity non-conserving amplitudes.

The results in both conventions clearly show non-zero values for those SDMEs which are not restricted to be zero in the case of SCHC. This suggests significant helicity conserving amplitudes for both transitions, $\gamma_L^* \to \rho_L^0$ and $\gamma_T^* \to \rho_T^0$, and a substantial interference between

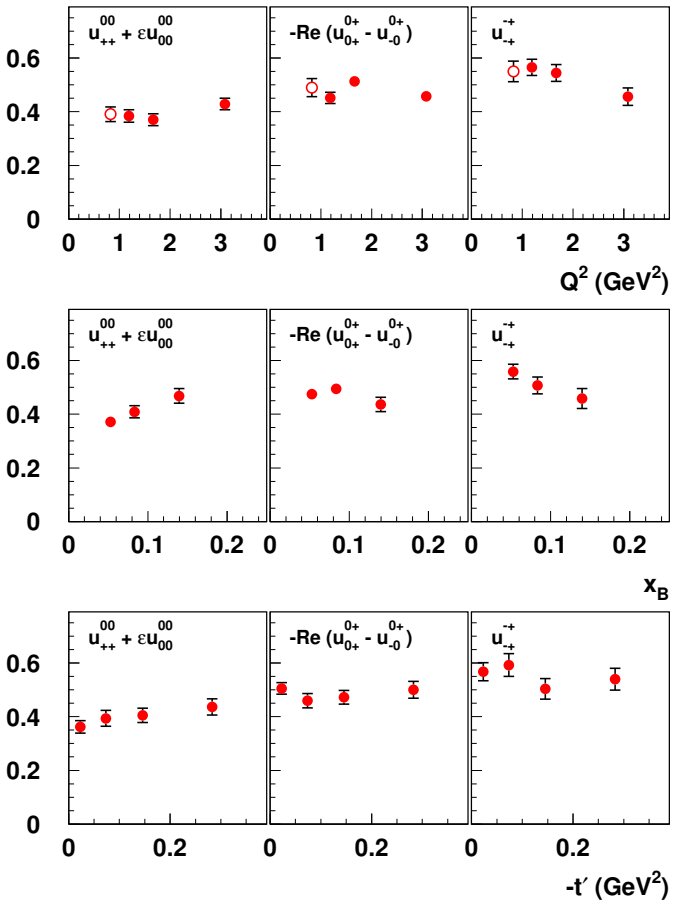

Figure 7.5: The unpolarized SDMEs which describe the dominant transitions in the Diehl formalism as a function of Q^2, x_B and t'. The error bars represent the statistical uncertainties only.

them. In the Schilling-Wolf notation there are five of such SDMEs, four of which should satisfy the following relations under the assumption of SCHC:

$$r^1_{1-1} = -\,\mathrm{Im}\, r^2_{1-1} \qquad\qquad \mathrm{Re}\, r^5_{10} = -\,\mathrm{Im}\, r^6_{10}\,. \tag{7.16}$$

These relations are mostly satisfied within the given uncertainties [52].

The consequences of approximate SCHC are more explicit in the Diehl notation where there are only three of such SDMEs, which should satisfy, *e.g.*, the following relations:

$$|\,\mathrm{Re}(u^{0+}_{0+} - u^{0+}_{-0})| >> |\,\mathrm{Re}(u^{0+}_{0-} - u^{0+}_{+0})| \qquad\qquad u^{-+}_{-+} >> u^{-+}_{+-}\,. \tag{7.17}$$

These expectations are supported by the data.

However, the data indicates values different from zero also for some SDMEs involving s-channel helicity non-conserving transitions. In particular, the SDMEs from the third class in the Schilling-Wolf notation, which are associated with the helicity amplitudes $T_{01}T^*_{11}$, are much

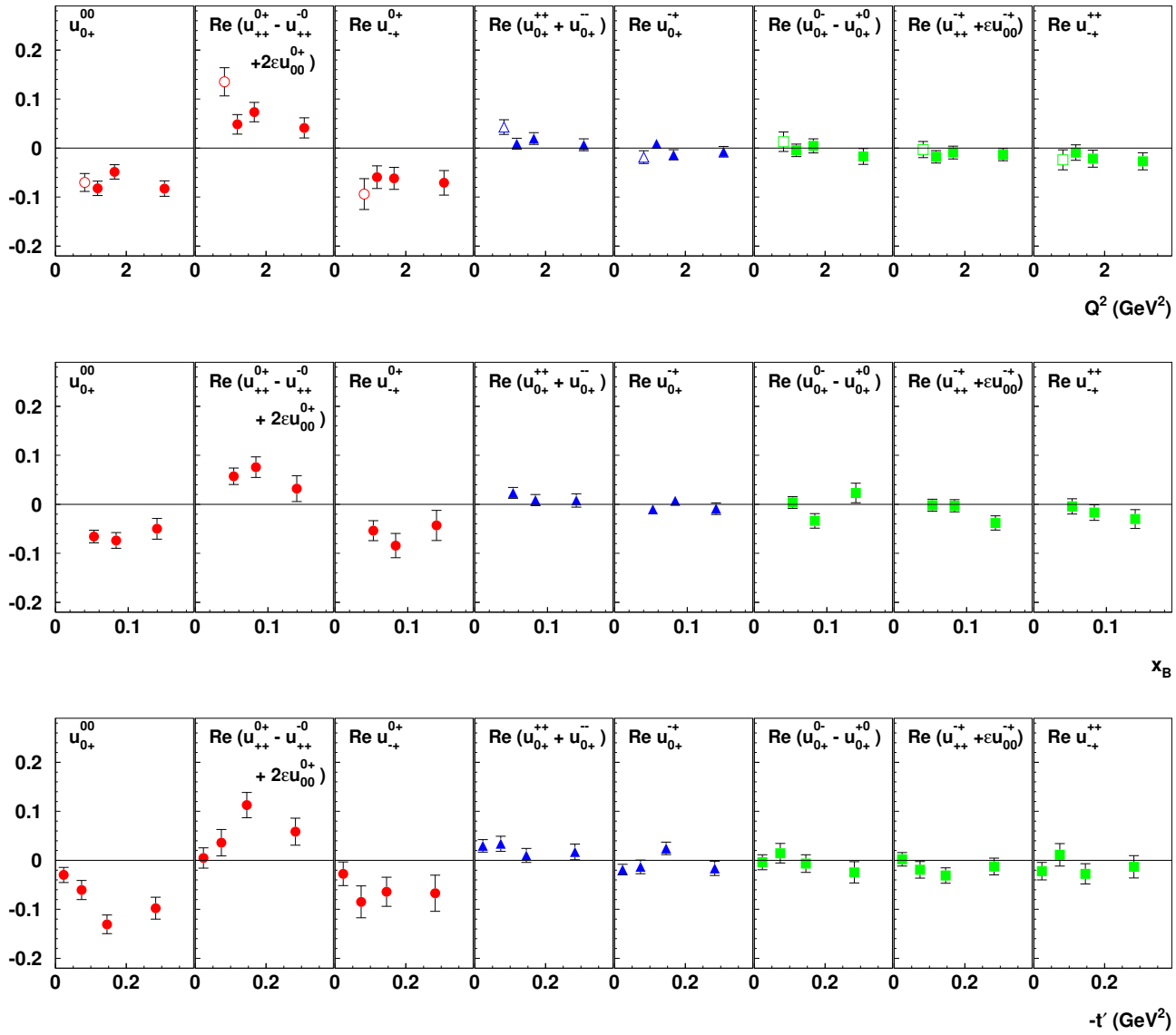

Figure 7.6: The unpolarized SDMEs associated with helicity flip amplitudes in the Diehl formalism as a function of Q^2, x_B and t'. Red circles are used to display transitions $\gamma^*_T \to \rho^0_L$, blue triangles stand for transitions $\gamma^*_L \to \rho^0_T$, and green squares for transition $\gamma^*_{-T} \to \rho^0_T$. The error bars represent the statistical uncertainties only.

smaller compared to the ones from the first two classes, but still significantly non-zero. The SDME r^5_{00} is observed to be the largest element violating the SCHC hypothesis. The offset from zero, expressed in units of standard deviations, is found to be of the order of nine. This was already observed earlier by the HERA collider experiments [50, 51]. For the SDMEs Re $\left(r^{04}_{10}\right)$, Re $\left(r^1_{10}\right)$ and Im $\left(r^2_{10}\right)$, representing significant s-channel helicity non-conservation, HERMES observes offsets of about $2-4$ times the total uncertainty. The SDMEs from the fourth and fifth classes are compatible with zero indicating a suppression for transitions $\gamma^*_L \to \rho^0_T$ and $\gamma^*_{-T} \to \rho^0_T$.

Also in the Diehl formalism transitions with single helicity-flip are smaller compared with dominant transitions. The SDME Re u^{00}_{0+}, corresponding to the SDME r^5_{00} in Shilling-Wolf

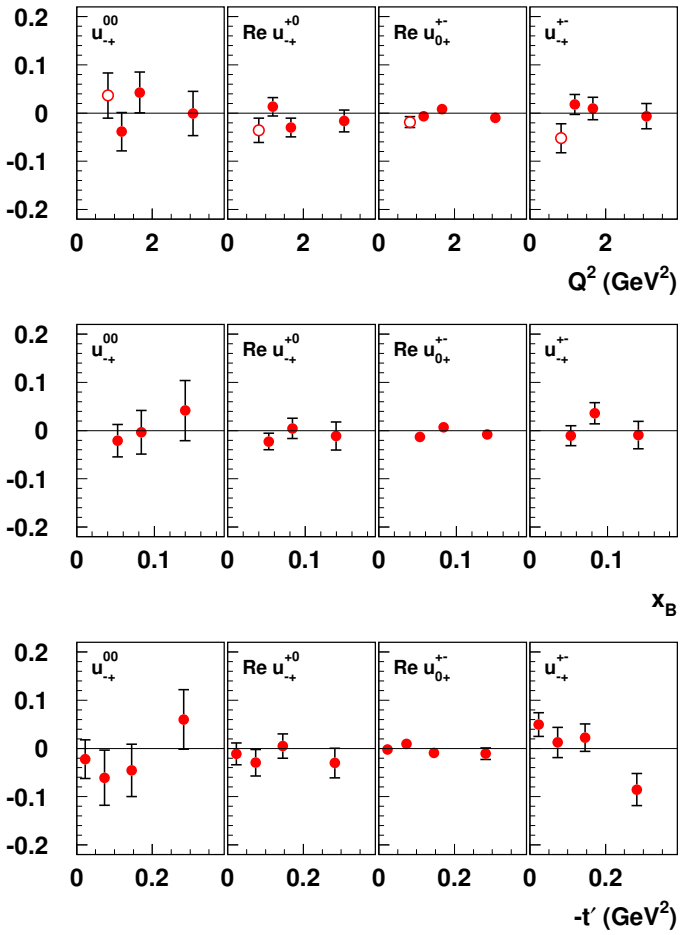

Figure 7.7: The unpolarized SDMEs associated with two helicity flip amplitudes in the Diehl formalism as a function of Q^2, x_B and t'. The error bars represent the statistical uncertainties only.

notation, shows the same offset from zero. The other two SDMEs Re $\left(u^{0+}_{++} - u^{-0}_{++} + 2\epsilon u^{0+}_{00}\right)$ and Re u^{0+}_{-+}, corresponding to transitions $\gamma^*_T \to \rho^0_L$, are of the same order. The transitions $\gamma^*_L \to \rho^0_T$ and $\gamma^*_{-T} \to \rho^0_T$ are much smaller compared with those of $\gamma^*_T \to \rho^0_L$.

The SDMEs of the third class, corresponding to double helicity-flip amplitudes, are compatible with zero that is in agreement with the predictions by the factorization theorem.

Altogether, the results for SDMEs calculated at average kinematics show non-negligible contributions of spin-flip amplitude $\gamma^*_T \to \rho^0_L$ in exclusive ρ^0 production at intermediate energies.

All SDMEs are also calculated in bins of Q^2, x_B or t'. In the following the results using the Diehl notation are discussed:

- SDMEs for the dominant transitions (see Figure 7.5):
  while the SDME Re$(u^{0+}_{0+} - u^{0+}_{-0})$, which corresponds to interference between the transitions $\gamma^*_L \to \rho^0_L$ and $\gamma^*_T \to \rho^0_T$, exhibits a weak dependence on Q^2 and x_B, there is an indication of opposite behavior for longitudinal and transverse transitions, $\gamma^*_L \to \rho^0_L$ $(u^{++}_{00} + \epsilon u^{00}_{00})$ and $\gamma^*_T \to \rho^0_T$ (u^{-+}_{-+}), for both Q^2 and x_B dependences. All three elements exhibit a weak t'

dependence.

- SDMEs involving one helicity-flip amplitude (see Figure 7.6):
  this class of SDMEs is subdivided into three classes, displayed by three different colors and symbols. For some of the SDMEs from the first class, corresponding to the transitions, $\gamma_T^* \to \rho_L^0$, some Q^2 and x_B dependence can not be excluded, while there is a prominent t' dependence. No Q^2, x_B or t' dependences are observed for other SDMEs corresponding to transitions $\gamma_L^* \to \rho_T^0$ and $\gamma_{-T}^* \to \rho_T^0$.

- SDMEs involving two helicity-flip amplitudes (see Figure 7.7):
  they are found to be almost constant over the measured Q^2-, x_B- and t'-ranges.

The values obtained for the unpolarized SDMEs are used in the further analysis.

7.4.2 Polarized SDMEs on a transversely polarized target

In the case of a transversely polarized target and an unpolarized beam, the likelihood function is given as:

$$L(\lambda) = \prod_i^{N_\rho} \frac{W(\lambda;\ P_i,\ \phi_{s_i},\ \phi_i,\ \cos\vartheta_i,\ \varphi_i)}{\mathcal{N}(\lambda)}\,. \tag{7.18}$$

The normalization integral $\mathcal{N}(\lambda)$ of the p.d.f. reduces to the normalization integral $\mathcal{N}_{UU}(\lambda)$ of the unpolarized p.d.f., if the unpolarized and polarized cross sections are factorized and, in addition, if the yields for both target polarization states are equal, *i.e.* the net target polarization is zero [102]:

$$L(\lambda) = \prod_i^{N_\rho} \frac{W_{UU}(\lambda;\ \phi,\vartheta,\varphi) + P_T W_{UT}(\lambda;\ P_i,\phi_{s_i},\phi_i,\vartheta_i,\varphi_i)}{\mathcal{N}_{UU}(\lambda)}\,, \tag{7.19}$$

In addition, if the normalization of the p.d.f. does not depend on the fit parameters λ, it can be omitted. This can be done by fixing the unpolarized angular distribution by the already measured unpolarized SDMEs. In this case the denominator of the equation above does not depend on the fit parameters and can be omitted. Since there are two independent transverse polarizations, the number of transverse SDMEs, thus the number of fit parameters is larger compared to the unpolarized case.

$$L(\lambda) = \prod_i^{N_\rho} W_{UU}(\phi,\vartheta,\varphi) + P_T W_{UT}(\lambda;\ P_i,\phi_{s_i},\phi_i,\vartheta_i,\varphi_i)\,, \tag{7.20}$$

The background subtraction is performed with both methods described above, parameterizing the background angular distribution and assigning a negative weight to the background events. A maximum likelihood fit is performed in the entire kinematic region $1 < Q^2 < 7$ GeV^2,

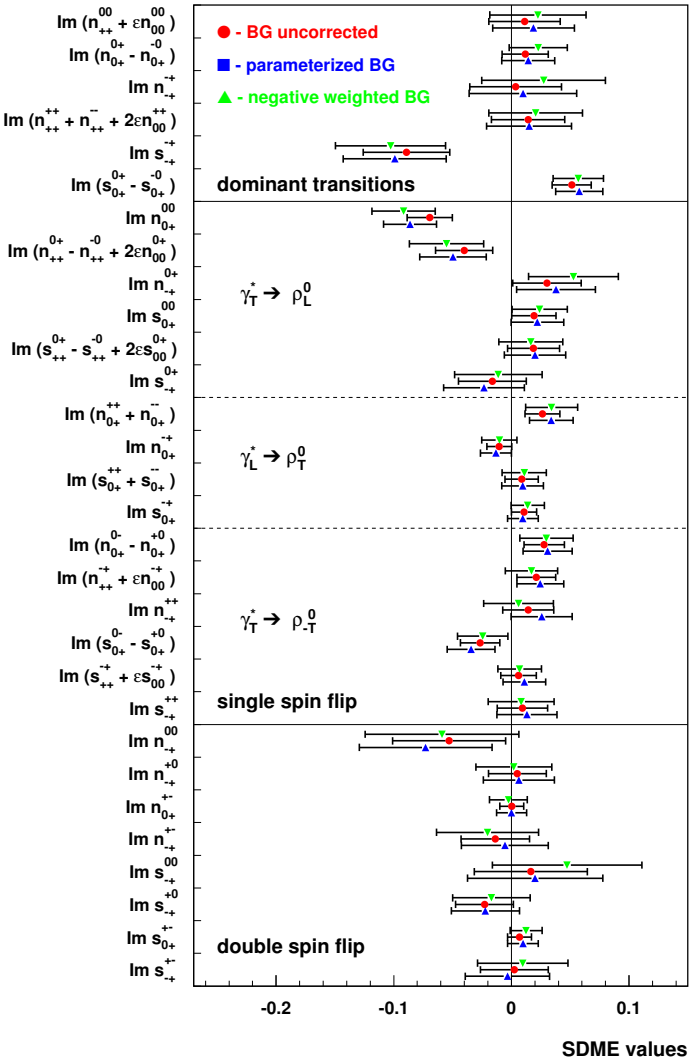

Figure 7.8: The transverse SDMEs extracted at average kinematics: $1 < Q^2 < 7$ GeV^2, $0.02 < x_B < 0.4$ and $-t' < 0.4$ GeV^2. The error bars represent the statistical uncertainties only.

$0.02 < x_B < 0.4$ and $-t' < 0.4$ GeV^2. The resulting transverse SDMEs of exclusive ρ^0 production at average kinematics corrected for the background contribution using both methods, as well as the uncorrected values of the SDMEs are presented in Figure 7.8. Both correction methods for all transverse SDMEs agree. In the following the method of parameterizing the background angular distribution is used.

The exclusive ρ^0 production on a transversely polarized target is related to the proton helicity-flip amplitude which is suppressed by a factor $\sqrt{-t}/2M_p$ [19]. This suppression factor is reflected in the absolute magnitude of the transverse SDMEs that are smaller compared to the unpolarized ones.

The transverse SDMEs are ordered according to the same hierarchy as the unpolarized SDMEs, divided into three classes. First, those SDMEs are displayed which involve the dominant transitions $\gamma_L^* \rightarrow \rho_L^0$ and $\gamma_T^* \rightarrow \rho_T^0$ and the interference between them. Similar to the

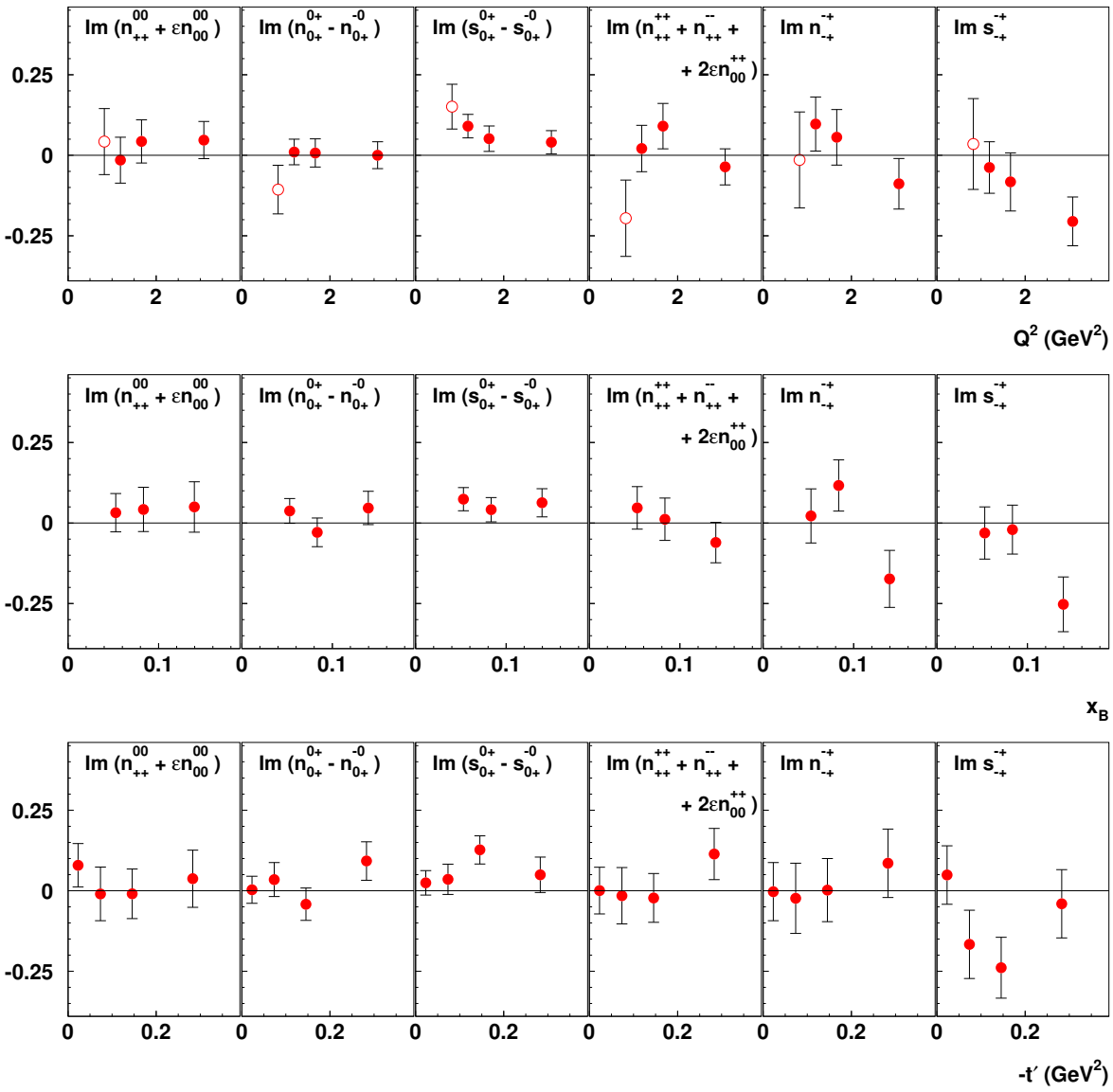

Figure 7.9: The transverse SDMEs corresponding to dominant transitions as a function of Q^2, x_B and t'. The error bars represent the statistical uncertainties only.

unpolarized case, the second class consists of SDMEs associated with helicity-conserving and helicity-flip amplitudes, where the three transitions $\gamma^*_T \to \rho^0_L$, $\gamma^*_L \to \rho^0_T$ or $\gamma^*_{-T} \to \rho^0_T$ are possible. The SDMEs, involving two helicity-flip amplitudes, are displayed in the third class. The results are discussed in details in Section 8.1.

The results are also presented in bins of Q^2, x_B and t'. The first bin in Q^2 ($Q^2 < 1$ GeV^2) is presented by open symbols which data is not used in the extraction of x_B and t' dependences. The background correction is done by parameterizing the background angular distribution.

The kinematic dependences of the SDMEs from the first class are shown in Figure 7.9. All six elements are found to be approximately constant over the measured Q^2 and x_B ranges. There is an indication of a slight t' dependence for the SDMEs Im s^{-+}_{-+} and Im$\left(s^{0+}_{0+} - s^{-0}_{0+}\right)$.

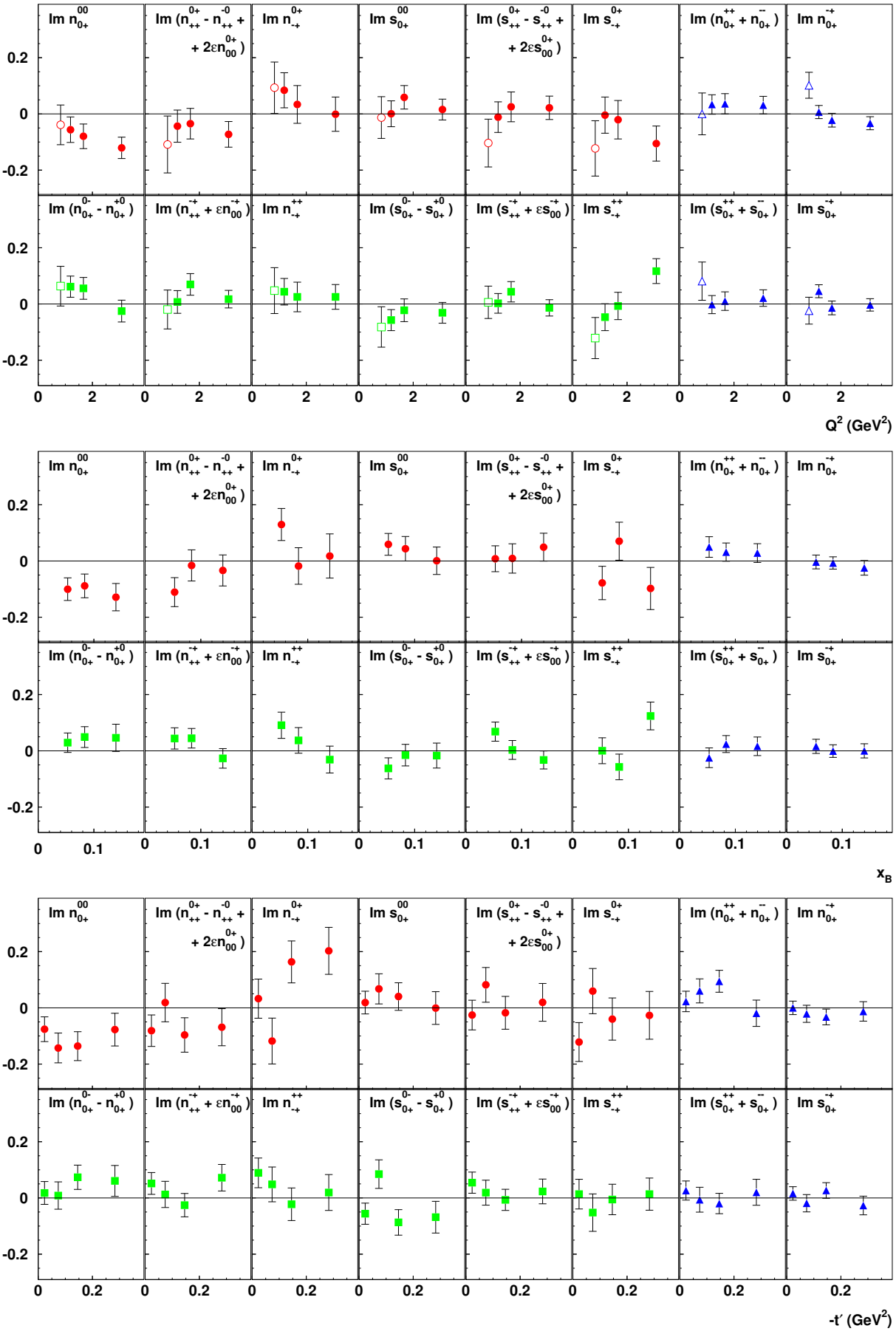

Figure 7.10: The transverse SDMEs associated with one helicity flip amplitudes in the Diehl formalism as a function of Q^2, x_B and t'. The red circles are used to display the transitions $\gamma_T^* \to \rho_L^0$, the blue triangles stand for the transitions $\gamma_L^* \to \rho_T^0$, and green squares for the transition $\gamma_{-T}^* \to \rho_T^0$.

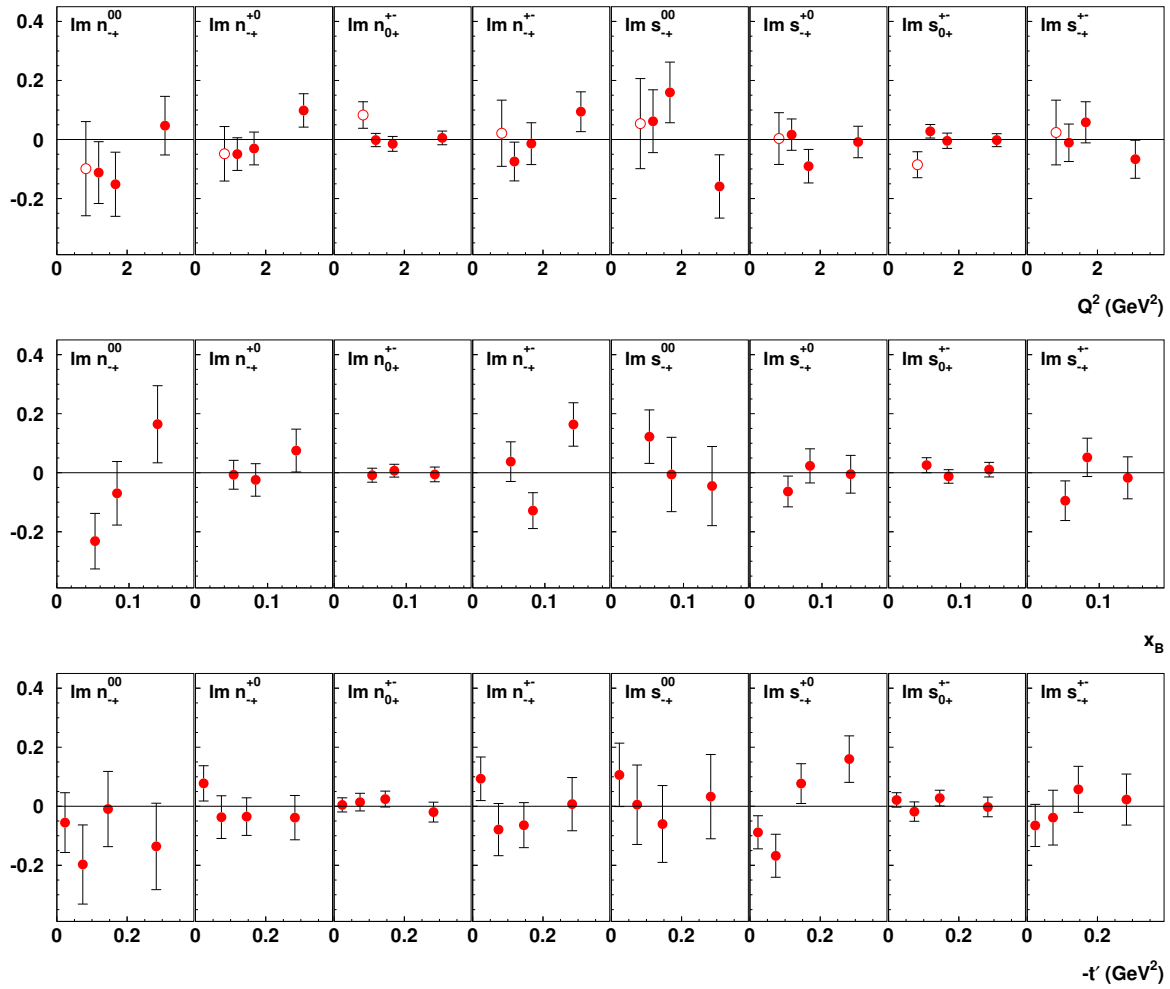

Figure 7.11: The transverse SDMEs associated with two helicity flip amplitudes in the Diehl formalism as a function of Q^2, x_B and t'. The error bars represent the statistical uncertainties only.

The Q^2, x_B and t' dependences of the SDMEs from the second class are displayed in Figure 7.10. With three different colors and symbols are indicated the three helicity-flip transitions $\gamma^*_T \to \rho^0_L$, $\gamma^*_L \to \rho^0_T$ and $\gamma^*_{-T} \to \rho^0_T$. A slightly negative tendency is observed for the Q^2 and x_B dependences of the SDME $\mathrm{Im}\, u^{00}_{0+}$.

The SDMEs from the third class are found to be constant over the entire kinematic region. The SDMEs having smaller statistical uncertainties are consistent with zero, while the ones with larger uncertainties fluctuate around zero within one standard deviation.

Since the target polarization is defined with respect to the beam direction, the existence of a longitudinal component of the target polarization with respect to the virtual photon direction gives rise to additional terms in the angular distribution. This makes the equation for the whole angular distribution quite complicated (see Appendix E.2). The angular dependence of the cross section depends on linear combinations of terms $\cos\theta_\gamma\, \mathrm{Im}\, n$ $(\cos\theta_\gamma\, \mathrm{Im}\, s)$ and $\sin\theta_\gamma\, \mathrm{Im}\, l$. The separation of these terms requires an additional measurement with both transverse and longitudinal target polarizations. Since it is out of the scope of the current thesis, in this analysis

$P_T \approx S_T$ is assumed and a systematic uncertainty is assigned to the measured transverse SDMEs due to the admixture of the longitudinal component S_L of the target polarization with respect to the virtual-photon direction (see Section 7.7.6).

7.5 Extraction of the transverse target-spin asymmetry in exclusive ρ^0 meson production

7.5.1 Comparison of Diehl-Sapeta and Diehl formalisms

The first measurement of the transverse target-spin asymmetry in exclusive longitudinal ρ^0_L meson production on a transversely polarized target has been performed neglecting the interference between longitudinal and transverse ρ^0 helicity states (see Section 6.6). The interference amplitudes do not cancel and can be taken into account, if the cross section is not integrated over the azimuthal angle φ, unlike in the Diehl-Sapeta formalism [33]. While in the Diehl-Sapeta formalism (see Section 6.4) the cross section of exclusive ρ^0 meson production is presented in terms of photoabsorption cross sections or interference terms σ^{ij}_{mn}, not emphasizing the ρ^0 helicity state, the Diehl formalism (see Section 6.8) relates the total cross section of exclusive ρ^0 meson production to angle-independent and angular-dependent cross sections. The angular-dependent cross section, *i.e.* the angular distribution parameterized through SDMEs, reflects the production of ρ^0 mesons in various helicity states originating from a longitudinal or transverse virtual photon γ^*.

The results from both formalisms are identical if the angular distribution in the Diehl formalism is integrated over the azimuthal angle φ. In that case the angular distribution $W(\phi, \phi_s, \vartheta, \varphi)$ given by equation (6.50) reduces to $W(\phi, \phi_s, \vartheta)$ given by equation (6.30). The unpolarized asymmetry $A_{UU}(\phi)$ has the same $\cos\phi$- and $\cos 2\phi$-dependent terms in both cases (see equation (6.32)). These are not treated as free parameters during the fit, but instead fixed using the values of the already extracted unpolarized SDMEs. In the Diehl-Sapeta formalism, the polarized asymmetry $A^l_{UT}(\phi, \phi_s)$ is given by equation (6.32), both longitudinal and transverse asymmetries, $A^{l,LL}_{UT}(\phi, \phi_s)$ and $A^{l,TT}_{UT}(\phi, \phi_s)$, contain the same number of independent terms. In the Diehl formalism, since the longitudinal component of the asymmetry has no φ dependence (see equation (6.55)), it does not change after the integration over that angle. The transverse component of the asymmetry reduces to the same number of independent terms as the longitudinal component, and is given by a similar equation as equation (6.55), replacing the notations LL by TT.

A maximum likelihood fit is performed with the corresponding likelihood function,

$$L(\lambda) = \prod_i^{N_\rho} \widehat{W}_{UU}(\vartheta_i)(1 + A_{UU}(\phi_i, \vartheta_i) + P_T A^l_{UT}(\lambda; P_i, \phi_{s_i}, \phi_i, \vartheta_i)) \tag{7.21}$$

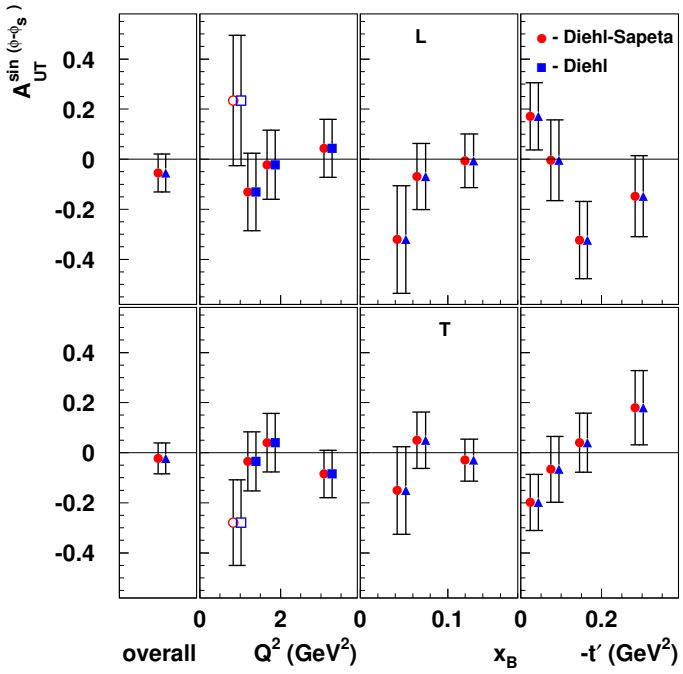

Figure 7.12: The $\sin(\phi - \phi_s)$ azimuthal amplitude of the asymmetry $A_{UT}^{l}(\phi, \phi_s)$ for longitudinal (L) and transverse (T) ρ^0 mesons at average kinematics as well as the Q^2, x_B or t' dependences in the Diehl-Sapeta and Diehl formalisms.

and compared to previous results (see Figure 7.12). The panels show as before (see Section 6.6), the $\sin(\phi - \phi_s)$ azimuthal amplitude of the asymmetry at average kinematics and its dependences on Q^2, x_B and t'. The upper (L) and lower (T) panels represent the asymmetries separated for longitudinal ρ_L^0 and transverse ρ_T^0 contributions. For the x_B and t' dependences, Q^2 is required to be above 1 GeV^2, while the Q^2 dependence is shown also for $0.5 < Q^2 < 1$ GeV^2.

Both results are identical, as expected.

7.5.2 Extraction of the asymmetry with respect to the virtual photon direction

A more precise way of extracting the longitudinal component of the asymmetry is using the full expression for the angular distribution (see Section 6.8). If the target polarization is defined with respect to the direction of the virtual photon, there are two possibilities for the asymmetry measurement: i) extract the transverse SDMEs and further relate the corresponding SDMEs to the transverse target-spin asymmetry, or ii) extract the asymmetries directly, as it was done in the previous section. In the case when the asymmetry measurement is related to the extraction of SDMEs, the asymmetry that is of theoretical interest is computed from the measured values

of SDMEs (see Section 6.8.1):

$$A_{UT}^{LL,\,\sin(\phi-\phi_s)}(\phi,\phi_s) = \frac{\mathrm{Im}\left(n_{++}^{00} + \epsilon n_{00}^{00}\right)}{u_{++}^{00} + \epsilon u_{00}^{00}}\,. \tag{7.22}$$

In the case of a direct asymmetry measurement, the full angular distribution is parameterized through unpolarized and polarized asymmetries (see equation (6.50)), $A_{UU}(\phi,\varphi,\vartheta)$ and $A_{UT}^{\gamma^*}(\phi,\phi_s,\vartheta,\varphi)$, and is used to extract the $\sin(\phi-\phi_s)$ azimuthal amplitude of the asymmetry. The results are displayed in Figure 7.13. Only small differences are observed which are due to the explicit usage of the values of ϵ while extracting the SDMEs.

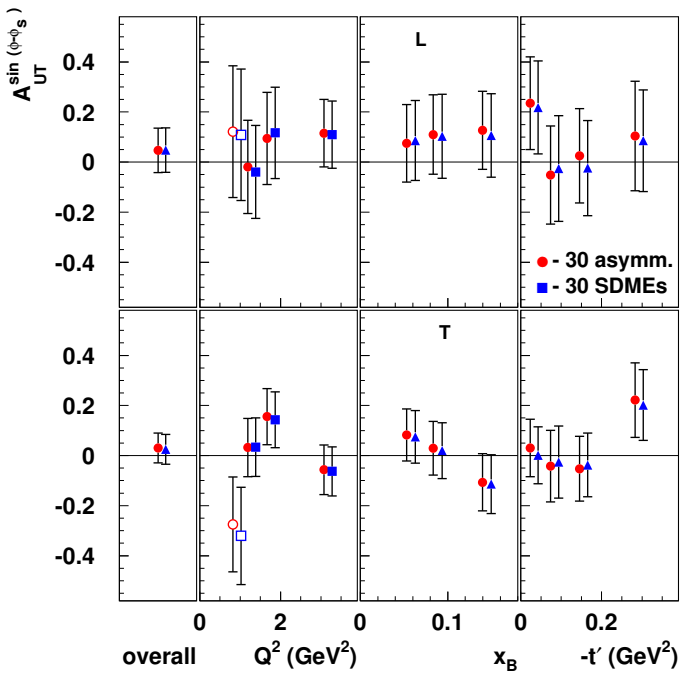

Figure 7.13: The $\sin(\phi-\phi_s)$ azimuthal amplitude of the asymmetry $A_{UT}^{l}(\phi,\phi_s)$ for longitudinal (L) and transverse (T) ρ^0 mesons at average kinematics as well as the Q^2, x_B or t' dependences, extracted directly or through the measured values of SDMEs.

However, since the target polarization is defined with respect to the lepton beam direction, both results do not account for the additional terms arising from the admixture of the longitudinal component S_L of the target polarization with respect to the direction of the virtual photon. The systematic uncertainty due to this admixture is estimated in Section 7.7.6.

7.6 Monte Carlo studies of the extraction method

Earlier studies[101] on asymmetry extraction methods have shown that although the various sin and cos azimuthal amplitudes of asymmetries are independent, the limited acceptance can cause a significant cross talk between them, *e.g.* $\sin(\phi-\phi_s)$ and $\sin(\phi+\phi_s)$, and only the simultaneous

extraction of these moments suppresses such cross talks. The results on transverse target-spin asymmetry and SDMEs described in the previous sections are extracted using the unbinned maximum likelihood method. In this section studies of possible cross talks for this extraction method are described. If the acceptance is taken into account correctly, *i.e.* the normalization of the p.d.f. is accurate, then the cross talk between various terms should be negligible.

Since the PYTHIA Monte Carlo production is for an unpolarized target[1], for this study the target polarization is assigned randomly. For each event the sign of the target polarization is chosen by a comparison with a random number R that varies between 0 and 1. A positive target polarization is assigned if

$$0.5(1 + A(\phi_s, \phi, \cos\vartheta, \varphi)) > R \,, \tag{7.23}$$

otherwise a negative polarization is assigned[2]. In this way, to the unpolarized Monte Carlo sample an asymmetry $A(\phi_s, \phi, \cos\vartheta, \varphi)$ is assigned which may be chosen on purpose. In the case of exclusive ρ^0 production, the asymmetry is given as a ratio of polarized and unpolarized angular distributions (see Section 6.5):

$$A = W_{UT}/W_{UU} \,. \tag{7.24}$$

In the studies performed, an 'isotropic' PYTHIA simulation has been used which restricts the values of unpolarized SDMEs to zero, and the value of r^{04}_{00} to 1/3, resulting in

$$W_{UU}(\cos\vartheta) = \frac{3}{4\pi}\left(\cos^2\vartheta\, r^{04}_{00} + \frac{1}{2}\sin^2\vartheta\,(1 - r^{04}_{00})\right) = \frac{1}{4\pi} \,. \tag{7.25}$$

First, the unpolarized and polarized SDMEs are extracted from the isotropic PYTHIA simulation without the random target spin assignment. All SDMEs are consistent with zero except the SDME r^{04}_{00} which equals 1/3 as expected. Further, various values have been assigned to polarized SDMEs that parameterize the polarized angular distribution W_{UT}. The difference between assigned and extracted values of those SDMEs gives an estimate of the cross talk in the extraction procedure. In the following figures, the polarized SDMEs corresponding to the longitudinal angular distribution W^{LL}_{UT} are marked as red circles, the ones corresponding to the transverse angular distribution W^{TT}_{UT} as blue triangles, and the interference terms as green squares.

First, values are assigned to some polarized SDMEs corresponding to the longitudinal angular distribution W^{LL}_{UT} (see upper-left panel of Figure 7.14). The dashed line indicates the assigned values. The extracted SDME values are found to be in good agreement with the assigned values, while the other SDMEs are consistent with zero. This indicates that the corre-

[1]PYTHIA generates only unpolarized cross sections.

[2]This method is similar to the 'accept/reject' method used in Monte Carlo generators, *e.g.* in PYTHIA.

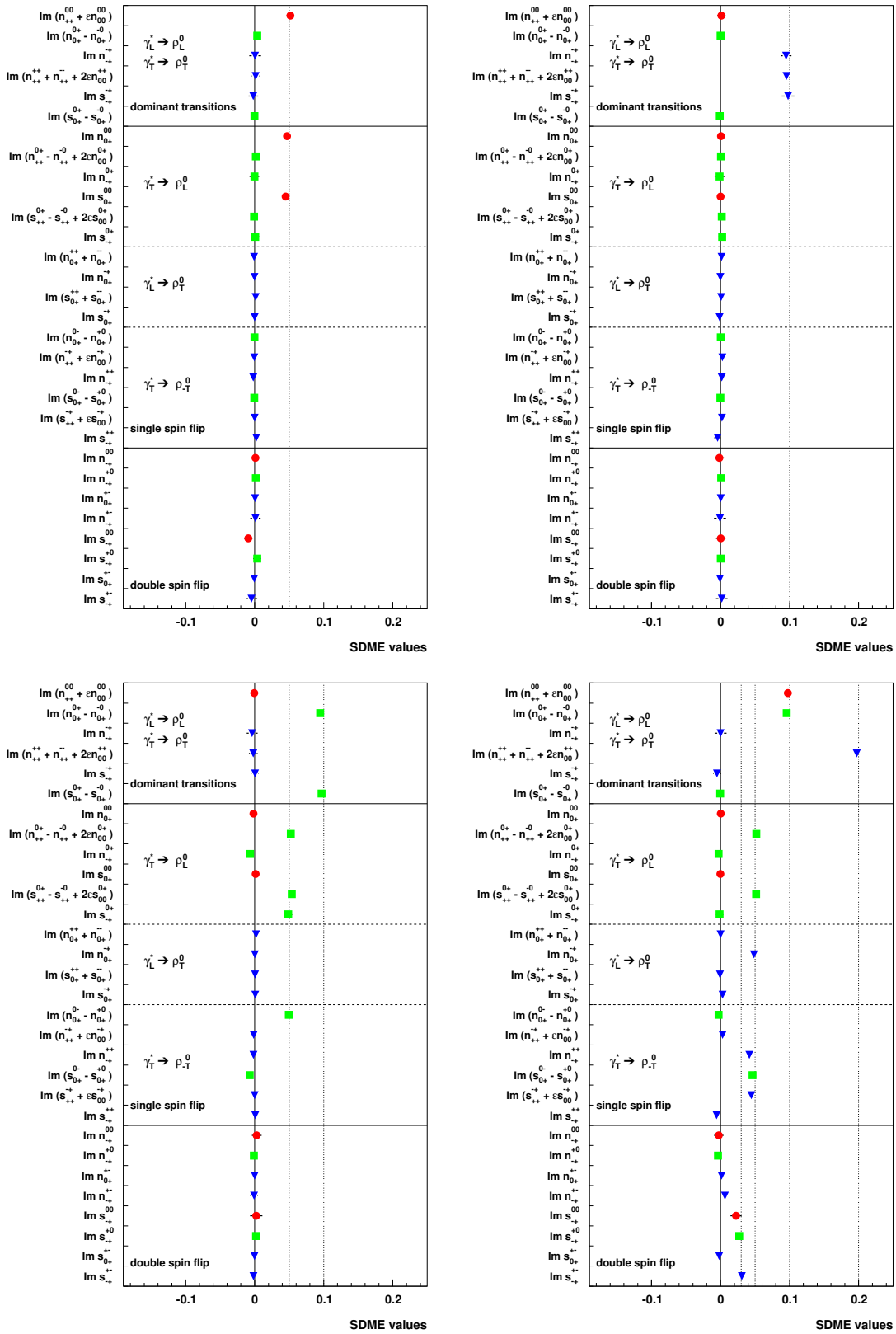

Figure 7.14: Monte Carlo studies performed on high-statistics sample testing the extraction method for polarized SDMEs. Non-zero values are assigned to some of longitudinal (upper-left panel), transverse (upper-right), interference (lower-left) terms and, simultaneously, to random number of terms from all contributions (lower-right). The red circles denote the SDMEs corresponding to the angular distribution of longitudinal ρ^0_L mesons, the ones corresponding to the transverse angular distribution are marked as blue triangles, and for interference terms green squares are used. Dashed lines denote the input values.

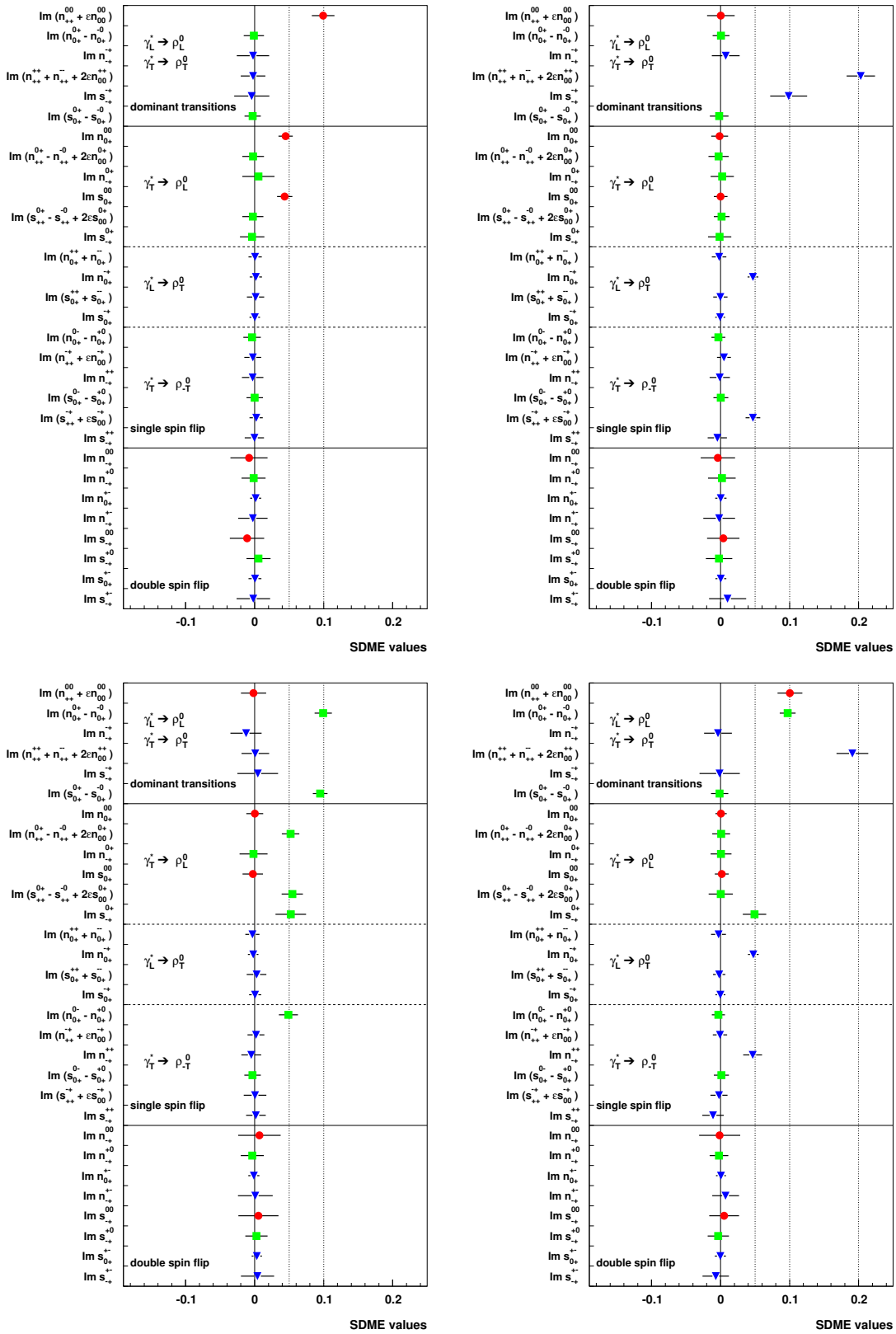

Figure 7.15: Monte Carlo studies performed on low-statistics, corresponding to the available data sample, testing the extraction method of polarized SDMEs. Non-zero values are assigned to some of longitudinal (upper-left panel), transverse (upper-right), interference (lower-left) terms and, simultaneously, to random number of terms from all contributions (lower-right). The red circles denote the SDMEs corresponding to the angular distribution of longitudinal ρ^0_L mesons, the ones corresponding to the transverse angular distribution are marked as blue triangles, and for interference terms green squares are used. Dashed lines denote the input values.

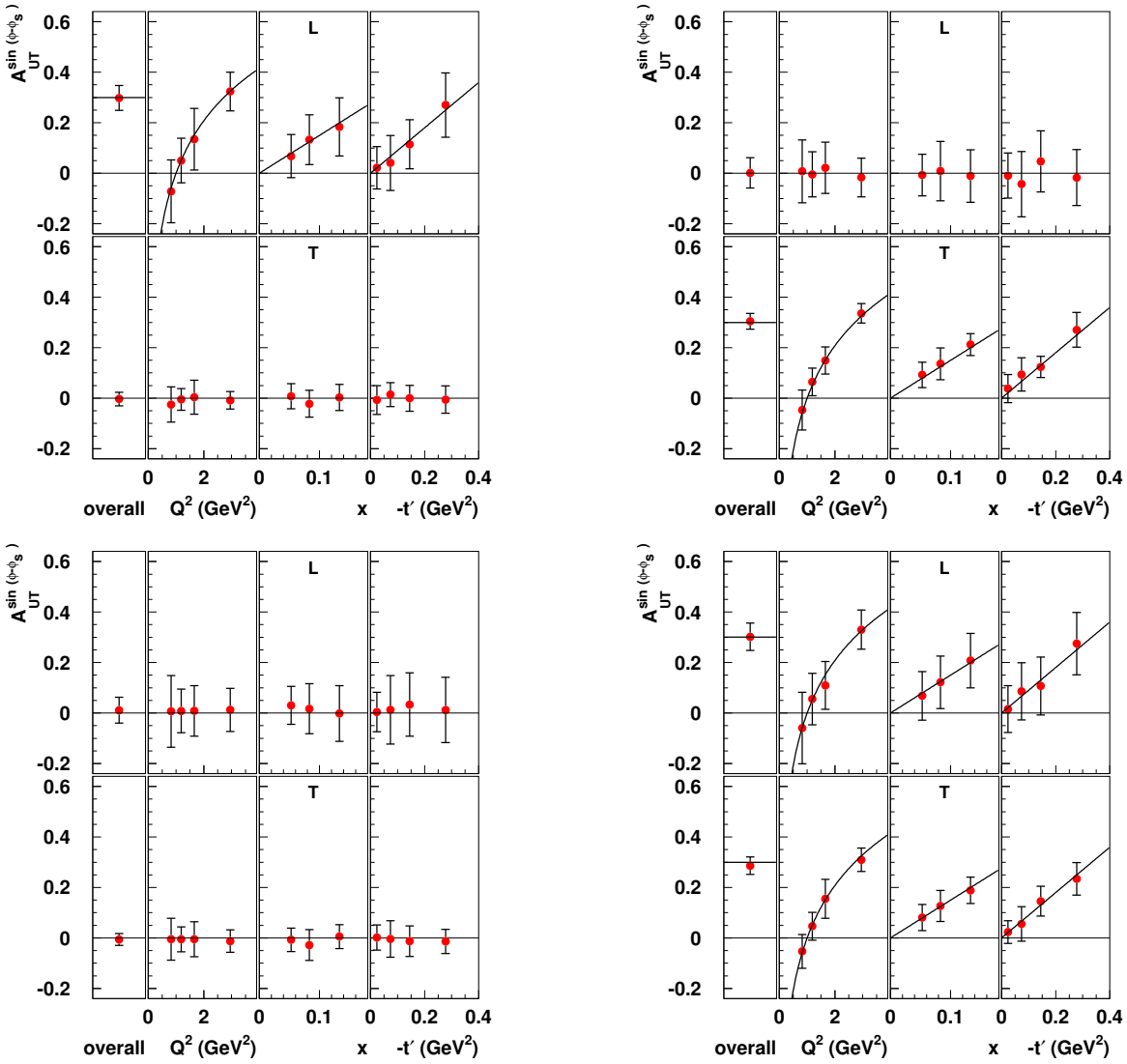

Figure 7.16: Monte Carlo studies performed on low-statistics, corresponding to the available data sample, testing the extraction method of the $\sin(\phi - \phi_s)$ azimuthal amplitude of the asymmetry and its kinematic dependences. Non-zero values are assigned to some of longitudinal (upper-left panel), transverse (upper-right), or interference (lower-left) terms and, simultaneously, to a random number of terms from all contributions (lower-right).

lation between various terms through the acceptance is correctly taken into account. The same test has been performed for only transverse or interference terms, as well as for some random SDMEs (see Figure 7.14). A good agreement is observed in all cases between the assigned and extracted values which shows the high efficiency of the extraction method.

Similar studies are performed also for samples with lower statistics, corresponding to that of the available data. In order to reduce the fluctuations imposed by the method of random spin assignment and also due to the low statistics, the procedure of random target spin assignment and the extraction of polarized SDME has been performed 30 times. The averaged values of all SDMEs as the central values, and the root mean squared (RMS) from the central values as

the uncertainties of extracted polarized SDMEs, are presented in Figure 7.15. The averaged extracted values of polarized SDMEs are in good agreement with the input values.

The extraction method is also tested concerning kinematic dependences. The $\sin(\phi - \phi_s)$ azimuthal amplitude of the asymmetry for longitudinal (L) and transverse (T) ρ^0 mesons as a function of Q^2, x_B and t', as well as the asymmetry at the average kinematics are displayed in Figure 7.16. The studies have been performed using a low-statistics Monte Carlo sample, thus the central values correspond to the averaged values of polarized SDMEs over 30 random target spin assignments and the uncertainties represent the RMS. Similar to the previous studies, four cases have been considered: assignment of longitudinal, transverse, interference terms and random terms from all contributions. In all cases a good agreement is observed between assigned and extracted values of the $\sin(\phi - \phi_s)$ azimuthal amplitude of the asymmetry.

These studies prove the high efficiency of the extraction method.

7.7 Systematic uncertainties

In this section an overview of the sources of systematic uncertainties and their effect on the measurement are presented. While only results at the average kinematics are shown, the studies have also been performed for each kinematic bin.

7.7.1 Target polarization

The measurement of the transverse SDMEs and transverse target-spin asymmetry requires a transversely polarized target. The measured value of the target polarization is 0.724 ± 0.059 (see Section 3.2.5). This results in a scale uncertainty of about 8.1%, which is not included in the total systematic uncertainty but quoted separately.

7.7.2 Transverse magnet correction

The transverse holding field of the target magnet that defines the polarization axis of the target protons, causes a bending of the trajectories of scattered lepton and produced charged particles (see Section 3.2.6). The vertex position and the scattering angles are corrected for those deflections. There are two methods of transverse magnet corrections for 04c1 and 05c1 data productions, while only one of the methods is available for 02c0 and 03c0 data productions. The measured values of SDMEs are compared using two transverse magnet correction methods for 04c1 and 05c1 data productions (see left panel of Figure 7.17).

Most of SDMEs measured with both transverse magnet correction methods agree, however for some of them the differences between two measurements are sizable. The origin of these differences is not quite well understood. However, one may argue that the large differences observed correspond to SDMEs involving longitudinal ρ^0_L mesons. As discussed in Section 5.3.2,

the transverse and longitudinal ρ^0 mesons have different signatures not only in the ρ^0 rest frame, but also in the laboratory frame. While the transverse ρ^0 mesons preferably lie in the plain nearly perpendicular to the incoming lepton beam, the longitudinal ρ^0 mesons fly nearly parallel to it. Thus the transverse holding field of the target magnet will affect the scattering angles stronger for the longitudinal ρ^0 mesons. For this case the two transverse magnet correction methods can give different results. This issue is under investigation. Meanwhile, the difference between the central values of the extracted SDMEs is assigned as a systematic uncertainty due to the transverse magnet correction.

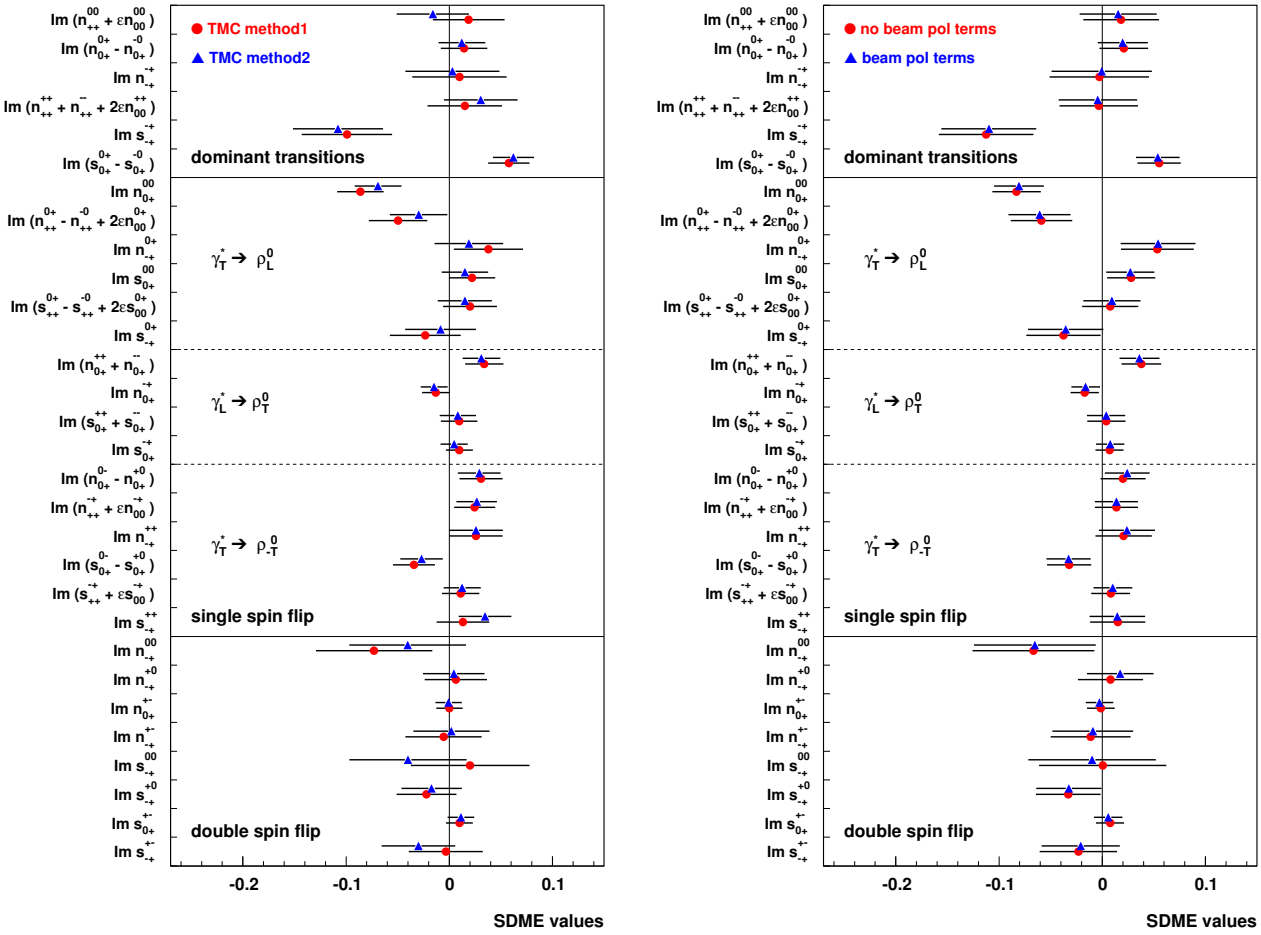

Figure 7.17: Left: Measurement of transverse SDMEs using two different target magnet correction methods. Right: The transverse SDMEs measured on the 2003-2005 data set, including and excluding the beam helicity dependent terms.

7.7.3 Residual beam polarization

In the years 2002-2005 the beam was longitudinally polarized (see Figure 7.18). In the year 2002, which contains only a small fraction of the available data, the beam polarization was not very low, but was not measured. The resulting average polarization for 2003-2005 data

is 33.5% for positive helicity (spin oriented parallel to the beam momentum) and 29.4% for negative helicity (spin antiparallel to the beam momentum). Thus the two helicity states yield a non-zero average polarization.

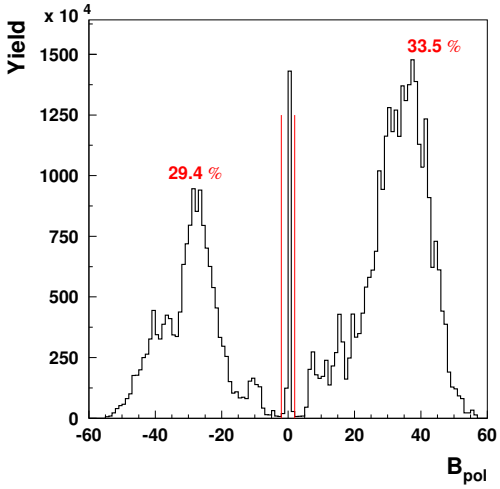

Figure 7.18: The beam polarization for 2002-2005 data taking periods. The excluded peak at the polarization value 0 corresponds to 2002 data when the polarization value was not measured.

Although the average beam polarization is small, the presence of a non-zero beam polarization gives rise to additional cross section terms associated with longitudinal beam polarization:

$$W(\phi_s,\phi,\vartheta,\varphi) = W_{UU}(\phi,\vartheta,\varphi) + P_\ell W_{LU}(\phi,\vartheta,\varphi) + S_T W_{UT}(\phi_s,\phi,\vartheta,\varphi)\ . \tag{7.26}$$

The angular distribution $W_{LU}(\phi,\vartheta,\varphi)$ for unpolarized target and longitudinally polarized beam is parameterized with 8 beam polarized SDMEs. These additional terms are discussed in Section 2.5.2 in the notation of Schilling-Wolf. In the notation of Diehl the angular distribution $W_{LU}(\phi,\vartheta,\varphi)$ is given as:

$$\begin{aligned}
W_{LU}^{LL}(\phi) &= -2\sin\phi\,\sqrt{\epsilon(1-\epsilon)}\,\mathrm{Im}\,u_{0+}^{0\,0}\,,\\
W_{LU}^{LT}(\phi,\varphi) &= \sin(\phi+\varphi)\,\sqrt{\epsilon(1-\epsilon)}\,\mathrm{Im}\big(u_{0+}^{0+}-u_{0+}^{-0}\big)\\
&\quad -\sin\varphi\,\sqrt{1-\epsilon^2}\,\mathrm{Im}\big(u_{++}^{0+}-u_{++}^{-0}\big)\\
&\quad -\sin(\phi-\varphi)\,\sqrt{\epsilon(1-\epsilon)}\,\mathrm{Im}\big(u_{0+}^{0-}-u_{0+}^{+0}\big)\,,\\
W_{LU}^{TT}(\phi,\varphi) &= -\sin\phi\,\sqrt{\epsilon(1-\epsilon)}\,\mathrm{Im}\big(u_{0+}^{++}+u_{0+}^{--}\big)+\sin(\phi+2\varphi)\,\sqrt{\epsilon(1-\epsilon)}\,\mathrm{Im}\,u_{0+}^{-+}\\
&\quad -\sin(2\varphi)\,\sqrt{1-\epsilon^2}\,\mathrm{Im}\,u_{++}^{-+}\\
&\quad +\sin(\phi-2\varphi)\,\sqrt{\epsilon(1-\epsilon)}\,\mathrm{Im}\,u_{0+}^{+-}\,.
\end{aligned} \tag{7.27}$$

The relation between both notations is given in Appendix E.1.

In order to study the influence of additional terms on the extracted values of SDMEs, the small fraction of the data with beam polarization $-2 < B_{pol} < 2$ is discarded. The 2003-2005 data is analyzed once taking into account the additional terms, and then neglecting these terms.

Only marginal differences are observed between both results, as shown in the right panel of Figure 7.17, which indicates that the acceptance effects were treated correctly in the extraction method, and the additional orthogonal terms did not influence the result. Hence no systematic uncertainty is assigned due to the residual beam polarization.

7.7.4 Background subtraction

Normalization

A fully tracked PYTHIA Monte Carlo simulation is used to estimate the semi-inclusive background contamination in the exclusive sample. The absolutely normalized yields from data and Monte Carlo simulation give an estimate of the background contribution (see Figure 7.1). In the region $2.4 < \Delta E < 5$ GeV, which is 3σ away from the exclusive peak, the data distribution can be considered not to be diluted by exclusive ρ^0 events (see Figure 7.19). Thus the deviation of the ratio of ΔE distribution for data and PYTHIA Monte Carlo simulation from unity in that region is taken as a measure for the systematic uncertainty on the number of exclusive ρ^0 events.

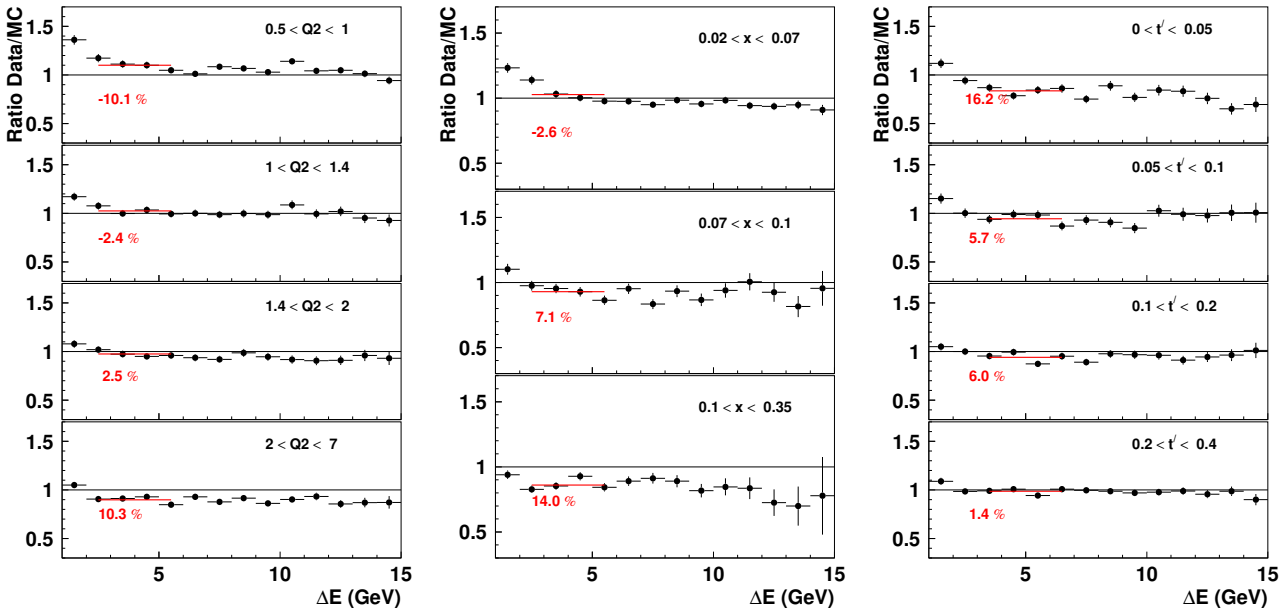

Figure 7.19: Ratios of ΔE distributions from data and Monte Carlo simulation in the semi-inclusive ΔE region in each bin of Q^2, x and t'.

The SDMEs, as well as the transverse target-spin asymmetry are extracted with background

fractions N_{bg}/N_{tot} that are corrected for the deviations of the data-to-simulation ratios from unity. Due to the small fractions of the background contamination, the results are not sensitive to the varied background fractions (see left panel of Figure 7.20). Hence no systematic uncertainty due to the background contamination is assigned.

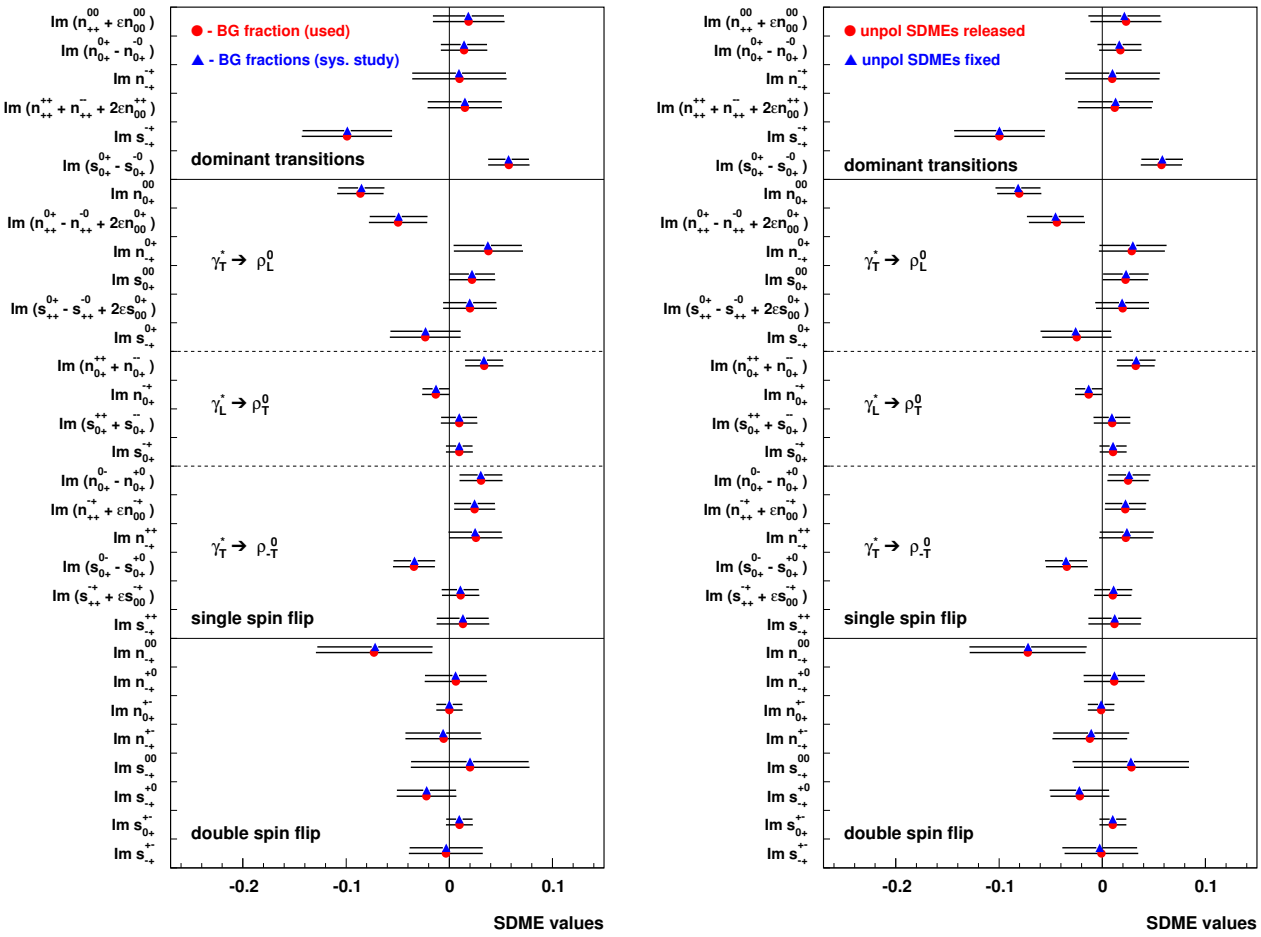

Figure 7.20: Left: Comparison of the transverse SDMEs after the background correction testing the influence of the uncertainty on the background fractions. Right: Measurement of the transverse SDMEs with released or fixed unpolarized SDMEs.

Background sample

The complication in the background correction is the unknown background angular distribution. Although the fraction of the background contribution is predicted by the PYTHIA Monte Carlo simulation, the angular distributions of various background processes are not fully described by the simulation.

So far the PYTHIA background sample was used for background correction, *i.e.* it was assumed that the background parameters corresponding to the transversely polarized angular distribution W_{UT} are zero. Since there is no Monte Carlo generator that generates all background processes contributing to exclusive ρ^0 production, there is no possibility to estimate the

background parameters for a transversely polarized target. In addition, the $\cos\vartheta$ distributions of the PYTHIA simulation seem to be mirrored compared to the real data in various ΔE regions (see Figure 7.3) and there is no other generator for unpolarized events to cross check the unpolarized angular distributions predicted by PYTHIA.

Thus the systematic uncertainty due to an imperfect background correction is estimated as difference between uncorrected and background-corrected SDME values (see Figure 7.8). This uncertainty is larger than the one between different background subtraction methods, hence no additional systematic uncertainty is assigned for this source.

7.7.5 Correlation of unpolarized and polarized SDMEs

Until now the normalization of the p.d.f. was not taken into account, since the measured values of unpolarized SDMEs have been used. In this case the normalization integral does not depend on the unknown parameters, thus was omitted (see Section 7.4.2). The 15 unpolarized and 30 transverse SDMEs are completely independent, however the SDMEs are correlated through the acceptance. These correlations are not taken into account when computing the unpolarized angular distribution with already measured unpolarized SDMEs. Therefore a study has been performed releasing the unpolarized SDMEs and normalizing the p.d.f. as given in equation (7.19). The normalization integral is calculated similar to equation (7.14). In this case all 45 SDMEs are treated as free parameters.

The extracted values of transverse SDMEs from this study are in agreement with the ones extracted with fixed values of unpolarized SDMEs (see right panel of Figure 7.22). This is another prove that the acceptance was taken into account correctly and the additional orthogonal terms do not affect the result. No systematic uncertainty is assigned to account for the correlation of unpolarized SDMEs.

7.7.6 Admixture of longitudinal target polarization S_L

Systematic uncertainty on the extracted values of the transverse SDMEs

If the target polarization is defined with respect to the lepton beam direction, the angular distribution receives an additional contribution due to the longitudinal component of the target polarization S_L with respect to the virtual photon direction:

$$W(\phi_s, \phi, \vartheta, \varphi) = W_{UU}(\phi, \vartheta, \varphi) + S_L W_{UL}(\phi, \vartheta, \varphi) + S_T W_{UT}(\phi_s, \phi, \vartheta, \varphi) \; . \tag{7.28}$$

The two definitions of the target polarization, P_T and S_T, are related to each other through the angle θ_γ (see equation (6.7)). Although the angle θ_γ is small, it results in non-negligible values of $|S_L/P_T|$. Still, the ratio S_T/P_T is very close to unity (see Figure 7.21).

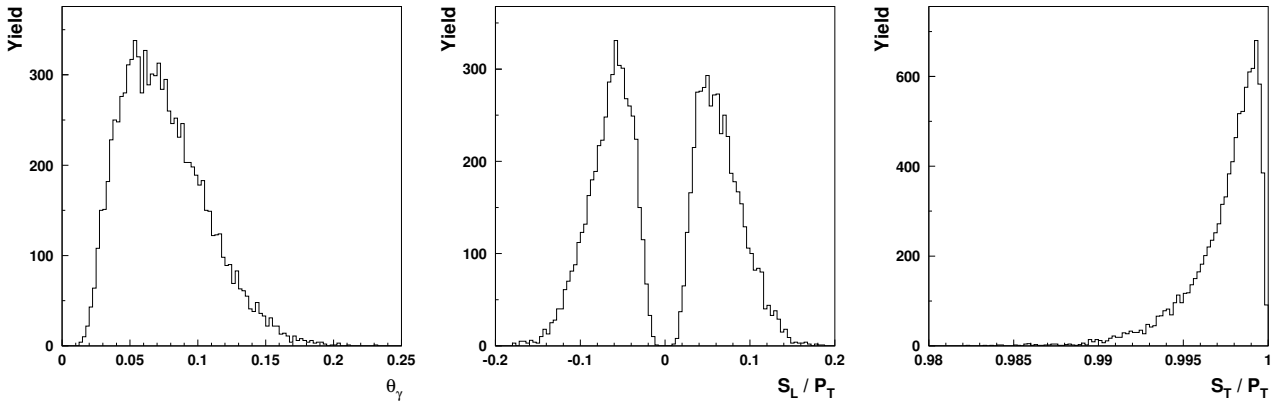

Figure 7.21: From left to write: Yield distributions for the angle θ_γ, the ratios S_L/P_T and S_T/P_T.

The angular distribution W_{UL} is described by 14 SDMEs:

$$
\begin{aligned}
W_{UL}^{LL}(\phi) &= -2\sin\phi\,\sqrt{\epsilon(1+\epsilon)}\,\mathrm{Im}\,l_{0+}^{0\,0} - \sin(2\phi)\,\epsilon\,\mathrm{Im}\,l_{-+}^{0\,0}\,,\\
W_{UL}^{LT}(\phi,\varphi) &= \sin(\phi+\varphi)\,\sqrt{\epsilon(1+\epsilon)}\,\mathrm{Im}\big(l_{0+}^{0+} - l_{0+}^{-0}\big)\\
&\quad - \sin\varphi\;\mathrm{Im}\big(l_{++}^{0+} - l_{++}^{-0} + 2\epsilon l_{0\,0}^{0+}\big) + \sin(2\phi+\varphi)\,\epsilon\,\mathrm{Im}\,l_{-+}^{0+}\\
&\quad - \sin(\phi-\varphi)\,\sqrt{\epsilon(1+\epsilon)}\,\mathrm{Im}\big(l_{0+}^{0-} - l_{0+}^{+0}\big) + \sin(2\phi-\varphi)\,\epsilon\,\mathrm{Im}\,l_{-+}^{+0}\,,\\
W_{UL}^{TT}(\phi,\varphi) &= \tfrac{1}{2}\sin(2\phi+2\varphi)\,\epsilon\,\mathrm{Im}\,l_{-+}^{-+}\\
&\quad - \sin\phi\,\sqrt{\epsilon(1+\epsilon)}\,\mathrm{Im}\big(l_{0+}^{++} + l_{0+}^{--}\big) + \sin(\phi+2\varphi)\,\sqrt{\epsilon(1+\epsilon)}\,\mathrm{Im}\,l_{0+}^{-+}\\
&\quad - \sin(2\varphi)\;\mathrm{Im}\big(l_{++}^{-+} + \epsilon l_{0\,0}^{-+}\big) - \sin(2\phi)\,\epsilon\,\mathrm{Im}\,l_{-+}^{++}\\
&\quad + \sin(\phi-2\varphi)\,\sqrt{\epsilon(1+\epsilon)}\,\mathrm{Im}\,l_{0+}^{+-} + \tfrac{1}{2}\sin(2\phi-2\varphi)\,\epsilon\,\mathrm{Im}\,l_{-+}^{+-} \quad .
\end{aligned}
\tag{7.29}
$$

As in previous cases, these SDMEs can be correlated with the transverse SDMEs through the acceptance. They can not be treated as free parameters (see Section 7.4.2), instead random values are assigned to them in ranges given by positivity constraints.

The positivity constraints are calculated for the squared sum of real and imaginary parts of the s-channel helicity conserving SDME, l_{0+}^{0+}

$$
\big(\mathrm{Re}\,l_{0+}^{0+}\big)^2 + \big(\mathrm{Im}\,l_{0+}^{0+}\big)^2 \le u_{0\,0}^{0\,0}\,u_{++}^{++} - \big(\mathrm{Re}\,u_{0+}^{0+}\big)^2 - \big(\mathrm{Im}\,u_{0+}^{0+}\big)^2\,, \tag{7.30}
$$

and for the combination of two helicity-conserving SDMEs:

$$
\big(l_{++}^{++}\big)^2 + \big(\mathrm{Im}\,l_{-+}^{-+}\big)^2 \le \big(u_{++}^{++}\big)^2 - \big(u_{-+}^{-+}\big)^2\,. \tag{7.31}
$$

But the positivity constraints of SDMEs $\mathrm{Im}\, l^{0+}_{0+}$ and $\mathrm{Im}\, l^{-+}_{-+}$ are required, therefore the following relations are used:

$$\left(\mathrm{Im}\, l^{0+}_{0+}\right)^2 \leq u^{0\,0}_{0\,0}\, u^{++}_{++} - \left(\mathrm{Im}\, u^{0+}_{0+}\right)^2 \qquad \left(\mathrm{Im}\, l^{-+}_{-+}\right)^2 \leq \left(u^{-+}_{-+}\right)^2 . \tag{7.32}$$

Since the s-channel helicity non-conserving SDMEs are expected to be smaller than the s-channel helicity conserving SDMEs, the positivity constraints are also used for the other SDMEs. Repeating the procedure of random values assignment for SDMEs l several times, mean values as well as RMS values are obtained for the transverse SDMEs. The RMS values represent the deviation of the SDMEs n and s from the central values due to the possible contributions of additional terms l to the angular distribution (see Figure 7.22).

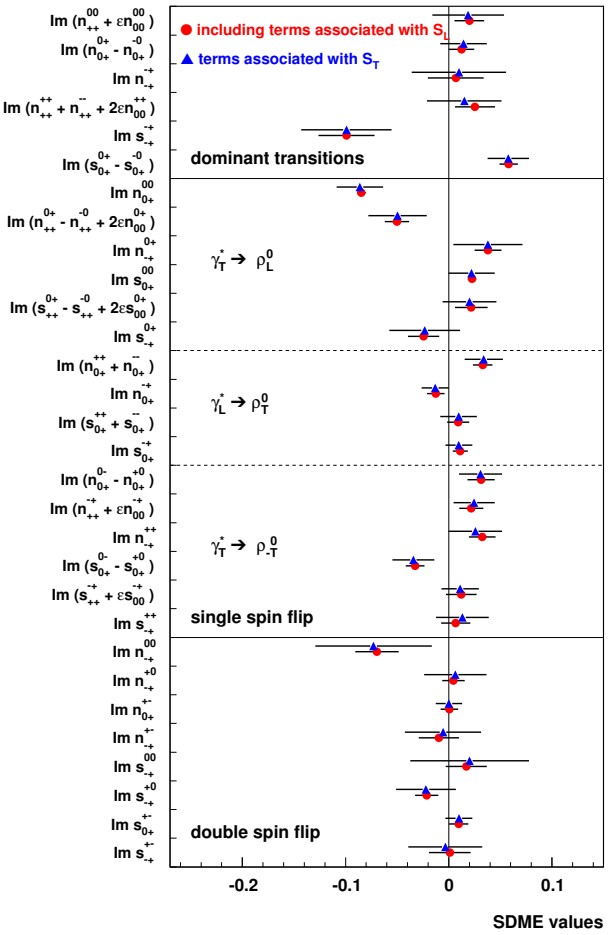

Figure 7.22: The transverse SDMEs extracted including and excluding the terms associated with the longitudinal component of the target polarization with respect to the virtual photon direction. The error bars represent the RMS values of the measurement which includes the additional terms.

The RMS of the deviations is assigned as systematic uncertainty due to the admixture of the longitudinal target polarization S_L.

Extraction of the asymmetry with respect to the lepton beam direction

The two methods of asymmetry extraction (see Section 7.5.2) are in principle also applicable in the case that the target polarization is defined with respect to the lepton beam direction. However, practically only the direct measurement of asymmetries is possible, since the simultaneous extraction of both longitudinal and transverse SDMEs, entangled with $\cos\theta_\gamma$ and $\sin\theta_\gamma$ terms (see Appendix E.2), is not possible due to limited statistics and too small values of the angle θ_γ. As for the asymmetries, the angular distribution parameterized through asymmetries receives additional terms (see Section 6.8.2). The $\sin(\phi - \phi_s)$ amplitude of the asymmetry $A_{UT}^{LL\,\gamma^*}(\phi, \phi_s)$ is extracted taking into account these additional terms. The results are presented in Figure 7.23.

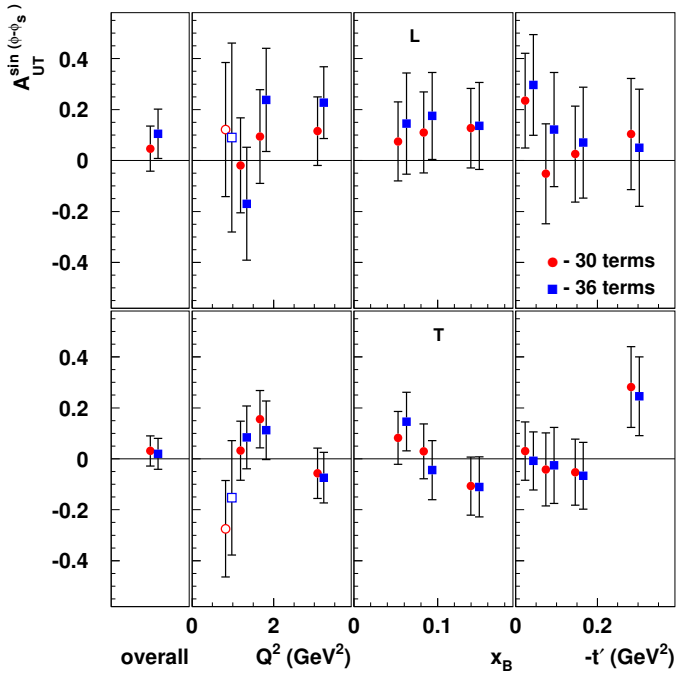

Figure 7.23: The $\sin(\phi - \phi_s)$ azimuthal amplitude of the asymmetry, extracted with respect to the lepton beam direction $A_{UT}^{l}(\phi, \phi_s)$ or with respect to the virtual-photon direction $A_{UT}^{l}(\phi, \phi_s)$ for longitudinal (L) and transverse (T) ρ^0 mesons at average kinematics as well as the Q^2, x_B and t'.

The difference of the central values is assigned as systematic uncertainty due to the admixture of the longitudinal target polarization S_L.

7.7.7 Radiative corrections

The effect of radiative corrections has been discussed in Section 5.1.2. Studies (see Section 5.3.3) for exclusive ρ^0 production have shown that the emission of a real photon, which affects the virtual photon kinematics, enlarge the values of ΔE and smear the events out of the ΔE peak. This results in a reduction of the cross section in the exclusive region ($\Delta E < 0.6$ GeV) by

about 10%. For the events found inside the ΔE peak although a real photon was radiated, the scattered lepton is detected with a four-momentum that does not account for the loss of energy by the photon radiation. As a consequence also the computed values of Q^2 and x_B will differ from the true kinematics. Such an event appears to have a higher energy transfer than it had in reality, *i.e.* for final state radiation $\nu_{obs} = E - E' > E - (E' + E_\gamma) = \nu_{true}$. The relations $Q^2_{obs} < Q^2_{true}$ and $x_{B_{obs}} < x_{B_{true}}$ always hold true for initial and final state radiation. The loop corrections and vertex corrections, where there is no a real photon radiated, do not change the kinematics of the reaction. Depending on the magnitude of the change in these variables and also on the bin size, the events may be reconstructed in a bin that the event does not belong to.

For exclusive ρ^0 production the lepton kinematics is not affected considerably, since the events with a radiated photon which are found inside the exclusive region ($\Delta E < 0.6$ GeV), are the ones with a low-energy photon radiated. In addition the binning used for the analysis is wide enough, so no sizable migration from bin to bin is observed. Since the angular distribution receives only marginal distortions from radiative corrections (the ratios of normalized angular distributions with and without radiative corrections are flat within statistics) the influence of radiative corrections on the measurement of SDMEs is negligible. In the transverse target-spin asymmetry measurement, since radiative corrections are not target-spin dependent, they should be of equal size for both polarization states, and therefore have no effect on the measurement. Hence no additional systematic uncertainty is applied to account for radiative effects.

7.7.8 Detector smearing

The scattered lepton can encounter multiple scattering with detector material after the scattering off the target nucleon. This might change the momentum (energy) of the reconstructed track compared with original kinematics. *Detector smearing effects* may cause a migration of events into adjacent bins, hence they define the physical limit on the resolution of the spectrometer. Thus the minimum bin size is limited by the physical resolution of the spectrometer. The resolution of the spectrometer for a certain kinematic quantity can be quantified by Monte Carlo simulations (see Section 5.4). The binning used for the analysis presented in this thesis is much larger than the actual detector resolution, therefore no large smearing effects are take place. Hence no additional systematic uncertainty is applied due to detector smearing effects.

7.7.9 Detector misalignment

Detailed studies concerning the misalignment of the HERMES detector have shown that the two halves of the HERMES spectrometer are not perfectly aligned to each other. The tilt and the offset of each detector half was estimated with respect to a perfectly aligned detector [104]. The estimated misalignment does not necessarily come from the real tilt and offset of the

spectrometer, but can be introduced by the HERMES reconstruction software that uses the force bridge technique (see Section 3.3.2). Misalignment leads to an overall shift in the kinematic distributions as it affects the reconstructed angles of the particles.

The measurement of azimuthal quantities can be biased by a misaligned spectrometer leading to misreconstruction of the particle tracks. The effect of the detector misalignment can be estimated by two Monte Carlo simulations reconstructed in the HERMES acceptance using two different sets for the detector geometry: one set corresponding to a perfectly aligned detector, and the other for a 'misaligned' detector. The systematic uncertainty due to the detector misalignment is the resulting difference between the extracted values of SDMEs or transverse target-spin asymmetry from the two Monte Carlo simulations.

At the moment there is no Monte Carlo generator for a transversely polarized target. Hence a systematic uncertainty due to detector misalignment can presently not be calculated. The uncertainty is however expected to be small compared to statistical uncertainties, because the effects caused by the misalignment do not depend on the polarization of the target proton and should thus cancel in the measurements of transverse target-spin asymmetry and polarized SDMEs.

Chapter 8

Final results and comparison with theory predictions

"Prediction is very difficult, especially about the future."
— Niels Bohr (1885 - 1962)

8.1 Results on SDMEs

The extraction of 15 unpolarized and 30 transverse SDMEs from the HERMES data accumulated during the 2002-2005 data taking periods using the maximum likelihood method was described in the previous chapter. Studies of the systematic uncertainties for the unpolarized SDMEs can be found in [52]. In the course of this thesis, studies have been performed to estimate the systematic uncertainties of the transverse SDMEs due to the target polarization (see Section 7.7.1), transverse magnet correction (see Section 7.7.2), residual beam polarization (see Section 7.7.3), background subtraction (see Section 7.7.4), correlation of unpolarized and polarized SDMEs (see Section 7.7.5) and the admixture of longitudinal target polarization S_L (see Section 7.7.6). The systematic uncertainties due to radiative corrections, misalignment and detector smearing have been considered to be negligible. The dominant systematic uncertainty is that due to the transverse magnet correction.

8.1.1 Unpolarized SDMEs

The values of the unpolarized SDMEs that were used for the extraction of the transverse SDMEs, are extracted from the 2002-2005 data sample and listed in Tables F.1-F.4 in the notation of Diehl. The t' dependence of the unpolarized SDMEs is shown in Figure 8.1, where it is compared to the theoretical expectations suggested by the partial wave decomposition of the transition amplitudes [17]. For each unpolarized SDME, a $(-t')^{p/2}$ dependence is expected with a certain minimum value of the parameter p given by equation (6.40) [17]. The actual power controlling the t' dependence of the SDME can be larger than the minimum value p_{min} if

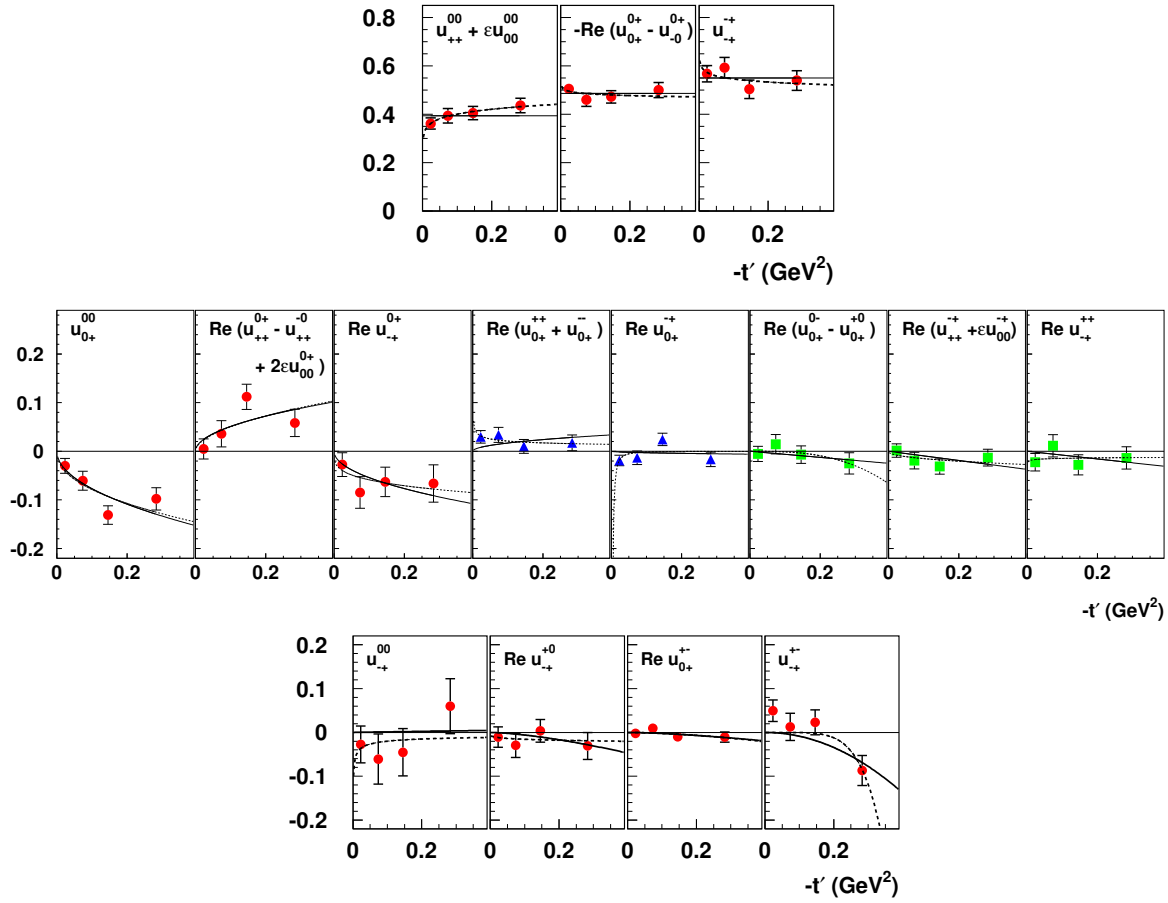

Figure 8.1: The t' dependence of unpolarized SDMEs ordered into three classes according to the hierarchy predicted by the factorization theorem (notations hold as in Figure 7.10). The data are fitted with a functional form $\propto (-t')^{p/2}$, where p is either a constant (solid line), fixed at the minimum value of p_{min}, or a free parameter p_{fit} (dotted line). The values of p_{min}, p_{fit} and the corresponding reduced $\chi^2/n.f.d.$ values of the fits are listed in Table 8.1.

there is, *e.g.*, no helicity transferred by the t-channel exchange. The values of p_{min} are presented in Table 8.1.

First, the t' dependences of the unpolarized SDMEs are fitted according to these expectations (solid lines), then the distributions are also fitted treating p as a free parameter (see Figure 8.1). The corresponding values of the parameter p as well as the reduced $\chi^2/n.f.d.$ of the fits performed are presented in Table 8.1. The SDMEs are ordered according to the hierarchy suggested by the factorization theorem (see Section 6.7.4). For the SDMEs involving SCHC, the predicted values p_{min} and the fitted values p_{fit} are mostly in agreement. As for the SDMEs corresponding to the transition $\gamma^*_T \to \rho^0_L$, the fitted values p_{fit} agree within statistical uncertainties with the minimum values p_{min}. In other words, although these SDMEs contain s-channel helicity non-conserving amplitudes, the actual value of the power controlling the t' dependence of the SDMEs is not larger than the minimum value, which was not excluded by theory. For the SDMEs corresponding to the other transitions, the t' dependence is weak, so

that the fit can not reveal any sensitivity to the power p_{fit}.

transition	SDME	p_{min}	$\chi^2/n.d.f.$	p_{fit}	$\chi^2/n.d.f.$
$\gamma_L^* \to \rho_L^0$ $\gamma_T^* \to \rho_T^0$	$u_{++}^{00} + \epsilon u_{00}^{00}$	0	1.35	0.14 ± 0.07	0.04
	$u_{0+}^{0+} - u_{0+}^{-0}$	0	0.78	-0.03 ± 0.07	0.97
	u_{-+}^{-+}	0	0.93	-0.07 ± 0.08	0.96
$\gamma_T^* \to \rho_L^0$	u_{0+}^{00}	1	2.06	0.90 ± 0.24	3.02
	$u_{++}^{0+} - u_{++}^{-0} + 2\epsilon \operatorname{Re} u_{00}^{0+}$	1	1.90	1.05 ± 0.50	2.86
	u_{-+}^{0+}	1	0.60	0.54 ± 0.47	0.61
$\gamma_L^* \to \rho_T^0$	$\operatorname{Re}(u_{0+}^{++} + u_{0+}^{--})$	1	1.79	-0.56 ± 0.62	0.45
	$\operatorname{Re} u_{0+}^{-+}$	1	2.86	-3.33 ± 0.61	2.85
$\gamma_T^* \to \rho_{-T}^0$	$\operatorname{Re}(u_{0+}^{0-} - u_{0+}^{+0})$	2	0.37	5.82 ± 2.82	0.36
	$\operatorname{Re}(u_{++}^{-+} + \epsilon u_{00}^{-+})$	2	0.82	0.87 ± 0.83	0.86
	$\operatorname{Re} u_{-+}^{++}$	2	0.88	-0.21 ± 0.94	0.93
double spin flip	u_{-+}^{00}	2	1.05	-0.81 ± 1.41	1.06
	$\operatorname{Re} u_{-+}^{+0}$	3	0.45	0.38 ± 1.32	0.53
	$\operatorname{Re} u_{0+}^{+-}$	3	0.52	3.40 ± 2.35	0.77
	u_{-+}^{+-}	4	2.24	11.19 ± 1.02	2.46

Table 8.1: Minimum and fitted values of the exponent p, p_{min} and p_{fit}, controlling the $(-t')^{p/2}$ behavior of each unpolarized SDMEs at $t' \to 0$. The reduced $\chi^2/n.d.f.$ values of fits are presented in corresponding columns.

8.1.2 Transverse SDMEs

The final results on transverse SDMEs calculated at average kinematics are presented in Figure 8.2 and listed in Table F.5. The SDMEs are ordered according to the hierarchy suggested by the factorization theorem (see Section 6.7.4).

Although the six SDMEs of the first class are not restricted to be zero in the case of SCHC, only for two of them, $\operatorname{Im} s_{-+}^{-+}$ and $\operatorname{Im}\left(s_{0+}^{0+} - s_{0+}^{-0}\right)$, there is an indication of non-zero values. The SDME of special interest related to the $\sin(\phi - \phi_s)$ azimuthal amplitude of the asymmetry (see Section 6.8.1), $\operatorname{Im}\left(n_{++}^{00} + \epsilon n_{00}^{00}\right)$, is consistent with zero within a large uncertainty.

In the second class, there is an indication of non-zero values for s-channel helicity non-conserving SDMEs only for two SDMEs, $\operatorname{Im} n_{0+}^{00}$ and $\operatorname{Im}\left(n_{++}^{0+} - n_{++}^{-0} + 2\epsilon n_{00}^{0+}\right)$. The observed value of the SDME $\operatorname{Im} n_{0+}^{00}$ is the strongest indication of s-channel helicity non-conservation in the measured set of transverse SDMEs. This SDME is the polarized equivalent of the

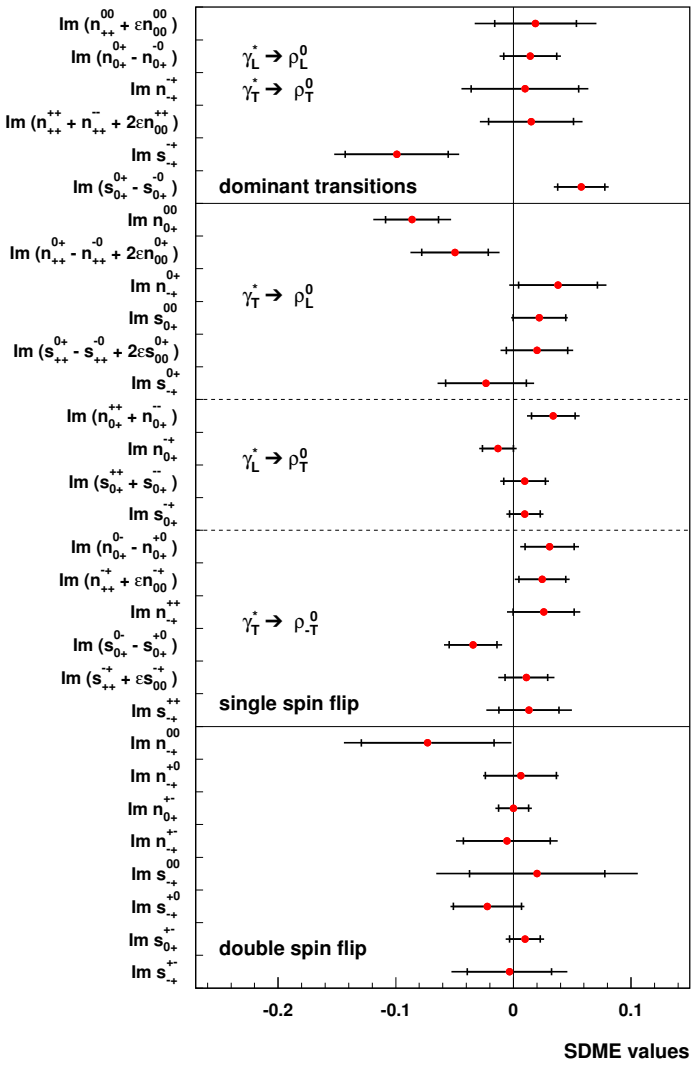

Figure 8.2: The transverse SDMEs calculated at the average kinematics in the entire region $1 < Q^2 < 7$ GeV^2, $0.02 < x_B < 0.4$ and $-t' < 0.4$ GeV^2. While the inner error bars show the statistical uncertainty only, the outer error bars represent the total uncertainty with statistical and systematic uncertainties combined in quadrature. There is an additional 8.1 % scale uncertainty from the target polarisation measurement.

largest unpolarized s-channel helicity non-conserving SDME $\mathrm{Im}\, u^{00}_{0+}$. However, the strength of s-channel helicity non-conservation is smaller in the polarized case. All other transverse SDMEs are consistent with zero.

As for the SDMEs of the third class, involving two helicity-flip amplitudes, no s-channel helicity violation is observed.

According to theoretical expectations (see Section 6.7.4), the SDMEs s may be smaller compared to the SDMEs n having the same indices, $s^{ij}_{kl} < n^{ij}_{kl}$, although exceptions are not excluded. Indeed, the SDME s^{-+}_{-+} is larger compared to its counterpart n^{-+}_{-+}, and the same holds for $\mathrm{Im}(s^{0+}_{0+} - s^{-0}_{0+})$ compared to $\mathrm{Im}(n^{0+}_{0+} - n^{-0}_{0+})$. In terms of natural and unnatural-parity-

exchange amplitudes these SDMEs read:

$$\begin{aligned} s^{-+}_{-+} &\propto \sum_{\sigma} \left[N^{-\sigma}_{-+} \left(U^{+\sigma}_{+-}\right)^* + U^{-\sigma}_{-+} \left(N^{+\sigma}_{+-}\right)^* \right], \\ s^{0+}_{0+} &\propto \sum_{\sigma} \left[N^{0\sigma}_{0+} \left(U^{+\sigma}_{+-}\right)^* + U^{0\sigma}_{0+} \left(N^{+\sigma}_{+-}\right)^* \right]. \end{aligned} \tag{8.1}$$

Both SDMEs, $\mathrm{Im}\, s^{-+}_{-+}$ and $\mathrm{Im}\left(s^{0+}_{0+} - s^{-0}_{0+}\right)$, involve biggest natural-parity-exchange amplitude N^{-+}_{-+} and N^{0+}_{0+}, respectively, and biggest unnatural-parity-exchange amplitude U^{++}_{+-}. From results on an unpolarized target [52], the unnatural-parity-exchange contribution was measured to be non-zero [52]. In particular, the amplitude U^{++}_{+-} which corresponds to the pion-exchange in the Regge theory, was found to be sizable. The non-zero values of SDMEs $\mathrm{Im}\, s^{-+}_{-+}$ and $\mathrm{Im}\left(s^{0+}_{0+} - s^{-0}_{0+}\right)$ are not surprising and suggest the existence of unnatural-parity exchange also in the case of a transversely polarized target [105].

The extracted values of transverse SDMEs in bins of Q^2, x_B or t' are listed in Table F.6, Table F.7, Table F.8.

Up to this point, in the context of the GPD formalism only the longitudinal amplitude $\gamma^*_L p \to \rho^0_L p'$ has been considered, since the transverse amplitude has a infrared singularity and hence cannot be calculated. In a recent analysis by Goloskokov and Kroll [19], the quark transverse momentum is retained in a modified perturbative approach (for a more detailed discussion see Section 8.3) in order to be able to regularize the singularity of the transverse amplitude. Thus the amplitude describing the transition between transversely polarized photons and mesons, $\gamma^*_T p \to \rho^0_T p'$, is calculated. Using the GPD models by Goloskokov, Kroll (see Section G.3), the Q^2 dependence of SDMEs associated with the longitudinal and transverse amplitudes, $\gamma^*_L p \to \rho^0_L p'$ and $\gamma^*_T p \to \rho^0_T p'$, are estimated for the case that the proton target polarization is perpendicular (*i.e.* 'normal') with respect to the scattering plane $\gamma^* p \to \rho^0 p'$. The model predictions obtained for $W = 5$ GeV and $Q^2 > 2$ GeV^2 are in good agreement with the extracted values of SDMEs (see Figure 8.3).

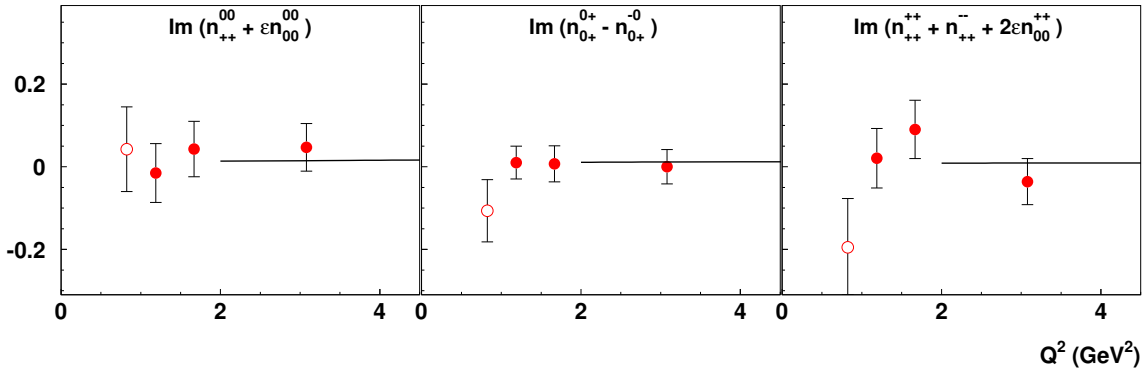

Figure 8.3: The Q^2 dependence of three 'normal' transverse SDMEs associated with the amplitudes $\gamma^*_L p \to \rho^0_L p'$ and $\gamma^*_T p \to \rho^0_T p'$ compared to the model predictions by Goloskokov, Kroll [19].

Similar to the unpolarized case, the partial wave decomposition of the transition amplitudes [17] suggests a $(-t')^{q/2}$ dependence of the transverse SDMEs, with predictions available [17] for the minimum value of the exponent q_{min} (see equation (6.45)). However, due to large experimental uncertainties, only for some SDMEs the data indicates a possible t' dependences that can be tested. These dependences are fitted with a functional form $(-t')^{q/2}$, where q is either a constant, fixed at the minimum values of q_{min} suggested by [17], or a free parameter that gives the actual power q_{fit} that controls the t' dependence of the SDMEs (see Figure 8.4). The minimum values q_{min}, the actual power q_{fit} with its uncertainty and the corresponding reduced $\chi^2/n.f.d.$ of the fits are listed in Table 8.2 for each SDME. Similar to the unpolarized case, the values of the fitted parameters are in agreement with the predicted values of q_{min}, although the large experimental uncertainties prevent clear conclusions.

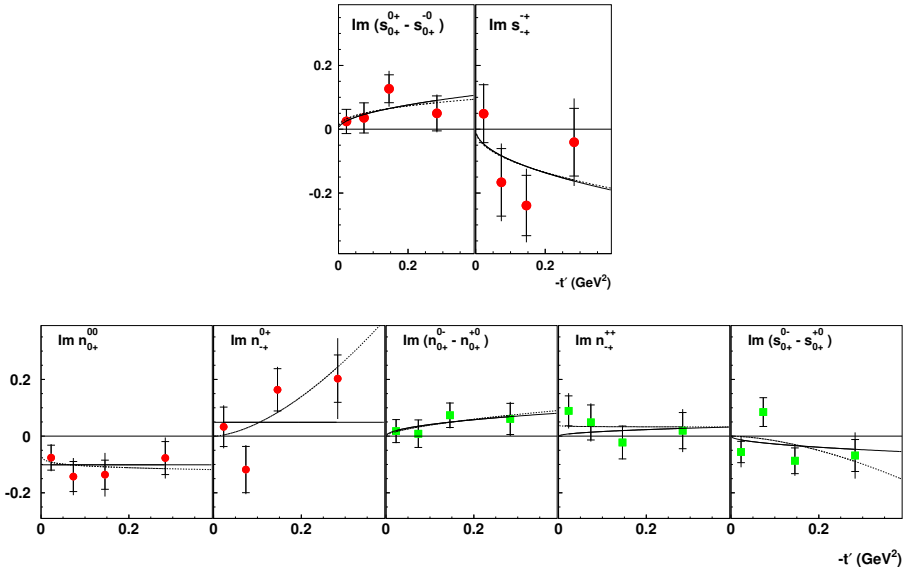

Figure 8.4: The t' dependence of some transverse SDMEs. The data are fitted with a functional form $\propto (-t')^{q/2}$, where q is either a constant (solid line), fixed at the minimum value of q_{min}, or a free parameter q_{fit} (dotted line). The values of q_{min}, q_{fit} and the corresponding reduced $\chi^2/n.f.d.$ values of the fits are listed in Table 8.2.

8.1.3 RhoMC with transversely polarized target

Another result, which will complete the discussion on SDMEs, is a Monte Carlo generator simulating the exclusive electroproduction and decay of ρ^0 mesons for both unpolarized and polarized targets. The rhoMC Monte Carlo generator, capable of simulating such a process in the case of an unpolarized or a longitudinally polarized beam and an unpolarized target, is described in detail in Section 5.2. An extension of rhoMC in order to also include a transversely polarized target would be of special interest for the semi-inclusive analysis of pion leptoproduction on a transversely polarized target, where the $\rho^0 \to \pi^+\pi^-$ decay products constitute

transitions	SDMEs	q_{min}	$\chi^2/n.d.f.$	q_{fit}	$\chi^2/n.d.f.$
$\gamma^*_L \to \rho^0_T$	$\mathrm{Im}(s^{0+}_{0+} - s^{-0}_{0+})$	1	0.58	0.75 ± 0.86	0.84
$\gamma^*_L \to \rho^0_T$	$\mathrm{Im}\, s^{-+}_{-+}$	1	1.13	0.94 ± 0.81	1.69
$\gamma^*_T \to \rho^0_L$	$\mathrm{Im}\, n^{00}_{0+}$	0	0.33	0.18 ± 0.49	0.45
$\gamma^*_T \to \rho^0_L$	$\mathrm{Im}\, n^{0+}_{-+}$	0	2.31	3.23 ± 1.74	2.02
$\gamma^*_T \to \rho^0_{-T}$	$\mathrm{Im}(n^{0-}_{0+} - n^{+0}_{0+})$	1	0.19	1.24 ± 1.49	0.28
$\gamma^*_T \to \rho^0_{-T}$	$\mathrm{Im}\, n^{++}_{-+}$	1	0.82	-0.05 ± 0.95	0.85
$\gamma^*_T \to \rho^0_{-T}$	$\mathrm{Im}(s^{0-}_{0+} - s^{+0}_{0+})$	1	2.06	3.30 ± 1.68	2.81

Table 8.2: Minimum and fitted values of the exponent q, q_{min} and q_{fit}, controlling the $(-t')^{q/2}$ behavior of some transverse SDMEs at $t' \to 0$. The reduced $\chi^2/n.d.f.$ values of the fits are also presented in corresponding columns.

background contamination. The background fractions could then be estimated by Monte Carlo simulations using the PYTHIA and rhoMC generators [106, 107]. However, up to now, it was not possible to derive the asymmetry transferred from the ρ^0 meson to the decay pions without the knowledge of transverse SDMEs. In this section first attempts are presented to modify the rhoMC generator in order to simulate exclusive ρ^0 production in the case of a transversely polarized target.

The total cross section of exclusive ρ^0 production is a superposition of unpolarized and polarized cross sections: $\sigma = \sigma_{UU} + S_T \sigma_{UT}$, and additionally it can be factorized in terms of angle-dependent and independent parts (see equation (5.9)). The angle-independent part is generated for both unpolarized and transversely polarized targets in a similar way. While in the case of an unpolarized target the electroproduction and decay of the ρ^0 meson is described by 8 independent variables (see Table 5.1), in the case of a transversely polarized target there is an additional degree of freedom, ϕ_s, which describes the orientation of the target polarization with respect to the virtual-photon direction. Another difference occurring when introducing the transversely polarized target is the definition of the ρ^0 production angle. The existing two definitions of angles (see Section 6.3) differ by sign: $\Phi = -\phi$. As discussed in Section 6.3, the definition of the production angle ϕ in accordance with the Trento convention [97] is currently used to describe the angular distribution of exclusive ρ^0 production, particularly in the case of a transversely polarized target. Thus the rhoMC generator was given the flexibility to switch between two modes and generate the production angle in accordance with two notations used to describe the angular distribution. If the transversely polarized target is considered, also the unpolarized angular distribution is defined using the Diehl notation.

The shapes of the angular distributions ϕ, ϑ, φ and ϕ_s simulated by rhoMC are compared to the ones from data (see Figure 8.5). As for the unpolarized case, the absolute cross section

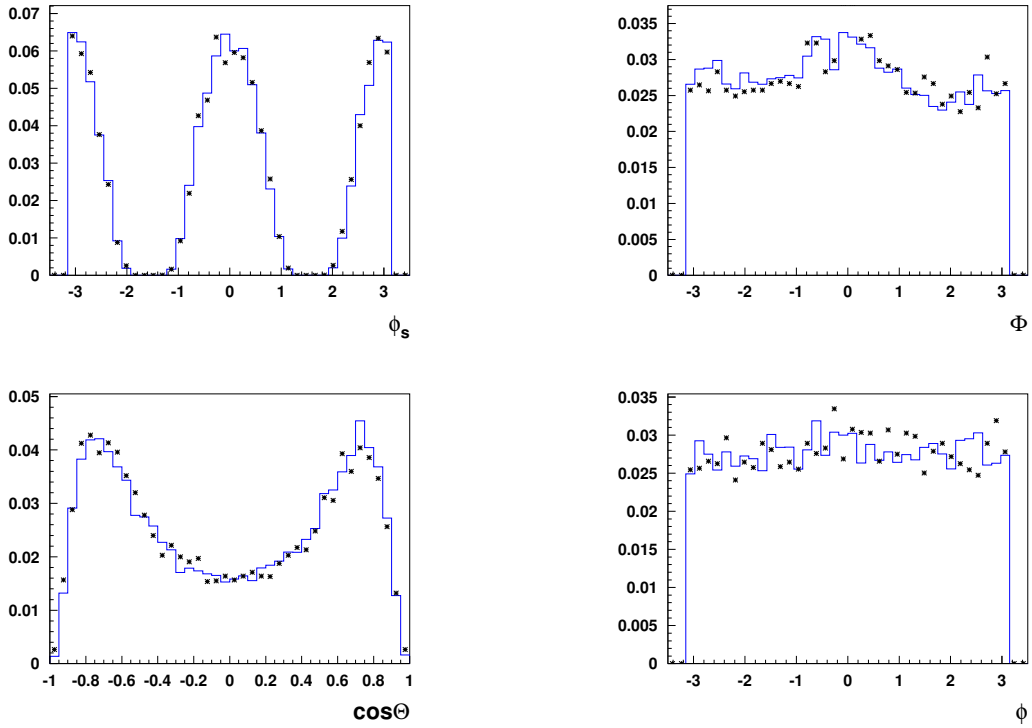

Figure 8.5: The reconstructed kinematic distributions from rhoMC Monte Carlo (blue solid histograms) simulation and data (black points). Arbitrary normalization has been used.

is described by rhoMC within $30-40\%$, while the shapes of angular distributions are very well reproduced by rhoMC.

Further checks of new Monte Carlo codes are in progress. With the new enhanced rhoMC it will be possible to estimate the systematic uncertainty in 'three in one' approach which will include the systematic uncertainties due to the misalignment, beam curving and transverse magnet correction in one shot.

8.2 Final results on transverse target-spin asymmetry in exclusive ρ^0 production

The asymmetry of longitudinally polarized ρ^0_L mesons induced by longitudinally polarized virtual photons γ^*_L is of special interest, since it is related to the GPDs $H^{q,g}$ and $E^{q,g}$ and may provide information about the total angular momenta J^q and J^g of quarks and gluons in the nucleon (see Section 6.1). In Section 6.8.1 it has been shown that at leading twist this asymmetry is related to the SDMEs $u^{0\,0}_{0\,0}$ and $\mathrm{Im}\, n^{0\,0}_{0\,0}$ (see equation (6.49)) which are the only ones describing the production of longitudinally polarized mesons by longitudinal virtual photons. The usage of the full expression of a 4-dimensional angular distribution has the advantage that all the other transitions, both s-channel helicity conserving and non-conserving, are described by other SDMEs. Although experimentally these SDMEs can be measured only in the com-

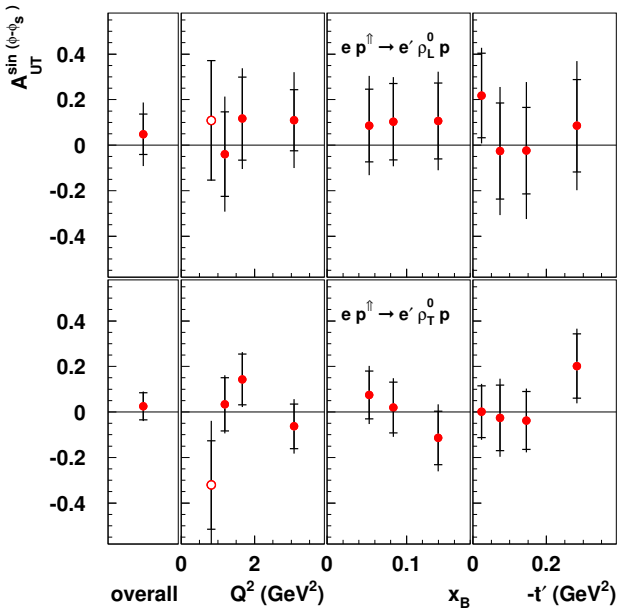

Figure 8.6: The azimuthal amplitude $A_{UT}^{\sin(\phi-\phi_s)}$ of the transverse target-spin asymmetry in exclusive ρ_L^0 and ρ_T^0 meson productions at average kinematics and its dependences on Q^2, x_B or t'. While the inner error bars show the statistical uncertainty only, the outer error bars represent the total uncertainties with statistical and systematic uncertainties combined in quadrature. There is an additional 8.1 % scale uncertainty from the target polarisation measurement.

binations $u_{++}^{00} + \epsilon u_{00}^{00}$ and $\mathrm{Im}\big(n_{++}^{00} + \epsilon n_{00}^{00}\big)$, the terms u_{++}^{00} and n_{++}^{00}, involving two helicity-flip amplitudes, are expected to be negligible compared to the terms u_{00}^{00} and $\mathrm{Im}\, n_{0\,0}^{0\,0}$, respectively. According to this recipe, the $\sin(\phi - \phi_s)$ azimuthal amplitude of transverse target-spin asymmetry has been obtained from the measured values of corresponding combinations of SDMEs. Studies have been performed to estimate the systematic uncertainties of the transverse target-spin asymmetry originating from the same sources as those for the measured values of SDMEs (see Section 8.1).

Similarly the combination of SDMEs $u_{++}^{++} + u_{++}^{--} + 2\epsilon u_{00}^{++} = 1 - (u_{++}^{00} + \epsilon u_{00}^{00})$ and $\mathrm{Im}(n_{++}^{++} + n_{++}^{--} + 2\epsilon n_{00}^{++})$ describe the production of transversely polarized ρ_T^0 mesons by transverse virtual photons. Correspondingly, the measured values of these SDMEs can be used to extract the asymmetry of transversely polarized mesons by transverse virtual photons using an equation similar to 6.49.

The central values of the asymmetries together with the statistical and systematical uncertainties for both longitudinally and transversely polarized ρ^0 mesons induced by longitudinal and transverse virtual photons, respectively, are listed in Table 8.3 and presented in Figure 8.6 at average kinematics, as well as in bins of Q^2, x_B or t'. The mean kinematics for each case are also listed in Table 8.3. For the x_B and t' dependences, Q^2 is required to be above 1 GeV^2, while the Q^2 dependence is shown also for $Q^2 < 1$ GeV^2. The upper and lower panels represent the asymmetries of longitudinally and transversely polarized ρ^0 productions, respectively.

kinematic bin		$\langle Q^2 \rangle$ (GeV^2)	$\langle x_B \rangle$	$\langle -t' \rangle$ (GeV^2)	$A_{UT}^{\sin(\phi-\phi_s),\rho_L}$ $\pm\,\delta_{stat} \pm \delta_{syst}$	$A_{UT}^{\sin(\phi-\phi_s),\rho_T}$ $\pm\,\delta_{stat} \pm \delta_{syst}$
overall		1.95	0.08	0.13	$0.048 \pm 0.089 \pm 0.107$	$0.025 \pm 0.059 \pm 0.026$
Q^2(GeV^2)	$0.5 - 1.0$	0.82	0.03	0.12	$0.109 \pm 0.262 \pm 0.038$	$-0.321 \pm 0.194 \pm 0.204$
	$1.0 - 1.4$	1.19	0.06	0.13	$-0.039 \pm 0.186 \pm 0.171$	$0.034 \pm 0.117 \pm 0.052$
	$1.4 - 2.0$	1.67	0.08	0.13	$0.117 \pm 0.182 \pm 0.126$	$0.143 \pm 0.112 \pm 0.046$
	$2.0 - 7.0$	3.08	0.12	0.14	$0.110 \pm 0.134 \pm 0.162$	$-0.063 \pm 0.098 \pm 0.069$
x_B	$0.02 - 0.07$	1.33	0.05	0.13	$0.086 \pm 0.160 \pm 0.148$	$0.075 \pm 0.105 \pm 0.073$
	$0.07 - 0.10$	1.83	0.08	0.13	$0.103 \pm 0.168 \pm 0.101$	$0.020 \pm 0.111 \pm 0.065$
	$0.10 - 0.40$	3.14	0.14	0.14	$0.106 \pm 0.167 \pm 0.139$	$-0.114 \pm 0.118 \pm 0.088$
t'(GeV^2)	$0.0 - 0.1$	1.89	0.08	0.02	$0.218 \pm 0.186 \pm 0.098$	$0.001 \pm 0.114 \pm 0.046$
	$0.1 - 0.1$	1.97	0.08	0.07	$-0.025 \pm 0.211 \pm 0.186$	$-0.026 \pm 0.144 \pm 0.093$
	$0.1 - 0.2$	1.97	0.09	0.15	$-0.024 \pm 0.190 \pm 0.233$	$-0.037 \pm 0.127 \pm 0.059$
	$0.2 - 0.4$	2.00	0.09	0.28	$0.085 \pm 0.203 \pm 0.198$	$0.202 \pm 0.141 \pm 0.085$

Table 8.3: The azimuthal amplitude $A_{UT}^{\sin(\phi-\phi_s)}$ of the transverse target-spin asymmetry in exclusive ρ_L^0 and ρ_T^0 meson productions at average kinematics and its dependences on Q^2, x_B or t'. The presented uncertainties do not including the 8.1 % scale uncertainty from the target polarisation measurement.

According to equation (6.1), because of the prefactor $\sqrt{t_0 - t}$, the asymmetry as a function of t' is expected to vanish at $t' \to 0$. The data is consistent with zero within the quite large total uncertainty in the entire region of t', so that the data can not prove this expectation.

Further conclusions drawn from model predictions are discussed in the next section.

8.3 Predictions for asymmetry in exclusive ρ^0 production

As discussed in Chapter 2, the description of ρ^0 production in the context of the GPD formalism requires the knowledge of the unpolarized GPDs $H^{q,g}$ and $E^{q,g}$. The extraction of their dependences on the variables (x, ξ, t) from hard electroproduction data is quite challenging. Thus phenomenological parameterizations for the GPDs have to be used, which allow one to test their sensitivity on the parameterization variables. Two kinds of parameterizations have been briefly discussed in Section 2.4.6, the *factorized ansatz* where the t-dependence of the GPDs is factorized out, and a non-factorized ansatz based on a Regge-type parameterization, the *Regge ansatz*. In the following sections model predictions for the asymmetry in exclusive ρ^0 production are discussed. The descriptions of the parameterizations used in the calculations are given in Appendix G for each case.

For model calculations discussed in Section 8.3.1, Section 8.3.2 and Section 8.3.3, the GPD E^g is neglected. A strongly simplified representation of the transverse target-spin asymmetry in ρ^0 production reads [18]:

$$A_{UT} \propto \frac{E}{H} \propto \frac{E^q + E^g}{H^q + H^g}\,. \tag{8.2}$$

Thus, if the measured asymmetry would be found to be large compared to the theoretical calculations, this could imply the gluon GPD E^g, which contributes to the numerator of equation (8.2), to be not negligible, *i.e.* $E^g \neq 0$.

The model calculations discussed in Section 8.3.1 and Section 8.3.2 are performed in leading-order (LO) of α_s, using the collinear factorization approach for the leading helicity amplitudes, *i.e.* $\gamma_L^* \to \rho_L^0$, in which the intrinsic transverse momentum $k_\perp$ of the active quark is neglected. In this case, the hard exclusive electroproduction amplitude is written as a one-dimensional convolution of a hard-scattering kernel and non-perturbative soft quantities which depend only on the longitudinal momentum fraction of the quark (see Figure 2.5). The effect of the transverse momentum $k_\perp$ of partons is one of the sources of corrections at higher orders in $1/Q^2$, called *power corrections* to the collinear approximation. It is a challenge to calculate these power corrections, since the factorization theorem suggests these corrections to not factorize into hard-scattering and soft parts. A consistent simultaneous treatment of gluon radiative corrections, called *next-to-leading order (NLO) correction*, and power corrections is even more challenging and up to now has not been performed for exclusive ρ^0 production.

In the model calculations by Goloskokov, Kroll [19] (see Section 8.3.3), the power corrections are modeled by employing the modified perturbative approach [108]. In this approach the transverse momenta of the quark and antiquark defined with respect to the meson's momentum, $k_\perp$, are not neglected but kept in the mesonic vertex. In this case, the meson distribution amplitude $\Psi(z;\mu)$ (see equation (2.36)) is transformed to $\Psi(z, k_\perp;\mu)$. In contrast, the partons being emitted and reabsorbed by the proton are considered to be collinear.

In the model calculations by Diehl, Kugler [20] (see Section 8.3.4), the collinear approximation is considered, but the size of the NLO corrections has been estimated. Since the transverse target-spin asymmetry involves a ratio of cross sections, the dependence on the strong coupling constant α_s was expected to drop out and the LO expressions were expected to be already accurate. However, it turned out that the transverse target-spin asymmetry of exclusive ρ^0 production changes dramatically from LO to NLO in a wide range of kinematics.

Another recent attempt [109] to resume higher orders seems to indicate that the sum of all higher order corrections to the LO term is not large. In view of this unsettled situation it seems reasonable to proceed with the available model predictions with specifically considering possible problems with NLO corrections.

8.3.1 Asymmetry prediction by Goeke, Polyakov, Vanderhaeghen

The first prediction for the transverse spin-asymmetry in exclusive ρ^0 production for an unpolarized beam and transversely polarized proton target was presented in [16], where the cross section asymmetry was defined as

$$\mathcal{A} = \frac{1}{S_T} \frac{\int_0^{\pi} d\beta\sigma(\beta) - \int_{\pi}^{2\pi} d\beta\sigma(\beta)}{\int_0^{2\pi} d\beta\sigma(\beta)} \tag{8.3}$$

with the target polarization S_T defined with respect to the virtual-photon direction and β being the angle between the transverse target spin vector S_T and the plane spanned by the virtual photon and the produced meson. It differs from the asymmetry defined in equation (6.15) by a factor $-\pi/2$:

$$\mathcal{A}_{UT}^{\gamma^*}(\phi, \phi_s) = -\frac{\pi}{2}\mathcal{A} \,, \tag{8.4}$$

where the minus sign originates from the different definition of the angle β with respect to ϕ and ϕ_s: $\beta = -(\phi - \phi_s)$.

Since the comparison of the electroproduction cross section of longitudinally polarized ρ^0 mesons from data [28, 90] with model predictions [16] at intermediate values of x_B points towards the dominance of the quark exchange mechanism, the gluon contribution in exclusive ρ_L^0 electroproduction was neglected for the predictions of transverse target-spin asymmetry. The GPD models which have been used to compute the prediction for transverse target-spin asymmetry in exclusive ρ^0 production, are discussed in Appendix G.1. In this framework, the total angular momentum J^u and J^d of u and d quarks, respectively, enter directly as free parameters into the parameterization of the GPD E^q, so that the predictions of the asymmetry in exclusive ρ^0 production are sensitive to various values of J^u and J^d.

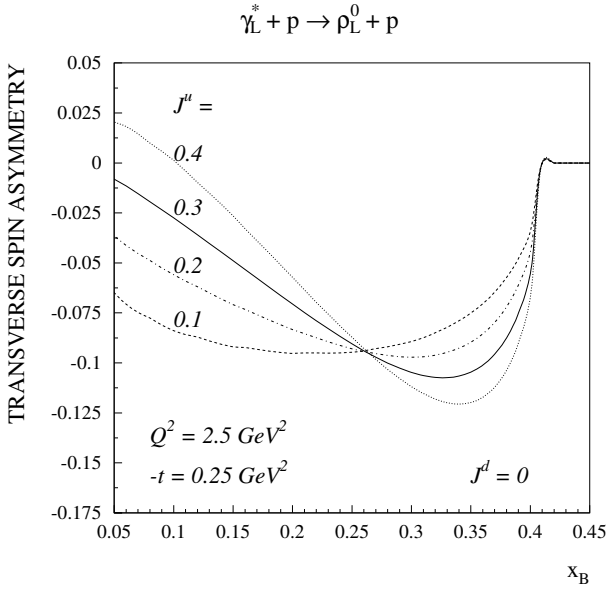

Figure 8.7: Predictions for the x_B-dependence of the transverse target-spin asymmetry of exclusive production of longitudinally polarized ρ_L^0 mesons at $t = -0.25$ GeV^2 and $Q^2 = 2.5$ GeV^2 which is close to the average kinematics of HERMES. The curves show the sensitivity of the asymmetry to the value of J^u at $J^d = 0$.

In Figure 8.7, the asymmetry of longitudinal ρ^0 mesons induced by longitudinal virtual photons is shown for different values of J^u, as indicated on the plot, and at a fixed value of $J^d = 0$. Nevertheless, theoretically it is possible to vary the value of J^d and exploit the corresponding dependence of the asymmetry.

However, the comparison of model calculations with the extracted asymmetry values might be misleading, since only the contribution of quark distributions to exclusive ρ^0 production has been considered. It has been shown [96] that the gluon contribution to exclusive ρ^0 production is not negligible at intermediate energies typical for HERMES, and also the interference between both contributions has to be taken into account. The improved predictions, taking into account also the gluon contribution, are discussed in the next section.

8.3.2 Asymmetry predictions by Ellinghaus, Nowak, Vinnikov, Ye

Predictions for the longitudinal component of the asymmetry in exclusive ρ^0 production are available at average kinematics typical for HERMES, taking into account both quark and gluon contributions, as well as the interference between these contributions [18]. Parameterizations discussed in the previous section for the quark GPDs H^q and E^q (see Appendix G.1) are identical with the ones used in this theoretical calculations. The asymmetries are computed for two cases of sea contribution for GPD $H^{\bar{q}}$, $b_{sea} = 1$ or $b_{sea} = \infty$ (see equation (G.5)). The parameterization of the gluon GPD H^g is discussed in Appendix G.2. Since there was no hint [18] how to model the spin-flip gluon GPD E^g, in this theoretical model calculations the gluon GPD E^g is neglected: $E^g = 0$ (*passive* gluons). This is based on the expectation that E^g is small compared to E^u and E^d (see Section 2.4.6). No large contribution is expected from sea quarks in the valence-like x_B range of HERMES, thus the sea quark contribution $E^{\bar{q}}$ is also neglected.

As for the previous predictions, since the GPD E^q is related to the total angular momenta J^u and J^d carried by u and d quarks, respectively, the $A_{UT}^{\sin(\phi-\phi_s)}$ azimuthal amplitude of the asymmetry is found to be sensitive to J^u and J^d. The results show much larger sensitivity to various values of J^u than to different values of b_{sea}. It was also found [18] that the difference between the results using factorized or Regge ansätze is negligible. Compared to earlier calculations [16], the asymmetry is smaller in the absolute values because of the term H^g in the denominator of equation (8.2).

The longitudinal component of the asymmetry $A_{UT}^{\sin(\phi-\phi_s)}$ at the average kinematics and its x_B and t dependences[1] are compared to theoretical calculations (see Figure 8.8). The various curves represent the calculations for $J^u = 0$, 0.2, 0.4. The choice $J^d = 0$ is motivated by the results of a recent lattice calculation [110–112].

The fact that the measured values of asymmetries and the model calculations are of the

[1] Since the predictions are for the t-dependence of the asymmetry, the results are also presented as a function of t instead of t'.

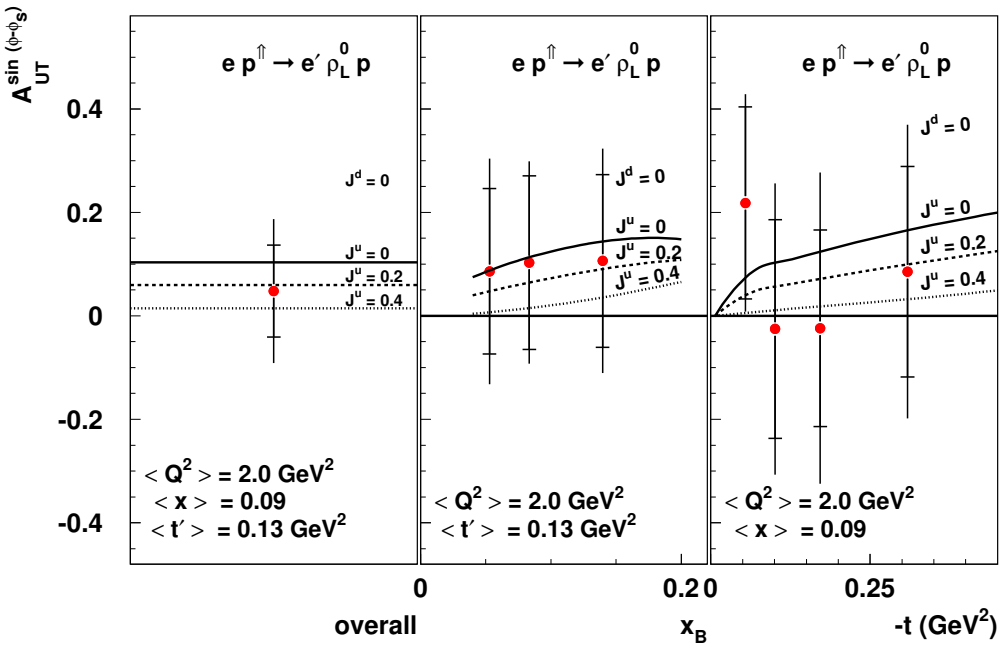

Figure 8.8: The azimuthal amplitude $A_{UT}^{\sin(\phi-\phi_s)}$ of the transverse target-spin asymmetry in exclusive ρ_L^0 production at the average kinematics and its x_B and t dependences compared to theoretical calculations [18] based on the Regge ansatz for various values of $J^u = 0$, 0.2 and 0.4 and $J^d = 0$.

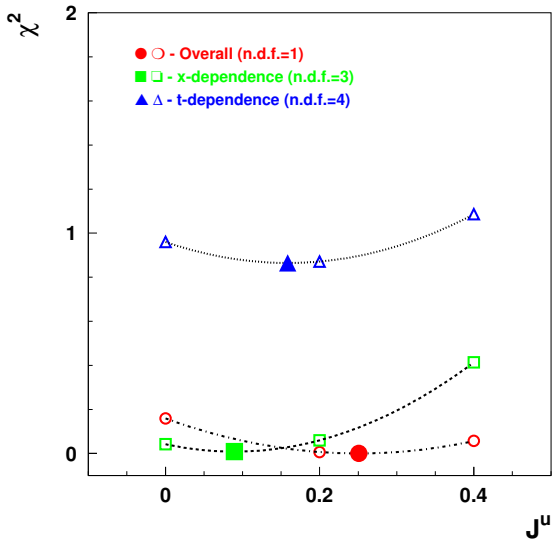

Figure 8.9: The χ^2 values calculated using the extracted azimuthal amplitude $A_{UT}^{\sin(\phi-\phi_s)}$ and the theoretical calculations [18] for various values of $J^u = 0$, 0.2 and 0.4 and $J^d = 0$ at the average kinematics (red circles), and for the x_B (green squares) and t (blue triangles) dependences. The curves represent parabolic fits to the χ^2 values.

same order, implies that neglecting the sea quark contribution at HERMES kinematics the helicity-flip GPD E^g is not large (see equation (8.2)). In addition, a conclusion may be drawn by comparing the theoretical predictions with the longitudinal component of the asymmetry

$A_{UT}^{\sin(\phi-\phi_s)}$ extracted from data. For every given value of J^u the following χ^2 criterion was constructed:

$$\chi^2 = \sum_{i=1}^{n} \frac{\left[A_{UT,i}^{\sin(\phi-\phi_S)}|_{exp} - A_{UT,i}^{\sin(\phi-\phi_S)}|_{theor}\right]^2}{\delta A_{stat,i}^2 + \delta A_{syst,i}^2} \,. \tag{8.5}$$

where $A_{UT,i}^{\sin(\phi-\phi_S)}|_{exp}$ are the amplitudes extracted from the HERMES data and $A_{UT,i}^{\sin(\phi-\phi_S)}|_{theor}$ denote the results of the theoretical calculations, $\delta A_{stat,i}$ and $\delta A_{syst,i}$ represent the experimental statistical and systematic uncertainties. The total number of kinematic bins is denoted by n: for the overall data set $n = 1$, while $n = 3, 4$ for the data binned in x_B and t, respectively. The χ^2 values are interpolated by fitting with a second order polynomial to obtain the minima (see Figure 8.9) which represent the preferred values for J^u. The minimum values of χ^2 obtained from the results binned in x_B and t are in agreement with the one obtained from the result at average kinematics, as expected. The suggested preferred value of J^u ranges between 0.08 and 0.25. The large statistical uncertainties of the data prevent a reliable determination of the uncertainty of the value of J^u.

8.3.3 Asymmetry predictions by Goloskokov, Kroll

In the framework of Goloskokov and Kroll [19] exclusive ρ^0 electroproduction is also analyzed within the factorization scheme, based on GPDs and hard-partonic subprocesses, but in contrast to the previous models the hard-partonic subprocesses are calculated within the modified perturbative approach in which the quark transverse momenta are retained. The emission and reabsorption of partons from the proton is still treated in the collinear approximation.

The parameterizations for the sea and valence quark GPDs $H^{q_v,\bar{q}}$ and for the gluon GPD H^g are constructed from the CTEQ6 PDFs [113] and using the double distribution ansatz [43, 44] (see Appendix G.3). The valence quark GPD E^q is not parameterized through the total angular momentum J^u and J^d of u and d quarks, respectively, as in previous theoretical models. Instead, it is related to the electromagnetic Pauli form factor of the nucleon at zero-skewness [114], $\xi \to 0$, and evaluated at non-zero skewness through the double distributions (see Appendix G.3). The forward limits of GPDs for gluons (E^g) and sea quarks ($E^{\bar{q}}$) are unknown which makes the parameterization considerably complicated. The relative importance of gluon and valence quark GPDs is very different for GPDs E and H. It seems unlikely that E^g plays an analogously prominent role as H^g (see Section 2.4.6). Using the sum rule [36],

$$\int_0^1 dx\, x\, e_g(x) = -\sum_q \int_0^1 dx x\, e_{q_v}(x) - 2\sum_q \int_0^1 dx x\, e_{\bar{q}}(x)\,, \tag{8.6}$$

and the result $\sum_q \int_0^1 dx x\, e_{q_v}(x) = 0.008 \pm 0.007$, based on current models for the forward limit e_{q_v} of the GPD E^q, it has been shown [19] that the moment of e^g is only about as large as the sum of the sea quark moments, having an opposite sign. Therefore, in this framework the

proton helicity flip is assumed to be dominated by valence quarks at HERMES kinematics.

Using the GPD models discussed above, the transverse target-spin asymmetry predictions are available for transitions from longitudinal virtual photons to longitudinally polarized ρ^0 mesons $\gamma_L^* p \to \rho_L^0 p'$ in the kinematic region $Q^2 > 2$ GeV^2 and $W = 5$ GeV. The Q^2 dependence of the asymmetry is compared to this model calculations (see Figure 8.10). As in the previous section, the main conclusion that can be drawn, is the agreement of the model predictions with the data within uncertainties which indicates that the total contribution from the GPD $E^{\bar{q},g}$ of sea quarks and gluon is probably not large at HERMES kinematics.

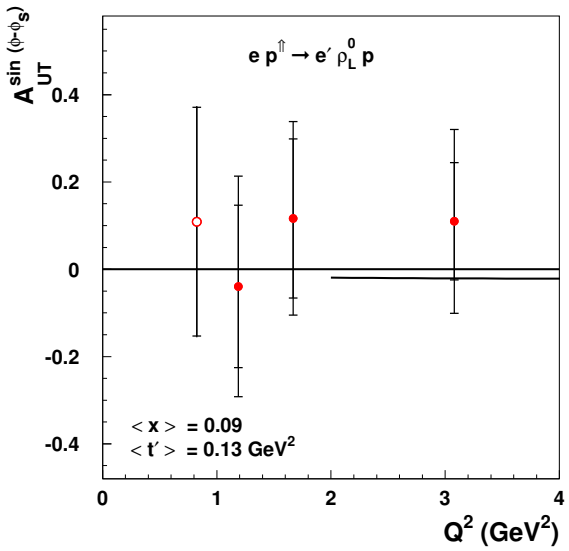

Figure 8.10: The Q^2 dependence of the azimuthal amplitude $A_{UT}^{\sin(\phi-\phi_s)}$ of the transverse target-spin asymmetry in exclusive ρ_L^0 compared to model predictions by Goloskokov, Kroll [19].

8.3.4 Asymmetry predictions by Diehl, Kugler

The model predictions discussed in this section are the only ones, for which all contributions from valence and sea quarks, as well as from gluons are considered for both GPDs H and E. In addition, NLO corrections are also computed.

For the proposed parameterizations [20], at zero-skewness ($\xi \to 0$) the GPDs are modeled in the regions of very small and very large x and then interpolated into the intermediate x region [114]. The t and ξ dependences are evaluated using the Regge ansatz based on double distributions [43, 44]. The free parameters of this parameterizations are fitted to the experimental data on the Dirac and Pauli form factors of the nucleon [114]. From this analysis only the valence quark GPDs can be constrained. Simple ansätze are used for sea quarks and gluons for the forward limits (see Appendix G.4).

Since it turns out that the transverse target-spin asymmetry in exclusive ρ^0 production is very sensitive to the helicity-flip distributions, which are completely unknown, two models are

considered:

model 1: the sea quark distribution $e_{\bar{q}}$ behaves similarly to the valence distributions e_{q_v}.

model 2: the sea quark distribution $e_{\bar{q}}$ behaves similarly to the gluon distribution e_g.

In model 2, both sea quark and gluon distributions are found to be close to zero, while in model 1 distributions larger in magnitude, but opposite in sign are obtained [20]. Both scenarios of model predictions are presented in Figure 8.11 at LO and NLO for $Q^2 = 4$ GeV^2 and $t = -0.4$ GeV^2, somewhat higher than the average HERMES kinematics. The reason is that according to these calculations, the NLO corrections are even larger in the region $Q^2 \approx 2$ GeV^2. At higher Q^2 the discrepancy between LO and NLO calculations is less pronounced, and in model 2 the corrections are quite small. The large size of the NLO corrections is due to the numerator of equation (6.1) defining the transverse target-spin asymmetry, $\mathrm{Im}\big(\mathcal{E}^*_\rho \mathcal{H}_\rho\big)$. The large perturbative corrections are mainly due to the large corrections to both $\mathrm{Re}\,\mathcal{H}_\rho$ and $\mathrm{Re}\,\mathcal{E}_\rho$. These hardly affect the unpolarized cross section, which is strongly dominated by $\mathrm{Im}\,\mathcal{H}_\rho$ [20].

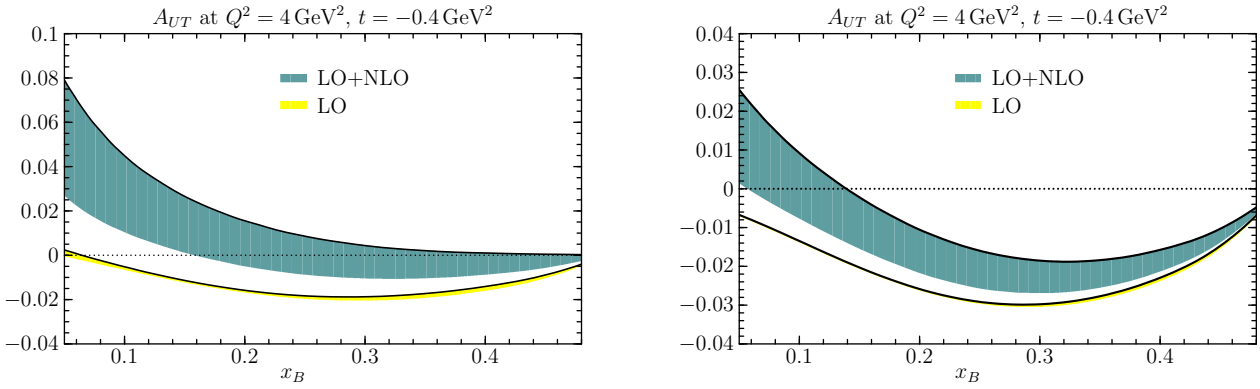

Figure 8.11: Predictions at LO and NLO for the x_B dependence of the azimuthal amplitude $A_{UT}^{\sin(\phi-\phi_s)}$ of the transverse target-spin asymmetry in exclusive ρ^0_L production for two scenarios of sea quark and gluon distributions. (Left: model 1. Right: model 2.)

The data from HERMES is for somewhat lower average kinematics than these model predictions. However, the large uncertainties would not allow to draw a conclusion within the models.

In this framework, the asymmetry predictions are not directly sensitive to the total angular momentum J^q carried by quarks. However, recalling Ji's sum rule [15], this information can be calculated. With the parameters obtained for the parameterization for the GPDs $H^{q,g}$ and $E^{q,g}$ and the CTEQ6M distributions, it was found [20]

$$\begin{aligned} J^u &= 0.25\,, & J^d &= -0.01\,, & &\text{(model 1)} \\ J^u &= 0.24\,, & J^d &= 0.03\,, & &\text{(model 2)}\,. \end{aligned} \tag{8.7}$$

Given that the theoretical uncertainties are not available, the model 1 and 2 give essentially the same result, *i.e.* the sea quarks are of little influence, as can be expected for the HERMES valence-like kinematic region.

Chapter 9

Summary and Outlook

"Where lipstick is concerned, the important thing is not color, but to accept God's final word on where your lips end."

— Jerry Seinfeld

In this thesis exclusive production of ρ^0 mesons was studied using HERMES data taken on transversely polarized hydrogen targets in the kinematic region $1 < Q^2 < 7$ GeV^2, $0.02 < x_B < 0.35$ and $-t' < 0.4$ GeV^2. Exclusive ρ^0 mesons were identified through their two-pion decay mode in the invariant mass region $0.6 < M_{2\pi} < 1$ GeV, imposing requirements on the missing energy ($\Delta E < 0.6$ GeV) and the squared four-momentum transfer ($-t' < 0.40$ GeV^2). Due to experimental resolution and limited acceptance, semi-inclusive pion production contributes to the exclusive sample. This is the main background which is well reproduced by the PYTHIA Monte Carlo simulation and is estimated to be of the order of 11%.

Measurements of angular and momentum distributions of the scattered lepton and decay products yield information about the ρ^0 production mechanism and in a model-dependent way, the structure of the nucleon. In the kinematic region of HERMES theoretical approaches based on the Vector Meson Dominance (VMD) model and on the Generalized Parton Distributions (GPD) formalism are applicable. According to the VMD model, an incoming real or virtual photon is assumed to interact with the nucleon first resulting in a neutral vector meson. Subsequently the interaction of this fluctuated vector meson and the nucleon is similar to those of purely hadronic processes, the strong interaction of which can be described by Regge theory. Since the cross sections of hadronic processes become equal at higher energies for particle and antiparticle off the same target, the basic properties of these processes are independent of the quark constituents of the interacting hadrons. Thus the VMD model do not yield information on the structure of the nucleon. The investigation of the structure of the nucleon was the main goal of the HERMES experiment. While the measurements of form-factors or PDFs in elastic or deep-inelastic lepton-nucleon scattering experiments provide information about the distribution of charge and magnetic moment or of the longitudinal momentum of partons in the nucleon, a full picture of the nucleon structure is still missing. The formalism of GPDs contains a wealth of information about the quark and gluon structure of the nucleon, in par-

ticular about their total angular momentum and their spin, and provide a three-dimensional picture of partons in the nucleon: the transverse localization of partons for a given longitudinal momentum fraction of the nucleon. GPDs can be accessed experimentally, *e.g.* in exclusive ρ^0 production through making highly demanding requirements on luminosity and on the detector capabilities to ensure the exclusivity of the process. It has been shown that for longitudinal virtual photons and longitudinally polarized ρ^0 mesons, the $\gamma^* p$ amplitude can be factorized into a hard lepton-scattering part and two soft parts which parameterize the structure of the nucleon by GPDs and the structure of the produced meson by a distribution amplitude. Hard exclusive production of longitudinally polarized ρ^0 mesons is then sensitive to the quark and gluon GPDs $H^{q,g}$ and $E^{q,g}$ in the same order of α_s. The same functions are related to the total angular momenta J^q and J^g of quarks and gluons in the nucleon.

The spin-density matrix elements (SDMEs), which parameterize the ρ^0 production and decay angular distribution, describe the transitions between different initial helicity states of the virtual photon and different final helicity states of the produced ρ^0. Two main ordering principles of SDMEs are discussed, s-channel helicity conservation (SCHC) and the dominance of natural-parity exchange (NPE), which are valid for both VMD and GPD formalisms. SCHC implies that the produced ρ^0 meson conserves the helicity of the virtual photon γ^*. In Regge phenomenology, NPE suggests an exchange of a pomeron or reggeons like ρ, ω, f_2, a_2, while the unnatural-parity exchange (UPE) proceeds with an exchange of π, a_1, b_1 mesons. In the GPD formalism NPE and UPE processes are described by unpolarized (H and E) and polarized ($\widetilde{H}^q$ and $\widetilde{E}^q$) GPDs, respectively.

Long ago the decomposition of the angular distribution in terms of SDMEs was theoretically available for the case of an unpolarized nucleon target and unpolarized or longitudinally polarized lepton beams. The corresponding SDMEs have been determined in various experiments. Recently, also for a transversely polarized target the angular distribution was theoretically decomposed in terms of SDMEs. From 2002 to 2005 HERMES was running with a transversely polarized hydrogen target which allowed the first measurement of transverse SDMEs from the HERMES data. A good agreement has been observed between the unpolarized SDMEs extracted from 2002-2005 data and the ones extracted from the whole data set. These unpolarized SDMEs were used in this thesis for the extraction of the transverse SDMEs. While the results calculated at average kinematics clearly show non-zero values for unpolarized SDMEs associated with the dominant transitions $\gamma^*_L \to \rho^0_L$ and $\gamma^*_T \to \rho^0_T$ (which are not restricted to be zero in case of SCHC), only for two such transverse SDMEs there is an indication of non-zero values. Similarly, the results show non-negligible contributions of spin-flip amplitudes $\gamma^*_T \to \rho^0_L$ for unpolarized SDMEs, while for transverse SDMEs there is only an indication of s-channel helicity non-conservation. For other single or double spin-flip amplitudes s-channel helicity appears conserved. In addition, the results on a transversely polarized target do not exclude the existence of unnatural-parity exchange in exclusive ρ^0 production, clear indication of which was seen for the case of an unpolarized target. The t' dependence of unpolarized SDMEs is in

general agreement with the theoretical expectations based on the partial wave decomposition of the transition amplitudes. Due to large experimental uncertainties, only for some transverse SDMEs the data indicates a possible t' dependences, which is in rough agreement with the theoretical expectations, although the large experimental uncertainties prevent clear conclusions. The Q^2 dependences of three transverse SDMEs associated with the amplitudes $\gamma_L^* \to \rho_L^0$ and $\gamma_T^* \to \rho_T^0$ are in agreement with the GPD model predictions using the modified perturbative approach for the calculation of the transverse amplitude.

Two Monte Carlo generators, PYTHIA and rhoMC, based on the VMD model, are described in this thesis. Both Monte Carlo generators were modified according to the best present knowledge and describe the absolute cross section of exclusive ρ^0 production. Exclusive ρ^0 production is only one of the processes out of the wide spectrum that PYTHIA generates. However, it simulates 1-dimensional angular distribution only, and thus the description of the production and decay angular distributions together with the decay pion kinematics is not complete. In addition, PYTHIA is restricted to simulate exclusive ρ^0 production only for unpolarized beam and target. In contrast, rhoMC is capable of generating exclusive vector mesons only, but with the full angular distribution which yields better description of the real data. In addition, rhoMC is capable of simulating exclusive ρ^0 production for both unpolarized and polarized beam and target. As one result of the development work on rhoMC in this thesis, the measured transverse SDMEs were implemented into the rhoMC generator, so that it can be used in the future to estimate the systematic uncertainty of the measured SDMEs due to the misalignment of the HERMES detector and effects caused by the transverse holding field of the target magnet. This development also opens for the first time a perspective to estimate the asymmetry transferred from the ρ^0 meson to the decay pions which is very important to know for the extraction of transversity and the Collins/Sievers distributions functions.

The interest in exclusive ρ^0 production, in particular in transverse SDMEs arose after it was shown that the $\sin(\phi - \phi_s)$ azimuthal amplitude of the transverse target-spin asymmetry is sensitive to the nucleon helicity-flip GPDs $E^{q,g}$ without a kinematic suppression of their contribution with respect to the GPDs $H^{q,g}$. For the first time the $\sin(\phi - \phi_s)$ azimuthal amplitude was extracted from the HERMES data relating it to the measured values of SDMEs $u^{00}_{++} + \epsilon u^{00}_{00}$ and $\mathrm{Im}\big(n^{00}_{++} + \epsilon n^{00}_{00}\big)$. No s-channel non-conservation has been observed for SDMEs involving two helicity-flip amplitudes. Therefore the SDMEs $u^{00}_{++} + \epsilon u^{00}_{00}$ and $\mathrm{Im}\big(n^{00}_{++} + \epsilon n^{00}_{00}\big)$ are assumed to be the once that isolate the production of longitudinally polarized ρ^0 mesons by longitudinal virtual photons.

Interpretations suggested in the context of the GPD formalism are also discussed in this thesis, based on the available models of the quark and gluon GPDs $H^{q,g}$ and $E^{q,g}$. Exclusive ρ^0 production is a process with a complicated theoretical description. It involves the gluon GPD E^g, for which the transverse target-spin asymmetry is a key observable. However, it is difficult to parameterize it, because the GPD E^g is completely unknown and can not be related to PDFs or form-factors. In addition, there are complications in the next-to-leading

order (NLO) calculations. A recent study by Diehl, Kugler [20] indicates substantial NLO corrections, while another attempt by Ivanov [109] predicts smaller corrections. A simultaneous treatment of NLO and power corrections has not been performed yet for the transverse target-spin asymmetry. However, the statistical accuracy of the presently available data prevents drawing any conclusion on differences between models. Neglecting these corrections for the moment, two main conclusions can be drawn from the first results on the ρ^0 transverse target-spin asymmetry and its comparison to the available model predictions:

i) A model-based parameterization of the GPD E^q using the total angular momentum J^u of u-quarks as a free parameter suggests a J^u value in the range $0.08 \div 0.25$ while its uncertainty can not be reliably determined.

ii) As expected (see Section 2.4.6), the gluon GPD E^g should be relatively small compared to the u- and d-quark contributions. It can only be of the same size but of opposite sign as the sum of the sea quark contributions, which is not expected to be large at HERMES energies. The model predictions with the sea-quark and gluon GPDs $E^{\bar{q},g}$ neglected, agree with the extracted values of the asymmetry within large uncertainty. This suggests that the combined contribution of sea quarks and gluons in the GPD E is indeed not large. Given the small contribution of the sea quark at HERMES energies, the gluon GPD E^g contribution is expected to be small as well.

The other measurement that is sensitive to the GPD E is the transverse target-spin asymmetry associated with Deeply Virtual Compton Scattering (DVCS). This is a theoretically cleaner process giving mainly information about the quark GPDs, as the gluon GPDs enter as NLO corrections. Several parameterizations of quark GPDs are available that are sensitive to the total angular momentum of u- and d-quarks, J^u and J^d. A model-dependent constraint on the J^u and J^d is obtained using the HERMES data which suggests the values of $J^u \approx 0.2$ and $J^d \approx 0$ [115].

New results on transverse SDMEs measured in exclusive ρ^0 production and on the transverse target-spin asymmetry for longitudinally polarized ρ^0 mesons will be available soon[1] from the COMPASS experiment at CERN, which uses a muon beam with an energy of 160 GeV that scatters off a transversely polarized solid-state ^{6}LiD or hydrogen target. Future accurate measurements of transverse-target data are planned at JLAB. The CLAS experiment will use a transversely polarized HD-Ice target [117] using the CEBAF 6 GeV polarized electron beam, and for CLAS12 an experiment is planned once the accelerator will be upgraded to a beam energy of 12 GeV [118].

[1]The results for unseparated longitudinal and transverse ρ^0 contributions is already available [116].

Appendix A

Standard Model

flavour	electric charge (e)	mass (MeV/c^2)
up $(u, \bar{u})$	$2/3$	$1.5 - 4.0$
down $(d, \bar{d})$	$-1/3$	$4 - 8$
strange $(s, \bar{s})$	$-1/3$	$80 - 130$
charm $(c, \bar{c})$	$2/3$	$1150 - 1350$
bottom $(b, \bar{b})$	$-1/3$	$4100 - 400$
top $(t, \bar{t})$	$2/3$	170900 ± 1800

Table A.1: The elementary particles quarks and antiquarks with baryon number $B = 1/3$, lepton number $L = 0$ and spin $S = 1/2$.

flavour	electric charge (e)	mass (MeV/c^2)
electron (e^-, e^+)	$-1/+1$	0.511
electron neutrino $(\nu_e, \overline{\nu}_e)$	0	< 0.0000022
muon (μ^-, μ^+)	$-1/+1$	105.7
muon neutrino $(\nu_\mu, \overline{\nu}_\mu)$	0	< 0.17
tau lepton (τ^-, τ^+)	$-1/+1$	1777
tau neutrino $(\nu_\tau, \overline{\nu}_\tau)$	0	< 15.5

Table A.2: The leptons form a family of elementary particles with three known flavours: electron, muon, and tau. Each flavor is represented by a pair of weak doublet particles: a massive charged particle and a nearly massless neutral particle called a neutrino. The baryon number of each lepton is $B = 0$, instead the lepton number is $L = 1$. Leptons are spin-1/2 particles. Charged leptons have two possible spin states, while only one helicity is observed for neutrinos: all neutrinos are left-handed, and all antineutrinos are right-handed.

flavour	electric charge (e)	mass (MeV/c^2)
photon (γ)	0	0
W^- boson	-1	80.39
W^+ boson	$+1$	80.39
Z boson	0	91.188
gluon (g)	0	0

Table A.3: The gauge bosons with spin $S = 1$. The three gauge bosons $W^\pm$ and Z together with the photon are grouped together because they mediate the electroweak interaction.

Appendix B

Crossing symmetry in Regge theory

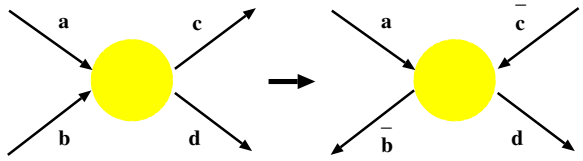

Figure B.1: The crossing symmetry of the $a + b \to c + d$ and $a + \bar{c} \to \bar{b} + d$ reactions.

In the Regge theory, an incoming particle of momentum p is regarded as an outgoing antiparticle of momentum $-p$. This interchange is referred as crossing symmetry (Figure B.1). The reaction $a(p_a) + b(p_b) \to c(p_c) + d(p_d)$ has a squared center of mass energy s_1 and squared four-momentum transfer t_1

$$\begin{aligned} s_1 &= (p_a + p_b)^2 > 0 \\ t_1 &= (p_a - p_c)^2 < 0\,. \end{aligned} \tag{B.1}$$

The scattering angle is related to t_1. In the crossed reaction $a(p_a) + \bar{c}(-p_c) \to \bar{b}(-p_b) + d(p_d)$, the squared center of mass energy s_2 and the squared four-momentum transfer t_2 are defined as:

$$\begin{aligned} s_2 &= (p_a - p_c)^2 < 0 \\ t_2 &= (p_a + p_b)^2 > 0\,, \end{aligned} \tag{B.2}$$

where the scattered angles are now realted to the t_2. The kinematic variables t_1 and s_1 of the original reaction correspond to the squared center of mass s_2 and squared four-momentum transfer t_2 of the crossed reaction. The original reaction is referred as s-channel reaction, while the crossed reaction is its t-channel counterpart. Both reactions are described by the same amplitude, however, in different non-overlapping kinematical regions in s and t.

Appendix C

Measurement of absolute luminosity

Measurement of absolute luminosity in data

The absolute yield of the data can be determined using the absolute luminosity L_{Lumi}. As it was described in section 3.4, the absolute luminosity is the ratio of the measured e^+e^- or e^-e^- scattering rate and the effective cross section of the process (see equation 3.8). The inverse effective cross section, called luminosity constant L_C, depends on the beam settings and on the alignment of the luminosity monitor with respect to the target cell. Thus it can vary within different data taking periods. The values of those constants for various data taking periods are listed on HERMES web-page [119].

The total accumulated luminosity is the dead time and burst length corrected, integrated rate of the luminosity monitor multiplied with the luminosity constant L_C:

$$L_{Lumi} = L_C \sum_{N_{bursts}} g1Beam\_rLumiRate \cdot g1DAQ\_rLength \cdot g1DAQ\_rDeadCorr \qquad \text{(C.1)}$$

It has been found that for 2005 data the luminosity constant is estimated with 15% accuracy leading to worse cross section description of the data.

There is an alternative absolute yield determination method, using the DIS lepton yield N_{DIS}. First N_{DIS} is corrected for a charge symmetric background N_{CS} by subtracting the number of oppositely charged leptons which fulfill the DIS cuts. The correction amounts to 1% of the DIS yield. In order to express the DIS lepton number in micro-barns, the latter one is corrected for the detection efficiency ϵ_{DIS} of DIS leptons and the total DIS cross-section σ_{DIS} within the HERMES acceptance:

$$L_{DIS} = \frac{N_{DIS} - N_{CS}}{\epsilon_{DIS}\ \sigma_{DIS}} \qquad \text{(C.2)}$$

where the detection efficiency was found to be equal to 0.81 and DIS cross-section to 60 nb [120].

Measurement of absolute luminosity in Monte Carlo

The quantities *extraweight* and *ievgen* stored in the $*.norm.kumac$ files which are produced during the generation, represent the total cross-section of the processes generated in PYTHIA Monte-Carlo and the number of attempts to generate good events, respectively. Thus for N Monte Carlo μDSTs the absolute luminosity is defined as:

$$L_{MC} = \frac{\sum_{i=1}^{N} \mathrm{ievgen_i}}{\sum_{i=1}^{N} \mathrm{extraweight_i/N}}. \tag{C.3}$$

Appendix D

Kinematic distributions and ratios of them generated by RhoMC

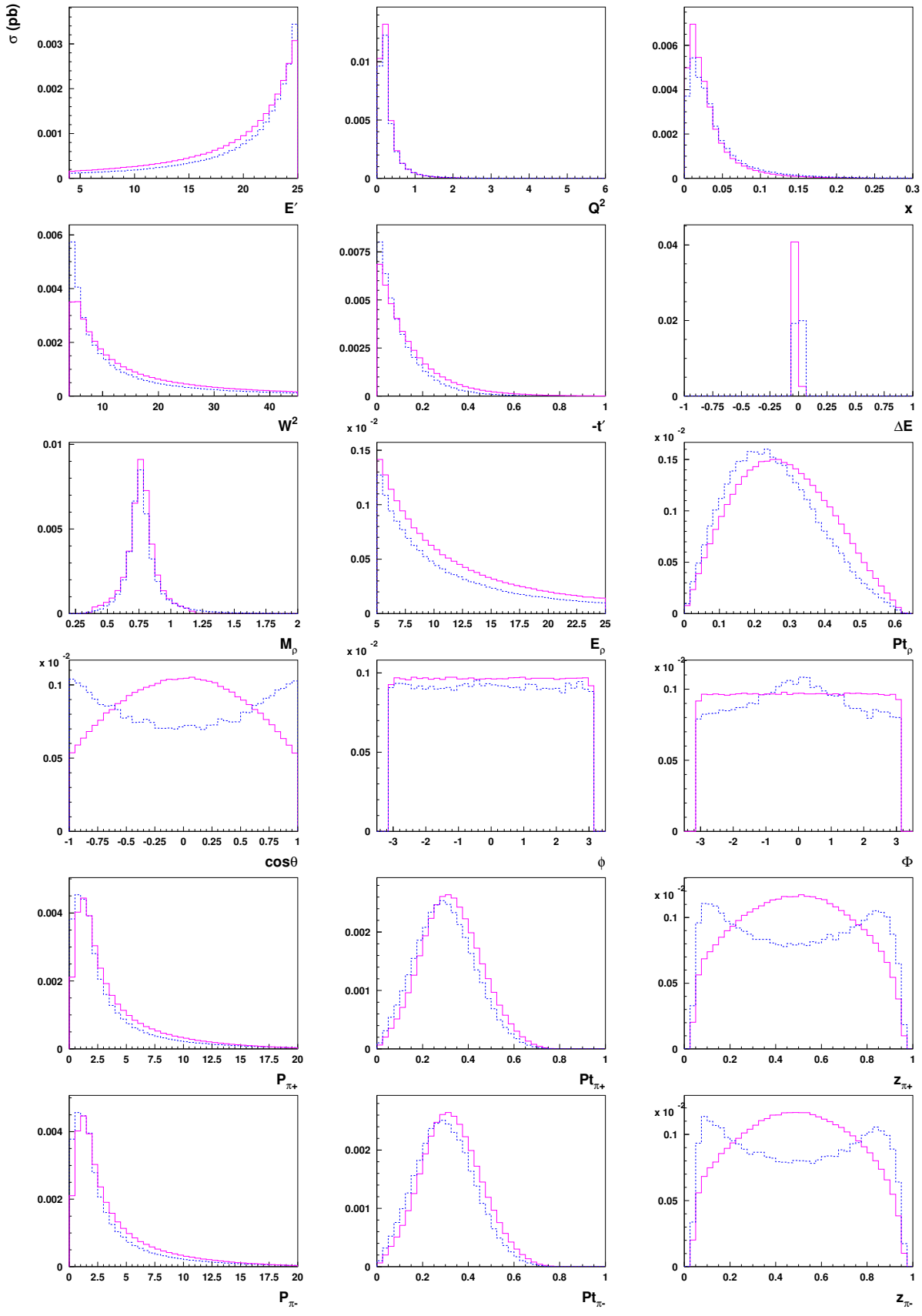

Figure D.1: The generated kinematic distributions in 4π from rhoMC (blue dashed histograms) with full angular distribution $W_{UU}(\cos\theta, \phi, \Phi)$ and from PYTHIA (magenta solid histograms) with $W(\cos\theta)$.

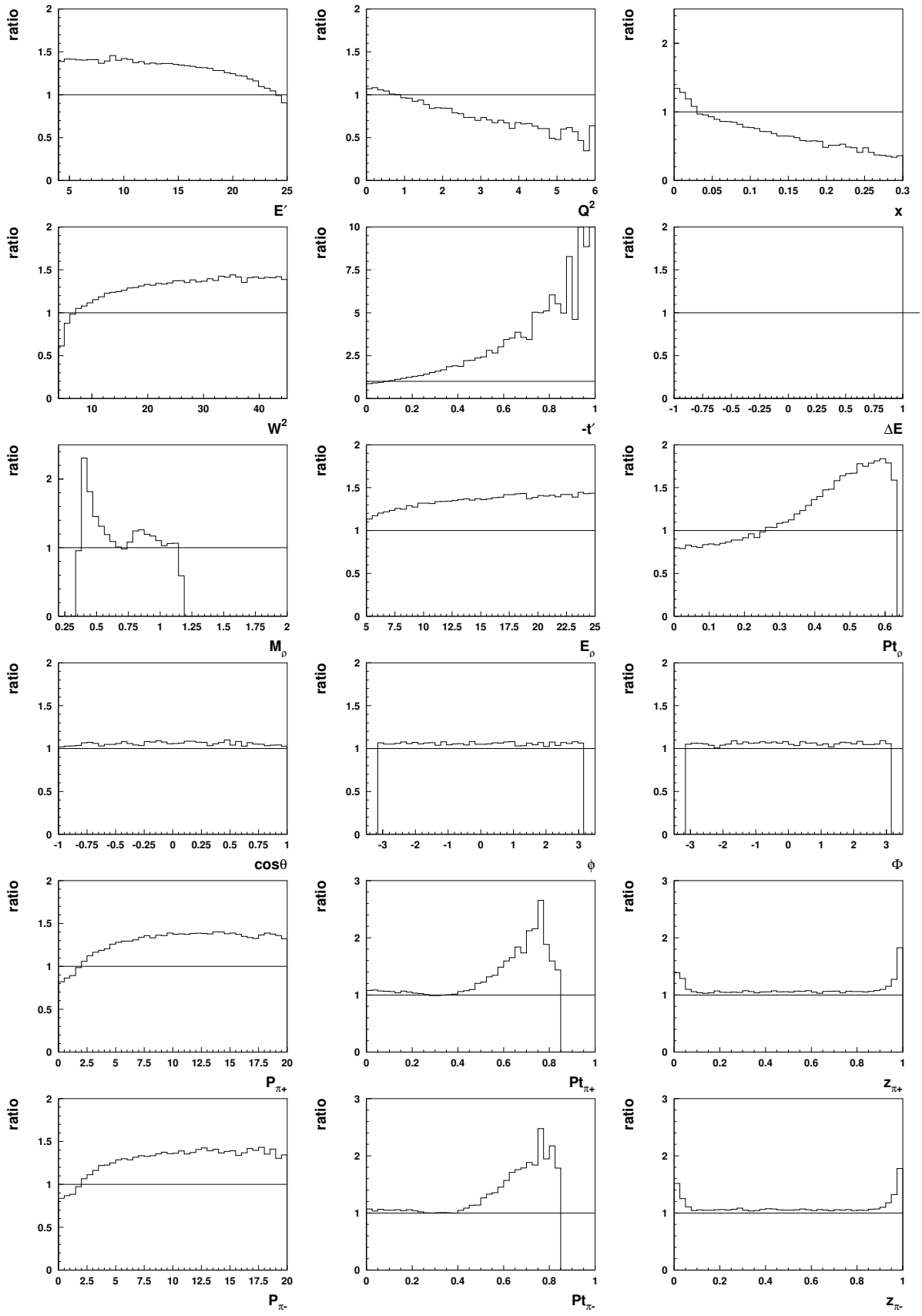

Figure D.2: The ratio of the generated kinematic distributions from rhoMC and PYTHIA Monte Carlo generators illustrated on Figure 5.10.

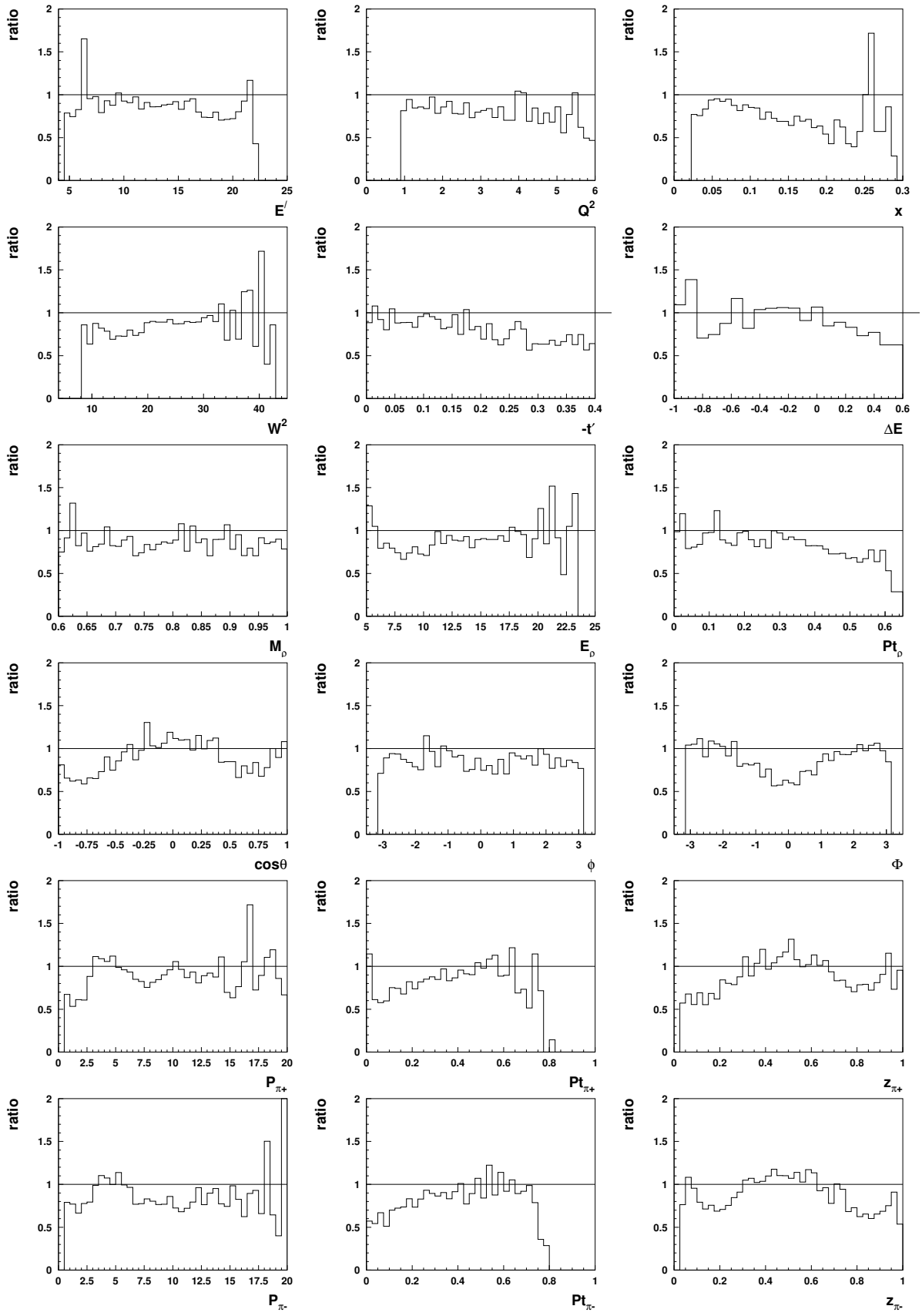

Figure D.3: The ratio of reconstructed kinematic distributions from PYTHIA Monte Carlo and data illustrated on Figure 5.11.

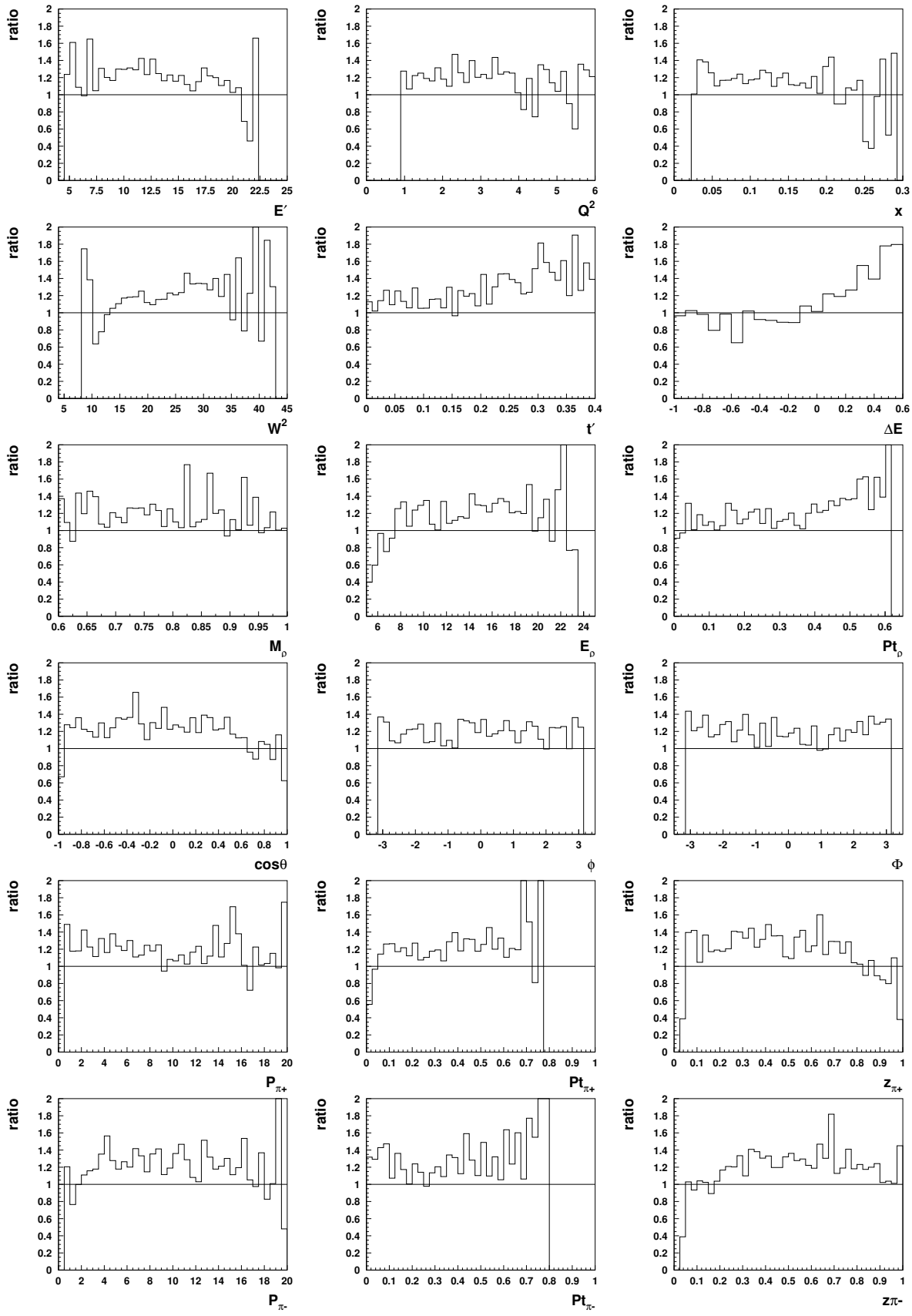

Figure D.4: The ratio of reconstructed kinematic distributions from rhoMC Monte Carlo and data illustrated on Figure 5.12.

Appendix E

SDMEs and angular distributions

E.1 Relations between SDMEs ρ^{α}_{ik} and $u^{\nu'\nu}_{\mu'\mu}$

The SDMEs in Schiling-Wolf and Diehl notations, ρ^{α}_{ik} and $u^{\nu'\nu}_{\mu'\mu}$, respectively, are related [17] to each other as:

$$
\begin{aligned}
u^{0\,0}_{++} + \epsilon u^{0\,0}_{0\,0} &= r^{04}_{00}\,, \\
\mathrm{Re}\big(u^{0+}_{0+} - u^{-0}_{0+}\big) &= \sqrt{2}\,\big(\mathrm{Im}\, r^{6}_{10} - \mathrm{Re}\, r^{5}_{10}\big)\,, \\
u^{++}_{++} + u^{--}_{++} + 2\epsilon u^{++}_{0\,0} &= 1 - r^{04}_{00}\,, \\
u^{-+}_{-+} &= r^{1}_{1-1} - \mathrm{Im}\, r^{2}_{1-1}\,, \\
\mathrm{Re}\, u^{0\,0}_{0+} &= -r^{5}_{00}/\sqrt{2}\,, \\
\mathrm{Re}\big(u^{0+}_{++} - u^{-0}_{++} + 2\epsilon u^{0+}_{0\,0}\big) &= 2\,\mathrm{Re}\, r^{04}_{10}\,, \\
\mathrm{Re}\, u^{0+}_{-+} &= \mathrm{Re}\, r^{1}_{10} - \mathrm{Im}\, r^{2}_{10}\,, \\
\mathrm{Re}\big(u^{0-}_{0+} - u^{+0}_{0+}\big) &= \sqrt{2}\,\big(\mathrm{Im}\, r^{6}_{10} + \mathrm{Re}\, r^{5}_{10}\big)\,, \\
\mathrm{Re}\big(u^{-+}_{++} + \epsilon u^{-+}_{0\,0}\big) &= r^{04}_{1-1}\,, \\
\mathrm{Re}\, u^{++}_{-+} &= r^{1}_{11}\,, \\
\mathrm{Re}\big(u^{++}_{0+} + u^{--}_{0+}\big) &= -\sqrt{2}\, r^{5}_{11}\,, \\
\mathrm{Re}\, u^{-+}_{0+} &= \big(\mathrm{Im}\, r^{6}_{1-1} - r^{5}_{1-1}\big)/\sqrt{2}\,, \\
u^{0\,0}_{-+} &= r^{1}_{00}\,, \\
\mathrm{Re}\, u^{+0}_{-+} &= \mathrm{Re}\, r^{1}_{10} + \mathrm{Im}\, r^{2}_{10}\,, \\
\mathrm{Re}\, u^{+-}_{0+} &= -\big(\mathrm{Im}\, r^{6}_{1-1} + r^{5}_{1-1}\big)/\sqrt{2}\,, \\
u^{+-}_{-+} &= r^{1}_{1-1} + \mathrm{Im}\, r^{2}_{1-1}\,.
\end{aligned}
\qquad
\begin{aligned}
\mathrm{Im}\big(u^{0+}_{0+} - u^{-0}_{0+}\big) &= \sqrt{2}\,\big(\mathrm{Im}\, r^{7}_{10} + \mathrm{Re}\, r^{8}_{10}\big)\,, \\
\mathrm{Im}\, u^{0\,0}_{0+} &= r^{8}_{00}/\sqrt{2}\,, \\
\mathrm{Im}\big(u^{0+}_{++} - u^{-0}_{++}\big) &= -2\,\mathrm{Im}\, r^{3}_{10}\,, \\
\mathrm{Im}\big(u^{0-}_{0+} - u^{+0}_{0+}\big) &= \sqrt{2}\,\big(\mathrm{Im}\, r^{7}_{10} - \mathrm{Re}\, r^{8}_{10}\big)\,, \\
\mathrm{Im}\, u^{-+}_{++} &= -\,\mathrm{Im}\, r^{3}_{1-1}\,, \\
\mathrm{Im}\big(u^{++}_{0+} + u^{--}_{0+}\big) &= \sqrt{2}\, r^{8}_{11}\,, \\
\mathrm{Im}\, u^{-+}_{0+} &= \big(\mathrm{Im}\, r^{7}_{1-1} + r^{8}_{1-1}\big)/\sqrt{2}\,, \\
\mathrm{Im}\, u^{+-}_{0+} &= -\big(\mathrm{Im}\, r^{7}_{1-1} - r^{8}_{1-1}\big)/\sqrt{2}\,.
\end{aligned}
$$

The lower indices of the matrix elements $\rho^{\alpha}_{\lambda\lambda'}$ refer to the ρ^0 helicity and correspond to the upper indices of $u^{\nu'\nu}_{\mu'\mu}$. The upper indices of $\rho^{\alpha}_{\lambda\lambda'}$ represent the virtual photon spin density matrix decomposed in terms of nine hermitian matrices $\Sigma^{0\ldots8}$ (see equation (2.57)) and correspond to the lower indices of $u^{\nu'\nu}_{\mu'\mu}$, where the helicity basis for the photon are used: $\mu', \mu = 0; \pm 1$.

E.2 Mixing between transverse and longitudinal polarization

For a target having transverse polarization P_T with respect to the lepton beam, the angular distribution recieves two contributions: from transverse S_T and longitudinal S_L components of the target polarization each multipled by, respectively, $\cos\theta_\gamma$ and $\sin\theta_\gamma$:

$$\begin{aligned} W &= W_{UU} + S_T W_{UT} + S_L W_{UL} \\ &= W_{UU} + P_T \frac{\cos\theta_\gamma\, W_{UT} + \sin\theta_\gamma \cos\phi_s\, W_{UL}}{\left(1 - \sin^2\theta_\gamma\, \sin^2\phi_s\right)^{1/2}} \,. \end{aligned} \tag{E.1}$$

The angular distributions for separate contributions from longitudinal and transverse ρ^0 mesons, as well as the interference angular distribution are presented [17]:

$$\begin{aligned} &\cos\theta_\gamma\, W_{UT}^{LL}(\phi_S,\phi) + \sin\theta_\gamma \cos\phi_S\, W_{UL}^{LL}(\phi) \\ &\quad = \sin(\phi-\phi_S)\Bigg[\cos\theta_\gamma\, \mathrm{Im}\big(n_{++}^{00} + \epsilon n_{00}^{00}\big) - \sin\theta_\gamma \sqrt{\epsilon(1+\epsilon)}\, \mathrm{Im}\, l_{0+}^{00} \\ &\qquad\qquad - \cos(2\phi)\left\{\cos\theta_\gamma\, \epsilon\, \mathrm{Im}\, n_{-+}^{00} - \sin\theta_\gamma \sqrt{\epsilon(1+\epsilon)}\, \mathrm{Im}\, l_{0+}^{00}\right\} \\ &\qquad\qquad - 2\cos\phi\left\{\cos\theta_\gamma \sqrt{\epsilon(1+\epsilon)}\, \mathrm{Im}\, n_{0+}^{00} + \tfrac{1}{4}\sin\theta_\gamma\, \epsilon\, \mathrm{Im}\, l_{-+}^{00}\right\}\Bigg] \\ &\quad + \cos(\phi-\phi_S)\Bigg[-\sin(2\phi)\left\{\cos\theta_\gamma\, \epsilon\, \mathrm{Im}\, s_{-+}^{00} + \sin\theta_\gamma \sqrt{\epsilon(1+\epsilon)}\, \mathrm{Im}\, l_{0+}^{00}\right\} \\ &\qquad\qquad - 2\sin\phi\left\{\cos\theta_\gamma \sqrt{\epsilon(1+\epsilon)}\, \mathrm{Im}\, s_{0+}^{00} + \tfrac{1}{4}\sin\theta_\gamma\, \epsilon\, \mathrm{Im}\, l_{-+}^{00}\right\}\Bigg] \\ &\quad - \tfrac{1}{2}\sin\theta_\gamma \sin(\phi_S+2\phi)\, \epsilon\, \mathrm{Im}\, l_{-+}^{00} \quad , \end{aligned} \tag{E.2}$$

$$
\begin{aligned}
&\cos\theta_\gamma\, W_{UT}^{LT}(\phi_S,\phi,\varphi) + \sin\theta_\gamma\cos\phi_S\, W_{UL}^{LT}(\phi,\varphi) \\
&\quad = \sin(\phi-\phi_S)\Bigg[\cos(\phi+\varphi)\Big\{\cos\theta_\gamma\sqrt{\epsilon(1+\epsilon)}\,\mathrm{Im}\big(n_{0+}^{0+}-n_{0+}^{-0}\big) \\
&\qquad\qquad + \tfrac{1}{2}\sin\theta_\gamma\Big[\mathrm{Im}\big(l_{++}^{0+}-l_{++}^{-0}+2\epsilon l_{00}^{0+}\big)+\epsilon\,\mathrm{Im}\,l_{-+}^{0+}\Big]\Big\} \\
&\qquad - \cos(\phi-\varphi)\Big\{\cos\theta_\gamma\sqrt{\epsilon(1+\epsilon)}\,\mathrm{Im}\big(n_{0+}^{0-}-n_{0+}^{+0}\big) \\
&\qquad\qquad + \tfrac{1}{2}\sin\theta_\gamma\Big[\mathrm{Im}\big(l_{++}^{0+}-l_{++}^{-0}+2\epsilon l_{00}^{0+}\big)-\epsilon\,\mathrm{Im}\,l_{-+}^{+0}\Big]\Big\} \\
&\qquad + \cos(2\phi+\varphi)\Big\{\cos\theta_\gamma\,\epsilon\,\mathrm{Im}\,n_{-+}^{0+}-\tfrac{1}{2}\sin\theta_\gamma\sqrt{\epsilon(1+\epsilon)}\,\mathrm{Im}\big(l_{0+}^{0+}-l_{0+}^{-0}\big)\Big\} \\
&\qquad + \cos(2\phi-\varphi)\Big\{\cos\theta_\gamma\,\epsilon\,\mathrm{Im}\,n_{-+}^{+0}+\tfrac{1}{2}\sin\theta_\gamma\sqrt{\epsilon(1+\epsilon)}\,\mathrm{Im}\big(l_{0+}^{0-}-l_{0+}^{+0}\big)\Big\} \\
&\qquad - \cos\varphi\Big\{\cos\theta_\gamma\,\mathrm{Im}\big(n_{++}^{0+}-n_{++}^{-0}+2\epsilon n_{00}^{0+}\big) \\
&\qquad\qquad - \tfrac{1}{2}\sin\theta_\gamma\sqrt{\epsilon(1+\epsilon)}\,\Big[\mathrm{Im}\big(l_{0+}^{0+}-l_{0+}^{-0}\big)-\mathrm{Im}\big(l_{0+}^{0-}-l_{0+}^{+0}\big)\Big]\Big\}\Bigg] \\
&\quad + \cos(\phi-\phi_S)\Bigg[\sin(\phi+\varphi)\Big\{\cos\theta_\gamma\sqrt{\epsilon(1+\epsilon)}\,\mathrm{Im}\big(s_{0+}^{0+}-s_{0+}^{-0}\big) \\
&\qquad\qquad - \tfrac{1}{2}\sin\theta_\gamma\Big[\mathrm{Im}\big(l_{++}^{0+}-l_{++}^{-0}+2\epsilon l_{00}^{0+}\big)-\epsilon\,\mathrm{Im}\,l_{-+}^{0+}\Big]\Big\} \\
&\qquad - \sin(\phi-\varphi)\Big\{\cos\theta_\gamma\sqrt{\epsilon(1+\epsilon)}\,\mathrm{Im}\big(s_{0+}^{0-}-s_{0+}^{+0}\big) \\
&\qquad\qquad - \tfrac{1}{2}\sin\theta_\gamma\Big[\mathrm{Im}\big(l_{++}^{0+}-l_{++}^{-0}+2\epsilon l_{00}^{0+}\big)+\epsilon\,\mathrm{Im}\,l_{-+}^{+0}\Big]\Big\} \\
&\qquad + \sin(2\phi+\varphi)\Big\{\cos\theta_\gamma\,\epsilon\,\mathrm{Im}\,s_{-+}^{0+}+\tfrac{1}{2}\sin\theta_\gamma\sqrt{\epsilon(1+\epsilon)}\,\mathrm{Im}\big(l_{0+}^{0+}-l_{0+}^{-0}\big)\Big\} \\
&\qquad + \sin(2\phi-\varphi)\Big\{\cos\theta_\gamma\,\epsilon\,\mathrm{Im}\,s_{-+}^{+0}-\tfrac{1}{2}\sin\theta_\gamma\sqrt{\epsilon(1+\epsilon)}\,\mathrm{Im}\big(l_{0+}^{0-}-l_{0+}^{+0}\big)\Big\} \\
&\qquad - \sin\varphi\Big\{\cos\theta_\gamma\,\mathrm{Im}\big(s_{++}^{0+}-s_{++}^{-0}+2\epsilon s_{00}^{0+}\big) \\
&\qquad\qquad - \tfrac{1}{2}\sin\theta_\gamma\sqrt{\epsilon(1+\epsilon)}\,\Big[\mathrm{Im}\big(l_{0+}^{0+}-l_{0+}^{-0}\big)+\mathrm{Im}\big(l_{0+}^{0-}-l_{0+}^{+0}\big)\Big]\Big\}\Bigg] \\
&\quad + \tfrac{1}{2}\sin\theta_\gamma\Big\{\sin(\phi_S+2\phi+\varphi)\,\epsilon\,\mathrm{Im}\,l_{-+}^{0+}+\sin(\phi_S+2\phi-\varphi)\,\epsilon\,\mathrm{Im}\,l_{-+}^{+0}\Big\}\,,
\end{aligned}
\tag{E.3}
$$

$$
\begin{aligned}
&\cos\theta_\gamma\, W_{UT}^{TT}(\phi_S,\phi,\varphi) + \sin\theta_\gamma\cos\phi_S\, W_{UL}^{TT}(\phi,\varphi) \\
&\quad= \sin(\phi-\phi_S)\,\Bigg[\tfrac{1}{2}\cos\theta_\gamma\,\mathrm{Im}\big(n_{++}^{++}+n_{++}^{--}+2\epsilon n_{00}^{++}\big) - \tfrac{1}{2}\sin\theta_\gamma\sqrt{\epsilon(1+\epsilon)}\,\mathrm{Im}\big(l_{0+}^{++}+l_{0+}^{--}\big) \\
&\qquad - \cos(2\phi)\,\Big\{\cos\theta_\gamma\,\epsilon\,\mathrm{Im}\,n_{-+}^{++} - \tfrac{1}{2}\sin\theta_\gamma\sqrt{\epsilon(1+\epsilon)}\,\mathrm{Im}\big(l_{0+}^{++}+l_{0+}^{--}\big)\Big\} \\
&\qquad - \cos\phi\,\Big\{\cos\theta_\gamma\sqrt{\epsilon(1+\epsilon)}\,\mathrm{Im}\big(n_{0+}^{++}+n_{0+}^{--}\big) + \tfrac{1}{2}\sin\theta_\gamma\,\epsilon\,\mathrm{Im}\,l_{-+}^{++}\Big\} \\
&\qquad + \tfrac{1}{2}\cos(2\phi+2\varphi)\,\Big\{\cos\theta_\gamma\,\epsilon\,\mathrm{Im}\,n_{-+}^{-+} - \sin\theta_\gamma\sqrt{\epsilon(1+\epsilon)}\,\mathrm{Im}\,l_{0+}^{-+}\Big\} \\
&\qquad + \tfrac{1}{2}\cos(2\phi-2\varphi)\,\Big\{\cos\theta_\gamma\,\epsilon\,\mathrm{Im}\,n_{-+}^{+-} - \sin\theta_\gamma\sqrt{\epsilon(1+\epsilon)}\,\mathrm{Im}\,l_{0+}^{+-}\Big\} \\
&\qquad - \cos(2\varphi)\,\Big\{\cos\theta_\gamma\,\mathrm{Im}\big(n_{++}^{-+}+\epsilon n_{00}^{-+}\big) - \tfrac{1}{2}\sin\theta_\gamma\sqrt{\epsilon(1+\epsilon)}\,\Big[\mathrm{Im}\,l_{0+}^{-+}+\mathrm{Im}\,l_{0+}^{+-}\Big]\Big\} \\
&\qquad + \cos(\phi+2\varphi)\,\Big\{\cos\theta_\gamma\sqrt{\epsilon(1+\epsilon)}\,\mathrm{Im}\,n_{0+}^{-+} + \tfrac{1}{4}\sin\theta_\gamma\,\Big[\epsilon\,\mathrm{Im}\,l_{-+}^{-+} + 2\,\mathrm{Im}\big(l_{++}^{-+}+\epsilon l_{00}^{-+}\big)\Big]\Big\} \\
&\qquad + \cos(\phi-2\varphi)\,\Big\{\cos\theta_\gamma\sqrt{\epsilon(1+\epsilon)}\,\mathrm{Im}\,n_{0+}^{+-} + \tfrac{1}{4}\sin\theta_\gamma\,\Big[\epsilon\,\mathrm{Im}\,l_{-+}^{+-} - 2\,\mathrm{Im}\big(l_{++}^{-+}+\epsilon l_{00}^{-+}\big)\Big]\Big\}\Bigg] \\
&\quad+ \cos(\phi-\phi_S)\,\Bigg[-\sin(2\phi)\,\Big\{\cos\theta_\gamma\,\epsilon\,\mathrm{Im}\,s_{-+}^{++} + \tfrac{1}{2}\sin\theta_\gamma\sqrt{\epsilon(1+\epsilon)}\,\mathrm{Im}\big(l_{0+}^{++}+l_{0+}^{--}\big)\Big\} \\
&\qquad - \sin\phi\,\Big\{\cos\theta_\gamma\sqrt{\epsilon(1+\epsilon)}\,\mathrm{Im}\big(s_{0+}^{++}+s_{0+}^{--}\big) + \tfrac{1}{2}\sin\theta_\gamma\,\epsilon\,\mathrm{Im}\,l_{-+}^{++}\Big\} \\
&\qquad + \tfrac{1}{2}\sin(2\phi+2\varphi)\,\Big\{\cos\theta_\gamma\,\epsilon\,\mathrm{Im}\,s_{-+}^{-+} + \sin\theta_\gamma\sqrt{\epsilon(1+\epsilon)}\,\mathrm{Im}\,l_{0+}^{-+}\Big\} \\
&\qquad + \tfrac{1}{2}\sin(2\phi-2\varphi)\,\Big\{\cos\theta_\gamma\,\epsilon\,\mathrm{Im}\,s_{-+}^{+-} + \sin\theta_\gamma\sqrt{\epsilon(1+\epsilon)}\,\mathrm{Im}\,l_{0+}^{+-}\Big\} \\
&\qquad - \sin(2\varphi)\,\Big\{\cos\theta_\gamma\,\mathrm{Im}\big(s_{++}^{-+}+\epsilon s_{00}^{-+}\big) - \tfrac{1}{2}\sin\theta_\gamma\sqrt{\epsilon(1+\epsilon)}\,\Big[\mathrm{Im}\,l_{0+}^{-+}-\mathrm{Im}\,l_{0+}^{+-}\Big]\Big\} \\
&\qquad + \sin(\phi+2\varphi)\,\Big\{\cos\theta_\gamma\sqrt{\epsilon(1+\epsilon)}\,\mathrm{Im}\,s_{0+}^{-+} + \tfrac{1}{4}\sin\theta_\gamma\,\Big[\epsilon\,\mathrm{Im}\,l_{-+}^{-+} - 2\,\mathrm{Im}\big(l_{++}^{-+}+\epsilon l_{00}^{-+}\big)\Big]\Big\} \\
&\qquad + \sin(\phi-2\varphi)\,\Big\{\cos\theta_\gamma\sqrt{\epsilon(1+\epsilon)}\,\mathrm{Im}\,s_{0+}^{+-} + \tfrac{1}{4}\sin\theta_\gamma\,\Big[\epsilon\,\mathrm{Im}\,l_{-+}^{+-} + 2\,\mathrm{Im}\big(l_{++}^{-+}+\epsilon l_{00}^{-+}\big)\Big]\Big\}\Bigg] \\
&\quad+ \tfrac{1}{4}\sin\theta_\gamma\,\Big\{\sin(\phi_S+2\phi+2\varphi)\,\epsilon\,\mathrm{Im}\,l_{-+}^{-+} + \sin(\phi_S+2\phi-2\varphi)\,\epsilon\,\mathrm{Im}\,l_{-+}^{+-}\Big\} \\
&\quad- \tfrac{1}{2}\sin\theta_\gamma\sin(\phi_S+2\phi)\,\epsilon\,\mathrm{Im}\,l_{-+}^{++}\,. \qquad \text{(E.4)}
\end{aligned}
$$

Appendix F

Tables of results

transitions	SDME	value $\pm \delta_{\text{stat}} \pm \delta_{\text{syst}}$
$\gamma_L^* \to \rho_L^0$ $\gamma_T^* \to \rho_T^0$	$u_{++}^{00} + \epsilon u_{00}^{00}$	$0.392 \pm 0.013 \pm 0.010$
	$\text{Re}(u_{0+}^{0+} - u_{-0}^{0+})$	$-0.474 \pm 0.011 \pm 0.028$
	u_{-+}^{-+}	$0.525 \pm 0.018 \pm 0.029$
$\gamma_T^* \to \rho_L^0$	$\text{Re}\, u_{0+}^{00}$	$-0.072 \pm 0.009 \pm 0.006$
	$\text{Re}(u_{++}^{0+} - u_{++}^{-0} + 2\epsilon u_{00}^{0+})$	$0.055 \pm 0.012 \pm 0.016$
	$\text{Re}\, u_{-+}^{0+}$	$-0.065 \pm 0.014 \pm 0.027$
$\gamma_L^* \to \rho_T^0$	$\text{Re}(u_{0+}^{++} + u_{0+}^{--})$	$0.011 \pm 0.007 \pm 0.018$
	$\text{Re}\, u_{0+}^{-+}$	$-0.004 \pm 0.006 \pm 0.008$
$\gamma_T^* \to \rho_{-T}^0$	$\text{Re}(u_{0+}^{0-} - u_{0+}^{+0})$	$-0.005 \pm 0.009 \pm 0.015$
	$\text{Re}(u_{++}^{-+} + \epsilon u_{00}^{-+})$	$-0.015 \pm 0.007 \pm 0.005$
	$\text{Re}\, u_{-+}^{++}$	$-0.019 \pm 0.010 \pm 0.008$
double spin flip	u_{-+}^{00}	$-0.007 \pm 0.025 \pm 0.008$
	$\text{Re}\, u_{-+}^{+0}$	$-0.011 \pm 0.012 \pm 0.004$
	$\text{Re}\, u_{0+}^{+-}$	$-0.003 \pm 0.005 \pm 0.001$
	u_{-+}^{+-}	$0.006 \pm 0.014 \pm 0.011$

Table F.1: Values of unpolarized SDMEs in exclusive ρ^0 production at average kinematics $\left(\langle Q^2 \rangle = 1.95\ \text{GeV}^2, \langle x_B \rangle = 0.08, \langle -t' \rangle = 0.13\ \text{GeV}^2\right)$ ordered in classes by horizontal lines according to the hierarchy predicted by factorization theorem.

transition	SDME	$0.5 < Q^2 < 1.0$ GeV^2 $\langle Q^2\rangle = 0.82$ GeV^2 $\langle x_B\rangle = 0.03$ $\langle t'\rangle = 0.12$ GeV^2	$1.0 < Q^2 < 1.4$ GeV^2 $\langle Q^2\rangle = 1.19$ GeV^2 $\langle x_B\rangle = 0.06$ $\langle t'\rangle = 0.13$ GeV^2	$1.4 < Q^2 < 2.0$ GeV^2 $\langle Q^2\rangle = 1.67$ GeV^2 $\langle x_B\rangle = 0.08$ $\langle t'\rangle = 0.13$ GeV^2	$2.0 < Q^2 < 7.0$ GeV^2 $\langle Q^2\rangle = 3.08$ GeV^2 $\langle x_B\rangle = 0.12$ $\langle t'\rangle = 0.14$ GeV^2
$\gamma^*_L \to \rho^0_L$ $\gamma^*_T \to \rho^0_T$	$u^{00}_{++} + \epsilon u^{00}_{00}$	0.391 ± 0.027	0.383 ± 0.023	0.368 ± 0.023	0.428 ± 0.021
	$\mathrm{Re}(u^{0+}_{0+} - u^{0+}_{-0})$	-0.489 ± 0.034	-0.453 ± 0.022	-0.517 ± 0.019	-0.457 ± 0.019
	u^{-+}_{-+}	0.551 ± 0.038	0.566 ± 0.030	0.545 ± 0.032	0.456 ± 0.032
$\gamma^*_T \to \rho^0_L$	$\mathrm{Re}\, u^{00}_{0+}$	-0.071 ± 0.019	-0.081 ± 0.015	-0.050 ± 0.015	-0.083 ± 0.016
	$\mathrm{Re}(u^{0+}_{++} - u^{-0}_{++} + 2\epsilon u^{0+}_{00})$	0.135 ± 0.029	0.049 ± 0.020	0.072 ± 0.020	0.041 ± 0.021
	$\mathrm{Re}\, u^{0+}_{-+}$	-0.094 ± 0.032	-0.062 ± 0.024	-0.058 ± 0.024	-0.071 ± 0.025
$\gamma^*_L \to \rho^0_T$	$\mathrm{Re}(u^{++}_{0+} + u^{--}_{0+})$	0.043 ± 0.016	0.009 ± 0.011	0.021 ± 0.012	0.007 ± 0.012
	$\mathrm{Re}\, u^{-+}_{0+}$	-0.018 ± 0.014	0.009 ± 0.010	-0.014 ± 0.011	-0.007 ± 0.011
$\gamma^*_T \to \rho^0_{-T}$	$\mathrm{Re}(u^{0-}_{0+} - u^{+0}_{0+})$	0.013 ± 0.020	-0.006 ± 0.013	0.002 ± 0.015	-0.017 ± 0.016
	$\mathrm{Re}(u^{-+}_{++} + \epsilon u^{-+}_{00})$	-0.003 ± 0.017	-0.018 ± 0.013	-0.010 ± 0.013	-0.013 ± 0.013
	$\mathrm{Re}\, u^{++}_{-+}$	-0.024 ± 0.021	-0.010 ± 0.016	-0.021 ± 0.017	-0.027 ± 0.018
double spin flip	u^{00}_{-+}	0.036 ± 0.048	-0.038 ± 0.040	0.036 ± 0.043	-0.001 ± 0.046
	$\mathrm{Re}\, u^{+0}_{-+}$	-0.036 ± 0.026	0.014 ± 0.019	-0.034 ± 0.021	-0.016 ± 0.023
	$\mathrm{Re}\, u^{+-}_{0+}$	-0.019 ± 0.012	-0.007 ± 0.007	0.009 ± 0.008	-0.010 ± 0.009
	u^{+-}_{-+}	-0.053 ± 0.032	0.017 ± 0.021	0.008 ± 0.024	-0.007 ± 0.026

Table F.2: Values of unpolarized SDMEs in exclusive ρ^0 production in bins of Q^2 ordered in classes by horizontal lines according to the hierarchy predicted by factorization theorem.

transition	SDME	$0.02 < x_B < 0.07$ $\langle Q^2 \rangle = 1.33$ GeV^2 $\langle x_B \rangle = 0.05$ $\langle t' \rangle = 0.13$ GeV^2	$0.07 < x_B < 0.10$ $\langle Q^2 \rangle = 1.83$ GeV^2 $\langle x_B \rangle = 0.08$ $\langle t' \rangle = 0.13$ GeV^2	$0.10 < x_B < 0.40$ $\langle Q^2 \rangle = 3.14$ GeV^2 $\langle x_B \rangle = 0.14$ $\langle t' \rangle = 0.14$ GeV^2
$\gamma^*_L \to \rho^0_L$ $\gamma^*_T \to \rho^0_T$	$u^{00}_{++} + \epsilon u^{00}_{00}$	0.372 ± 0.020	0.409 ± 0.023	0.468 ± 0.027
	$\mathrm{Re}(u^{0+}_{0+} - u^{0+}_{-0})$	-0.476 ± 0.017	-0.495 ± 0.020	-0.437 ± 0.027
	u^{-+}_{-+}	0.559 ± 0.028	0.507 ± 0.031	0.459 ± 0.037
$\gamma^*_T \to \rho^0_L$	$\mathrm{Re}\, u^{00}_{0+}$	-0.067 ± 0.013	-0.074 ± 0.016	-0.050 ± 0.021
	$\mathrm{Re}(u^{0+}_{++} - u^{-0}_{++} + 2\epsilon u^{0+}_{00})$	0.058 ± 0.017	0.076 ± 0.021	0.032 ± 0.026
	$\mathrm{Re}\, u^{0+}_{-+}$	-0.053 ± 0.021	-0.084 ± 0.025	-0.043 ± 0.031
$\gamma^*_L \to \rho^0_T$	$\mathrm{Re}(u^{++}_{0+} + u^{--}_{0+})$	0.025 ± 0.012	0.009 ± 0.011	0.008 ± 0.014
	$\mathrm{Re}\, u^{-+}_{0+}$	-0.011 ± 0.010	0.007 ± 0.010	-0.009 ± 0.012
$\gamma^*_T \to \rho^0_{-T}$	$\mathrm{Re}(u^{0-}_{0+} - u^{+0}_{0+})$	0.005 ± 0.013	-0.034 ± 0.015	0.023 ± 0.020
	$\mathrm{Re}(u^{-+}_{++} + \epsilon u^{-+}_{00})$	-0.001 ± 0.013	-0.003 ± 0.012	-0.038 ± 0.015
	$\mathrm{Re}\, u^{++}_{-+}$	-0.003 ± 0.016	-0.017 ± 0.016	-0.030 ± 0.019
double spin flip	u^{00}_{-+}	-0.024 ± 0.035	-0.004 ± 0.045	0.042 ± 0.062
	$\mathrm{Re}\, u^{+0}_{-+}$	-0.025 ± 0.018	0.005 ± 0.021	-0.011 ± 0.029
	$\mathrm{Re}\, u^{+-}_{0+}$	-0.014 ± 0.008	0.007 ± 0.007	-0.008 ± 0.010
	u^{+-}_{-+}	-0.014 ± 0.022	0.036 ± 0.022	-0.009 ± 0.029

Table F.3: Values of unpolarized SDMEs in exclusive ρ^0 production in bins of x_B ordered in classes by horizontal lines according to the hierarchy predicted by factorization theorem.

transition	SDME	$0 < -t' < 0.05$ GeV^2 $\langle Q^2 \rangle = 1.89$ GeV^2 $\langle x_B \rangle = 0.08$ $\langle t' \rangle = 0.02$ GeV^2	$0.05 < -t' < 0.1$ GeV^2 $\langle Q^2 \rangle = 1.97$ GeV^2 $\langle x_B \rangle = 0.08$ $\langle t' \rangle = 0.07$ GeV^2	$0.1 < -t' < 0.2$ GeV^2 $\langle Q^2 \rangle = 1.97$ GeV^2 $\langle x_B \rangle = 0.09$ $\langle t' \rangle = 0.15$ GeV^2	$0.2 < -t' < 0.4$ GeV^2 $\langle Q^2 \rangle = 2.00$ GeV^2 $\langle x_B \rangle = 0.09$ $\langle t' \rangle = 0.28$ GeV^2
$\gamma^*_L \to \rho^0_L$ $\gamma^*_T \to \rho^0_T$	$u^{00}_{++} + \epsilon u^{00}_{00}$	0.362 ± 0.023	0.394 ± 0.030	0.405 ± 0.027	0.436 ± 0.030
	$\mathrm{Re}(u^{0+}_{0+} - u^{0+}_{-0})$	-0.505 ± 0.021	-0.460 ± 0.027	-0.472 ± 0.025	-0.500 ± 0.031
	u^{-+}_{-+}	0.567 ± 0.034	0.592 ± 0.043	0.503 ± 0.038	0.539 ± 0.040
$\gamma^*_T \to \rho^0_L$	$\mathrm{Re}\, u^{00}_{0+}$	-0.030 ± 0.015	-0.061 ± 0.019	-0.131 ± 0.019	-0.098 ± 0.023
	$\mathrm{Re}(u^{0+}_{++} - u^{-0}_{++} + 2\epsilon u^{0+}_{00})$	0.005 ± 0.021	0.036 ± 0.027	0.112 ± 0.026	0.058 ± 0.028
	$\mathrm{Re}\, u^{0+}_{-+}$	-0.027 ± 0.024	-0.085 ± 0.033	-0.063 ± 0.030	-0.066 ± 0.038
$\gamma^*_L \to \rho^0_T$	$\mathrm{Re}(u^{++}_{0+} + u^{--}_{0+})$	0.030 ± 0.013	0.034 ± 0.015	0.010 ± 0.014	0.017 ± 0.016
	$\mathrm{Re}\, u^{-+}_{0+}$	-0.019 ± 0.011	-0.013 ± 0.014	0.024 ± 0.013	-0.017 ± 0.015
$\gamma^*_T \to \rho^0_{-T}$	$\mathrm{Re}(u^{0-}_{0+} - u^{+0}_{0+})$	-0.005 ± 0.016	0.015 ± 0.020	-0.007 ± 0.018	-0.025 ± 0.022
	$\mathrm{Re}(u^{-+}_{++} + \epsilon u^{-+}_{00})$	0.002 ± 0.014	-0.019 ± 0.017	-0.031 ± 0.016	-0.013 ± 0.017
	$\mathrm{Re}\, u^{++}_{-+}$	-0.022 ± 0.018	0.011 ± 0.023	-0.028 ± 0.021	-0.014 ± 0.023
double spin flip	u^{00}_{-+}	-0.027 ± 0.042	-0.061 ± 0.057	-0.045 ± 0.054	0.060 ± 0.063
	$\mathrm{Re}\, u^{+0}_{-+}$	-0.011 ± 0.023	-0.029 ± 0.028	0.004 ± 0.026	-0.031 ± 0.031
	$\mathrm{Re}\, u^{+-}_{0+}$	-0.003 ± 0.008	0.010 ± 0.010	-0.010 ± 0.010	-0.011 ± 0.012
	u^{+-}_{-+}	0.050 ± 0.025	0.013 ± 0.031	0.023 ± 0.028	-0.087 ± 0.034

Table F.4: Values of unpolarized SDMEs in exclusive ρ^0 production in bins of t' ordered in classes by horizontal lines according to the hierarchy predicted by factorization theorem.

transition	SDME	value $\pm \delta_{\text{stat}} \pm \delta_{\text{syst}}$
$\gamma^*_L \to \rho^0_L$ $\gamma^*_T \to \rho^0_T$	$\text{Im}(n^{00}_{++} + \epsilon n^{00}_{00})$	$0.019 \pm 0.035 \pm 0.038$
	$\text{Im}(n^{0+}_{0+} - n^{-0}_{0+})$	$0.014 \pm 0.023 \pm 0.013$
	$\text{Im}\, n^{-+}_{-+}$	$0.010 \pm 0.046 \pm 0.029$
	$\text{Im}(n^{++}_{++} + n^{--}_{++} + 2\epsilon n^{++}_{00})$	$0.015 \pm 0.036 \pm 0.025$
	$\text{Im}\, s^{-+}_{-+}$	$-0.099 \pm 0.044 \pm 0.030$
	$\text{Im}(s^{0+}_{0+} - s^{-0}_{0+})$	$0.058 \pm 0.020 \pm 0.012$
$\gamma^*_T \to \rho^0_L$	$\text{Im}\, n^{00}_{0+}$	$-0.086 \pm 0.022 \pm 0.024$
	$\text{Im}(n^{0+}_{++} - n^{-0}_{++} + 2\epsilon n^{0+}_{00})$	$-0.050 \pm 0.028 \pm 0.025$
	$\text{Im}\, n^{0+}_{-+}$	$0.038 \pm 0.034 \pm 0.024$
	$\text{Im}\, s^{00}_{0+}$	$0.022 \pm 0.022 \pm 0.009$
	$\text{Im}(s^{0+}_{++} - s^{-0}_{++} + 2\epsilon s^{0+}_{00})$	$0.020 \pm 0.026 \pm 0.017$
	$\text{Im}\, s^{0+}_{-+}$	$-0.023 \pm 0.034 \pm 0.022$
$\gamma^*_L \to \rho^0_T$	$\text{Im}(n^{++}_{0+} + n^{--}_{0+})$	$0.034 \pm 0.018 \pm 0.012$
	$\text{Im}\, n^{-+}_{0+}$	$-0.013 \pm 0.013 \pm 0.009$
	$\text{Im}(s^{++}_{0+} + s^{--}_{0+})$	$0.009 \pm 0.018 \pm 0.011$
	$\text{Im}\, s^{-+}_{0+}$	$0.010 \pm 0.013 \pm 0.009$
$\gamma^*_T \to \rho^0_{-T}$	$\text{Im}(n^{0-}_{0+} - n^{+0}_{0+})$	$0.031 \pm 0.021 \pm 0.014$
	$\text{Im}(n^{-+}_{++} + \epsilon n^{-+}_{00})$	$0.025 \pm 0.020 \pm 0.012$
	$\text{Im}\, n^{++}_{-+}$	$0.026 \pm 0.026 \pm 0.017$
	$\text{Im}(s^{0-}_{0+} - s^{+0}_{0+})$	$-0.034 \pm 0.020 \pm 0.014$
	$\text{Im}(s^{-+}_{++} + \epsilon s^{-+}_{00})$	$0.011 \pm 0.018 \pm 0.016$
	$\text{Im}\, s^{++}_{-+}$	$0.013 \pm 0.025 \pm 0.026$
double spin flip	$\text{Im}\, n^{00}_{-+}$	$-0.073 \pm 0.056 \pm 0.044$
	$\text{Im}\, n^{+0}_{-+}$	$0.006 \pm 0.030 \pm 0.011$
	$\text{Im}\, n^{+-}_{0+}$	$0.000 \pm 0.013 \pm 0.009$
	$\text{Im}\, n^{+-}_{-+}$	$-0.006 \pm 0.037 \pm 0.022$
	$\text{Im}\, s^{00}_{-+}$	$0.020 \pm 0.058 \pm 0.063$
	$\text{Im}\, s^{+0}_{-+}$	$-0.022 \pm 0.029 \pm 0.012$
	$\text{Im}\, s^{+-}_{0+}$	$0.010 \pm 0.013 \pm 0.010$
	$\text{Im}\, s^{+-}_{-+}$	$-0.003 \pm 0.036 \pm 0.034$

Table F.5: The transverse SDMEs in exclusive ρ^0 production at average kinematics $\left(\langle Q^2 \rangle = 1.95\ \text{GeV}^2, \langle x_B \rangle = 0.08, \langle -t' \rangle = 0.13\ \text{GeV}^2\right)$ ordered in classes by horizontal lines according to the hierarchy predicted by factorization theorem. The presented uncertainties do not include the 8.1 % scale uncertainty from the target polarisation measurement.

transition	SDME	$0.5 < Q^2 < 1.0$ GeV^2 $\langle Q^2 \rangle = 0.82$ GeV^2 $\langle x_B \rangle = 0.03$ $\langle t' \rangle = 0.12$ GeV^2	$1.0 < Q^2 < 1.4$ GeV^2 $\langle Q^2 \rangle = 1.19$ GeV^2 $\langle x_B \rangle = 0.06$ $\langle t' \rangle = 0.13$ GeV^2	$1.4 < Q^2 < 2.0$ GeV^2 $\langle Q^2 \rangle = 1.67$ GeV^2 $\langle x_B \rangle = 0.08$ $\langle t' \rangle = 0.13$ GeV^2	$2.0 < Q^2 < 7.0$ GeV^2 $\langle Q^2 \rangle = 3.08$ GeV^2 $\langle x_B \rangle = 0.12$ $\langle t' \rangle = 0.14$ GeV^2
$\gamma^*_L \to \rho^0_L$ $\gamma^*_T \to \rho^0_T$	$\mathrm{Im}(n^{00}_{++} + \epsilon n^{00}_{00})$	$0.043 \pm 0.102 \pm 0.016$	$-0.015 \pm 0.071 \pm 0.044$	$0.043 \pm 0.067 \pm 0.020$	$0.047 \pm 0.058 \pm 0.052$
	$\mathrm{Im}(n^{0+}_{0+} - n^{-0}_{0+})$	$-0.106 \pm 0.075 \pm 0.030$	$0.010 \pm 0.040 \pm 0.020$	$0.007 \pm 0.044 \pm 0.018$	$0.000 \pm 0.042 \pm 0.028$
	$\mathrm{Im}\, n^{-+}_{-+}$	$-0.015 \pm 0.149 \pm 0.045$	$0.097 \pm 0.084 \pm 0.061$	$0.056 \pm 0.086 \pm 0.042$	$-0.088 \pm 0.079 \pm 0.051$
	$\mathrm{Im}(n^{++}_{++} + n^{--}_{++} + 2\epsilon n^{++}_{00})$	$-0.195 \pm 0.118 \pm 0.071$	$0.021 \pm 0.072 \pm 0.014$	$0.090 \pm 0.070 \pm 0.029$	$-0.036 \pm 0.056 \pm 0.043$
	$\mathrm{Im}\, s^{-+}_{-+}$	$0.035 \pm 0.141 \pm 0.040$	$-0.038 \pm 0.080 \pm 0.038$	$-0.083 \pm 0.090 \pm 0.046$	$-0.205 \pm 0.076 \pm 0.056$
	$\mathrm{Im}(s^{0+}_{0+} - s^{-0}_{0+})$	$0.151 \pm 0.070 \pm 0.018$	$0.090 \pm 0.036 \pm 0.022$	$0.051 \pm 0.040 \pm 0.013$	$0.041 \pm 0.036 \pm 0.017$
$\gamma^*_T \to \rho^0_L$	$\mathrm{Im}\, n^{00}_{0+}$	$-0.039 \pm 0.070 \pm 0.008$	$-0.056 \pm 0.045 \pm 0.024$	$-0.080 \pm 0.044 \pm 0.022$	$-0.121 \pm 0.038 \pm 0.033$
	$\mathrm{Im}(n^{0+}_{++} - n^{-0}_{++} + 2\epsilon n^{0+}_{00})$	$-0.109 \pm 0.101 \pm 0.028$	$-0.043 \pm 0.057 \pm 0.019$	$-0.035 \pm 0.054 \pm 0.050$	$-0.073 \pm 0.046 \pm 0.025$
	$\mathrm{Im}\, n^{0+}_{-+}$	$0.093 \pm 0.091 \pm 0.021$	$0.084 \pm 0.062 \pm 0.025$	$0.034 \pm 0.067 \pm 0.057$	$-0.001 \pm 0.061 \pm 0.017$
	$\mathrm{Im}\, s^{00}_{0+}$	$-0.013 \pm 0.074 \pm 0.017$	$0.001 \pm 0.046 \pm 0.008$	$0.059 \pm 0.042 \pm 0.006$	$0.016 \pm 0.037 \pm 0.006$
	$\mathrm{Im}(s^{0+}_{++} - s^{-0}_{++} + 2\epsilon s^{0+}_{00})$	$-0.103 \pm 0.085 \pm 0.021$	$-0.012 \pm 0.054 \pm 0.021$	$0.025 \pm 0.053 \pm 0.021$	$0.022 \pm 0.042 \pm 0.014$
	$\mathrm{Im}\, s^{0+}_{-+}$	$-0.123 \pm 0.098 \pm 0.054$	$-0.004 \pm 0.064 \pm 0.028$	$-0.021 \pm 0.068 \pm 0.046$	$-0.106 \pm 0.062 \pm 0.045$
$\gamma^*_L \to \rho^0_T$	$\mathrm{Im}(n^{++}_{0+} + n^{--}_{0+})$	$0.000 \pm 0.074 \pm 0.040$	$0.034 \pm 0.035 \pm 0.010$	$0.036 \pm 0.036 \pm 0.012$	$0.031 \pm 0.031 \pm 0.011$
	$\mathrm{Im}\, n^{-+}_{0+}$	$0.102 \pm 0.046 \pm 0.019$	$0.007 \pm 0.023 \pm 0.015$	$-0.022 \pm 0.024 \pm 0.007$	$-0.033 \pm 0.023 \pm 0.013$
	$\mathrm{Im}(s^{++}_{0+} + s^{--}_{0+})$	$0.081 \pm 0.068 \pm 0.018$	$-0.002 \pm 0.032 \pm 0.009$	$0.010 \pm 0.033 \pm 0.011$	$0.021 \pm 0.029 \pm 0.012$
	$\mathrm{Im}\, s^{-+}_{0+}$	$-0.024 \pm 0.048 \pm 0.007$	$0.045 \pm 0.023 \pm 0.012$	$-0.014 \pm 0.024 \pm 0.013$	$-0.003 \pm 0.022 \pm 0.014$
$\gamma^*_T \to \rho^0_{-T}$	$\mathrm{Im}(n^{0-}_{0+} - n^{+0}_{0+})$	$0.064 \pm 0.070 \pm 0.013$	$0.062 \pm 0.038 \pm 0.031$	$0.056 \pm 0.039 \pm 0.011$	$-0.025 \pm 0.039 \pm 0.018$
	$\mathrm{Im}(n^{-+}_{++} + \epsilon n^{-+}_{00})$	$-0.019 \pm 0.069 \pm 0.026$	$0.007 \pm 0.040 \pm 0.025$	$0.070 \pm 0.038 \pm 0.016$	$0.017 \pm 0.031 \pm 0.019$
	$\mathrm{Im}\, n^{++}_{-+}$	$0.048 \pm 0.082 \pm 0.037$	$0.044 \pm 0.047 \pm 0.022$	$0.025 \pm 0.053 \pm 0.026$	$0.025 \pm 0.044 \pm 0.020$
	$\mathrm{Im}(s^{0-}_{0+} - s^{+0}_{0+})$	$-0.082 \pm 0.072 \pm 0.056$	$-0.057 \pm 0.037 \pm 0.025$	$-0.022 \pm 0.040 \pm 0.023$	$-0.031 \pm 0.037 \pm 0.017$
	$\mathrm{Im}(s^{-+}_{++} + \epsilon s^{-+}_{00})$	$0.006 \pm 0.058 \pm 0.041$	$0.002 \pm 0.035 \pm 0.016$	$0.044 \pm 0.036 \pm 0.027$	$-0.014 \pm 0.029 \pm 0.016$
	$\mathrm{Im}\, s^{++}_{-+}$	$-0.121 \pm 0.073 \pm 0.015$	$-0.047 \pm 0.048 \pm 0.036$	$-0.007 \pm 0.049 \pm 0.018$	$0.117 \pm 0.044 \pm 0.032$
double spin flip	$\mathrm{Im}\, n^{00}_{-+}$	$-0.099 \pm 0.160 \pm 0.042$	$-0.112 \pm 0.105 \pm 0.018$	$-0.152 \pm 0.109 \pm 0.061$	$0.047 \pm 0.099 \pm 0.053$
	$\mathrm{Im}\, n^{+0}_{-+}$	$-0.048 \pm 0.092 \pm 0.014$	$-0.050 \pm 0.055 \pm 0.013$	$-0.030 \pm 0.056 \pm 0.027$	$0.099 \pm 0.056 \pm 0.043$
	$\mathrm{Im}\, n^{+-}_{0+}$	$0.083 \pm 0.045 \pm 0.012$	$-0.002 \pm 0.023 \pm 0.017$	$-0.015 \pm 0.025 \pm 0.010$	$0.005 \pm 0.023 \pm 0.010$
	$\mathrm{Im}\, n^{+-}_{-+}$	$0.021 \pm 0.112 \pm 0.122$	$-0.075 \pm 0.066 \pm 0.015$	$-0.014 \pm 0.071 \pm 0.028$	$0.094 \pm 0.067 \pm 0.043$
	$\mathrm{Im}\, s^{00}_{-+}$	$0.054 \pm 0.153 \pm 0.060$	$0.062 \pm 0.107 \pm 0.063$	$0.160 \pm 0.103 \pm 0.024$	$-0.159 \pm 0.107 \pm 0.105$
	$\mathrm{Im}\, s^{+0}_{-+}$	$0.003 \pm 0.088 \pm 0.052$	$0.017 \pm 0.053 \pm 0.014$	$-0.090 \pm 0.057 \pm 0.012$	$-0.009 \pm 0.053 \pm 0.017$
	$\mathrm{Im}\, s^{+-}_{0+}$	$-0.085 \pm 0.044 \pm 0.011$	$0.028 \pm 0.023 \pm 0.025$	$-0.004 \pm 0.026 \pm 0.016$	$-0.002 \pm 0.022 \pm 0.011$
	$\mathrm{Im}\, s^{+-}_{-+}$	$0.024 \pm 0.110 \pm 0.025$	$-0.011 \pm 0.063 \pm 0.019$	$0.058 \pm 0.070 \pm 0.035$	$-0.067 \pm 0.064 \pm 0.053$

Table F.6: The transverse SDMEs in exclusive ρ^0 production in bins of Q^2 ordered in classes by horizontal lines according to the hierarchy predicted by factorization theorem. The presented uncertainties do not include the 8.1 % scale uncertainty from the target polarisation measurement.

transition	SDME	$0.02 < x_B < 0.07$ $\langle Q^2 \rangle = 1.33$ GeV^2 $\langle x_B \rangle = 0.05$ $\langle t' \rangle = 0.13$ GeV^2	$0.07 < x_B < 0.10$ $\langle Q^2 \rangle = 1.83$ GeV^2 $\langle x_B \rangle = 0.08$ $\langle t' \rangle = 0.13$ GeV^2	$0.10 < x_B < 0.40$ $\langle Q^2 \rangle = 3.14$ GeV^2 $\langle x_B \rangle = 0.14$ $\langle t' \rangle = 0.14$ GeV^2
$\gamma^*_L \to \rho^0_L$ $\gamma^*_T \to \rho^0_T$	$\mathrm{Im}(n^{00}_{++} + \epsilon n^{00}_{00})$	$0.032 \pm 0.059 \pm 0.052$	$0.042 \pm 0.069 \pm 0.033$	$0.050 \pm 0.078 \pm 0.066$
	$\mathrm{Im}(n^{0+}_{0+} - n^{-0}_{0+})$	$0.037 \pm 0.038 \pm 0.012$	$-0.029 \pm 0.045 \pm 0.013$	$0.046 \pm 0.052 \pm 0.039$
	$\mathrm{Im}\, n^{-+}_{-+}$	$0.022 \pm 0.084 \pm 0.025$	$0.116 \pm 0.080 \pm 0.076$	$-0.173 \pm 0.088 \pm 0.083$
	$\mathrm{Im}(n^{++}_{++} + n^{--}_{++} + 2\epsilon n^{++}_{00})$	$0.047 \pm 0.066 \pm 0.017$	$0.012 \pm 0.066 \pm 0.020$	$-0.061 \pm 0.063 \pm 0.050$
	$\mathrm{Im}\, s^{-+}_{-+}$	$-0.031 \pm 0.081 \pm 0.040$	$-0.021 \pm 0.076 \pm 0.051$	$-0.252 \pm 0.085 \pm 0.056$
	$\mathrm{Im}(s^{0+}_{0+} - s^{-0}_{0+})$	$0.074 \pm 0.036 \pm 0.011$	$0.041 \pm 0.038 \pm 0.013$	$0.063 \pm 0.044 \pm 0.017$
$\gamma^*_T \to \rho^0_L$	$\mathrm{Im}\, n^{00}_{0+}$	$-0.100 \pm 0.040 \pm 0.030$	$-0.088 \pm 0.042 \pm 0.033$	$-0.129 \pm 0.049 \pm 0.030$
	$\mathrm{Im}(n^{0+}_{++} - n^{-0}_{++} + 2\epsilon n^{0+}_{00})$	$-0.111 \pm 0.052 \pm 0.055$	$-0.016 \pm 0.055 \pm 0.017$	$-0.033 \pm 0.055 \pm 0.021$
	$\mathrm{Im}\, n^{0+}_{-+}$	$0.130 \pm 0.057 \pm 0.076$	$-0.018 \pm 0.065 \pm 0.031$	$0.018 \pm 0.079 \pm 0.023$
	$\mathrm{Im}\, s^{00}_{0+}$	$0.059 \pm 0.039 \pm 0.016$	$0.044 \pm 0.044 \pm 0.023$	$0.001 \pm 0.049 \pm 0.018$
	$\mathrm{Im}(s^{0+}_{++} - s^{-0}_{++} + 2\epsilon s^{0+}_{00})$	$0.008 \pm 0.046 \pm 0.020$	$0.009 \pm 0.052 \pm 0.023$	$0.049 \pm 0.050 \pm 0.021$
	$\mathrm{Im}\, s^{0+}_{-+}$	$-0.078 \pm 0.059 \pm 0.037$	$0.070 \pm 0.068 \pm 0.024$	$-0.098 \pm 0.075 \pm 0.046$
$\gamma^*_L \to \rho^0_T$	$\mathrm{Im}(n^{++}_{0+} + n^{--}_{0+})$	$0.050 \pm 0.037 \pm 0.008$	$0.032 \pm 0.033 \pm 0.025$	$0.028 \pm 0.033 \pm 0.012$
	$\mathrm{Im}\, n^{-+}_{0+}$	$-0.003 \pm 0.025 \pm 0.009$	$-0.007 \pm 0.022 \pm 0.010$	$-0.024 \pm 0.026 \pm 0.010$
	$\mathrm{Im}(s^{++}_{0+} + s^{--}_{0+})$	$-0.025 \pm 0.035 \pm 0.013$	$0.024 \pm 0.030 \pm 0.020$	$0.016 \pm 0.033 \pm 0.020$
	$\mathrm{Im}\, s^{-+}_{0+}$	$0.016 \pm 0.025 \pm 0.018$	$-0.001 \pm 0.022 \pm 0.013$	$0.000 \pm 0.025 \pm 0.016$
$\gamma^*_T \to \rho^0_{-T}$	$\mathrm{Im}(n^{0-}_{0+} - n^{+0}_{0+})$	$0.029 \pm 0.035 \pm 0.014$	$0.049 \pm 0.037 \pm 0.014$	$0.046 \pm 0.048 \pm 0.016$
	$\mathrm{Im}(n^{-+}_{++} + \epsilon n^{-+}_{00})$	$0.044 \pm 0.038 \pm 0.011$	$0.045 \pm 0.035 \pm 0.017$	$-0.027 \pm 0.035 \pm 0.017$
	$\mathrm{Im}\, n^{++}_{-+}$	$0.091 \pm 0.046 \pm 0.015$	$0.037 \pm 0.045 \pm 0.028$	$-0.031 \pm 0.048 \pm 0.015$
	$\mathrm{Im}(s^{0-}_{0+} - s^{+0}_{0+})$	$-0.062 \pm 0.038 \pm 0.014$	$-0.015 \pm 0.038 \pm 0.028$	$-0.017 \pm 0.044 \pm 0.017$
	$\mathrm{Im}(s^{-+}_{++} + \epsilon s^{-+}_{00})$	$0.068 \pm 0.034 \pm 0.013$	$0.003 \pm 0.034 \pm 0.016$	$-0.032 \pm 0.032 \pm 0.013$
	$\mathrm{Im}\, s^{++}_{-+}$	$0.001 \pm 0.046 \pm 0.032$	$-0.057 \pm 0.046 \pm 0.047$	$0.124 \pm 0.049 \pm 0.033$
double spin flip	$\mathrm{Im}\, n^{00}_{-+}$	$-0.232 \pm 0.094 \pm 0.053$	$-0.070 \pm 0.108 \pm 0.063$	$0.164 \pm 0.131 \pm 0.038$
	$\mathrm{Im}\, n^{+0}_{-+}$	$-0.007 \pm 0.049 \pm 0.015$	$-0.024 \pm 0.055 \pm 0.029$	$0.075 \pm 0.073 \pm 0.065$
	$\mathrm{Im}\, n^{+-}_{0+}$	$-0.008 \pm 0.024 \pm 0.009$	$0.007 \pm 0.022 \pm 0.008$	$-0.006 \pm 0.025 \pm 0.009$
	$\mathrm{Im}\, n^{+-}_{-+}$	$0.037 \pm 0.067 \pm 0.019$	$-0.128 \pm 0.061 \pm 0.036$	$0.164 \pm 0.073 \pm 0.082$
	$\mathrm{Im}\, s^{00}_{-+}$	$0.122 \pm 0.091 \pm 0.068$	$-0.006 \pm 0.126 \pm 0.069$	$-0.045 \pm 0.134 \pm 0.089$
	$\mathrm{Im}\, s^{+0}_{-+}$	$-0.064 \pm 0.052 \pm 0.017$	$0.023 \pm 0.058 \pm 0.024$	$-0.005 \pm 0.064 \pm 0.020$
	$\mathrm{Im}\, s^{+-}_{0+}$	$0.025 \pm 0.025 \pm 0.007$	$-0.013 \pm 0.023 \pm 0.009$	$0.011 \pm 0.025 \pm 0.010$
	$\mathrm{Im}\, s^{+-}_{-+}$	$-0.095 \pm 0.067 \pm 0.047$	$0.052 \pm 0.065 \pm 0.035$	$-0.017 \pm 0.071 \pm 0.044$

Table F.7: The transverse SDMEs in exclusive ρ^0 production in bins of x_B ordered in classes by horizontal lines accorind to the hierarchy predicted by factorization theorem. The presented uncertainties do not include the 8.1 % scale uncertainty from the target polarisation measurement.

transition	SDME	$0.00 < -t' < 0.05$ GeV^2 $\langle Q^2 \rangle = 1.89$ GeV^2 $\langle x_B \rangle = 0.08$ $\langle t' \rangle = 0.02$ GeV^2	$0.05 < -t' < 0.10$ GeV^2 $\langle Q^2 \rangle = 1.97$ GeV^2 $\langle x_B \rangle = 0.08$ $\langle t' \rangle = 0.07$ GeV^2	$0.10 < -t' < 0.20$ GeV^2 $\langle Q^2 \rangle = 1.97$ GeV^2 $\langle x_B \rangle = 0.09$ $\langle t' \rangle = 0.15$ GeV^2	$0.20 < -t' < 0.40$ GeV^2 $\langle Q^2 \rangle = 2.00$ GeV^2 $\langle x_B \rangle = 0.09$ $\langle t' \rangle = 0.28$ GeV^2
$\gamma^*_L \to \rho^0_L$ $\gamma^*_T \to \rho^0_T$	$\mathrm{Im}(n^{00}_{++} + \epsilon n^{00}_{00})$	$0.079 \pm 0.067 \pm 0.025$	$-0.010 \pm 0.083 \pm 0.046$	$-0.010 \pm 0.077 \pm 0.088$	$0.037 \pm 0.089 \pm 0.085$
	$\mathrm{Im}(n^{0+}_{0+} - n^{-0}_{0+})$	$0.003 \pm 0.042 \pm 0.026$	$0.035 \pm 0.053 \pm 0.039$	$-0.042 \pm 0.050 \pm 0.050$	$0.092 \pm 0.060 \pm 0.062$
	$\mathrm{Im}\, n^{-+}_{-+}$	$-0.003 \pm 0.090 \pm 0.065$	$-0.024 \pm 0.109 \pm 0.077$	$0.002 \pm 0.098 \pm 0.041$	$0.085 \pm 0.106 \pm 0.021$
	$\mathrm{Im}(n^{++}_{++} + n^{--}_{++} + 2\epsilon n^{++}_{00})$	$0.001 \pm 0.073 \pm 0.034$	$-0.016 \pm 0.087 \pm 0.057$	$-0.022 \pm 0.076 \pm 0.036$	$0.114 \pm 0.079 \pm 0.043$
	$\mathrm{Im}\, s^{-+}_{-+}$	$0.049 \pm 0.091 \pm 0.029$	$-0.166 \pm 0.106 \pm 0.060$	$-0.239 \pm 0.095 \pm 0.066$	$-0.041 \pm 0.106 \pm 0.087$
	$\mathrm{Im}(s^{0+}_{0+} - s^{-0}_{0+})$	$0.024 \pm 0.038 \pm 0.007$	$0.035 \pm 0.047 \pm 0.012$	$0.127 \pm 0.044 \pm 0.035$	$0.050 \pm 0.055 \pm 0.022$
$\gamma^*_T \to \rho^0_L$	$\mathrm{Im}\, n^{00}_{0+}$	$-0.076 \pm 0.044 \pm 0.019$	$-0.143 \pm 0.053 \pm 0.039$	$-0.136 \pm 0.051 \pm 0.057$	$-0.077 \pm 0.058 \pm 0.043$
	$\mathrm{Im}(n^{0+}_{++} - n^{-0}_{++} + 2\epsilon n^{0+}_{00})$	$-0.081 \pm 0.056 \pm 0.026$	$0.019 \pm 0.068 \pm 0.017$	$-0.096 \pm 0.061 \pm 0.033$	$-0.069 \pm 0.066 \pm 0.070$
	$\mathrm{Im}\, n^{0+}_{-+}$	$0.033 \pm 0.070 \pm 0.031$	$-0.118 \pm 0.082 \pm 0.029$	$0.164 \pm 0.075 \pm 0.032$	$0.203 \pm 0.084 \pm 0.115$
	$\mathrm{Im}\, s^{00}_{0+}$	$0.019 \pm 0.041 \pm 0.003$	$0.068 \pm 0.053 \pm 0.016$	$0.040 \pm 0.049 \pm 0.039$	$-0.001 \pm 0.058 \pm 0.010$
	$\mathrm{Im}(s^{0+}_{++} - s^{-0}_{++} + 2\epsilon s^{0+}_{00})$	$-0.025 \pm 0.053 \pm 0.015$	$0.082 \pm 0.062 \pm 0.020$	$-0.018 \pm 0.058 \pm 0.019$	$0.020 \pm 0.067 \pm 0.037$
	$\mathrm{Im}\, s^{0+}_{-+}$	$-0.121 \pm 0.069 \pm 0.060$	$0.060 \pm 0.080 \pm 0.023$	$-0.040 \pm 0.075 \pm 0.023$	$-0.027 \pm 0.085 \pm 0.031$
$\gamma^*_L \to \rho^0_T$	$\mathrm{Im}(n^{++}_{0+} + n^{--}_{0+})$	$0.023 \pm 0.036 \pm 0.022$	$0.060 \pm 0.043 \pm 0.026$	$0.095 \pm 0.039 \pm 0.019$	$-0.019 \pm 0.047 \pm 0.026$
	$\mathrm{Im}\, n^{-+}_{0+}$	$0.000 \pm 0.024 \pm 0.009$	$-0.021 \pm 0.030 \pm 0.009$	$-0.032 \pm 0.028 \pm 0.010$	$-0.013 \pm 0.035 \pm 0.010$
	$\mathrm{Im}(s^{++}_{0+} + s^{--}_{0+})$	$0.026 \pm 0.034 \pm 0.018$	$-0.006 \pm 0.044 \pm 0.006$	$-0.020 \pm 0.036 \pm 0.031$	$0.020 \pm 0.046 \pm 0.011$
	$\mathrm{Im}\, s^{-+}_{0+}$	$0.016 \pm 0.024 \pm 0.010$	$-0.019 \pm 0.031 \pm 0.009$	$0.027 \pm 0.028 \pm 0.010$	$-0.027 \pm 0.033 \pm 0.017$
$\gamma^*_T \to \rho^0_{-T}$	$\mathrm{Im}(n^{0-}_{0+} - n^{+0}_{0+})$	$0.018 \pm 0.041 \pm 0.013$	$0.009 \pm 0.049 \pm 0.006$	$0.074 \pm 0.043 \pm 0.017$	$0.061 \pm 0.055 \pm 0.025$
	$\mathrm{Im}(n^{-+}_{++} + \epsilon n^{-+}_{00})$	$0.052 \pm 0.039 \pm 0.014$	$0.013 \pm 0.047 \pm 0.028$	$-0.025 \pm 0.042 \pm 0.024$	$0.072 \pm 0.047 \pm 0.026$
	$\mathrm{Im}\, n^{++}_{-+}$	$0.089 \pm 0.053 \pm 0.033$	$0.048 \pm 0.062 \pm 0.027$	$-0.022 \pm 0.058 \pm 0.013$	$0.019 \pm 0.064 \pm 0.041$
	$\mathrm{Im}(s^{0-}_{0+} - s^{+0}_{0+})$	$-0.056 \pm 0.037 \pm 0.039$	$0.085 \pm 0.051 \pm 0.007$	$-0.087 \pm 0.045 \pm 0.027$	$-0.068 \pm 0.056 \pm 0.059$
	$\mathrm{Im}(s^{-+}_{++} + \epsilon s^{-+}_{00})$	$0.054 \pm 0.038 \pm 0.016$	$0.019 \pm 0.044 \pm 0.027$	$-0.007 \pm 0.038 \pm 0.013$	$0.023 \pm 0.044 \pm 0.029$
	$\mathrm{Im}\, s^{++}_{-+}$	$0.014 \pm 0.053 \pm 0.030$	$-0.052 \pm 0.067 \pm 0.025$	$-0.005 \pm 0.054 \pm 0.026$	$0.014 \pm 0.057 \pm 0.041$
double spin flip	$\mathrm{Im}\, n^{00}_{-+}$	$-0.055 \pm 0.101 \pm 0.030$	$-0.197 \pm 0.134 \pm 0.077$	$-0.009 \pm 0.128 \pm 0.073$	$-0.136 \pm 0.146 \pm 0.131$
	$\mathrm{Im}\, n^{+0}_{-+}$	$0.077 \pm 0.060 \pm 0.011$	$-0.037 \pm 0.072 \pm 0.032$	$-0.035 \pm 0.064 \pm 0.017$	$-0.039 \pm 0.075 \pm 0.040$
	$\mathrm{Im}\, n^{+-}_{0+}$	$0.005 \pm 0.024 \pm 0.028$	$0.014 \pm 0.030 \pm 0.014$	$0.024 \pm 0.027 \pm 0.029$	$-0.020 \pm 0.034 \pm 0.019$
	$\mathrm{Im}\, n^{+-}_{-+}$	$0.093 \pm 0.074 \pm 0.027$	$-0.079 \pm 0.088 \pm 0.024$	$-0.064 \pm 0.076 \pm 0.025$	$0.007 \pm 0.090 \pm 0.028$
	$\mathrm{Im}\, s^{00}_{-+}$	$0.106 \pm 0.107 \pm 0.084$	$0.005 \pm 0.135 \pm 0.062$	$-0.060 \pm 0.130 \pm 0.091$	$0.033 \pm 0.143 \pm 0.106$
	$\mathrm{Im}\, s^{+0}_{-+}$	$-0.088 \pm 0.056 \pm 0.021$	$-0.168 \pm 0.073 \pm 0.031$	$0.077 \pm 0.067 \pm 0.039$	$0.160 \pm 0.079 \pm 0.058$
	$\mathrm{Im}\, s^{+-}_{0+}$	$0.021 \pm 0.024 \pm 0.013$	$-0.018 \pm 0.033 \pm 0.010$	$0.028 \pm 0.027 \pm 0.021$	$-0.002 \pm 0.033 \pm 0.010$
	$\mathrm{Im}\, s^{+-}_{-+}$	$-0.065 \pm 0.071 \pm 0.043$	$-0.039 \pm 0.093 \pm 0.031$	$0.057 \pm 0.078 \pm 0.040$	$0.023 \pm 0.086 \pm 0.027$

Table F.8: The transverse SDMEs in exclusive ρ^0 production in bins of t' ordered in classes by horizontal lines accorind to the hierarchy predicted by factorization theorem. The presented uncertainties do not include the 8.1 % scale uncertainty from the target polarisation measurement.

Appendix G

Modeling Generalized Parton Distributions

G.1 Parameterizations used by Goeke, Polyakov, Vanderhaeghen

G.1.1 The helicity non-flip GPD H^q

In the **factorized ansatz**, the main constraint on the t-dependences of the GPDs H^q is the first moment of the GPDs given by the elastic Dirac form factors (see equation (2.51)). In this framework, the helicity non-flip GPD H^q for quarks is parameterized as a superposition of t-independent and t-dependent parts:

$$H^q(x,\xi,t) = \frac{1-(1+\kappa_p)t/4M_p^2}{1-t/4M_p^2}\frac{H^q(x,\xi)}{(1-t/0.71)^2}\ , \tag{G.1}$$

where κ_p is the anomalous magnetic moment of the proton. The t-independent part $H^q(x,\xi)$ consists of two components,

$$H^q(x,\xi)\ =\ H^q_{DD}(x,\xi)\ +\ \theta(\xi-|x|)D^q\left(\frac{x}{\xi}\right)\ . \tag{G.2}$$

These are the D-term [45], $D^q\left(\frac{x}{\xi}\right)$, and H^q_{DD} obtained from the double distribution [43, 44] F^q:

$$H^q_{DD}(x,\xi) = \int\limits_{-1}^{1} d\beta \int\limits_{-1+|\beta|}^{1-|\beta|} d\alpha\ \delta(x-\beta-\alpha\xi)\ F^q(\beta,\alpha)\ . \tag{G.3}$$

For each flavor q, the double distribution itself is related to the ordinary PDFs, $q(\beta)$ [43]:

$$F^q(\beta,\alpha) = h(\beta,\alpha)q(\beta), \tag{G.4}$$

where the profile function $h(\beta,\alpha)$ is given as [43]:

$$h(\beta,\alpha) = \frac{\Gamma(2b+2)}{2^{2b+1}\Gamma^2(b+1)} \frac{\left[(1-|\beta|)^2-\alpha^2\right]^b}{(1-|\beta|)^{2b+1}}. \tag{G.5}$$

In case of $\beta > 0$, $q(\beta)$ is the ordinary quark density for the flavor q, $q(\beta) = q_v(\beta) + \bar{q}(\beta)$. The negative β range corresponds to the antiquark density: $q(-\beta) = -\bar{q}(\beta)$. The parameter b characterizes the strength of the ξ dependence of the GPD $H^q(x,\xi)$. The limiting case $b \to \infty$ corresponds to the ξ-independence, *i.e.*, $H^u(x,\xi) = u(x)$, $H^d(x,\xi) = d(x)$ and $H^s(x,\xi) = s(x)$.

In the **Regge ansatz**, the t-dependence is modeled keeping the t-dependence of GPDs in the double distributions, unlike equation (G.2) and equation (G.3):

$$F^q(\beta,\alpha,t) = F^q(\beta,\alpha)\frac{1}{|\beta|^{\alpha' t}} , \tag{G.6}$$

where α' is the slope of the Regge trajectory, $\alpha' = 0.8$ GeV^{-2} [18].

G.1.2 The helicity-flip GPD E^q

The parameterization for helicity-flip quark GPDs E^q is more complicated, since there is no constraints on its x-dependences in the forward limit (see Section 2.4.4). In the **Regge ansatz**, the t-dependence is modeled in analogy to equation (G.6). In the **factorized ansatz** the helicity-flip quark GPD E^q is given similarly as a superposition of t-independent and t-dependent parts [16],

$$E^q(x,\xi,t) = \frac{E^q(x,\xi)}{(1-t/0.71)^2} , \tag{G.7}$$

where the t-independence is constrained by the Pauli form factor (see equation (2.51)). The t-independent part is parameterized using the double distribution ansatz with an opposite sign of D-term with respect to $H^q(x,\xi)$:

$$E^q(x,\xi) = E^q_{DD}(x,\xi) - \theta(\xi-|x|)D^q\left(\frac{x}{\xi}\right) . \tag{G.8}$$

The t-independent part $E^q(x,\xi)$ has a form analogous to the helicity-non flip case:

$$E^q_{DD}(x,\xi) = \int\limits_{-1}^{1} d\beta \int\limits_{-1+|\beta|}^{1-|\beta|} d\alpha\ \delta(x-\beta-\alpha\xi)\ K^q(\beta,\alpha) . \tag{G.9}$$

In the forward limit, the double distribution $K^q(\beta,\alpha)$ reduces to the function $e_q(\beta)$,

$$K^q(\beta,\alpha) = h(\beta,\alpha)\, e_q(\beta) \tag{G.10}$$

which is unknown and can not be related to the DIS data. However a constraint exists for the normalization of $e_q(\beta)$ [16],

$$\int_{-1}^{+1} dx\; e_q(x) \;=\; \kappa_q \;, \tag{G.11}$$

κ_q is the anomalous magnetic moment of quark of flavor q: $\kappa_u = 2\kappa_p + \kappa_n = 1.67$, $\kappa_d = \kappa_p + 2\kappa_n = -2.03$. Under the assumption that the function e_q has the same x-dependence as the valence quark distributions,

$$e_u(x) = 1/2 u_v(x)\kappa_u \;, \qquad e_d(x) = d_v(x)\kappa_d \;, \qquad e_s(x) = 0 \;, \tag{G.12}$$

the Ji's sum rule is evaluated:

$$J^q = \frac{1}{2}\int_{-1}^{1} dx\, x\, \left[\, q(x) + e_q(x) \,\right] \;. \tag{G.13}$$

The total fraction of momentum M_q of the proton carried by the quarks and antiquarks of flavor q and the fraction of momentum M_{q_v} of valence quarks are then given as:

$$M_q = \int_0^1 x\,[q_v(x) + 2\bar{q}(x)]\,dx \;, \qquad\qquad M_{q_v} = \int_0^1 x q_v(x) dx \;. \tag{G.14}$$

Based on the chiral quark soliton model [16], the helicity-flip density e_q is taken as a sum of valence and sea quarks contributions with the sea part narrowly peaked around $x = 0$:

$$e_q(x) = A_q q_v(x) + B_q \delta(x) \;. \tag{G.15}$$

The coefficients A_q and B_q are constrained by the total angular momentum sum rule and the normalization condition

$$A_q \;=\; \frac{2\,J^q \,-\, M_q}{M_{q_v}}, \tag{G.16}$$

$$B_u \;=\; 2\left[\frac{1}{2}\kappa_u - \frac{2J^u - M_u}{M_{u_v}}\right] \;, \tag{G.17}$$

$$B_d \;=\; \kappa_d - \frac{2J^d - M_d}{M_{d_v}}. \tag{G.18}$$

In the given framework, the total angular momenta carried by u- and d-quarks, J^u and J^d, enter directly as free parameters in the parameterization of the helicity-flip GPDs $E^q(x,\xi,t)$ which is exploited to probe the sensitivity of transverse target-spin asymmtery on J^u and J^d.

G.2 Parameterizations used by Ellinghaus, Nowak, Vinnikov, Ye

G.2.1 The helicity non-flip GPD H^g

In the **factorized ansatz**, for the helicity non-flip gluon GPD H^g

$$H^g(x,\xi,t) = \frac{1-(1+\kappa_p)t/4M_p^2}{1-t/4M_p^2}\frac{H^g(x,\xi)}{(1-t/0.71)^2} \ , \tag{G.19}$$

the t-independent part $H^g(x,\xi)$) is directly given by the double distribution,

$$H^g(x,\xi) = H^g_{DD}(x,\xi) = \int\limits_{-1}^{1} d\beta \int\limits_{-1+|\beta|}^{1-|\beta|} d\alpha \ \delta(x-\beta-\alpha\xi) \ \beta F^g(\beta,\alpha) \tag{G.20}$$

with the same form of the profile function $h(\beta,\alpha)$ as in equation (G.5)

$$F_g(\beta,\alpha) = h(\beta,\alpha)g(\beta) \ . \tag{G.21}$$

In the **Regge ansatz**, the t-dependence of the double distributions is modeled as:

$$F^g(\beta,\alpha,t) = F^g(\beta,\alpha)\frac{1}{|\beta|^{\alpha' t}} \ , \tag{G.22}$$

with the slope of the Regge trajectory $\alpha' = 0.25$ GeV^{-2}.

G.3 Parameterizations used by Goloskokov, Kroll

G.3.1 The helicity non-flip GPDs H^q and H^g

The GPDs $H^i(x,\xi,t)$ for valence and sea quarks, as well as for gluons are related to the double distributions $F^i(\beta,\alpha,t)$ by the integral

$$H^i(x,\xi,t) = \int\limits_{-1}^{1} d\beta \int\limits_{-1+|\beta|}^{1-|\beta|} d\alpha\, \delta(\beta+\xi\alpha-x)\, F^i(\beta,\alpha,t) \qquad\qquad i = q_v, \bar{q}, g\,. \tag{G.23}$$

In this framework, the double distributions $F^i(\beta,\alpha,t)$ are parameterized as:

$$F^i(\beta,\alpha,t') = e^{(b_i+\alpha_i' \ln(1/|\beta|))t'}\; h_i(\beta)\, \frac{\Gamma(2n_i+2)}{2^{2n_i+1}\,\Gamma^2(n_i+1)}\, \frac{[(1-|\beta|)^2-\alpha^2]^{n_i}}{(1-|\beta|)^{2n_i+1}}\,, \tag{G.24}$$

and are further decomposed into valence and sea contribution [36]:

$$\begin{aligned} F^{q_v}(\beta,\alpha,t) &= \big[F^q(\beta,\alpha,t) + F^q(-\beta,\alpha,t)\big]\,\Theta(\beta)\,, \\ F^{\bar{q}}(\beta,\alpha,t) &= F^q(\beta,\alpha,t)\,\Theta(\beta) \;-\; F^q(-\beta,\alpha,t)\,\Theta(-\beta)\,. \end{aligned} \tag{G.25}$$

The motivation for parameterizations of the double distributions given by equation (G.24) is given below. At low x the PDFs behave as powers δ_i of x which are assumed to be generated by Regge poles [121], identified with the usual Regge intercepts for valence and sea quarks, $\delta_v = \alpha_i(0)$, and shifted by 1 for gluons[1], $\delta_g = \alpha_g(0) - 1$. In this framework, this behavior of the PDFs is generalized, assuming the t dependence of the double distributions and hence of the GPDs to be also controlled by Regge behavior. At small values of t, two linear Pomeron and Regge trajectories, $\alpha_i = \alpha_i(0) + \alpha_i' t$, are considered. While the Pomeron trajectory is used for gluons and sea quarks, the Regge trajectory corresponds to the valence quarks and represents the family of the leading Regge poles that couple to the valence quarks of the proton (ρ, ω, a_2 and f_2). The trajectories are accompanied by Regge residues assuming to have an exponential t dependence with slop parameters b_i. So the t dependence of the double distribution is given by the form $e^{b_i t}\,|\,\beta|^{\,-\alpha_i' t}$.

In the forward limit the of double distributions are reduced to the usual PDFs:

$$\begin{aligned} h_{q_v}(\beta) &= q_v(\beta)\,\Theta(\beta) && n_{\rm val} = 1\,, \\ h_{\bar{q}}(\beta) &= \bar{q}(|\beta|)\,\mathrm{sign}(\beta) && n_{\rm sea} = 2\,, \\ h_g(\beta) &= |\beta| g(|\beta|) && n_g = 2\,. \end{aligned}$$

[1]The power δ_g is shift by -1 since in gluon GPDs reduces to $xg(x)$ in the forward limit.

At low β, the expansion of the PDFs in powers of δ_i reads:

$$h_i(\beta) = \beta^{-\delta_i} (1-\beta)^{2n_i+1} \sum_{j=0}^{3} c_{ij} \beta^{j/2} , \tag{G.26}$$

which results in a corresponding expansion of the GPDs

$$H_i(x,\xi,t) = \mathrm{e}^{b_i t} \sum_{j=0}^{3} c_{ij} H_{ij}(x,\xi,t) . \tag{G.27}$$

The power δ_g has been extracted [122] from the data on the electroproduction cross section of Zeus and H1 experiments [51, 123, 124]. This result suggests $\delta_{sea} = \delta_g + 1$ for the sea quarks. For the slope of the gluon trajectory the value $\alpha'_g = 0.15$ GeV^{-2} is used and assumed to be $\alpha_{\mathrm{sea}}(t) = \alpha_g(t)$. A standard trajectory is adopted for the valence quarks: $\alpha_{\mathrm{val}}(t) = 0.48 + 0.9t$. Keeping these results on δ_i fixed, the coefficients c_{ij} are fitted to the CTEQ6M gluon and quark PDF [113] in the range $4 < Q^2 < 40$ GeV^2 and $10^{-4} < \beta < 0.5$. The resulted parameters are listed in [19].

The parameter of the gluon residue is fixed from a fit against the HERA data for ρ [51] and ϕ production [124]:

$$b_g = b_{\mathrm{sea}} = 2.58\,\mathrm{GeV}^{-2} + 0.25\,\mathrm{GeV}^{-2} \ln \frac{m^2}{Q^2+m^2} , \tag{G.28}$$

The parameter of the valence quark residue is taken to be zero. This is in accordance with the findings of the nucleon form factor analysis proposed in [114].

G.3.2 The helicity-flip GPD E^q

The construction of the GPD E^q through double distributions is analogous to that of H^q, with the only difference that the forward limit $e(x) = E(x,0,0)$ (which is inaccessible in DIS) has been determined phenomenologically [114]. The parameters of e_{u_v} and e_{d_v} expanded according to

$$e_i(\beta) = \beta^{-\tilde{\delta}_i} (1-\beta)^{2n_i+1} \sum_{j=0}^{3} \tilde{c}_{ij} \beta^{j} , \tag{G.29}$$

are taken from [114].

G.4 Parameterizations used by Diehl, Kugler

G.4.1 The helicity non-flip GPDs H^q and H^g

The GPDs $H^{q(+)}(x,\xi,t) = H^q(x,\xi,t) - H^q(-x,\xi,t)$ and H^g are parameterized using the Regge ansatz based on double distributions [16], where the ξ dependence is generated according to

$$\begin{aligned} H^{q(+)}(x,\xi,t) &= \int_{-1}^{1} d\beta \int_{-1+|\beta|}^{1-|\beta|} d\alpha\ \delta(x-\beta-\xi\alpha)\, h^{(2)}(\beta,\alpha)\, H^{q(+)}(\beta,0,t)\ , \\ H^{g}(x,\xi,t) &= \int_{-1}^{1} d\beta \int_{-1+|\beta|}^{1-|\beta|} d\alpha\ \delta(x-\beta-\xi\alpha)\, h^{(2)}(\beta,\alpha)\, H^{g}(\beta,0,t) \end{aligned} \tag{G.30}$$

with

$$h^{(b)}(\beta,\alpha) = \frac{\Gamma(2b+2)}{2^{2b+1}\Gamma^2(b+1)} \frac{[(1-|\beta|)^2-\alpha^2]^b}{(1-|\beta|)^{2b+1}}\ . \tag{G.31}$$

The distributions at zero skewness ($\xi = 0$) are taken as

$$\begin{aligned} H^{q(+)}(x,0,t) &= q_v(x)\, e^{t f_{q_v}(x)} + 2\,\bar{q}(x) e^{t f_{\bar{q}}(x)}\ , \\ H^{g}(x,0,t) &= x g(x)\, e^{t f_g(x)}\ , \end{aligned} \tag{G.32}$$

where the $q_v(x) = q(x) - \bar{q}(x)$, $\bar{q}(x)$ and $g(x)$ are the usual PDFs for valence quarks, antiquarks and gluons, respectively, for which the CTEQ6M parameterization [113] has been used. The t dependence of the double distributions is modeled as an exponential behavior in t with an x dependent slope [16]:

$$f_{q_v}(x) = \alpha'_v (1-x)^3 \ln\frac{1}{x} + B_{q_v}(1-x)^3 + A_{q_v} x(1-x)^2 \tag{G.33}$$

for valence quarks, with parameters $\alpha'_v = 0.9$ GeV^{-2}.

Since the first Mellin x-moments of GPDs $H^q(x,0,t)$ are related to the electromagnetic Dirac form factors of proton and neutron by appropriate quark flavor combinations,

$$F_1^q(t) \int_{-1}^{1} dx\, H^q(x,0,t) = \int_{0}^{1} dx\, q_v(x)\, e^{t f_{q_v}(x)}\ . \tag{G.34}$$

the parameters $A_{u_v} = 1.26$ GeV^{-2}, $A_{d_v} = 3.82$ GeV^{-2}, $B_{u_v} = 0.59$ GeV^{-2} and $B_{d_v} = 0.32$ GeV^{-2} are obtained from the fits of $H_v^q(x,0,t)$ to the form factor data treating those parameters as free [114].

For gluons the t dependence of the double distributions is modeled as

$$f_g(x) = \alpha'_g (1-x)^2 \ln\frac{1}{x} + B_g (1-x)^2 \,, \tag{G.35}$$

with $\alpha'_g = 0.164$ GeV^{-2} and $B_g = 1.2$ GeV^{-2} matching the recent H1 data [125] on J/Ψ photoproduction.

For antiquarks, as an simple ansatz, their slope functions $f_{\bar{q}_v}$ are taken equal to those of the valence quarks,

$$f_{\bar{u}} = f_{u_v} \,, \qquad f_{\bar{d}} = f_{d_v} \,, \qquad f_{\bar{s}} = f_{d_v} \,, \tag{G.36}$$

since nothing is so far known about their t dependences.

G.4.2 The helicity-flip GPDs E^q and E^g

Similar to the equation (G.30), the Regge ansatz based on the double distributions have been used to parameterize the nucleon helicity-flip distributions $E^{q,g}$:

$$\begin{aligned} E^{q(+)}(x,\xi,t) &= \int\limits_{-1}^{1} d\beta \int\limits_{-1+|\beta|}^{1-|\beta|} d\alpha\; \delta(x-\beta-\xi\alpha)\, h^{(2)}(\beta,\alpha)\, E^{q(+)}(\beta,0,t) \,, \\ E^{g}(x,\xi,t) &= \int\limits_{-1}^{1} d\beta \int\limits_{-1+|\beta|}^{1-|\beta|} d\alpha\; \delta(x-\beta-\xi\alpha)\, h^{(2)}(\beta,\alpha)\, E^{g}(\beta,0,t) \end{aligned} \tag{G.37}$$

with the double distributions at $\xi = 0$

$$\begin{aligned} E^{q(+)}(x,0,t) &= e_{q_v}(x)\, e^{t g_{q_v}(x)} + 2 e_{\bar{q}}(x)\, e^{t g_{\bar{q}}(x)} \,, \\ E^{g}(x,0,t) &= x e_g(x)\, e^{t g_g(x)} \,. \end{aligned} \tag{G.38}$$

The forward limit of the valence distribution

$$e_{q_v}(x) = \kappa_q\, N(\alpha_v, \beta_{q_v})\, x^{-\alpha_v} (1-x)^{\beta_{q_v}} \,, \tag{G.39}$$

with the parameters $\alpha_v = 0.55$ and the normalization factor

$$N(\alpha,\beta) = \frac{\Gamma(2-\alpha+\beta)}{\Gamma(1-\alpha)\,\Gamma(1+\beta)} \tag{G.40}$$

is completely unknown. Only the absolute normalization is under the control (see equation (G.11)). The slope functions controlling the t dependence are taken with the same form

as for the GPDs H_v^q:

$$g_{q_v}(x) = \alpha'_v(1-x)^3 \ln\frac{1}{x} + D_{q_v}(1-x)^3 + C_{q_v}x(1-x)^2 \,, \tag{G.41}$$

where $\alpha'_v = 0.9$ GeV^{-2} is taken the same as for the GPD H_v^q. This is motivated by the fact that at very small x the Regge exchanges contributing to H_v^q or to E_v^q are the same, and only their coupling strengths are different. The parameters $\beta_u = 3.99$, $\beta_d = \beta_u + 1.60 = 5.59$, $C_{u_v} = 1.22$ GeV^{-2}, $C_{d_v} = 2.59$ GeV^{-2}, $D_{u_v} = 0.38$ GeV^{-2} and $D_{d_v} = -0.75$ GeV^{-2} are obtained from the fits to the electromagnetic Pauli form factor data of proton and neutron [114].

For antiquarks and gluons the same simple ansatz are used for the forward limit of the distributions as in equation (G.39),

$$e_{\bar{q}}(x) = k_{\bar{q}}\, x^{-\alpha_{\bar{q}}}(1-x)^{\beta_{\bar{q}}} \,, \qquad\qquad e_g(x) = k_g\, x^{-\alpha_g}(1-x)^{\beta_g} \,, \tag{G.42}$$

and for the t dependence in the gluon sector we set

$$g_g(x) = \alpha'_g(1-x)^2 \ln\frac{1}{x} + D_g(1-x)^2 \,. \tag{G.43}$$

There is no information on these distributions, but two theoretical constraints that ensure positive semidefinite densities of partons in the transverse plane [126], which read in the current ansatz as: GPDs reads [114]

$$\left[\frac{e_{\bar{q}}(x)}{\bar{q}(x)}\right]^2 \le 8\mathrm{e}m_p^2 \left[\frac{g_{\bar{q}}(x)}{f_{\bar{q}}(x)}\right]^3 \left[f_{\bar{q}}(x) - g_{\bar{q}}(x)\right] \,, \quad \left[\frac{e_g(x)}{g(x)}\right]^2 \le 8\mathrm{e}m_p^2 \left[\frac{g_g(x)}{f_g(x)}\right]^3 \left[f_g(x) - g_g(x)\right] \tag{G.44}$$

The positivity condition given by equation (G.44) can be fulfilled if D_g is slightly smaller than its counterpart B_g for H^g, $D_g = 1.08$ GeV^{-2} and α'_g as in (**??**), $\alpha'_g = 0.164$ GeV^{-2}.

Assuming a similar small-x behavior of the proton helicity-flip and non-flip distributions, the values $\alpha_{\bar{q}} = 1.25$ and $\alpha_g = 1.10$ are taken in (**??**), which are obtained by fitting the CTEQ6M distributions to a power law in the x range from 10^{-4} to 10^{-3}.

Bibliography

[1] F. Halzen and A. D. Martin, Quarks and Leptons. An Introductory Course in Modern Particle Physics (1984), by John Wiley and Sons, Inc.

[2] J. Arrington, C. D. Roberts, and J. M. Zanotti, J. Phys. **G34**, S23 (2007), nucl-th/0611050.

[3] M. Gell-Mann, Phys. Lett. **8**, 214 (1964).

[4] G. Zweig, CERN-TH-401.

[5] R. P. Feynman, (1969), Proceedings of the 3rd Topical Conference on High Energy Collision of Hadrons.

[6] E. D. Bloom *et al.*, Phys. Rev. Lett. **23**, 930 (1969).

[7] R. P. Feynman, Photon-hadton interaction, 1972.

[8] F. E. Close, Rep. Prog. Phys. **42**, 1285 (1979).

[9] J. D. Bjorken and E. A. Paschos, Phys. Rev. **185**, 1975 (1969).

[10] European Muon Collaboration, J. Ashman *et al.*, Phys. Lett. **B206**, 364 (1988).

[11] European Muon Collaboration, J. Ashman *et al.*, Nucl. Phys. **B328**, 1 (1989).

[12] G. Altarelli and G. Parisi, Nucl. Phys. **B126**, 298 (1977).

[13] Y. L. Dokshitzer, Sov. Phys. JETP **46**, 641 (1977).

[14] J. C. Collins, L. Frankfurt, and M. Strikman, Phys. Rev. **D56**, 2982 (1997), hep-ph/9611433.

[15] X.-D. Ji, Phys. Rev. Lett. **78**, 610 (1997), hep-ph/9603249.

[16] K. Goeke, M. V. Polyakov, and M. Vanderhaeghen, Prog. Part. Nucl. Phys. **47**, 401 (2001), hep-ph/0106012.

[17] M. Diehl, JHEP **09**, 064 (2007), arXiv:0704.1565 [hep-ph].

[18] F. Ellinghaus, W. D. Nowak, A. V. Vinnikov, and Z. Ye, Eur. Phys. J. **C46**, 729 (2006), hep-ph/0506264.

[19] S. V. Goloskokov and P. Kroll, (2007), arXiv:0708.3569 [hep-ph].

[20] M. Diehl and W. Kugler, Eur. Phys. J. **C52**, 933 (2007), arXiv:0708.1121 [hep-ph].

[21] L. N. Hand, Phys. Rev. **129**, 1834 (1963).

[22] M. L. Perl, *High Energy Hadron Physics* (Wiley-Sons, 1974).

[23] T. H. Bauer, R. D. Spital, D. R. Yennie, and F. M. Pipkin, Rev. Mod. Phys. **50**, 261 (1978).

[24] J. J. Sakurai, Annals Phys. **11**, 1 (1960).

[25] D. R. Yennie, Rev. Mod. Phys. **47**, 311 (1975).

[26] J. J. Sakurai, Phys. Rev. Lett. **22**, 981 (1969).

[27] C. del Papa *et al.*, Phys. Rev. **D19**, 1303 (1979).

[28] E665 Collaboration, M. R. Adams *et al.*, Z. Phys. **C74**, 237 (1997).

[29] P. D. B. Collins, Cambridge 1977, 445p.

[30] A. Donnachie and P. V. Landshoff, Phys. Lett. **B478**, 146 (2000), hep-ph/9912312.

[31] A. Donnachie and P. V. Landshoff, Phys. Lett. **B296**, 227 (1992), hep-ph/9209205.

[32] A. V. Belitsky and D. Mueller, Nucl. Phys. **A711**, 118 (2002), hep-ph/0206306.

[33] M. Diehl and S. Sapeta, Eur. Phys. J. **C41**, 515 (2005), hep-ph/0503023.

[34] S. J. Brodsky, L. Frankfurt, J. F. Gunion, A. H. Mueller, and M. Strikman, Phys. Rev. **D50**, 3134 (1994), hep-ph/9402283.

[35] X.-D. Ji, J. Phys. **G24**, 1181 (1998), hep-ph/9807358.

[36] M. Diehl, Phys. Rept. **388**, 41 (2003), hep-ph/0307382.

[37] R. Jakob, (2002), postdoctoral thesis.

[38] M. Diehl, Eur. Phys. J. **C25**, 223 (2002), hep-ph/0205208.

[39] M. Burkardt, Phys. Rev. **D62**, 094003 (2000), hep-ph/0005209.

[40] Spin Muon Collaboration, B. Adeva *et al.*, Phys. Rev. **D60**, 072004 (1999).

[41] E143 Collaboration, K. Abe *et al.*, Phys. Lett. **B364**, 61 (1995), hep-ex/9511015.

[42] HERMES Collaboration, A. Airapetian *et al.*, Phys. Rev. **D75**, 012007 (2007), hep-ex/0609039.

[43] A. V. Radyushkin, Phys. Rev. **D59**, 014030 (1999), hep-ph/9805342.

[44] I. V. Musatov and A. V. Radyushkin, Phys. Rev. **D61**, 074027 (2000), hep-ph/9905376.

[45] M. V. Polyakov and C. Weiss, Phys. Rev. **D60**, 114017 (1999), hep-ph/9902451.

[46] LHPC Collaboration, P. Hagler *et al.*, Phys. Rev. **D68**, 034505 (2003), hep-lat/0304018.

[47] QCDSF Collaboration, M. Gockeler *et al.*, Phys. Rev. Lett. **92**, 042002 (2004), hep-ph/0304249.

[48] K. Schilling and G. Wolf, Nucl. Phys. **B61**, 381 (1973).

[49] Particle Data Group, S. Eidelman *et al.*, Phys. Lett. **B592**, 1 (2004).

[50] ZEUS Collaboration, J. Breitweg *et al.*, Eur. Phys. J. **C12**, 393 (2000), hep-ex/9908026.

[51] H1 Collaboration, C. Adloff *et al.*, Eur. Phys. J. **C13**, 371 (2000), hep-ex/9902019.

[52] HERMES Collaboration, A. Airapetian *et al.*, European Physical Journal **C**.

[53] A. C. Irving and R. P. Worden, Phys. Rept. **34**, 117 (1977).

[54] A. A. Sokolov and I. M. Ternov, Phys. Dokl. **8**, 1203 (1964).

[55] M. Beckmann *et al.*, Nucl. Instrum. Meth. **A479**, 334 (2002), physics/0009047.

[56] D. P. Barber *et al.*, Nucl. Instrum. Meth. **A329**, 79 (1993).

[57] HERMES Collaboration, A. Airapetian *et al.*, Nucl. Instrum. Meth. **A540**, 68 (2005), physics/0408137.

[58] A. Nass *et al.*, Nucl. Instrum. Meth. **A505**, 633 (2003).

[59] C. Baumgarten *et al.*, Nucl. Instrum. Meth. **A496**, 277 (2003).

[60] C. Baumgarten *et al.*, Nucl. Instrum. Meth. **A508**, 268 (2003).

[61] HERMES Target Group, C. Baumgarten *et al.*, Nucl. Instrum. Meth. **A482**, 606 (2002).

[62] HERMES Collaboration, A. Airapetian *et al.*, Eur. Phys. J. **D29**, 21 (2004), physics/0408138.

[63] HERMES Collaboration, K. Ackerstaff *et al.*, Nucl. Instrum. Meth. **A417**, 230 (1998), hep-ex/9806008.

[64] M. G. Beuzekom, E. Garutti, D. Heesbeen, J. J. M. Steijger, and J. Visser, Nucl. Instrum. Meth. **A461**, 247 (2001).

[65] J. T. Brack *et al.*, Nucl. Instrum. Meth. **A469**, 47 (2001).

[66] A. Andreev *et al.*, Nucl. Instrum. Meth. **A465**, 482 (2001).

[67] S. Bernreuther *et al.*, Nucl. Instrum. Meth. **A416**, 45 (1998), hep-ex/9803005.

[68] W. Wander, DESY-HERMES-96-23.

[69] W. Augustyniak *et al.*, DESY-HERMES-07-008.

[70] N. Akopov *et al.*, Nucl. Instrum. Meth. **A479**, 511 (2002), physics/0104033.

[71] H. Avakian *et al.*, Nucl. Instrum. Meth. **A417**, 69 (1998), hep-ex/9810004.

[72] J. Wendland, DESY-THESIS-2003-032.

[73] T. Benisch *et al.*, Nucl. Instrum. Meth. **A471**, 314 (2001).

[74] CERN Programming Techniques Group, ADAMO - Entity-Relationship Programming System, Users Guide, Version 3.3, 1993.

[75] Offline Data Quality, `http://www-hermes.desy.de/groups/daqlgrp/OFFLINE_DQ/uDST/`.

[76] Beam energy correction, `http://www-hermes.desy.de/PLOTS/0703/zaven/newbeamenergy.pdf`.

[77] T. Sjostrand, L. Lonnblad, S. Mrenna, and P. Skands, (2003), hep-ph/0308153.

[78] M. Tytgat, DESY-THESIS-2001-018.

[79] HERMES Collaboration, `http://www-hermes.desy.de/hmc/RhoMC/index.html`.

[80] P. Liebing, DESY-THESIS-2004-036.

[81] A. Hillenbrand, DESY-THESIS-2005-036.

[82] P. Liebing, Internal-Report-03-020.

[83] I. Akushevich, H. Bottcher, and D. Ryckbosch, (1998), hep-ph/9906408.

[84] T. Sjostrand, Comput. Phys. Commun. **82**, 74 (1994).

[85] B. Andersson, Camb. Monogr. Part. Phys. Nucl. Phys. Cosmol. **7**, 1 (1997).

[86] CERN Computing and Network Division, (1993), CERN Program Library Long Writeup W5013.

[87] L. W. Mo and Y.-S. Tsai, Rev. Mod. Phys. **41**, 205 (1969).

[88] T. Sjostrand, Int. J. Mod. Phys. **A3**, 751 (1988).

[89] D. G. Cassel *et al.*, Phys. Rev. **D24**, 2787 (1981).

[90] HERMES Collaboration, A. Airapetian *et al.*, Eur. Phys. J. **C17**, 389 (2000), hep-ex/0004023.

[91] HERMES Collaboration, K. Ackerstaff *et al.*, Eur. Phys. J. **C18**, 303 (2000), hep-ex/0002016.

[92] CLAS Collaboration, C. Hadjidakis *et al.*, Phys. Lett. **B605**, 256 (2005), hep-ex/0408005.

[93] A. Kreisel, DESY-THESIS.

[94] A. Levy, Private Comunications.

[95] P. Joos *et al.*, Nucl. Phys. **B113**, 53 (1976).

[96] M. Diehl and A. V. Vinnikov, Phys. Lett. **B609**, 286 (2005), hep-ph/0412162.

[97] A. Bacchetta, U. D'Alesio, M. Diehl, and C. A. Miller, Phys. Rev. **D70**, 117504 (2004), hep-ph/0410050.

[98] J. Dreschler and A. Rostomyan, `http://www-hermes.desy.de/reports/0407/AUT-exclrho/release-AUTexclrho-p%relim.pdf`, Release report.

[99] HERMES Collaboration, A. Rostomyan and J. Dreschler, (2007), arXiv:0707.2486 [hep-ex].

[100] S. V. Goloskokov and P. Kroll, Eur. Phys. J. **C42**, 281 (2005), hep-ph/0501242.

[101] J. Dreschler and A. Rostomyan, `http://www-hermes.desy.de/reports/0205/TSSA-rho/ami+jeroen_release.ps.g%z`, Release report.

[102] C. A. Miller, `http://www-hermes.desy.de/groups/mgmtgrp/COLLABMEETINGS/TRANSVERSITY_JUNE06/MaxLike.pdf`, Maximum Likelihood.

[103] F. T. Solmitz, Ann. Rev. Nucl. Part. Sci. **14**, 375 (1964).

[104] A. Bruell and A. Kisselev, Top/bottom misalignment for 1996-2003 data (2003), http://www-hermes.desy.de/majord/arch.closed/offline-list/msg090603.0.t%xt.

[105] S. Manaenkov, (2008), private communication.

[106] HERMES Collaboration, A. Airapetian *et al.*, Phys. Rev. Lett. **94**, 012002 (2005), hep-ex/0408013.

[107] HERMES Collaboration, A. Airapetian *et al.*, Phys. Lett. **B648**, 164 (2007), hep-ex/0612059.

[108] J. Botts and G. Sterman, Nucl. Phys. **B325**, 62 (1989).

[109] D. Y. Ivanov, (2007), 0712.3193.

[110] M. Goekeler *et al.*, Phys. Rev. Lett. **92**, 042002 (2004).

[111] LHPC Collaboration, P. Hagler *et al.*, (2007), 0705.4295.

[112] QCDSF-UKQCD Collaboration, D. Brommel *et al.*, PoS **LAT2007**, 158 (2007), 0710.1534.

[113] J. Pumplin *et al.*, JHEP **07**, 012 (2002), hep-ph/0201195.

[114] M. Diehl, T. Feldmann, R. Jakob, and P. Kroll, Eur. Phys. J. **C39**, 1 (2005), hep-ph/0408173.

[115] HERMES Collaboration, A. Airapetian *et al.*, (2008), arXiv:0802.2499 [hep-ex].

[116] Compass Collaboration, N. D'HOSE, Presentation at DSPIN07 conference (2007), http://theor.jinr.ru/~spin/Spin-Dubna07/1%2003MoB/1%20d%27Hose/NdH_GPD_%DubnaSpin_2007.pdf.

[117] H. Avakian *et al.*, JLab proposal E-08-015 (2008), http://www.jlab.org/~avakian/talks/PAC/pac33.sidis.HDIce.pdf.

[118] H. Avakian *et al.*, JLab proposal (2008), http://www.jlab.org/~avakian/upgrade/pac30/pac30loiaut.pdf.

[119] Luminocity Constant, http://www-hermes.desy.de/groups/daqlgrp/OFFLINE_DQ/uDST/general/docu/D%ISstats.html.

[120] C. Hadjidakis and D. Hasch, Release report (2004).

[121] P. V. Landshoff and J. C. Polkinghorne, Nucl. Phys. **B28**, 240 (1971).

[122] S. V. Goloskokov and P. Kroll, Eur. Phys. J. **C50**, 829 (2007), hep-ph/0611290.

[123] ZEUS Collaboration, J. Breitweg *et al.*, Eur. Phys. J. **C6**, 603 (1999), hep-ex/9808020.

[124] ZEUS Collaboration, S. Chekanov *et al.*, Nucl. Phys. **B718**, 3 (2005), hep-ex/0504010.

[125] H1 Collaboration, A. Aktas *et al.*, Eur. Phys. J. **C46**, 585 (2006), hep-ex/0510016.

[126] M. Burkardt, Phys. Lett. **B582**, 151 (2004), hep-ph/0309116.

Acknowledgements

With the last pages of my thesis, where I have summarized all I have done in the last years (in physics), I also complete this phase in my life consisting of writing, writing and writing... It's finally nice sunny summer weather outside and now I say 'thank you so very much' to all of you, it's time to go out for a sunny day...

First of all I would like to thank all my supervisors who supported me in my thesis work. My thanks go to Wolf-Dieter Nowak and Yorck Holler who gave me the opportunity to work at HERMES and to accomplish this thesis. Special thanks to Wolf-Dieter who gave me the freedom to find my way in the analysis and in understanding of physics. Thanks a lot for carefully proofreading in the final stage when I learned even more during the discussions and from the question marks 'why?' on the drafts of my thesis.

I would also like to give my gratitude to Prof. Dr. Rolf-Dieter Heuer, who had taken over the role of my official supervisor at the Hamburg university and to Prof. Dr. Joachim Meyer, who was so kind to agree to substitute Prof. Dr. Rolf-Dieter Heuer in the final stage.

Many HUGE thanks go to Elke-Caroline Aschenauer, who always believed that 'I can do that!' even when I was not even sure how to do "that"; who's always been available to help when I got stuck during my work and cheer me up when I felt lost; always had a minute (actually often hours!) for discussions, even being overloaded with her own work.

I appreciate the help and support from Delia Hasch. It was always a pleasure to discuss the physics aspects of the analysis, motivations, goals. She was always available even not being in Hamburg; helped me not to loose the overview on the important stuff and not let it bury in too many unimportant details. I hope I have learned a little bit from her to put the emphasize in the right place.

I am thankful to HERMES management for supporting my attendance to various workshops and conferences all around the world. There I learned not only physics, but also have seen different cultures and realized that things might be different from what one is used to.

I have enjoyed the great atmosphere in the HERMES collaboration, being surrounded with so many nationalities and having so many possibilities to learn a lot from them. Besides the physics discussions it was such a pleasure to do little chats, shopping and dining in sushi bars

with Elke; getting lost in Venice with Charlotte late at night and being guided back by a stranger; sharing a hotel room with Delia when it is too noisy in her room because of an all-night-long music festival right under her window; playing darts and bowling, watching soccer and having drinks with Achim, Alessandro, Andy, Antje, Beni, Caro, Craig, Dominik, Ed K., Frank, Jim, Josh, Ivana, Luciano, Markus, Naomi, Rebbecca and Uli. Thanks to Gunar I know how to make ikebanas (in the airport) now.

To all my italian colleagues (a looong list) and especially the Frascati group (of course including Cynthia and Delia) - it took me quite a while till I convinced everyone that I am NOT actually a member of the Frascati group, neither italian, though often I feel I am! Alessandra, Cynthia, Delia, Enzo, Nicola, Pasquale, thanks for all the lovely dinners and barbecues and great hospitality I enjoyed every time visiting Frascati! The beautiful italian music I borrowed from Paolo, chatting with Riccardo on the way to the office and sharing the office with Ignazio - I enjoyed that all a lot!

It was a real pleasure to know Aaron, Alexander, Andreas, Bino, Bohdan, Henk, Ingrid, Inti, Larry, both Yoshis, Patty, Paul, Polina, Roberto, Sabine, Shibata-san, Taiki, Wolfgang, Wouter, Yves, Zhenyu. I could have missed a few names, sorry if I did!

I did not work on this very old (VMD) and the same time very young (GPD) topic alone but together with the exclusive group: Avetik, Delia, Cynthia (for any question I got a complete answer, thanks a lot), and Jeroen. We had hard time trying to find that last missing ρ^0 to complete the cross check, digesting the maximum likelyhood technique, and had very useful discussions even when we had no time for that.

Whenever I had problems with Maximum Likelihood I knew I can ask Andy, Luciano and Markus.

While working on the rhoMC Monte Carlo generator and trying to understand what goes wrong there, I usually got useful hints from Elke, Cynthia, Bohdan and Matthias. Thanks a lot for your help to bring the rhoMC to the shape it is in now.

And of course I can not deny the help from the theory side. Being an experimentalist, I had a lot of questions 'why' and 'how'... Thanks to Markus Diehl for being available for any discussion and explaining things without loading me with formulas. I appreciate the very useful discussions also with Thorsten Feldman, Sergey Goloskokov, Peter Kroll, Sergey Manaenkov and Andrey Vinnikov.

And last but not least I want to express my deepest gratitude towards my family and friends. Towards Dr. Gerhard Söhngen and his wife Brigitte who had a strong impact on my life and the life of my family. This thesis wouldn't be possible if not all the help and support from their side.

Each chapter of this thesis contains a background music, - the music provided by Bzzz (can't call you Olga) and my best friend Falz (can't call you Michael either). It was a pleasure to hear

that nice music while writing the thesis. Iga, I know you always had your fingers crossed for me. Gago your energy and optimism cheered me up when I was getting too tired. It is more than thanks that go to my friends and neighbors Lusine and Tigran.

Towards my parents for their love and support, who had inspired me to love the science from my early childhood. If not you, I would never be a physicist. Towards my brothers, Tigran and Hayk, who put a lot of humor in all my life, and made me laugh even when I wanted to cry. I devote this thesis to my late father.

Another 'thank you' goes back to Yerevan, to the family of Ed for their kindness and support.

My very special bunch of emotions goes to Ed. You certainly know what I would like to tell you. Don't you? :) I am really thankful to you since I always knew - whatever happens, you would try to understand and help me. My life, my work would never be what they are now, if not you throughout all these years. To the MOST important person in my life, my son Bert, I am thankful for your never ending love. Even though I didn't always have enough time for you and was being stressed sometimes during writing of this thesis, you were never angry on me and gave me your smile and love in full!